The Influence of Geometric Model Complexity on Near-Wall Flow Phenomena and their Resolution in Large-Eddy Simulations

Dissertation
zur Erlangung des Doktorgrades
an der Fakultät für Mathematik, Informatik und Naturwissenschaften
Fachbereich Erdsystemwissenschaften
der Universität Hamburg

vorgelegt von
Benedikt Paul Hermann Seitzer

Hamburg, 2023

Fachbereich Erdsystemwissenschaften

Datum der Disputation: 29.06.2023

Gutachter/innen der Disertation: Prof. Dr. Bernd Leitl
Prof. Dr. Felix Ament

Zusammensetzung der Prüfungskommission: Prof. Dr. Bernd Leitl
Prof. Dr. Felix Ament
Prof. Dr. Matthias Hort
Prof. Dr. Jörn Behrens
Prof. Dr. Jürgen Böhner

Vorsitzender des Fach-Promotionsausschusses
Erdsystemwissenschaften: Prof. Dr. Hermann Held

Dekan der Fakultät MIN: Prof. Dr. Ing. Norbert Ritter

Abstract

Large-eddy simulation models are increasingly used to study the urban climate. Technological advances in the field of high performance computing enable modelers to calculate urban flow phenomena at increasingly high resolutions. Thus, the focus of urban climate studies using large-eddy simulations is moving gradually closer to the wall. It is particularly in these near-wall regions where two integral components of large-eddy simulations no longer function reliably. Surface boundary conditions, on the one hand, cannot account for heterogeneity in surface roughness. Furthermore, sub-grid scale models are often based on heuristic assumptions about eddy geometries. In the course of this work, two wind-tunnel experiments are designed and carried out at the *Environmental Wind Tunnel Laboratory* using the *WOTAN* wind tunnel. Results of these experiments are then compared to the results of corresponding large-eddy simulation studies carried out with the contemporary urban climate model *PALM*. The aim of the comparison is to validate the replication of near-wall turbulence at rough surfaces in large-eddy simulation models. Findings from both experiments indicate an underestimation of wall-normal turbulent fluxes by *PALM* with respect to the wind-tunnel results. This difference can be significantly eliminated either by artificially increasing the roughness lengths in the surface boundary condition, or by increasing the grid resolution, or by choosing scale-dependent sub-grid scale models. Furthermore, the wind-tunnel flow exhibits near-wall anisotropy of the turbulent motions as a function of surface roughness. The large-eddy simulation results do not show any anisotropy of the turbulent motions near the wall. Future sub-grid scale models must be able to address these differences. Until then, modelers need to cultivate an awareness of the uncertainties of the large-eddy simulation technique especially in the near-wall region.

Keywords: large-eddy simulation, wall-bounded flows, wind tunnel, surface boundary condition, sub-grid scale model, model validation, PALM, urban climate

Kurzfassung

Large-Eddy Simulationen werden zunehmend zur Untersuchung des Stadtklimas eingesetzt. Leistungsstärkere Supercomputer ermöglichen es Modellierern, urbane Strömungsphänomene in immer höherer Auflösung zu berechnen. Damit rückt der Fokus von Stadtklimastudien mit Large-Eddy Simulationen immer weiter in Richtung wandnaher Strömungen. Gerade in Wandnähe funktionieren zwei integrale Bestandteile der Modelle nicht mehr zuverlässig. Zum einen berücksichtigen Oberflächenrandbedingungen die Heterogenität der Oberflächenrauhigkeit nicht. Zum anderen beruhen die Turbulenzparametrisierungen häufig auf heuristischen Annahmen zur Wirbelgeometrie. Im Rahmen dieser Arbeit werden zwei Windkanalexperimente entworfen und im *Environmental Wind Tunnel Laboratory* unter Verwendung des *WOTAN*-Windkanals durchgeführt. Die Ergebnisse dieser Experimente werden dann mit den Ergebnissen entsprechender Large-Eddy Simulationen verglichen, die mit dem Stadtklimamodell *PALM* durchgeführt wurden. Ziel des Vergleichs ist es, die Auflösung von wandnahen Turbulenzen an rauen Oberflächen in Large-Eddy Simulationen zu validieren. Die Ergebnisse deuten darauf hin, dass *PALM* die Intensität der wandnormalen turbulenten Fluktuationen im Vergleich zu den Windkanalergebnissen unterschätzt. Dies kann entweder durch ein künstliches Anheben der Rauhigkeitslängen in der Oberflächenrandbedingung, durch eine Erhöhung der Gitterauflösung, oder durch die Wahl von skalenabhängigen Parametrisierungen behoben werden. In Abhängigkeit von der Oberflächenrauhigkeit ist die Turbulenz der Windkanalströmung zudem unterschiedlich stark anisotrop. Die Ergebnisse der Large-Eddy-Simulation weisen jedoch keine Anisotropie der turbulenten Fluktuationen in Wandnähe auf. Künftige Turbulenzparametrisierungen müssen in der Lage sein, dies zu berücksichtigen. Bis dahin müssen Modellierer ein Bewusstsein für die Unsicherheiten der Large-Eddy Simulationen entwickeln, insbesondere was die wandnahe Strömung betrifft.

Stichworte: Large-Eddy Simulationen, Wandnahe Strömung, Windkanal, Oberflächenrandbedingung, Turbulenzparametrisierung, Modellvalidierung, PALM, Stadtklima

Acknowledgements

First and foremost, I would like to thank my supervisors Bernd Leitl and Felix Ament as well as my panel chair Matthias Hort who supported me not only professionally but also personally. I started my doctoral studies as a fluid dynamicist who had previously dealt with flows more theoretically and numerically than experimentally. As a matter of fact, I have never measured fluid flows experimentally until May 2020. Without the patient, friendly and competent help of Frank Harms, getting started in experimental fluid dynamics would certainly have been more difficult, if not impossible to me. Special thanks go to the University of Hamburg and especially the staff of the Meteorological Institute and the mechanical workshop for their practical support in my work.

I would also like to thank my esteemed colleague and sparring partner Simon Michel. Thank you for the wind-tunnel boundary layer you designed, it saved me a lot of work. Thank you also for the company at the many lunches and for introducing me to the institute's social ecosystem.

I would like to thank my mother Beate, my siblings Carlotta and Konstantin and my grandparents Egon and Hedwig for their love and support. Hedwig in particular took us to the Natural History Museum in Münster almost every month. A factor not to be underestimated.

Georg, Alexander, Öttchen, Mano, Sabeth, Matthias and Johannes, some of you have been with me since I was a child. Talking to you is better than reading a book. Thank you for the leisurely strolls through Hamburg, Berlin, Bochum, Warendorf and Münster. Many thanks to my band mates for constantly making me realise what is really important.

Thanks also to you, Kevin, for taking the trouble to read all the work and put it through its paces. Thank you Veit for the valuable comments on the first and last chapter of this work. You both are friends I can rely on when I need help.

Dear Johanna, thank you for being my partner. You are a great support in my life. Without you, I would not have gone through with the PhD.
You know I dreamed about you, for twenty-nine years before I saw you

Table of Contents

Acronyms

ABL Atmospheric Boundary Layer
BSA Burst Spectrum Analyser
CEN Centrum für Erdsystemforschung und Nachhaltigkeit
CFD Computational Fluid Dynamics
CFL Courant–Friedrichs–Levy
CPU Central Processing Unit
D80 Deardorff 1980
DKRZ Deutsches Klimarechenzentrum
DNS Direct Numerical Simulation
EWTL Environmental Wind Tunnel Laboratory
FFT Fast Fourier Transform
FFTW Fastest Fourer Transform in the West
G91 Germano 1991
IL Instantaneous Logarithm
ISL Inertial Sublayer
JPDF Joint Probability Density Function
K41 Kolmogorov 1941
LDA Laser-Doppler Anemometry
LES Large-Eddy Simulation
MKP Marusic–Kunkel–Porté-Agel
MOST Monin–Obukhov Similarity Theory
MPI Message Passing Interface
NetCDF Network Common Data Form
OpenMP Open Multi-Processing Interface
PALM Parallelised Large-Eddy Simulation Model
PE Processor Element
PIV Particle Image Velocimetry
RANS Reynolds-Averaged Navier–Stokes

RSL Roughness Sublayer
SG Schumann–Grötzbach
SGS Sub-Grid Scale
TKE Turbulence Kinetic Energy
UBL Urban Boundary Layer
UCL Urban Canopy Layer
URSL Urban Roughness Sublayer
USA Ultrasonic Anemometry

1 Introduction

> ”Woran arbeiten Sie?” wurde Herr K. gefragt.
> Herr K. antwortete: ”Ich habe viel Mühe, ich bereite meinen nächsten Irrtum vor.”
>
> **Bertolt Brecht**
> Geschichten vom Herrn Keuner

Global climate is changing and so is urban climate. This leads to a number of climate risks to cities, settlements and key infrastructure, as stated by Dodman et al. (2022) as part of the sixth IPCC report. Very high wind speeds already become more frequent as tropical cyclones and other hazardous events are intensified. Such events can cause structural damage to buildings with insufficient wind load design and urban trees can be uprooted causing human injury. Furthermore, microscale wind conditions affect the dispersion of air pollutants on the street level and the thermal comfort of pedestrians. As wildfires become more frequent in hotter regions, the dispersion of smoke into settled areas becomes increasingly of concern.

Climate change mitigation must therefore be considered by urban planners (Reiter, 2010). Even ten years ago, Castán Broto and Bulkeley (2013) observed a worldwide rise in climate-change mitigation experiments concerning cities. Data-driven decision-making processes are becoming increasingly popular in governance in order to review adaptation measures to crises. This was demonstrated not least by the COVID-19 pandemic.

Urban climate is usually investigated using spatially dependent and temporally highly variable field data (Scherer et al., 2019; Paas et al., 2020) or wind-tunnel experiments, which are usually idealised with respect to heat transfer or precipitation (Allegrini et al., 2013a; Llaguno-Munitxa et al., 2017; Tolias et al., 2018; Gronemeier et al., 2021). Predictive studies with e.g., dynamic boundary conditions, are left to numerical experiments (Letzel et al., 2012; Tolias et al., 2018; Gronemeier and Sühring, 2019; Auvinen et al., 2020). By means of numerical modeling, various realistic scenarios can be examined in advance of adaptation measures. As the urban morphology alters the wind conditions at multiple spatial scales, a sufficient resolution of these geometries is required in urban climate models.

Large-eddy simulations (LES) are one of the most widely used modeling techniques applied to turbulent flows. They are designed to be applied to flow problems mainly dominated by large energy-containing eddies and have therefore been used to study the atmospheric boundary layer. While large-scale eddies dominating the flow are explicitly resolved in an LES, the energy on smaller scales is parameterised. This leads to a gain in computational efficiency with a simultaneous reduction in accuracy for small-scale phenomena compared to direct numerical simulations where all scales are resolved explicitly.

Due to an ongoing increase in computing power, the use of large-eddy-simulation models in the scientific community grows continuously. With over 2500 publications per year, LES are one of the big players in computational fluid dynamics (Fig. 1.1).[1] As higher and higher grid resolutions can be achieved, the variety of applications is expanding towards obstacle-resolving models which are often used in urban climate studies. Thus, in the last 20 years, there has been an increase in urban climate studies making use of LES.

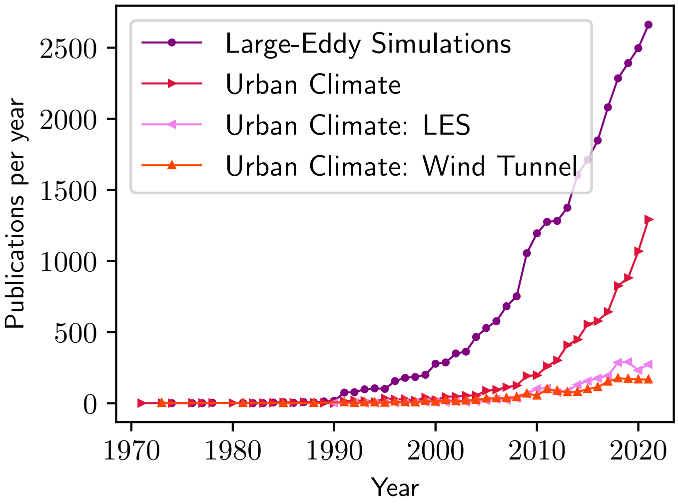

Figure 1.1: Temporal evolution of the publications on the topics of Large-eddy simulations, urban climate and urban climate studies using large-eddy simulations or wind-tunnel experiments.

---

[1] With help of the *Web of Science* all peer-reviewed publications were extracted. The filtering was applied to all publications per year on the topics of: LES, urban climate, urban climate & LES, urban climate & wind tunnel. Over 50% of LES publications come from the mechanical engineering community.

The new possibilities to use LES at very high resolutions for urban climate simulations fuel the demand for near-wall model results. LESs were originally developed to model flows whose largest and energy-carrying eddies are well resolved (eddy size $>>$ grid size). As the scope of simulations enters the near-wall region in urban environments, the energy-containing eddies are increasingly of the order of magnitude of the currently used grid sizes (1 m to 10 m). In this case, most of the flow's energy is parameterised, and, at the same time, the first grid level adjacent to the wall lies well within the flow region directly affected by the surface roughness. This can lead to problems in accuracy, which shall be addressed in this thesis.

1.1 Near-Wall Modeling in Obstacle-Resolving Large-Eddy Simulations

Computation of the near-wall flow in large-eddy simulations is sensitive to mainly two components of the model: the surface boundary conditions and the parameterisation models, referred to as the sub-grid scale models (SGS).

Surface boundary conditions in LES models are usually applied between the surface and the first adjacent grid level. Most of the boundary conditions are based on analytical solutions which are derived under assumptions that are often not fulfilled at urban morphologies. These assumptions usually include homogeneity of the surface roughness and infinitely extended surfaces. In addition, the boundary layer can be divided into sublayers. One of these sublayers is the roughness sublayer. The first grid level must lie far outside this layer in order for the analytical boundary conditions to be calculated properly (Basu and Lacser, 2017). One of the research questions of this thesis is whether a local roughness sublayer can be identified at urban surfaces like building facades, and if so, what are the local flow dynamics in the roughness sublayer?

The parameterising sub-grid scale models are applied at each grid cell in the modeling domain, but play a greater role close to surfaces. Near surfaces, integral eddy sizes decrease. Thus, the relative contribution of parameterised energy is rising if the grid is not adapted accordingly. The most common group of SGS models is based on heuristic assumptions about the mean free path length of the fluid particles (Smagorinsky, 1963; Deardorff, 1980). These models are scale-invariant. However, the mean free path length changes according to the flow case and should not be set in a heuristic way for flows at heterogeneous surface morphologies as in cities. Additionally, SGS models assume local isotropy of small-scale turbulent motions: a prerequisite that is seldomly fulfilled for flows in urban environments. In order to test the validity of the assumptions mentioned above and develop or modify SGS models, it is necessary to examine which statements can be made about the local anisotropy of turbulence close to such surfaces.

For a summary on surface boundary conditions in LES models, the reader is refered to the paper by Hultmark et al. (2013), which gives a good overview of the currently available boundary conditions. When it comes to SGS models for large-eddy simulations, the work of Gadde et al. (2021) provides a good overview.

1.2 Scope of this Work

The aim of this work is to investigate whether the above-mentioned conceptual weaknesses of large-eddy simulations in the vicinity of rough surfaces lead to significant deviations from real flows that are not computed numerically. The findings shall then be converged into practical implications and guidelines for users of large-eddy simulation models in the context of urban climate studies. The following research questions are formulated to gain a deeper understanding of near-wall flows in general and also to assess the extent to which a contemporary LES model performs near rough surfaces:

RQ 1 Can a roughness sublayer be identified in generic cases of flow above aerodynamically rough surfaces and for more complex model geometries?

RQ 2 How are local roughness sublayer dynamics (flow statistics, energy content) at urban building facades characterised?

RQ 3 What statements can be made about the local anisotropy of turbulence close to such surfaces?

RQ 4 Are local near-wall flows properly replicated in a contemporary LES model as *PALM*?

To this end, the results of the LES model *PALM* are compared with wind-tunnel flows. A comparison of the two flows (LES and wind tunnel) proves beneficial, because smaller length scales, which are usually missed by LES models, can still be resolved in wind-tunnel experiments. The parellelised large-eddy simulation model *PALM* is one of the world's most modern and widely used urban climate models (Maronga et al., 2020a). It is used in scientific applications, expert offices and increasingly also in administation and governance. As a real-flow reference, measurements are performed in the boundary-layer wind tunnel *WOTAN* at the *Environmental Wind Tunnel Laboratory* at the University of Hamburg.

Two comparative experiments were designed to answer the questions raised. One is the generic case of a flow over a horizontal surface of homogeneous roughness, the other is the flow around a free-standing building with varying facade roughness.

1.2.1 Thesis Outline

After the first introductory sentences in this chapter, the text proceeds in **Chapter 2** with a presentation of the basic theoretical and methodological principles that are necessary to follow the train of thought or to understand and even replicate the findings presented. The chapter first gives a broad introduction to turbulent flows in general before going into more detail concerning turbulent boundary layer flows in Section 2.2. The basics of the two methods used (LES and wind-tunnel experiments) are presented in Sections 2.3 and 2.4.

In **Chapter 3**, the boundary-layer wind tunnel *WOTAN* and the parallelised large-eddy-simulation model *PALM* are described. Further, the data-processing methods are explained in Section 3.2 such that all calculated flow quantities are understood and the replicability of this study is granted.

The two model configurations that were designed to investigate near-wall flow deviations due to surface roughness changes are presented in **Chapter 4**. For both configurations, the wind-tunnel and *PALM* setup is described. The first model configuration of a horizontal plate of homogeneous roughness is introduced in Section 4.1. The single building with different facade roughnesses is presented in Section 4.2.

The comparative results of the wind-tunnel measurements and *PALM* simulations for both model configurations are presented in **Chapter 5**. First, the near-wall flow at rough surfaces is investigated (Section 5.1). In particular, flow statistics are presented and the flow anisotropy is analysed by means of quadrant analysis and turbulence spectra. Second, practical implications and guidelines for users of LES models are given on the basis of the findings (Section 5.2)

The concluding **Chapter 6** contains a summary of the motivation and the main findings of this thesis. Furthermore, an outlook on future research questions and hints for the correct use of LES models in urban climate studies are given.

The four Appendices A to D contain technical drawings of the used boundary layer setup and model configurations for the *WOTAN* and *PALM* setups, specifications of the supercomputer *Levante*, a short reference to the used processing routines and a compilation of results placed in the appendix rather than in the main text for the sake of length and readability.

2 Theoretical and Methodological Principles

The study of near-wall turbulence representation in obstacle-resolving large-eddy simulations requires basic knowledge in many different branches of fluid dynamics. First, a basic theoretical understanding of turbulent flows is necessary (Sec. 2.1). Furthermore, basic terms and concepts of boundary layer theory in general and urban boundary layers in particular have to be introduced (Sec. 2.2). Especially the general concepts of wall-bounded flows are of high importance for the formulation of surface boundary conditions in large-eddy simulations. Section 2.3 is therefore first concerned with the core principles of large-eddy simulations and later discusses the difficulties of near-wall modeling in detail. The key issues to be addressed in this work are discussed in this chapter under Sec. 2.3.5. Finally, a general overview of physical flow modeling using boundary-layer wind tunnels is given with a focus on urban climate studies, validation of large-eddy simulation codes and near-wall flows (Sec. 2.4).

2.1 Turbulent Flows

A fluid's flow can either be laminar or turbulent. Both types of flows can be distinguished by the behaviour of their corresponding velocity fields. While turbulent flows are studied by many professional scientists, they can also be described in its qualitative properties by lay people. If one looks at the rising smoke of a candle that has just gone out, the smoke shows unsteady, three-dimensional, random and chaotic patterns. One can also see how the smoke spreads in large and small eddies, which behave similarly but are of different sizes. These are all properties of a turbulent flow (Pope, 2000; Tennekes and Lumley, 1972). Laminar flows do not show such irregular and seemingly complex behaviour in space and time.

The transition from a laminar to a turbulent flow depends on only a few quantities which can be summarised in one decisive dimensionless parameter, namely the Reynolds number $Re = \mathcal{U}\mathcal{L}/\nu$. Here, $\mathcal{U}$ and $\mathcal{L}$ are characteristic velocity and length scales and ν is the kinematic viscosity of the fluid. The higher the Reynolds number, the more turbulent the flow is. The onset of turbulent phenomena can be observed when a critical Reynolds number Re_{crit} is exceeded.

All features of a turbulent flow mentioned above can not only be described phenomenologically. They can also be traced down directly to the governing equations. Thus, it is possible to study turbulence quantitatively. In the following sections, I will give an overview of the governing equations of fluid motion and its statistical description, and I will elaborate on how energy is transported in turbulent flows across different scales.

2.1.1 Governing Equations

The introduction of the most important flow variables and equations mainly follows Pope (2000) as far as possible, but could also be taken from any other textbook on fluid mechanics like Tennekes and Lumley (1972) or Kundu et al. (2015). The equations and variables in this work are written in *Einstein notation*. As an example, the positional vector $\mathbf{x}$ is written with an index i which stands for the three spatial directions $x_i = (x, y, z)^T$. The *Einstein summation convention* is also used. This implies summation over indices that occur several times in an expression.[1]

Before the governing equations are derived, two concepts are introduced that form the prerequisite for the description of fluids in this work.

Continuum hypothesis In this work, the fluid will be treated as a continuum. Even though all fluids consist of discrete molecules, viewing them as continuous substances makes their treatment a lot easier since one does not have to solve the equations of motion for each individual molecule. The *continuum hypothesis* can be used, if dominating length and timescales of molecular motions are significantly smaller than those of the fluid flow.[2]

Eulerian description After the continuum hypothesis has been applied, variables such as the fluid's density $\rho(x_i, t)$ or the flow velocity $u_i(x_i, t)$ can be described as vector fields. To be more precise, these are *Eulerian* fields in which the quantities mentioned are described as a function of the position x_i and time t in a fixed reference frame.

---

[1] As an example, using the *Einstein summation convention*, the divergence of the velocity field $\nabla \cdot \mathbf{u} = \frac{\partial u}{\partial x} + \frac{\partial v}{\partial y} + \frac{\partial w}{\partial z}$ is written as $\frac{\partial u_i}{\partial x_i}$.

[2] This juxtaposition can also be described by the Knudsen number $Kn = \lambda_m / l_f$, where λ_m is the mean free path of a molecule and l_f is the smallest geometric length scale in a flow. If $Kn << 1$, the *continuum hypothesis* can be applied. For practical examples, see Pope (2000).

The conservation of mass for a fluid is described by the continuity equation

$$\frac{\partial \rho}{\partial t} + \frac{\partial \rho u_i}{\partial x_i} = 0. \tag{2.1}$$

Here, ρ is the density and u_i is the velocity vector. The flows studied in this work are not driven by any buoyancy differences and the density can be considered constant in space and time. Thus, the fluid is divergence-free, i.e. incompressible. As a consequence, Eq. 2.1 reduces to

$$\frac{\partial u_i}{\partial x_i} = 0. \tag{2.2}$$

Relationship 2.3 is the equation for conservation of momentum

$$\frac{\partial u_i}{\partial t} + u_j \frac{\partial u_i}{\partial x_j} = -\frac{1}{\rho}\frac{\partial p}{\partial x_i} + \frac{1}{\rho}\frac{\partial \sigma_{ij}}{\partial x_j}, \tag{2.3}$$

with σ_{ij} being the viscous stress tensor. The fluid is also viewed as a *Newtonian fluid*, which is a valid assumption for gas mixtures such as air. The viscosity is thus constant and not a function of the stress. The viscous stress tensor σ_{ij} can then be expressed as $\sigma_{ij} = 2\mu s_{ij}$ with

$$s_{ij} = \frac{1}{2}(\frac{\partial u_i}{\partial x_j} + \frac{\partial u_j}{\partial x_i}). \tag{2.4}$$

The molecular viscosity μ is then independent of external forces and $\nu = \mu/\rho$ is the kinematic viscosity of the fluid. The conservation of momentum (Eq. 2.3) can now be written as

$$\frac{\partial u_i}{\partial t} + u_j \frac{\partial u_i}{\partial x_j} = -\frac{1}{\rho}\frac{\partial p}{\partial x_i} + \nu \frac{\partial^2 u_i}{\partial x_j^2}. \tag{2.5}$$

This is the Navier–Stokes equation for a non-buoyant flow in a non-rotating reference system. The buoyancy effect is neglected in this work, as only the momentum properties of the flow are investigated. In non-experimental settings, buoyancy's influence on the flow becomes significant if the atmosphere under investigation is not neutrally stratified or if wind speeds are low. Rotational effects can be neglected in the urban climate, as inertial forces are significantly larger than rotational forces. This is mainly due to the small length scales of the phenomena under consideration.[3]

Note that the advection term on the left hand side is nonlinear. Even though the nonlinearity is only quadratic, this property makes the flow field particularly sensitive to small perturbations, which are ubiquitous in initial and boundary conditions in nearly every physical system like urban wind fields. Thus, even though the Navier–Stokes equations are deterministic, the velocity u_i is a random variable. The degree of that randomness, i.e. the chaotic behaviour of the flow, is not only dependent on the small perturbations but also on how far the fluid is able to inherently dampen the effects of these perturbations.

2.1.2 Statistical Description

As already pointed out, turbulent flows are a stochastic phenomenon and that stochastic behaviour is a direct result of the nonlinearity in Eq. 2.5. But how can this nonlinearity be treated analytically? And how can experimental results of a statistical nature be associated with those nonlinearities?

Reynolds-Averaged Equations

Reynolds (1895) proposed to treat a fluid in terms of its mean motion and the motions relative to that mean motion, i.e. the fluctuations. This has become known as the *Reynolds decomposition* which is defined as

$$u_i(x_i, t) = \overline{u_i}(x_i, t) + u_i'(x_i, t), \tag{2.6}$$

with $\overline{u_i}$ being the mean velocity and u_i' the velocity fluctuations. This decomposition can not only be applied to the velocity field, but also to other flow measures including pressure, temperature or other scalar fields like humidity or substance concentrations. Applying the Reynolds decomposition to the equation of conservation of mass (Eq. 2.2), one comes to the insight that not only the velocity field but also its mean value as well as the fluctuations are solenoidal, since differentiation and calculating the mean commute:

$$\frac{\partial u_i}{\partial x_i} = \frac{\partial}{\partial x_i}(\overline{u_i} + u_i') = 0, \tag{2.7}$$

then leads to the continuity equations for the mean and the fluctuations

---

[3] A decisive parameter here is the Rossby number $Ro = \frac{\mathcal{U}}{\mathcal{L} f_{Co}}$ with $\mathcal{U}$ being the characteristic velocity and $\mathcal{L}$ the characteristic length scale of the phenomenon studied. The Coriolis frequency f_{Co} depends on the planetary angular velocity and the latitude. The Rossby number describes the ratio of inertial forces to the Coriolis force. If it is very high, the inertial forces predominate; if it is low, the effects of Earth's rotation dominate.

$$\frac{\partial \overline{u_i}}{\partial x_i} = 0 \quad \text{and} \quad \frac{\partial u_i'}{\partial x_i} = 0. \tag{2.8}$$

By now averaging the momentum equation and applying the Reynolds decomposition, the *Reynolds-averaged Navier–Stokes* equations (RANS) can be derived. Averaging the left-hand side of Eq. 2.5 yields

$$\overline{\frac{\partial u_i}{\partial t} + u_j \frac{\partial u_i}{\partial x_j}} = \frac{\partial \overline{u_i}}{\partial t} + \frac{\partial}{\partial x_j} \overline{u_i u_j}, \tag{2.9}$$

where the Reynolds decomposition can now be applied to the nonlinear convective term from Eq. 2.5,

$$\begin{aligned} \overline{u_i u_j} &= \overline{(\overline{u_i} + u_i')(\overline{u_j} + u_j')} \\ &= \overline{\overline{u_i}\;\overline{u_j} + \overline{u_i} u_j' + u_i' \overline{u_j} + u_i' u_j'} \\ &= \overline{u_i}\;\overline{u_j} + \overline{u_i' u_j'}, \end{aligned} \tag{2.10}$$

which then leads to the *Reynolds-averaged Navier–Stokes* equation

$$\frac{\partial u_i}{\partial t} + \overline{u_j} \frac{\partial \overline{u_i}}{\partial x_j} = -\frac{1}{\rho} \frac{\partial \overline{p}}{\partial x_i} + \nu \frac{\partial^2 \overline{u_i}}{\partial x_j^2} - \frac{\partial \overline{u_i' u_j'}}{\partial x_j}. \tag{2.11}$$

The equation of momentum in its non-averaged (Eq. 2.5) and its Reynolds-averaged form (Eq. 2.11) do differ in one major point, namely the additional term in the latter equation. It was obtained by substituting the Reynolds decomposition into the averaged substantial derivative. The averaged (co)variances of the fluctuations $\overline{u_i' u_j'}$ are called *Reynolds stresses* or *kinematic momentum fluxes*. Together they form the *Reynolds stress tensor* $\tau_{ij} = -\rho \overline{u_i' u_j'}$.

Reynolds Stress Tensor

The Reynolds stress tensor represents the dynamic contributions of momentum fluctuations to the spatio-temporal evolution of the mean velocity field. As far as naming is concerned, a distinction is made between dynamic stresses τ_{ij} and kinematic fluxes $\overline{u_i' u_j'}$. Equations 2.5 and 2.11 are of the same form if $\overline{u_i' u_j'} = 0$ meaning that the evolution of the actual flow field u_i is then identical to that of its mean $\overline{u_i}$. This is the case for purely laminar flows. Thus, the contribution of the Reynolds stresses to the mean velocity increases as the flow is more turbulent, and at the same time the intermittency of the flow increases. In contrast to the Reynolds stresses, the viscous stresses $\nu \frac{\partial^2 \overline{u_i}}{\partial x_j^2}$ have a damping effect on the turbulence properties of the flow.

Let us now take a closer look at the mathematical properties of the Reynolds stress tensor and their physical meanings:

$$\tau = -\rho \begin{pmatrix} \overline{u_1' u_1'} & \overline{u_2' u_1'} & \overline{u_3' u_1'} \\ \overline{u_1' u_2'} & \overline{u_2' u_2'} & \overline{u_3' u_2'} \\ \overline{u_1' u_3'} & \overline{u_2' u_3'} & \overline{u_3' u_3'} \end{pmatrix}. \tag{2.12}$$

The tensor τ_{ij} is a symmetric tensor of second-order. The diagonal components (marked in red) are the *normal fluxes* or the *variances* $\sigma_i^2 = \overline{(u_i - \overline{u_i})^2} = \overline{u_i' u_i'} = \overline{u_i'^2}$ of the flow field. Halving the trace of the momentum flux tensor yields the *turbulence kinetic energy* (TKE):

$$e(x_i, t) = \frac{1}{2\rho} tr(\tau_{ij}) = \frac{1}{2}\overline{u_i'^2}. \tag{2.13}$$

This measure can be understood as the kinetic energy per unit mass generated only by the fluctuating velocity field.

The off-diagonal components of the Reynolds stress tensor marked in blue are the *shear stresses* or *shear fluxes* and are as well described by the covariances of the velocity fluctuations $\overline{u_i' u_j'}$ with $i \neq j$. The turbulent fluxes are thus the second statistical moments of the fluid's momentum field. If the covariance of two components is zero, there is no correlation between the corresponding velocity fluctuations. A negative value indicates a negative correlation, a positive value indicates a positive correlation. The *correlation coefficient tensor*

$$R_{ij} = \frac{\overline{u_i' u_j'}}{\sigma_i \sigma_j} \tag{2.14}$$

is a normalised measure of the correlation, and is defined within $R_{ij} \in [-1, 1]$. The Einstein summation convention is not applied in Eq. 2.14. In the application of velocity fluctuations in fluids, a negative correlation means that positive excursions in the signal of one component are associated with negative excursions in the signal of the other component and vice versa. Thus, the correlation coefficients also depend on the choice of the coordinate system.

Turbulence Closure

Through the introduction of the Reynolds stresses, the physical problem becomes an underdetermined system of equations. The equations explained in Sec. 2.1.1 represent a *closed* system of mathematical equations. For each of the four equations (the three components of the momentum equation and the continuity equation), there are four unknowns (the three velocity components and the pressure). By introducing the Reynolds stresses in Sec. 2.1.2, six new unknowns emerge, namely the three diagonal elements, i.e. the variances, and the three off-diagonal elements, the covariances. Note that the Reynolds stress tensor is a symmetric tensor. The system becomes *unclosed* and, thus, cannot be solved without additional information for estimating the Reynolds stresses.

Many numerical models of the RANS and LES classes differ in their approaches to turbulence closure. These approaches are manifold, but most of them are based on two basic heuristic hypotheses: the *turbulent-viscosity hypothesis* and the *gradient-diffusion hypothesis*. These two concepts do have their practical limitations, which will be discussed later together with their applications in LES (2.3.2). More important in this work is the turbulent-viscosity hypothesis proposed by Boussinesq in 1877, since scalar fluxes will not be studied. This hypothesis relates the deviatoric Reynold stresses to the mean rate of strain

$$-\rho\overline{u_i'u_j'} + \frac{2}{3}\rho e\delta_{ij} = \rho\nu_T\left(\frac{\partial\overline{u_i}}{\partial x_j} + \frac{\partial\overline{u_j}}{\partial x_i}\right) = 2\rho\nu_T\overline{s_{ij}} \tag{2.15}$$

with the unknown proportionality factor ν_T being the *turbulent viscosity* or *eddy viscosity*. It is therefore necessary to determine the eddy viscosity in order to close the system of equations. By considering the dimensions of the eddy viscosity ($\mathrm{m}^2\ \mathrm{s}^{-1}$), it becomes clear that the eddy viscosity can be expressed as the product of a length scale l_T and a velocity scale u_T. Turbulence closure can then be accomplished by again parameterising these two scales. There are several ways to solve this problem, which can be distinguished by the number of additional equations that have to be introduced in order to obtain u_T and l_T and by the statistical order of the terms being directly calculated.

The most straight-forward way is the *mixing-length model*, where u_T is expressed by local mean flow gradients and l_T is related to the eponymous mixing length l_m. It is a first-order turbulence closure, and no additional prognostic equation is introduced. The decisive disadvantage of the mixing-length model is the way in which the length scale l_m must be determined. Since the mean free path length of a fluid particle depends strongly on the local flow situation, it is not possible to define a non-heuristic approach that is generally valid.

The next order turbulence closure methods are 1.5-order closures using one additional equation to determine the eddy viscosity ν_T. This approach was initially proposed independently by Kolmogorov (1942) and Prandtl (1945), and the turbulence closure in the *PALM* model is based on an approach of this kind (Deardorff, 1980). The heuristic approach of determining the mixing length is kept here, but the relationship $u_T \sim e^{1/2}$ with a proportionality constant c_T is assumed for the velocity scale. The turbulence kinetic energy e is then solved with an additional prognostic equation. The individual steps of the model are as follows (Pope, 2000):

1. The mixing length l_m is determined.
2. A prognostic equation for $e(x_i, t)$ is solved.
3. The eddy viscosity is calculated by $\nu_T = c_T l_m e^{1/2}$.
4. The Reynold stresses are calculated using Eq. 2.15.
5. The momentum equation (Eq 2.11) is solved using the obtained Reynold stresses.

Besides the heuristic determination of l_m, a major downside of this method is that the prognostic equation for the turbulence kinetic energy e again contains unknowns, in particular the terms for turbulent production $\mathcal{P}$ and the *energy dissipation rate* ε.

Another well-known approach was mainly developed by Jones and Launder (1972), which introduces two equations to the closure and is based on the assumption that the eddy viscosity $\nu_T \sim e^2/\varepsilon$. The so called TKE-$\varepsilon$-model (or *k-$\varepsilon$-model*) uses prognostic equations to calculate e and ε. An advantage of this model is that by having two additional equations, no heuristic assumptions concerning the mixing length are needed and the closure thus gains generality.

Second-order turbulence closures solve transport equations for higher moments, i.e. Reynolds stresses and are therefore referred to as *Reynolds stress closures*. Since the Reynolds stresses are computed directly, the turbulent-viscosity hypothesis is not needed any more. However, turbulent third-order terms such as the pressure-rate-of-strain tensor and the Reynolds stress flux are parameterised (Pope, 2000).

2.1.3 A Unified Picture of Turbulence

In the previous sections, the Navier–Stokes equations were introduced and, in particular, the nonlinearity of the equations and the randomness of turbulence was emphasised. From the Reynolds decomposition, the mean velocity components as well as the associated fluctuations emerged. Especially the latter contribute to the momentum, i.e. the energy transfer in the fluid through the Reynolds stresses, a direct mathematical consequence of applying the Reynolds decomposition to the nonlinear terms in the momentum equation.

As well as dividing the flow into its mean and fluctuations, it is possible to view a fully turbulent flow ($Re > Re_{crit}$) as a collection of vortices of different sizes. These length scales interact with each other according to certain laws, which will be presented in the following. On the one hand there is the energy cascade of turbulence presented by Richardson (1922) and Taylor (1935, 1938) and on the other hand the hypothesis on local isotropy and universal scaling of turbulence presented by Kolmogorov (1941, 1991), referred to as the *K41 theory*.

Energy Cascade

As already stated above, Richardson (1922) notes that a turbulent, high-Re flow consists of eddies of different sizes l. Each eddy of size l has a characteristic velocity $u(l)$ and timescale $t(l) = l/u(l)$ and thus its own characteristic Reynolds number $Re(l) = lu(l)/\nu$. The largest vortices are of size $\mathcal{L}$. In sum, the most kinetic energy is carried by vortices of size l_0, as depicted in Fig. 2.1 and in the schematic turbulent energy spectrum in Fig. 2.2 (not all length scales in Fig. 2.1 have been introduced yet, but will be in the following). The Reynolds number of the eddies containing the most energy is thus $Re(l_0) = l_0 u(l_0)/\nu$ and is still comparable to the Reynolds number of the flow itself.

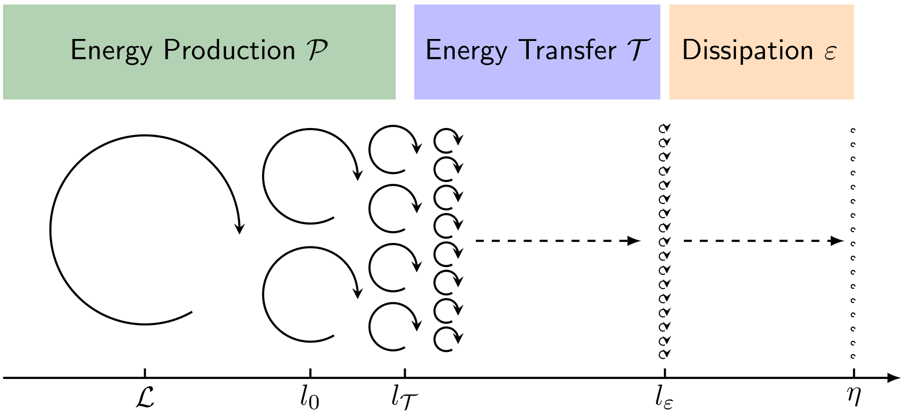

Figure 2.1: Schematic of the turbulent Energy cascade and corresponding length scales and processes. Each eddy of size $l > l_\varepsilon$ breaks up and transfers its kinetic energy to smaller eddies. At even smaller scales, dissipation sets on.

Richardson (1922) now states that, as long as the flow is turbulent, eddies collapse and transfer their kinetic energy into correspondingly smaller eddies. These eddies in turn go through the same process which leads to decreasing Reynolds numbers of the resulting eddies. This is the so called *energy cascade* and it goes on until the Reynolds number at length scales l_ε reaches the critical Reynolds number for the onset of turbulence. At this point in the cascade, the kinetic energy that has been passed through so far is dissipated by viscous forces. The rate of dissipation ε scales as $u(l_0)^3/l_0$ since the time scale is $t(l_0) = l_0/u(l_0)$ and $u(l_0)^2/t(l_0)$ is the rate of transfer of energy by the large eddies.

One question that arises when considering the energy cascade is of what size the smallest length scales in the system are. While the answer is obvious for the largest length scales, it is not so easy to answer for the lower limit. Furthermore, it is unknown whether the characteristic velocity scale $u(l)$ of each eddy is constant over l or also varies and what this means for the timescales $t(l)$ in the system. Kolmogorov (1941, 1991) dealt significantly with these questions in his theory. This will be examined in more detail in the next section.

Kolmogorov's Hypotheses — K41 Theory

Kolmogorov's hypothesis actually consists of three hypotheses (Pope, 2000). The first assumption refers to the isotropy of vortices in a turbulent flow. Large eddies direct themselves spatially according to the geometric conditions, i.e. the boundary conditions, and are thus anisotropic. According to Kolmogorov (1941, 1991), the directional features of large eddies get lost as soon as the energy is transferred to smaller eddies. Consequently, the small eddies are locally isotropic:

> **Local isotropy hypothesis:** Small-scale turbulent motions ($l \ll l_0$) are statistically isotropic at high enough Reynolds numbers if they are not close to the flow's boundary or other singularities.

The length scale $l_{\mathcal{T}}$ (as already seen in Fig. 2.1) marks the eddy size at which turbulent motions become locally isotropic. The notion that directional features of the large eddies get lost during the energy transfer can be extended to all geometric properties. The behaviour of small eddies is therefore universal in character.

The two physical processes of energy transfer for eddies with $l < l_{\mathcal{T}}$ are the transfer of turbulence kinetic energy $\mathcal{T}$ and the energy dissipation. These two processes are mainly determined by the viscosity ν and the energy dissipation rate ε. Since all kinetic energy in the flow that is transferred to smaller scales will sooner or later dissipate, the energy transfer rate is of the same size as the dissipation rate $\mathcal{T} \approx \varepsilon$. This is the essence of the first similarity hypothesis by Kolmogorov (1941, 1991):

> **First similarity hypothesis:** In every turbulent flow at sufficiently high Reynolds number, the statistics of the small-scale motions ($l < l_{\mathcal{T}}$) have a universal form that is uniquely determined by ν and ε.

Based on the first similarity hypothesis, the *Kolmogorov microscales* can be formulated with η being the Kolmogorov length scale, u_η the velocity scale and t_η the Kolmogorov time scale. They are defined as follows:

$$\eta \equiv \left(\frac{\nu^3}{\varepsilon}\right)^{\frac{1}{4}}, \tag{2.16}$$

$$u_\eta \equiv (\nu\varepsilon)^{\frac{1}{4}}, \tag{2.17}$$

$$t_\eta \equiv \left(\frac{\nu}{\varepsilon}\right)^{\frac{1}{2}}. \tag{2.18}$$

By calculating the Reynolds number based on these quantities as $Re_\eta = u_\eta \eta / \nu = 1$, it quickly becomes clear why they are called Kolmogorov microscales. As Re approaches unity, the viscous forces and inertia forces balance and the flow starts to get laminar. Thus, the Kolmogorov microscales are the smallest turbulent scales possible.

Using the ratios from the microscales and the scales for large vortices, the following Reynolds number dependent relationships can be derived:

$$\frac{\eta}{l_0} \sim Re^{-\frac{3}{4}}, \quad \frac{u_\eta}{u(l_0)} \sim Re^{-\frac{1}{4}}, \quad \frac{t_\eta}{t(l_0)} \sim Re^{-\frac{1}{2}}. \tag{2.19}$$

The above ratios show that velocity scales and time scales in turbulent flows change with decreasing eddy size l. Further, the more turbulent a flow is (higher Re), the smaller the turbulent scales become with respect to their large scale counterparts. For high Reynolds number flows, the region of energy transfer gets wider and the effect of viscosity ν is low at scales $l \gg \eta$. The second similarity hypothesis by Kolmogorov (1941, 1991) is therefore:

> **Second similarity hypothesis:** At sufficiently high Reynolds number, the statistics of the motions in the range $l_0 \gg l \gg \eta$ have a universal form that is only determined by ε and independent of ν.

The scale range addressed in the second similarity hypothesis can also be written as $l_{\mathcal{T}} > l > l_\varepsilon$ since dissipation already sets on before the Kolmogorov microscales are reached (at about $l_\varepsilon = 60\eta$ (Pope, 2000)). A distinction is drawn between the *inertial subrange* and the *dissipation range* (see also Fig. 2.1 and 2.2).

To gain a deeper understanding of the process of energy transfer $\mathcal{T}$, the energy distribution as a function of the wavenumber is of big interest. Kolmogorov (1941, 1991) not only formulated the three hypotheses, but was also able to derive universal scaling laws for homogeneous turbulence using the two similarity hypotheses and dimensional analysis. For the further analysis, the length scale is transformed into wavenumber space via $k = 2\pi/l$. The energy density spectrum within the inertial subrange is defined by

$$E(k) = C \cdot \varepsilon^{\frac{2}{3}} k^{-\frac{5}{3}}, \tag{2.20}$$

with C being the Kolmogorov constant.[4]

Experimental evidence of the K41 theory was given by multiple authors. In particular, Mestayer (1982) and Saddoughi and Veeravalli (1994) tested the local isotropy hypothesis, while the well-known study by Kaimal et al. (1972) proofed the isotropy hypothesis to be right and also confirmed the spectral scalings in the inertial subrange.

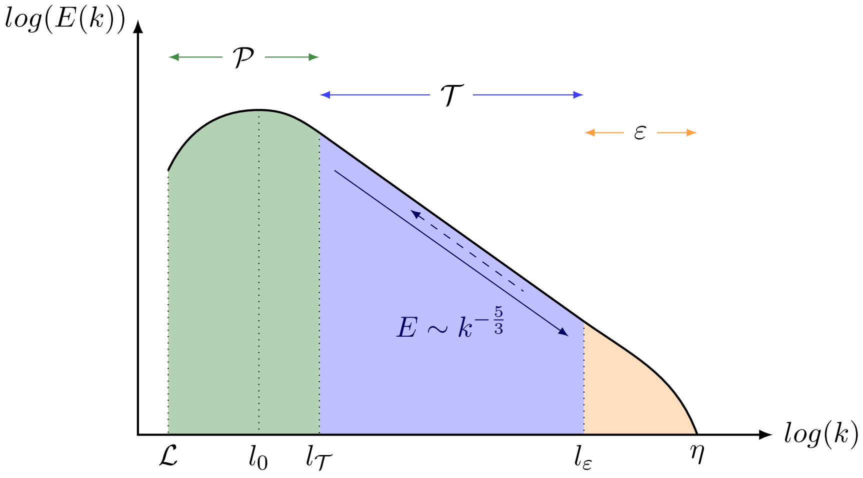

Figure 2.2: Theoretical shape of the turbulence energy density spectrum in wavenumber space for high Reynolds number flows. The colored areas show the energy containing eddies with turbulent production $\mathcal{P}$, the inertial subrange with energy transfer $\mathcal{T}$ and typical $5/3$-scaling and the dissipation range at rate ε. The black arrows indicate the energy transfer within the inertial subrange.

So far, it was assumed that Reynolds numbers are "sufficiently high" in order to formulate the concepts of the energy cascade, local isotropy and similarity. Although the concepts are basically valid, Reynolds number dependent behaviour is observable for higher order statistics as shown by Wyngaard and Tennekes (1970), Champagne (1978) and Anselmet et al. (1984). Already in 1962, Kolmogorov and Obukhov introduced the refined similarity hypotheses to tackle potential shortcomings of the theory, which will not be discussed further here for the sake of brevity.

---

[4] In an extensive literature review for various turbulent flows (grid turbulence, shear flows, geophysical flows), Sreenivasan (1995) documented a value of $C = 0.5$.

Richardson's (1922) main statement on the energy cascade is that turbulence kinetic energy is always transferred from large scales to small scales. At lower eddy Reynolds numbers, the energy transfer can be reversed for short times/events. This instantaneous behaviour is called the *inverse cascade* or *backscatter* and is depicted in Fig. 2.2 by the dashed arrow (Domaradzki and Rogallo, 1990). On average, however, the energy cascade is non-inverse and much of the energy is transferred as usual.

2.2 Turbulent Boundary-Layer Flows

In urban climates, boundary-layer flows are relevant on different length scales and in various spatial orientations. On the one hand, cities are located within the atmospheric boundary layer (ABL) and create a new subcategory of the ABL, the so-called urban boundary layer (UBL). The evolution of an UBL as an internal boundary layer within the ABL is due to their very high roughness, altered thermal radiation from buildings, reduced infiltration and many other factors (Oke, 1984). Considering the area of interest of the urban micro-climate, the ABL or the UBL are also referred to as the *global* boundary layer in this work, depending on the surface studied. In addition, on building facades within the cities further, micro-scale, *local* boundary layers can develop. Local boundary layers need a long fetch and often can not develop sufficiently. Nevertheless, it is important to gain an understanding of them because, firstly, they determine the flow in places that are particularly relevant for humans and, secondly, the formulation of surface boundary conditions in numerical models is determined precisely by this region.

In Sec. 2.2.1, we will first focus on the basic principles of wall-bounded flows and here will mainly follow Pope (2000) and Tennekes and Lumley (1972). After that, a short overview on atmospheric and urban boundary layers is given to roughly introduce the setting in which the application of obstacle-resolving LESs take place (Sec. 2.2.2).

2.2.1 Wall-Bounded Flows

It is a matter of fact that wall-bounded flows are ubiquitous in the natural sciences and engineering. While many studies have first contributed to an understanding of turbulent boundary layers over smooth surfaces (e.g. Kovasznay et al. (1970), Willmarth (1975), Cantwell (1981) and Sreenivasan (1989)), the study of rough surfaces has long been neglected. Rough-wall flows show complex dynamics because of the influence of roughness elements leading to an increase in surface drag and emergence of complex turbulent structures. Representative data have been difficult to obtain, due to the high intermittency and heterogeneity of near-wall turbulent flows over rough surfaces.

We start with the simple case of a stationary flow in x-direction over a horizontal plate of homogeneous roughness. The vertical axis is in z-direction. To formulate a fundamental law of the wall, characteristic length and velocity scales for the near-wall region have to be defined. The characteristic length scale is based on the mixing length l_m, which is understood to be proportional to the distance from the wall z with $l_m = \kappa z$. The von Kármán constant $\kappa = 0.41$ acts as a proportionality factor.[5] The characteristic velocity scale of the near-wall flow is the *friction velocity*, which is defined as the square root of the wall-normal Reynolds stress at the wall $u_*^2 = -\overline{u'w'}_0$. To derive a formulation for the mean stream-wise velocity $u(z)$ as a function of z, we can rely on Eq. 2.15. Writing down the equation for $i = 1$ and $j = 3$ leads to

$$\frac{\partial \overline{u}}{\partial z} = \frac{-\overline{u'w'}_0}{\nu_T} = \frac{u_*}{\kappa z}, \tag{2.21}$$

with $z = x_3$ and $\partial w / \partial x \approx 0$. Here, the turbulent fluxes were substituted by its values at the wall. This step makes sense once the notion of a *constant-flux layer* has been introduced. This idea implies that the near-wall turbulent fluxes are constant up to a certain wall distance δ_{cf} and is based on thorough experimental evidence and dynamic considerations for zero-pressure-gradient boundary layers (Raupach et al., 1991).

By now integrating Eq. 2.21 over z, one obtains the *logarithmic law* of the wall after Prandtl (1925, 1932), which relates the wall-parallel mean velocity to the natural logarithm of the distance to the wall:

$$\overline{u}(z) = \frac{\sqrt{-\overline{u'w'}_0}}{\kappa} \cdot \ln\left(\frac{z - d_0}{z_0}\right). \tag{2.22}$$

The integration constant z_0 in the denominator of the logarithm is the *roughness length*. It can be obtained by finding the extrapolated intersection of a measured wind profile with the z-axis, i.e. $z_0 = z(\overline{u} = 0)$ (see also Fig. 2.3). The roughness length is smaller than the mean height of the roughness elements h_r and often estimated to be around one tenth of h_r. While not resulting explicitly from integration of Eq. 2.21, the displacement height d_0 was added to the log-law. To account for the surface roughness, it shifts the vertical axes of the coordinate system up and adds an additional degree of freedom to the log-law. The roughness length z_0 is understood to be the more significant parameter, and $d_0 \approx 0$ is often assumed even though other estimates based on physical rather than geometrical reasoning exist (Jackson, 1981).

---

[5] Values given for κ vary from 0.32 up to 0.65 (Högström, 1996). In this work we set $\kappa = 0.41$ since the *PALM* model also uses this value (Maronga et al., 2020a) and it is also reported by Högström (1996) to be in the range of the most common values ($0.39 < \kappa < 0.41$).

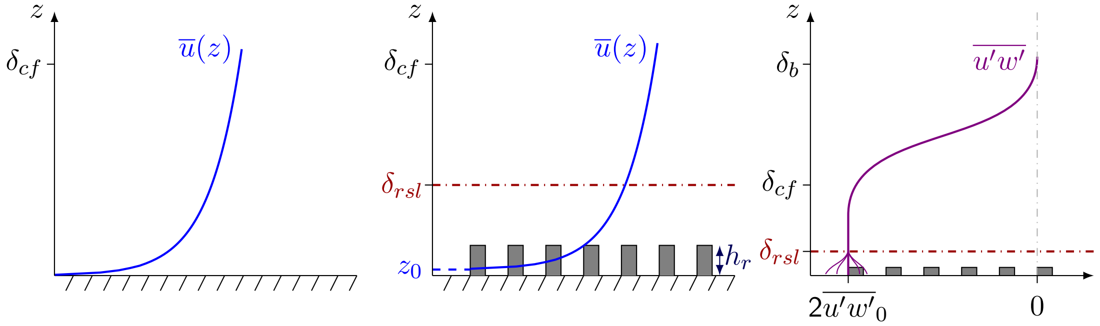

Figure 2.3: Sketch of the mean flow profile over a smooth plate without any roughness (left), over a homogeneous roughness (middle) and the expected profile of the wall-normal turbulent fluxes for wall-bounded flows (right). Note that the z-axis on the right plot has a different scaling. The height of the surface roughness elements is h_r and the roughness length is $z_0 < h_r < \delta_{rsl} < \delta_{cf}$.

Above the constant-flux layer the velocity profile can be calculated by the power-law

$$\overline{u}(z) = \left(\frac{z - d_0}{z_{pw} - d_0} \right)^{\alpha} u_{pw}, \tag{2.23}$$

where α is the profile exponent and u_{pw} is the mean velocity at reference height z_{pw} (Grötzbach, 1987). Although the power-law fit is valid in the whole boundary layer, it lacks of a proper physical foundation. Since the scope of this work is on the near-wall region anyhow, more focus is placed on the log-law.

The difference between the smooth and rough wall profile is the height at which $\overline{u}(z)$ equals zero, namely the roughness length z_0 for rough walls. Also visible is the depth δ_{rsl} of the so called *roughness sublayer*, which will be further introduced in the following. The constant-flux layer is depicted and it is also shown that mean turbulent fluxes tend to vanish at the upper height of the boundary layer $z = \delta_b$ (right sketch). Note also that turbulent fluxes for $z < \delta_{rsl}$ become inaccurate and vary strongly. This close to the rough wall, the log-law is not applicable any more and the direct influence of roughness elements dominates all flow statistics.

Subdividing Wall-Bounded Flows

There are different subdivisions of the layers in wall-bounded flows. Some classifications are made on the basis of physical flow quantities, others are based on purely geometrical reasoning according to existing length scales. Depending on the research area, it can also happen that one and the same layer has several names, or one name is used for different layers. To deal with this sometimes confusing situation, it is useful to define the most important names and regions that will play a greater role in the course of this work. Figure 2.4 shows these regions.

The simplest division of wall-bounded flows that has been made so far is into two layers, an *inner* and an *outer layer*. In principle, the outer layer is understood to scale mainly with the boundary layer thickness δ_b and the friction velocity u_*. It is characterised by low shear and little production $\mathcal{P}$ of turbulence kinetic energy. For smooth and for rough walls, the outer layer turbulent dynamics are basically the same. The inner layer for smooth walls scales with the viscous length scale ν/u_*. For rough walls though, the inner layer scaling not only depends on ν/u_*, but also on other characteristic length scales as the roughness height h_r and other descriptive parameters such as the shape of the roughness elements or the roughness density.[6] Within the inner layer though, as could be expected due to different scaling parameters, the dynamics between rough and smooth layers differ. Wind shear in rough-wall boundary layers is substantially stronger, which leads again to more intense turbulence kinetic energies. Turbulent production $\mathcal{P}$ is strong and so is dissipation ε. For sufficiently high Reynolds numbers though, the inner layer flow behaviour at rough walls is understood to be similar to the one at smooth walls and z_0 becomes negligible (Raupach et al., 1991). It remains a much studied topic up to which degree and how the dynamics in the inner layer can influence the outer-layer turbulence and vice versa.

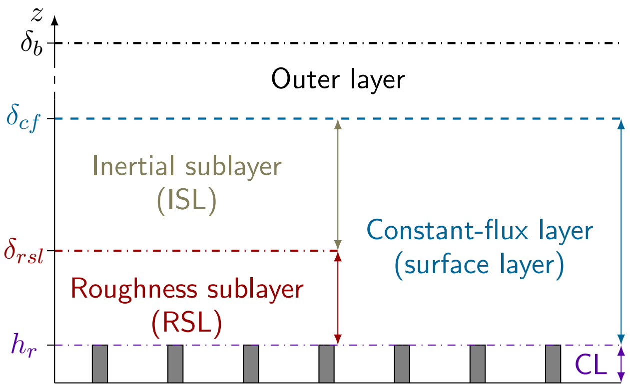

Figure 2.4: An overview of the sublayers in wall-bounded flows over a horizontally homogeneous surface roughness after Raupach, MR and Legg (1984). The canopy layer is abbreviated by CL.

The lowest layer is the *canopy layer* (CL), which covers the range from $z = 0$ up to the mean roughness height h_r. In this layer, dynamic structure of the individual vortices is directly influenced by the roughness elements. This concerns, for example, recirculation zones behind the roughness elements or flow separation at obstacles.

---

[6] For definitions and values of further geometrical parameters responsible for near-wall turbulence as frontal and plane area densities or shape factors, see Huang et al. (2016).

Above the CL lies a flow layer that is quite important for this work. It is the already mentioned *roughness sublayer* (RSL) present in flows over rough surfaces. The smooth-wall equivalent would be the viscous sublayer where viscous dissipation is dominant. The roughness sublayer is defined as the region that is dynamically influenced by roughness elements and was at first referred to as such by Raupach et al. (1980). They framed the RSL as the near-wall region where a 'roughness wake effect' is apparent, the local mean velocity profile can depart from the log-law and where there are unsteady turbulent fluxes depending strongly on the local roughness structure. Nevertheless, the log-law can also be applied within this layer if the surface roughness is horizontally homogeneous, and it is often applied in the RSL for even non-homogeneous surfaces because of a lack of knowledge due to the complexity of the physical problem. The length scale mainly determining the roughness sublayer is the roughness height h_r. Based on several laboratory studies, Raupach et al. (1991) state that the RSL height is in the range of

$$2h_r < \delta_{rsl} < 5h_r. \tag{2.24}$$

Until now, the exact RSL height is still a much-studied matter. Various criteria were used to define $\delta_{rsl}(h_r)$. Krogstad et al. (2005) identify the roughness sublayer height to be $\delta_{rsl} \approx 5h_r$ by calculating the mean velocity defect between smooth and rough walls. Also second-order statistics as the Reynolds stresses indicate the upper boundary of the roughness sublayer to be about five times the roughness height (Ashrafian et al., 2004). In this thesis, the question of roughness sublayer height is also examined on the basis of various additional criteria. Furthermore, it will be investigated for non-horizontal surfaces with more complex geometries (see Sec. 5.1).

Between the already mentioned outer layer and the RSL lies the *inertial sublayer* (ISL), which is also shown in Fig. 2.4. It can be understood as a transitional layer between the region of direct influence of the surface roughness (RSL) and the outer layer. In the ISL the log-law holds, which means that the curvature of the vertical velocity gradient is still influenced by surface properties as z_0, but only scales with z (Barlow and Coceal, 2009). Turbulent fluxes vary weakly with height globally and locally. Here, horizontal averages of a quantity equal the time average at a single point. For an inertial sublayer to develop, a long fetch is needed. For very rough walls, the roughness sublayer often is so thick that an inertial sublayer cannot develop sufficiently or often is very thin and has an extent of $\delta_{rsl} < z < 0.25\delta_b$ (Macdonald, 2000).

We have now introduced the main layers in wall-bounded flows and will in the next step have a closer look at certain flow phenomena close to the wall.

Near-Wall Flow Phenomena

Inside the roughness sublayer, roughness elements influence the flow and often lead to complex, recurring flow patterns. These patterns depend on how high and wide the free-standing elements are and how closely packed together. Hussain and Lee (1980) proposed three types of flow around roughness elements depending on their packing density. In the *isolated roughness flow regime* the elements are sufficiently far away from each other such that wakes behind each element can evolve independently from flow disturbances by other surrounding elements. The *wake interference flow regime* has a closer element density and the wakes cannot fully develop. Finally, in the *skimming-flow regime* the roughness elements are packed so densely that the canopy flow at $z < h_r$ is not influenced by the flow above. This decoupling also leads to a decrease in turbulent fluxes within the roughness sublayer and the flow over the rough surface acts more like a flow over a smooth surface at $z = h_r$.

Via a quadrant analysis the contributions of the single fluctuation components u' and w' to the total wall-normal turbulent flux can be analysed. This way, Rotach (1993) was able to identify dominant mechanisms of momentum transport called *ejections* ($u' < 0, w' > 0$) and *sweeps* ($u' > 0, w' < 0$). Close to the canopy layer and within, there is a dominance of wallwards motion, i.e. sweeps. Further away from the wall the anisotropy vanishes and there are no preferred directions in the fluctuation components. It remains an open question if the occurrence of ejection and sweep events and especially the dominance of wallwards sweeps is not only apparent in flows over horizontal walls. The study of such flow phenomena at vertical walls with roughness elements and flow cases more complex than the idealised case of an infinite homogeneous surface is of high interest for urban climate studies among others.

In addition to data-based investigations of near-wall turbulence, there are also conceptual models that allow predictions of turbulence statistics at least for smooth walls (for a detailed review, see Marusic and Monty (2019)). The most widely discussed models are based on the attached eddy hypothesis formulated by Townsend (1951, 1961, 1980), which holds for the logarithmic region above the RSL. The hypothesis is also based on experimental evidence of a strong wallwards flow of energy via turbulent motions. Townsend (1980) states that 'the velocity fields of the main eddies, regarded as persistent, organised flow patterns, extend to the wall and, in a sense, they are *attached* to the wall'. He was able to derive velocity and velocity fluctuation distributions based only on the distance from the wall and a characteristic velocity scale. Without going into further detail, Townsend's (1951,1961,1980) hypothesis states that the blocking effect of the wall on energy-containing eddies amplifies their wall-parallel motions and suppresses the wall-normal motions. Questions arising now are: how are the attached eddies shaped and what does the hypothesis mean for their characteristic length scales? Perry and Chong (1982) argued that so-called *hairpin vortices* consisting of two counter-rotating vortices are a candidate for the above mentioned coherent wall-attached structures. Based on this, they were able to derive the same distributions of momentum as Townsend (1980). In a numerical experiment of flow over a rough wall of an array of cubes, Coceal et al. (2007b) and Coceal et al. (2007a) were able to relate the above mentioned ejections to locations between hairpin legs and the dominating wallward sweeps to locations not associated with attached hairpin vortices.

2.2.2 Atmospheric and Urban Boundary Layers

The general concepts of wall-bounded flows can also be translated to the atmospheric boundary layer above cities, the urban boundary layer. Since this thesis deals exclusively with the dynamic properties of turbulent wall-driven flows and not with density-driven flows, it is not necessary to discuss the diurnal evolution of the ABL or specific energy budgets concerning heat or humidity (for further information, see Stull (1988) or Oke (1988)).

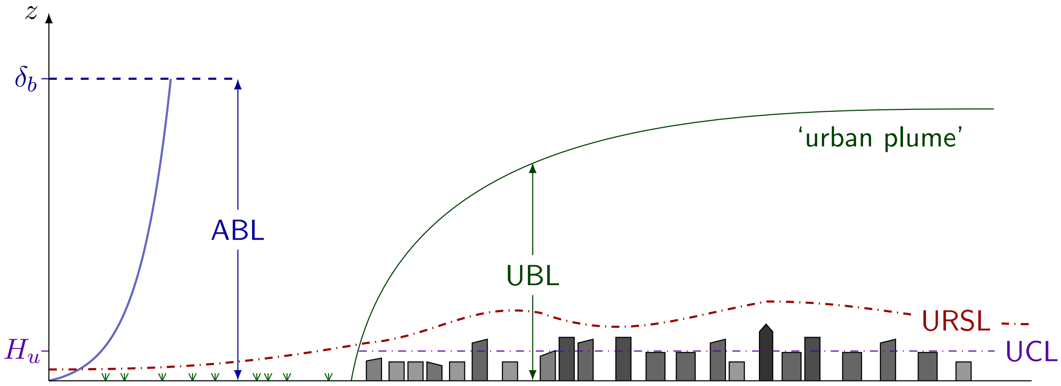

Figure 2.5: An overview of the urban boundary layer within the ABL after Oke (1988). An 'urban plume' evolves over the city and the canopy layer from Fig. 2.4 is now called the urban canopy layer or UCL.

The height of the atmospheric boundary layer under neutral conditions can vary between 500 m and 2000 m (Snyder, 1981). As with wall-bounded flows in general, when a stable atmospheric boundary layer meets the rough surface of a city, it takes a while for the flow to adjust to the new surface roughness (Fig. 2.5). This adjustment depends on factors as the urban surface heterogeneity leading to sudden roughness changes. In metropolitan areas, the city center is often dominated by dense high-rise buildings, which are surrounded by suburban residential areas with a lower mean building height H_u. Bottema (1997) derived a minimum fetch of $250H_u$ to reliably evaluate boundary layer characteristics as z_0 for an internal urban boundary layer in equilibrium. Another value of $300z_0$ has been reported by Cheng and Castro (2002) who investigated the flow field after a step change in surface roughness in a wind-tunnel study. They conclude that in many practical cases, the inertial sublayer may not exist in the UBL, because a fetch of several kilometers would be needed.

The urban roughness sublayer (URSL) over cities evolves similar to general rough-wall flows. The thickness of the URSL is two to five times the mean building height H_u, which corresponds to the values suggested by Raupach et al. (1991) from Eq. 2.24. In the upper part of the roughness sublayer the flow is highly three-dimensional and influenced by groups of buildings on the neighbourhood scale (Britter and Hanna, 2003).[7]

The local wall-bounded flows that are investigated in this work, all develop within the *urban canopy layer* (UCL), which forms the lower part of the roughness sub-layer over cities. This is the urban boundary layer equivalent to the canopy layer (compare Fig. 2.4 and Fig. 2.5). In the UCL, special focus lies on phenomena at the street scale and the flow is dominated by its immediate surroundings. A high intermittency of the flow due to separation at buildings, the occurrence of corner vortices and other small-scale phenomena make the flow hard to study because statistical fluctuations are high. Additionally, the heterogeneity of urban morphologies makes it difficult to find suitable boundary conditions for numerical models, since an ideal local boundary layer as described in Sec. 2.2.1 can usually not evolve.

To properly model urban climate on the neighbourhood and street scale, at least buildings have to be resolved individually. That is why obstacle-resolving large-eddy simulations, which will be introduced in the following section, are an essential tool for studying the urban micro-climate.

2.3 Large-Eddy Simulations

Ever since, studying turbulence has not just been about the flow itself, but always was an experimental, numerical and computational challenge as well. These difficulties result from the variety of spatio-temporal scales inherent to turbulent flows. There are basically three approaches to study ABL-flows applying Computational Fluid Dynamics (CFD). They can be distinguished by their attempts to deal with the previously mentioned variety of scales (see also Figure 2.2).

---

[7] Britter and Hanna (2003) divided urban climate phenomena into different groups of length scales. They define the regional scale (100 to 200km), the city scale (10 to 20km), the neighbourhood scale (1 to 2km) and the street scale (0.1 to 0.2 km).

The straight forward approach is to resolve all turbulent scales from the largest eddies $\mathcal{L}$ down to the Kolmogorov length scale η. Direct numerical simulations (DNS) are based on that idea. Here, the non-averaged Navier–Stokes equations are solved and all scales have to be resolved leading to an immense computational effort. The computational costs of DNS highly depend on the Reynolds number, the applied boundary conditions and the domain size. To reduce the computational costs, the Reynolds-averaged Navier–Stokes equations, as introduced in Sec. 2.1.2, can be modeled. With RANS, only the averaged equations (i.e. for $\overline{u_i}$) are resolved. As previously stated, due to averaging, the system of equation becomes *unclosed*, meaning that there are more unknowns than equations. The new unknown variables are the Reynolds stresses τ_{ij} describing turbulent fluctuations. The energy proportion contributed to the flow's total energy by the Reynolds stresses needs to be parameterised to close the system of equations. Turbulence closure can be done via various models, which are based on the closure concepts introduced earlier.

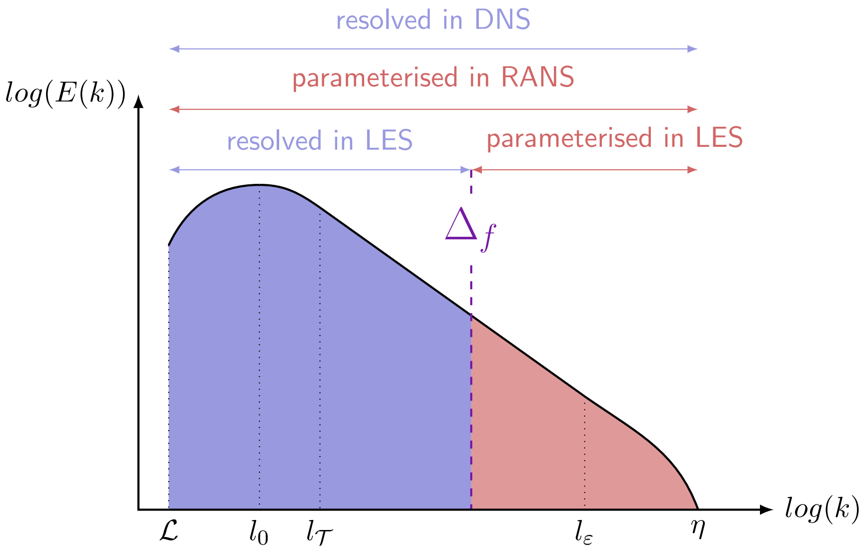

Figure 2.6: The schematic turbulence energy density spectrum from Fig. 2.2 is related to the three major CFD-approaches. The purple dashed line shows the filter cut-off at Δ_f. Indicated above are the different numerical methods to investigate flows and how they differ in resolving and parameterising the turbulent energy contributions.

Large-eddy simulations, in contrast to the two approaches briefly introduced above, are based on the idea to resolve the large-scale turbulent motions of the flow and, at the same time, parameterise the smaller eddies. LES, it seems, takes the best of the two worlds (DNS and RANS) as computational costs are saved to a certain degree, but large scale turbulent features are still resolved directly. Figure 2.6 shows the three approaches in CFD and how they can be represented in terms of length scales in the turbulent energy density spectrum.

The following sections will introduce the theory of large-eddy simulations, its applications and deficiencies and will mainly follow Pope (2000) and Maronga et al. (2020a) for the fundamentals and deviate from their descriptions when explicitly stated.

2.3.1 Filtered Equations

The LES technique is based on a separation of scales by applying a spatial filtering on the governing equations Eq. 2.2 and Eq. 2.5. Remember that in this work we consider the neutral case where thermal energy, humidity and density deviations are not considered. Turbulent scales larger than a chosen cut-off wavenumber or filter width Δ_f are resolved and the unfiltered equations are simulated directly. For scales smaller than the filter width, a parameterisation is needed and turbulence is modeled. These models are called *sub-filter scale models* (SFS models). The choice of the cut-off wavenumber is strongly dependend on the physics of the flow to be studied. Following Heus et al. (2010), a minimum of 90 % of the flows energy should be resolved directly. As described by Leonard (1975), the velocity field $u_i(x_i, t)$ is convoluted with the spatial filter function $G(x_i, \Delta_f)$ as follows

$$u_i(x_i, t) = \widetilde{u}_i(x_i, t) + u_i''(x_i, t) = \int_{-\infty}^{\infty} u_i(x_j', t) G(x_i - x_j', \Delta_f) dx_j' + u_i''(x_i, t), \quad (2.25)$$

with $\widetilde{u}_i(x_i, t)$ being the filtered variable and $u_i''(x_i, t)$ the SFS velocity. The filter function G is applied over the whole flow domain as denoted by the integration bounds $-\infty$ and ∞.

Applying the filtering process described in Eq. 2.25 to the equation of momentum conservation (Eq. 2.5) yields the filtered Navier–Stokes equation

$$\frac{\partial \widetilde{u}_i}{\partial t} + \frac{\partial \widetilde{u_i u_j}}{\partial x_j} = -\frac{1}{\rho} \frac{\partial \widetilde{p}}{\partial x_i} + \nu \frac{\partial^2 \widetilde{u}_i}{\partial x_j^2}. \quad (2.26)$$

The nonlinear advection term on the left hand side contains the filtered product of the velocities. In principle, this is no different to the steps done when deriving the Reynolds-averaged Navier–Stokes equation (see Eq. 2.10) and can equivalently be solved by introducing the SFS Reynolds stress tensor defined as

$$\begin{aligned} \widetilde{u_i u_j} &= \widetilde{(\widetilde{u}_i + u_i'') \cdot (\widetilde{u}_j + u_j'')}, \\ \widetilde{u_i u_j} &= \widetilde{\widetilde{u}_i \widetilde{u}_j + u_i'' \widetilde{u}_j + u_j'' \widetilde{u}_i + \widetilde{u_i'' u_j''}}, \\ \implies \quad \tau_{ij}'' &= \widetilde{u_i'' u_j''} = \widetilde{u_i u_j} - \widetilde{u}_i \widetilde{u}_j. \end{aligned} \tag{2.27}$$

The Reynolds stress tensor can be split into an isotropic part and an anisotropic part $\tau_{ij}^{'',a}$. Only the anisotropic part $(i \neq j)$ is also transporting momentum while the isotropic part $(i = j)$ is included in the modified pressure $\tilde{p}^m$. They are written as follows:

$$\tilde{p}^m = \tilde{p} + \frac{\rho}{3} \widetilde{u_j'' u_j''}, \tag{2.28}$$

$$\tau_{ij}^{'',a} = \tau_{ij}'' - \frac{1}{3} \widetilde{u_j'' u_j''} \delta_{ij}. \tag{2.29}$$

Including these considerations into Equation 2.26 yields

$$\frac{\partial \widetilde{u}_i}{\partial t} + \widetilde{u}_j \frac{\partial \widetilde{u}_i}{\partial x_j} = -\frac{1}{\rho} \frac{\partial \widetilde{p}^m}{\partial x_i} + \nu \frac{\partial^2 \widetilde{u}_i}{\partial x_j^2} - \frac{\partial}{\partial x_j} \left(\tau_{ij}'' - \frac{1}{3} \widetilde{u_j'' u_j''} \delta_{ij} \right). \tag{2.30}$$

Note that also the sub-filter scale turbulence kinetic energy e'', which was introduced earlier, can be described by $e'' = 1/2 \widetilde{u_i'' u_i''}$ and is hidden in both, the anisotropic and isotropic terms of the above equation.

The continuity equation i.e. conservation of mass is expressed by

$$\frac{\partial \widetilde{u}_i}{\partial x_i} = 0, \tag{2.31}$$

which also holds for the SFS velocity u_i''. The filtered and the SFS velocities both are solenoidal.

Besides the cut-off wavenumber Δ_f, the computational grid spacing $\Delta_i = (\Delta_x, \Delta_y, \Delta_z)$ acts as another determinant spatial scale. It has to be small enough so that the filtering can be applied $(\Delta_i \leq \Delta_f)$ properly. If one were to choose a filter width that is smaller than the grid size, this would only result in the grid spacing being decisive for which flow features are not directly resolved, so that the filter would not influence the flow. In this case, the usage of a proper SFS model would not be applicable anymore. This leaves one with practically two possibilities for choosing the grid size, shown in Table 2.1.

Table 2.1: The two general possibilities of choosing the grid size when it comes to filtering the Navier–Stokes equations.

Explicit filtering: $\Delta_i < \Delta_f$	Implicit filtering: $\Delta_i = \Delta_f$
• apply analytical filter explicitly	• no analytical filter is required
• known filter characteristics	• filter characteristics cannot be controlled
• additional computational costs	• only one determinant spatial scale
	• used in most LES models

In *PALM* and accordingly also in this work, the implicit filtering approach is chosen (Maronga et al., 2020a). From here on, the term *sub-grid scale* (SGS) is used analogously to SFS. Speaking of the grid size, implicitly the filter width is meant and vice versa.

The choice of the filter width in LES is linked to the before mentioned other numerical approaches in CFD. This becomes clear by again looking at the energy density spectrum in wavenumber space shown in Fig. 2.6. As $\Delta_f \to \eta$, the flow simulation can be understood as a DNS. If the full wavenumber range is being filtered and all turbulence is being parameterised, the simulation can be interpreted as a RANS model. In the latter case, only the ensemble average of the flow is resolved.

Filtering the Navier–Stokes equation comes with some implications to the flow modeled by the filtered equations Eq. 2.30 and Eq. 2.31 as the system becomes unclosed and inaccuracies can evolve in flow computation at surfaces. Those issues shall be addressed in the following.

2.3.2 Turbulence Closure

While the unfiltered equations consist of four unknowns (the three velocity components u, v and w and the pressure p) and four equations (the three components of the momentum equation plus the continuity equation), the filtering process of the Navier–Stokes Equation 2.5 additionally leads to the covariance terms $\widetilde{u_i''u_j''}$ (or SGS fluxes), which cannot be calculated explicitly. The system of equations becomes unclosed, since there are more unknowns to be calculated than equations available.

The challenge of turbulence closure is addressed in LES by the application of so called SGS models. The theoretical foundations for most SGS models are the assumption of local isotropy by Kolmogorov (1941, 1991) and the turbulent viscosity models for the RANS equations (see Sec. 2.1.2). The simplest approach was proposed by Smagorinsky (1963) and laid the foundation for many other SGS models to follow (Deardorff, 1980; Germano et al., 1991; Lilly, 1992). *PALM* offers various kinds of SGS models.

In this work, a modified version (Moeng and Wyngaard, 1988; Saiki et al., 2000) of the 1.5-order closure by Deardorff (1980) is used (abbreviated as the D80 model) and therefore focused on. The following equations are again customised versions of the ones by Maronga et al. (2015), which take into account the non-buoyant flow studied in this work. Based on the turbulent viscosity hypothesis, it is assumed that the SGS kinetic energy transport is proportional to the local mean velocity gradients:

$$\widetilde{u_i''u_j''} - \frac{2}{3}e''\delta_{ij} = -K_m\left(\frac{\partial \tilde{u}_i}{\partial x_j} + \frac{\partial \tilde{u}_j}{\partial x_i}\right), \tag{2.32}$$

with K_m being the local eddy diffusivity of momentum. Note the similarity between the above equation and Eq. 2.15. The eddy diffusivity can be related to the SGS-TKE e'' by applying the mixing-length model

$$K_m = c_m l''\sqrt{e''}, \tag{2.33}$$

where c_m is a model constant and l'' is the SGS mixing length.[8]

This brings us to the crucial point in SGS-modeling if near-wall flows in urban climate are concerned. The SGS mixing length l'' and c_m have to be specified. In simple isothermal flows, the mixing length is usually calculated as a function of the grid spacing Δ_i and the height above ground z. It is defined as the minimum of the third root of the grid-volume and 1.8 times the height above ground z, i.e. $l'' = min(1.8z, (\Delta_x\Delta_y\Delta_z)^{1/3})$.[9] In contemporary LES models including *PALM*, this definition is used in the whole model domain. If topography is used, the height above ground is substituted by the distance from the wall. The rather rigid approach of calculating the mixing length can lead to problems especially in complex flows within the urban canopy layer with surfaces of heterogeneous roughness, where the distance from the wall is not the only crucial length scale determining the mixing-length. Germano et al. (1991) tried to challenge this issue and developed a dynamic SGS-model (abbreviated as G91) where c_m is spatially and temporally variable. The value of c_m is not constant throughout the whole model domain anymore, but relies on the varying values of resolved stresses little larger than the grid size. Nevertheless, the model by Germano et al. (1991) was tested for turbulent channel flows where it outperformed the classical approach by Smagorinsky (1963) and Deardorff (1980), but it remains an open question if it actually performs better within very complex UCL flows.

---

[8] In *PALM* the value of $c_m = 0.1$ is set if not the dynamic sub-grid scale model (Germano et al., 1991) is used.

[9] Having a uniform grid size of e.g. $\Delta_i = 1$m, the calculation height for the wall-parallel velocity values at the first level above ground lies at $z = 0.5$m. In this case, the SGS-mixing length would be $l'' = 1.8 \cdot 0.5 = 0.9$ m. For heights further away ($z > 1$m) the mixing length in our example would equal the grid size. l'' is thus intrinsically required never to exceed the grid size Δ_i (Deardorff, 1980).

An additional unknown variable that arises is the SGS-TKE e''. It is calculated by the transport equation

$$\frac{\partial e''}{\partial t} + \tilde{u}_j \frac{\partial e''}{\partial x_j} = -(\widetilde{u_i'' u_j''}) \frac{\partial \tilde{u}_i}{\partial x_j} - \frac{\partial}{\partial x_j} \left[\widetilde{u_j'' \Big(e'' + \frac{\partial p''}{\rho} \Big)} \right] - \varepsilon'', \tag{2.34}$$

where ε'' is the SGS dissipation rate within one grid volume defined as

$$\varepsilon'' = c_\varepsilon \cdot \frac{e''^{\frac{3}{2}}}{l''}, \tag{2.35}$$

with $c_\varepsilon = 0.93$ for isothermal flows and uniform grids ($\Delta_x = \Delta_y = \Delta_z$) (Maronga et al., 2020b).

As already stated, the dissipation process is the conversion of kinetic energy into internal energy due to viscous stresses. In numerical simulations of neutral case flows, energy dissipation obviously cannot happen in a physical way since temperature changes are not permitted by the model. Thus, the residual energy ε'' is simply taken out of the system at the sub-grid scale. This is necessary to prevent the system's kinetic energy from diverging.

The filtered pressure term in Equation 2.34 is parameterised by the local gradient of SGS-TKE itself using twice the negative eddy diffusivity K_m as a factor of proportionality:

$$\widetilde{u_j'' \left(e'' + \frac{\partial p''}{\rho} \right)} = -2K_m \frac{\partial e''}{\partial x_j}. \tag{2.36}$$

There are various approaches of closing the system of filtered Navier–Stokes equations, and many are based on the original Smagorinsky model. In this thesis, the focus is on the modified approach by Deardorff (1980) and on the dynamic model by Germano et al. (1991). For more information on other modifications, see chapter 13.6 of Pope (2000) or the comprehensive summary by Gadde et al. (2021). Piomelli (1999) gives a broad overview of additional SGS models as *two-point closures*, *mixed models* or *one-equation models*.

As we have learned how the small-scale turbulence can be parameterised in LES, let us now focus on the region where these small scales occur most frequently - the near-wall region and the application of surface boundary conditions.

2.3.3 Surface Boundary Conditions

Any obstacle-resolving large-eddy simulation model in urban climate has to model the flow at solid surfaces at some point. Besides the SGS models, the boundary conditions at the grid point closest to a surface are the most critical component of such an LES. The reason for this criticality lies primarily in the complexity of real surfaces. In addition, strong gradients of the wall-parallel velocity components $\partial u/\partial z$ and $\partial v/\partial z$ and pronounced wall-normal turbulent fluxes $u'w'$ are found close to surfaces. Although wall boundary conditions in LES can be applied to walls of every orientation, we want to assume a horizontally aligned wall (x-y-plane) in the following explanations, in analogy to Sec. 2.2.1.

Most contemporary LESs choose the aforementioned log-law as a boundary condition between the wall and the wall-layer to calculate the local momentum fluxes (often called wall shear stress τ_w) and wall-parallel velocity components at the first grid level. The wall-layer is the horizontal layer at the first grid cell above ground. At first sight, the log-law seems to be a valid approach since the wall-layer should typically be located within the constant-flux layer.

For the neutral case and horizontal surfaces the equation for the vertical profile of the filtered horizontal wind $\tilde{u}_h = (\tilde{u}^2 + \tilde{v}^2)^{1/2}$ is

$$\frac{\partial \tilde{u}_h}{\partial z} = \frac{u_*}{\kappa z}. \tag{2.37}$$

With the friction velocity in LES being defined as $u_*^2 = [\widetilde{u''w''}_{wl}^2 + \widetilde{v''w''}_{wl}^2]^{1/2}$ and the index wl denoting the wall-layer, the equation for the wind profile can be split up into to single equations for components $\tilde{u}$ and $\tilde{v}$:

$$\frac{\partial \tilde{u}}{\partial z} = \frac{\widetilde{u''w''}_{wl}}{u_* \kappa z} \quad \text{and} \quad \frac{\partial \tilde{v}}{\partial z} = \frac{\widetilde{v''w''}_{wl}}{u_* \kappa z}. \tag{2.38}$$

The standard method to implement the boundary conditions in LES is to evaluate the integrated form of Eq. 2.37 to obtain the surface momentum fluxes. Integration over z takes place from z_0 up to the height of the first computational grid level, the evaluation height $z_{wl} = \Delta_i$, which then yields

$$u_*^2(x,y) = \left(\frac{\kappa}{\ln\left(\frac{z_{wl}}{z_0}\right)} \right)^2 \cdot u_h^2(x,y,z_{wl}). \tag{2.39}$$

A dependence of u_* on x and y was introduced since the local surface stresses are needed. This local approach allows heterogeneous surfaces to be taken into account but can lead to an overprediction of the mean shear stress (Hultmark et al., 2013). The concept introduced here is referred to as the *instantaneous logarithm* (IL) method (see e.g. Albertson and Parlange (1999)), since technically instantaneous values of u_h are used even though the log-law was initially derived for mean quantities.

In the past decades, various boundary conditions for LES have been formulated, which are modifications of the log-law implementation. The SG model (Schumann, 1975; Grötzbach, 1987) and the shifted SG model (Piomelli et al., 1989) provide the instantaneous local surface shear stress and require knowledge of the mean surface shear stress and the filtered stream-wise velocity. In a study by Marusic et al. (2001) though, wind-tunnel results were compared to three boundary conditions conventionally used in LES including the SG and the shifted SG model. None of the models did sufficiently reproduce the measured spectra of the wall shear stress. In the same work, a new model (MKP model) was then formulated to meet the measured results independent of the Reynolds number. A comparison by Stoll and Porté-Agel (2006) of the above-mentioned boundary conditions, among others, showed that the effect of higher roughness lengths in the SG and shifted SG model unexpectedly is associated with lower values of resolved velocity fluctuations. Kawai and Larsson (2012) pointed out that wall-modeled LES show a deviation of the wall shear stress of 10 up to 15 %, which is commonly called the "log-layer mismatch". This is due to numerical resolution constraints and sub-grid modeling errors. Anderson and Meneveau (2011) and Anderson et al. (2012) published a series of studies proposing and applying a dynamic roughness model (DSR) for LES over fractal-like surfaces. However, since building facades often represent patches of varying roughness, it still needs to be verified if this approach is applicable locally.

For the sake of completeness, it should be mentioned that there are also boundary layer models for density-driven flows. Monin and Obukhov (1954) formulated the so-called Monin–Obukhov similarity theory (MOST). In principle, the MOST equations add a factor Φ_m to the right-hand side of the log-law from Eq. 2.22. The similarity function for momentum $\Phi_m(z/L)$ equals one in the neutral case and is a function of the height above ground and the so-called Obukhov length L. The Obukhov length can be viewed as the height at which buoyant effects contribute more to turbulence generation than wind shear. Thus, the log-law is a special case of MOST for neutral flows.

2.3.4 Large-Eddy Simulations in Urban Climate Studies

Until about twenty years ago, the study of urban climate was more or less limited to field measurements or wind-tunnel studies. The application of LES was initially constrained to atmospheric boundary-layer flows. With increasing computing power, more and more available geometrical data on real urban surfaces and the pressing need to understand urban climate processes, LES has increasingly been used within the urban canopy layer. LES urban-climate studies can be divided into three different classes of which a short review is given without claiming completeness:

- *Generic experiments* (street canyons, arrays of cubes),
- *Validation studies* (e.g. with a supplementary wind-tunnel study),
- *Real world applications* (an actual model run of a city or neighbourhood).

Generic numerical experiments generally serve two purposes. First, they deliver a resource-efficient approach on applying LES, which is why early studies relied exclusively on generic settings as single building blocks (Baetke, 1990; Wengle and Werner, 1993), arrays of rib roughnesses (Cui et al., 2003) or street canyons (Letzel et al., 2008). Second, a generic model topography can also serve the differentiated consideration of a specific phenomenon and the targeted modification of certain parameters. For example, Bou-Zeid et al. (2009) studied the effect of building representation in CFD-models on the mean flow and its fluctuations by clustering urban canopies on three different levels of detail. To specifically investigate the effect of courtyard openings on ventilation and pollution in courtyards, Gronemeier and Sühring (2019) used a generic array of building blocks with varying courtyard widths and openings.

A link between generic studies and validation simulations is quickly established, since many validation studies of LES are set up in generic environments. One example is the *Michel-Stadt*, which was developed at the *EWTL* in Hamburg. The validation data stems from wind-tunnel measurements (Fischer et al., 2010; Bastigkeit, 2011) and has been used for validation of e.g. the *ADREA-HF* LES (Bartzis, 1991; Tolias et al., 2018). It is also reasonable to use realistic cases for LES validation as Hertwig et al. (2017a,b) proofed by comparing a wind-tunnel model of the inner city of Hamburg with results from *FAST3D-CT* (Patnaik and Boris, 2010) or Gronemeier et al. (2021) to validate the dynamic core of *PALM* (Maronga et al., 2020a).

LES are not an end in themselves. Practical applications in "realistic" urban environments are increasing in number and the areas of study are manifold. The study of pedestrian-level ventilation in Hong Kong (Letzel et al., 2012), the dispersion of pollutants in Boston (Akinlabi et al., 2022) or the effect of building retrofitting on the urban microclimate in Berlin (Maronga et al., 2022) are just a few recent examples. Modeling whole cities or districts of several square kilometres comes with new computational challenges as resolution constraints due to exceeding numbers of grid cells. Therefore, nesting approaches have been established, which enable modellers to set a fine grid at the region of interest and model the surrounding with a coarser grid. Auvinen et al. (2020) studied the effect of very high-resolution and nesting approaches in a realistic case study of Helsinki. With the smallest nested grid size being $\Delta_i = 1$ m, they also approached wall-distances associated with the RSL and are problematic when log-law boundary conditions are used as we will see in the following section.

2.3.5 Practical Limitations in Obstacle-Resolving LES

The morphology of urban surfaces and the flow within the UCL are influenced by many length scales. In this work, a distinction is made between two groups of length scales. The building scale H_u is in the order of 10^1 m up to 10^2 m, depending on the type of city studied (metropolitan or rural, European or Asian, etc.). The building scale can be interpreted as the URSL-dominating length scale, but is also a determinant factor if it comes to wake sizes and other larger-scale flow phenomena within the UCL. The smaller scales h_r are in the order of up to 10^1m. Objects on these scales include balconies on house facades, parked cars, or plants, whereby the latter represent a special case in flow modeling due to their permeability. The smaller scales affect the near-wall flow and are important to areas of interest like wind comfort and dispersion of pollutants. To study urban climate phenomena on the street or neighbourhood scale, the modeled flow is required to replicate flow statistics influenced by these two classes of length scales.

Large-eddy simulations do not model the unresolved energy contributions precisely enough when their relative contribution is too high. Pope (2000) and Heus et al. (2010) suggest that an LES can be viewed as well-resolved if 90% of the turbulence kinetic energy is resolved. The loss in resolved kinetic energy is mainly balanced by the energy contribution of the SGS model, but the contribution of numerical dissipation cannot be neglected as well (Gousseau et al., 2013). For implicit LES, the SGS-contributions increase with increasing grid size and thus, a flow-dependent upper limit for the grid size can be estimated. In an attempt to find an estimate for the grid size, Baggett et al. (1997) found that Δ_i should be one tenth of the local integral length scale.[10] For urban canopy flows, the integral length scales are determined by the above introduced building scale H_u and thus about ten grid cells per building height are required. This estimate is roughly supported by Gousseau et al. (2013) who studied the energy contributions in LES for the flow around a high-rise building with an aspect ratio of $1{:}1{:}2$ and found values of 20 to 30 grid cells per building side to be sufficient. By following Baggett et al. (1997) and Cabot and Moin (2000), an estimate for the maximum applicable grid size would

---

[10] Originally, Baggett et al. (1997) chose the integral dissipation length defined as $L_\varepsilon = \frac{e^{3/2}}{\varepsilon}$, but also state that it is always of the same order as the integral scales. This is also supported by Cabot and Moin (2000).

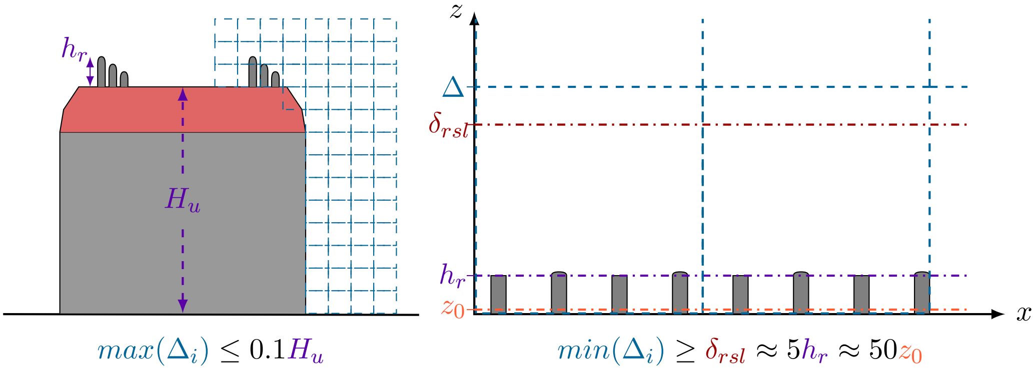

Figure 2.7: The grid requirements in obstacle-resolving LES depend on multiple factors. A building of length scale H_u has to be resolved sufficiently (left). At the same time, small scales of length scale h_r challenge the proper implementation of boundary conditions (right).

be $max(\Delta_i) \leq 0.1H_u$. On the left side of Figure 2.7, a uniform computational grid is sketched, which fulfills the above requirement.

It was stated in Sec. 2.2.1, that the mean wind profile can depart from the log-law in the RSL and, based on laboratory studies, Raupach et al. (1991) defined a roughness sublayer height between $2h_r$ and $5h_r$ (Eq. 2.24). For a valid application of LES boundary conditions, the lowest grid level has to be located outside the roughness sublayer and within the inertial sublayer. With increasing computing power, high-resolution LES become more and more frequent and in many studies, the lowest grid level was located within the RSL (Beare et al., 2006; Basu et al., 2012; Maronga, 2014; Sullivan et al., 2016; Udina et al., 2016). According to Townsend (1980), the roughness length can be estimated as $z_0 \approx 0.1h_r$ and thus $\delta_{rsl} \approx 50z_0$. Basu and Lacser (2017) consequently discussed the choice of the evaluation height, i.e. the grid size Δ_i, for the boundary conditions and justify their recommendation for the smallest possible grid size $min(\Delta_i) \geq \delta_{rsl} \approx 5h_r \approx 50z_0$. These considerations are sketched on the right hand side of Fig. 2.7. Recently, Maronga et al. (2020b) considered the above recommendations, formulating new boundary conditions by rising the evaluation height to a higher grid level. While this approach allows LES at very small grid sizes $\Delta_i \ll 5h_r$ and seems feasible for empty ABL flows, it is questionable to link the mean flow velocity at wall distances $\geq 5h_r$ to the wall shear stress close at the wall-layer for UCL flows.

The considerations on maximum and minimum grid sizes lead to very practical limitations for the correct application of obstacle-resolving LES in urban climate studies. With H_u being in the order of 10 m to 10^2 m and h_r being in the order of up to 10 m, the maximum allowed grid size often even has to be smaller than the minimum allowed grid size. Large-eddy simulations can therefore not be applied within the urban canopy without compromising the accuracy and correctness of the resulting flow statistics.

A modeller in urban climate might now want to consider if rather the correct application of the log-law based boundary conditions ($\Delta_i \geq 5h_r$) or the gain of a well-resolved LES ($\Delta_i \leq 0.1H_u$) is more crucial. Since the boundary conditions depend on the near-wall mean flow, which is driven by the larger scales, one cannot model the wall region correctly without resolving larger motions sufficiently. The condition for the maximum grid size allowed in obstacle-resolving LES should therefore not be touched. These limitations motivate the study of the flow at multi-scaled (H_u and h_r) buildings to distinguish the UCL flow dominated by the larger length scales H_u and the near-wall flow dominated by the smaller roughness length scales h_r. A more thorough understanding of the near-wall flow statistics for such cases is needed in order to assess emerging inaccuracies and to formulate new adapted boundary conditions.

2.4 Physical Flow Modeling

Physical flow modeling has a tradition that goes far back into the past. While the philosophers of the ancient world and the renaissance had to rely on qualitative observations, with the ages of enlightenment and then industrialisation, a new era of fluid mechanical experiments began. During that time, Osborne Reynolds, Lord Rayleigh, Ludwig Prandtl and a little later also G.I. Taylor set milestones in modern fluid mechanics also by means of experimental works. If we jump forward to nowadays' physical flow modeling, there are still concepts at work, which were introduced back then such as Taylor's *frozen turbulence hypothesis* or the Reynolds number independence.

If boundary-layer flows are to be studied experimentally, a first decision to be made is which fluid shall be used for a certain experiment. Water and air are common choices for physical flow modeling of atmospheric boundary layers. The kinematic viscosity of water is 15 times smaller than that of air, and consequently higher Reynolds numbers can be reached. Nevertheless, high wind speeds are achieved with a far lower energy consumption and lower material costs using air as a fluid. Other physical parameters as the heat capacity or thermal conductivity can also play big role in terms of buoyant flows. If buoyancy comes into play and stratified boundary layers are studied, modeling flows with water can bring advantages. Even though rotational effects cannot be modeled easily and the neutral ABL hardly ever exists, in the end, wind tunnels are a valid choice (Snyder, 1981).

Boundary-Layer Wind Tunnels

There are various types of wind tunnels, but in this thesis the focus is on specialised open-return boundary-layer wind tunnels. The attribute "open-return" indicates that the wind tunnel sucks in the surrounding air by means of a fan and blows it out again after passing through.[11] The attribute "boundary-layer" comes from the fact that these types of wind tunnels are specially designed to model boundary layer flows. Rather than for aeronautical applications, they are therefore used in the field of wind engineering.

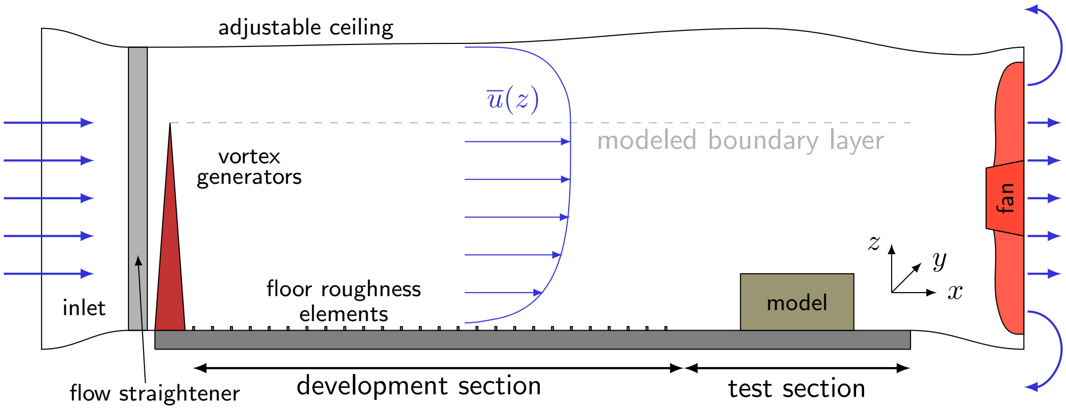

Figure 2.8: Schematic drawing of an open-return boundary-layer wind tunnel after Plate (1999) with inlet, development section, test section, a scaled model and the fan.

Figure 2.8 shows a schematic of an open-return boundary-layer wind tunnel. The rotating fan on the right hand side sucks in the air such that the flow goes through the wind tunnel from left to right. The air is sucked into the channel and not blown into it. This prevents the aerodynamic properties of the wind tunnel drive from affecting the flow in the test section. While passing through the inlet, a flow straightener ensures uniform flow statistics over the z-y-plane. While the air passes the development section, two types of obstacles modify the flow in such a way that it represents a fully developed, statistically stationary, atmospheric boundary layer similar to nature. The large scale vortex generators (or "spires") influence the turbulence statistics also higher above ground, and the floor roughness elements are of importance when it comes to near-wall flow statistics and the mean wind profile. After the modeled boundary layer has fully evolved, the flow reaches the test section. In the test section, models of reduced scale are placed, and measurements can be taken. Larger models can displace a lot of air and lead to a longitudinal pressure gradient and thus a speedup of the flow in the test section. To prevent this effect from happening, many boundary-layer wind tunnels have a height-adjustable ceiling.

---

[11] Often, open-return wind tunnels are called Eiffel-type wind tunnel, because the french engineer Gustave Eiffel significantly contributed to the evolution of open-return wind tunnels.

Flow Similarity and Reynolds Number Independence

Wind-tunnel models and other flow experiments are usually far smaller than their real world equivalents they search to model. The concept of flow similarity and parameters as the Reynolds number make it possible to scale up the experimental results to reality. Similarity parameters can be obtained by transforming the conservation laws into a dimensionless form. Flows with similar Reynolds number $Re = LU/\nu$ show the same non-dimensional flow statistics if boundary conditions are similar. For example, if in a wind-tunnel experiment of the ABL the length scales L in a model are scaled down by, say $1{:}100$, and the kinematic viscosity ν is kept since air is used, the velocity U would have to rise by a factor of 100 for the Reynolds number to be the same. Such high wind speeds are usually not achievable in wind-tunnel experiments.

The concept of Reynolds number independence helps out here. Townsend (1951) stated that "geometrically similar flows are similar at all sufficiently high Reynolds numbers", meaning that the Reynolds number does not need to be in the same order for two flows to develop comparable flow statistics. Rather, two flows need only have values sufficiently above the critical Reynolds number. This holds nearly everywhere except in regions very close to solid surfaces where the eddy sizes become smaller than l_ε and dissipative effects start to dominate (Snyder, 1981). It is therefore crucial to test an experimental setup for Reynolds number independence especially close to walls. Sufficient Reynolds number independence testing has been done multiple times for all experimental setups presented in this thesis, as we will see later.

Taylor's Frozen Turbulence Hypothesis

Wind-tunnel modeling often involves qualitative flow-visualisation imaging techniques. Most quantitative measurement techniques deliver single-point time series as for example Prandtl-tubes, hot-wire anemometers or Laser-Doppler anemometers (LDA) do. Measurements always include placing a probe and thus an obstacle into the flow (Prandtl-tube or hot-wires) or in the vicinity of the region of interest (LDA). The probes do disturb the flow and measuring at each time at each location simply would not prove practical. One question that now arises is whether information on the spatial variability is lost by only measuring at distinct locations.

Taylor's (1938) frozen turbulence hypothesis relates the single-point time series of the turbulent variables to the spatial distribution of that same variable upstream from the single-point location. Small-scale eddies of size l move with the flow and are advected by the mean velocity $\overline{u}$. For a sensor that measures a time series at a single point, the advected eddies passing by stay unvaried during the time span $l/\overline{u}$. The frozen turbulence hypothesis is only reliable, if the turbulent fluctuations are small compared to the mean flow and $u'/\overline{u} \ll 1$ (Pope, 2000). Besides, the turbulence has to be statistically homogeneous in the main flow direction. There are flows, in which mean flow amplitudes and turbulent fluctuations are of the same size or where the homogeneity along the main flow direction is not given. Examples are free shear flows, stagnation points and near-wall flows over rough surfaces. In such cases, it is important to take this drawback into account when interpreting the data. This is particularly important for measurements where the spatial and temporal behaviours are evaluated, such as energy density spectra or the calculation of integral length scales.

2.4.1 Wind-Tunnel Modeling in Urban-Climate Studies

As with large-eddy simulations, in this work we divide wind-tunnel studies into three branches of applications. An overview of recent and older, but still relevant, examples of such studies is given. The three classes of contemporary wind-tunnel modeling studies are:

- *Generic experiments* (street canyons, arrays of cubes),
- *Validation studies* (for CFD codes),
- *Real world applications* (an actual model of a city or neighbourhood).

Generic wind-tunnel studies made considerable contributions to the understanding of turbulent boundary layers. As already stated in Sec. 2.2.1, Raupach et al. (1980) identified the roughness sublayer by conducting wind-tunnel experiments of boundary-layer flows over different rough surfaces. The motivation of their experiment was to find out how deep into the boundary layer the influence of surface roughnesses is. Their data was intended to serve as a complement to natural measurements over forested areas (Thom et al., 1975; Garratt, 1978). Wind-tunnel experiments also play a major role in wind-load studies on free-standing buildings of various geometries which are of high interest in structural and civil engineering. Stathopoulos and Zhu (1988, 1990) as well as Stathopoulos and Luchian (1990) investigated the influence of near-wall turbulence on buildings of different geometries (roof, facade), but focused on pressure-coefficient distributions on facades. For structural-engineering purposes, the pressure coefficient is of higher interest than the near-wall flow characteristics. Newer studies by e.g. Addepalli and Pardyjak (2013, 2015) investigate the flow in step-up and step-down street canyons by applying two-dimensional particle image velocimetry (PIV) measurements. Allegrini et al. (2013b) investigated the influence of heated building surfaces on vortices in street canyons and found windward wall heating to influence the street-canyon flow the most.

The precise control that can be exerted on the flow boundary conditions in wind-tunnel experiments makes them good tools for validating numerical models. Especially LES codes can be validated by wind-tunnel experiments. The smaller length scales which are usually missed by LES models can still be resolved in wind-tunnel experiments. Validation experiments can be conducted with generic city models and with realistic cases. The above mentioned *Michel-Stadt* is an example of a generic city model generated for validation purposes (Fischer et al., 2010; Bastigkeit, 2011). Models of actual urban geometries were used in the validation studies of Hertwig et al. (2017a,b) (Hamburg), Hertwig et al. (2019) (London) and Gronemeier et al. (2021) (HafenCity in Hamburg). The advantages of such studies are an additional gain in knowledge about the area of study and a use-case related validation. A disadvantage is that due to the complexity of the particular case, it is often not possible to make general statements about the reasons for the deviations that occur.

3 Experimental Setup

In this chapter, the experimental setup for data generation on near-wall flow phenomena is introduced. In the first section the methods of investigation are introduced (Sec. 3.1). This involves a facility for physical flow modeling and a large-eddy simulation code. The calculation of flow quantities is explained in Sec. 3.2.

3.1 Methods of Investigation

The chosen methods of investigation, namely the wind-tunnel facility of *WOTAN* and the large-eddy simulation code *PALM* are now briefly introduced.

3.1.1 Wind Tunnel WOTAN

The open-return boundary-layer wind tunnel *WOTAN* is located at the *Environmental Wind Tunnel Laboratory* (*EWTL*) of the University of Hamburg. Figure 3.1 shows a side view of the wind tunnel, which follows the typical design of boundary-layer wind tunnels (see also Sec. 2.4 and Fig. 2.8). In total, *WOTAN* is 25 m long and the air is sucked into the channel by an axial blower with a diameter of 3.15 m, which is located at the end of the wind tunnel. The development section and test section together are 18 m long and 4 m wide. To ensure a constant pressure in along-wind direction, 22 pressure sensors are placed on both sides of the wind tunnel and the height adjustable ceiling can be elevated between 2.75 m and 3.25 m. This is necessary if a non-zero pressure-gradient is caused by blocking of large models. The mean wind speed can be adjusted between 0.5 m/s and 20 m/s, measured at the inlet behind the spires. In this work, mean wind speeds at the inlet of the wind tunnel are in the order of ≈ 5 m/s.

The models used in this work were placed on the downwind turntable (right circle in top-view sketch of *WOTAN* in Fig. 3.2) such that the length of the development section could be maximised. The two circles in Fig. 3.2 mark the positions of the two turntables which are part of the test section and enable the modeller to change the approach wind direction by rotating the model in the reference coordinate system. The inlet on the left and the ventilator on the right are visible. The wind-tunnel coordinate origin was located

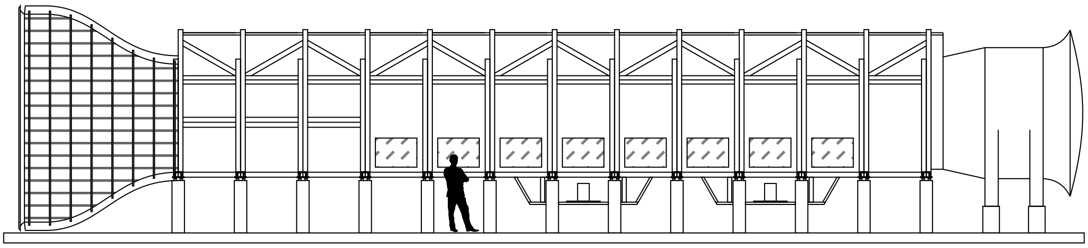

Figure 3.1: A sketch of the wind tunnel *WOTAN* at the *Environmental Wind Tunnel Laboratory* in Hamburg. The view is from the side with the wind blowing from left to right. This sketch was provided by Simon Michel.

in the centre of this turntable. The x-axis is always aligned along the longitudinal axis of the wind tunnel and accordingly parallel to the main flow direction, regardless of the rotation of the turntable. The y-axis is oriented horizontally and perpendicular to the longitudinal wind-tunnel direction. Starting from the wind-tunnel floor and increasing positively with height, the z-axis is defined.

The test section of *WOTAN* is equipped with an automated traverse system. Measurement probes can be mounted onto the traverse and thus driven to desired locations in the test section. The accuracy of the traverse system in positioning a probe is in the order of ± 0.1 mm for each spatial direction. However, the inaccuracy increases with the number of measuring points approached per profile and increases even more when the probe on the traverse moves along diagonals (e.g. x and y at the same time). Unordered measurement profiles or measurement profiles with an extreme number of points should therefore be avoided if possible.

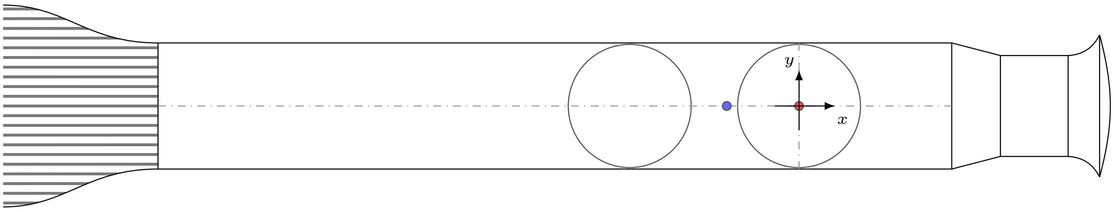

Figure 3.2: A sketch of the wind tunnel *WOTAN* at the *Environmental Wind Tunnel Laboratory* in Hamburg. The view is from the top with the wind blowing from left to right. The two circles show the turntables. The wind-tunnel coordinate system is marked and the blue dot shows the position of the vertical reference profiles.

Vertical **reference profiles** for both experiments were measured 2.3 m upwind from the coordinate origin on the centre line of the wind tunnel (blue dot in Fig. 3.2). The reference profiles have several purposes. Firstly, the reference values u_{ref} are derived from the wind speeds measured here at constant-flux layer height δ_{cf}. In addition, the mean wind profile measured at the reference position is used to initialise the *PALM* simulations (reference profile). Finally, the profile measurements ensure that the necessary boundary-layer parameters correspond to a natural-like boundary layer. We now want to take a closer look at how the two boundary layers are configured in *WOTAN*.

Boundary-Layer Configuration

The configuration of vortex generators (spires) and floor roughness elements can be varied almost arbitrarily to achieve different boundary-layer properties. The development of a proper boundary-layer configuration might take up to several months and is crucial if models with real-world equivalents are investigated. In both experiments presented here, the same configuration of vortex generators and floor roughness elements was used (see Fig. 3.3 and, for more detail, read Appendix A). This configuration is based on an already existing boundary-layer configuration developed by Simon Michel with the aim to achieve a medium rough boundary layer according to the corresponding guidelines (Counihan, 1975; Snyder, 1981; VDI 3783 Blatt 12, 2000). The exact configuration of the vortex generators and the positioning of roughness elements are shown in Figures A.1 and A.2.

The only thing that was changed between the two experiments was the model scale and hence the vertical extent of the boundary layer with its sublayers and parameters including z_0. A detailed description of the approach boundary layer parameters and flow properties at scales $1{:}100$ and $1{:}150$ is given in Sec. 4.

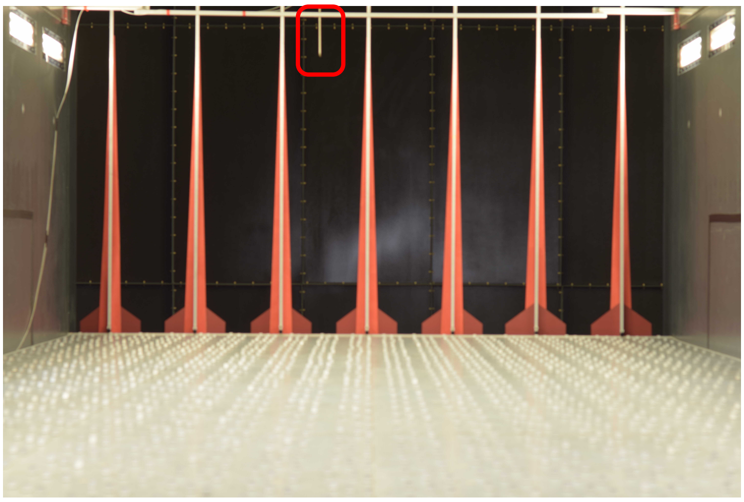

Figure 3.3: Photography taken from the inside of *WOTAN*. The view is in the direction of the inlet. Vortex generators are seen in red (see also Fig. A.1). In front of the vortex generators, the flow roughness elements are visible, which are configured as described in Fig. A.2. The Prandtl tube (and in the second experiment the ultrasonic anemometer) is located at the top end of the vortex generators between the third and fourth spire from the left.

Laser Doppler Anemometry

The single-point 2D-flow measurements were performed using a *laser Doppler anemometer* (LDA; Dantec Dynamics, Skovlunde, Denmark). Many flow measurements, such as hot-wires, are placed in the flow and the hardware of the probes changes the flow. Being optical measurement systems, LDA are non-intrusive because the probe has a sufficiently large distance from the actual measurement. Also the temporal and spatial resolution of LDA measurements is high, which is another advantage if small-scale turbulence is of interest.

In LDA measurements, laser light which is backscattered by small particles passively drifting in the flow is measured (Fig. 3.4). At the *WOTAN* facility, an *Argon* ion-gas laser creates laser light of which two distinct wavelengths of 488 nm (blue) and 514.5 nm (green) are used. This allows for the acquisition of two velocity components (one velocity component per wavelength). Each laser beam is split up into two laser beams of the same colour of which one beam, respectively, is slightly shifted in frequency by a *Bragg cell*. The light is then guided through fibre optic cables into the wind tunnel and to the probe located on the traverse arm. Here, a lens and a mirror focus and direct the laser beam pairs to meet at the region of interest, where they form an ellipsoidal measurement volume. The size of the measurement volume is determined by the focal length, the diameter of the probe and the diameter of the laser beams, since these parameters geometrically determine the length of the principal axes of the ellipsoid (see Tab. 3.1 and Fig. 3.4b). The orientation of the measurement volume in the flow determines which channel (pair of blue or green coloured beams) is measuring which velocity component. In Fig. 3.4a for example, the blue channel samples the u-component, and the green channel samples the v-component; the LDA is operating in UV-mode. For sampling in UW-mode, the probe has to be rotated by $90°$ and the measurement volume is located not below, but laterally to the probe.

So far, the probe has just sent light into the wind tunnel, but there is no signal to receive yet. To that end, the backscattered light from seeding particles that act as passive tracers in the investigated flow is recorded. The required homogeneous seeding of the flow was established by an industrial type hazer system (Smoke Factory, Burgwedel, Germany) placed outside of the wind tunnel in the return section of the flow. According to the manufacturer, passive tracers have a mean particle size of up to 3 μm. Each particle that passes through the measurement volume emits a single *Doppler burst*, which is detected. The bursts get processed by a commercial *burst spectrum analyser* (BSA F70/F90x) developed by Dantec Dynamics (Skovlunde, Denmark). Since in this work, turbulent fluxes (i.e. covariances) are of interest as well, the LDA was operated in

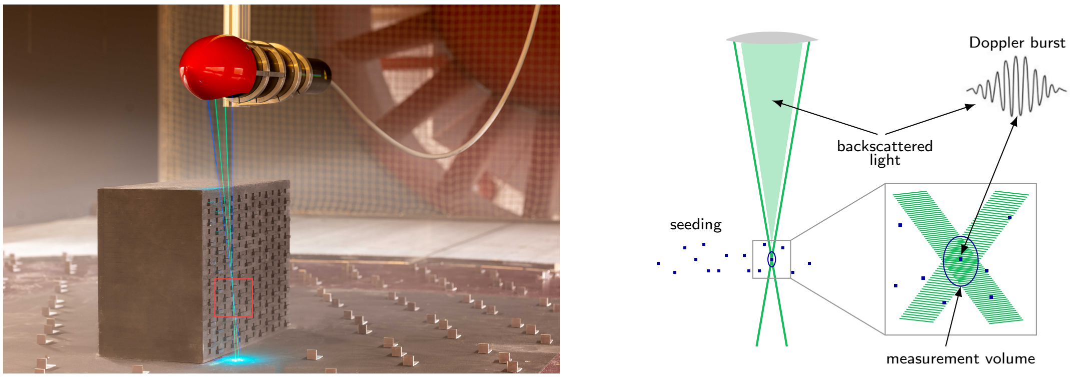

(a) **(b)**

Figure 3.4: (a) The large probe of the 2D LDA operating in UV-mode next to an obstacle placed into the test section in *WOTAN*. The blue and green pairs of laser beams intersect in the measurement volume (red rectangle). The picture was taken by Frank Harms. (b) Schematic of the measurement principle in LDA. Two laser beams intersect in the measurement volume. If a seeding particle crosses the volume, a Doppler Burst is backscattered.

coincidence mode, meaning that only the velocity samples are taken, where bursts could be detected by both channels, blue and green, simultaneously. From the properties of the received signal, the velocities of the particles and thus the flow velocity is calculated.

Two LDA probes were used in this work (Tab. 3.1). The small probe was used during the investigation of the flow over a horizontal plate of homogeneous roughness (Sec. 4.1). The large probe was used for the investigation of the single building case (Sec. 4.2), due to the longer focal length. The focal length of the small probe (160 mm) was too short and the probe would have touched the building model at near-wall measurements in UV-mode.

Table 3.1: The two used LDA probes, their diameters, focal lengths and the principal axis of the ellipsoid measurement volume

	probe diameter	focal length	dx	dy	dz
Small probe	26 mm	160 mm	0.078 mm	0.078 mm	1.658 mm
Large probe	85 mm	500 mm	0.077 mm	0.077 mm	1.102 mm

The non-intrusive approach and high temporal and spatial resolutions are the major advantages of the LDA technique. The optical sensing is moreover mainly independent of ambient conditions as temperature or humidity. Nevertheless, there are some drawbacks of the approach that need to be addressed while measuring but also in data processing.

First, the seeding particle size changes significantly with ambient conditions and the deflecting mirror fogs up quickly under warm and humid conditions. This can lead to insufficient data rates, and the humidity in the wind-tunnel facility has to be regarded while measuring.

Second, LDA time series are discontinuous, since samples are only taken if particles fly through the measurement volume; the time series is non-uniform. If turbulent spectra or integral length scales are to be calculated, a uniform time step is required for the fast Fourier transform (FFT) to work. Thus, a resampling of the data is necessary and will be further explained later on in Sec. 3.2.

Third, it has to be ensured that the region of interest is seeded homogeneously. By looking at the probability distribution of the *inter-arrival time* $\delta t = t_i - t_{i-1}$, it is estimated if this is the case. The inter-arrival time is the time span between two successively arriving velocity signals. For homogeneous seeding, the distribution can be described by a *Poisson distribution*

$$P(\delta t) = \frac{N}{T_{mes}} e^{-\frac{N}{T_{mes}}\delta t} \tag{3.1}$$

with T_{mes} being the total measurement duration and N being the number of signals detected during T_{mes} (Tropea et al., 2007). This is the *particle arrival law* after Adrian and Yao (1986), which is also illustrated in Fig. 3.5a. If seeding was inhomogeneous, clouds of higher particle density would alternate with phases of low particle density and the high flow velocities in the distribution would be clearly overestimated.

The last downside of LDA measurements is that, at higher velocities, more particles pass the measurement volume per time which leads to a bias for higher velocities. This relationship is independent of the homogeneity or intensity of seeding. Figure 3.5b illustrates the matter for an exemplary wind-tunnel measurement. This bias is overcome during data processing by taking advantage of the *transit time* θ that each detected particle needs to fly through the measurement volume. It depends on the velocity of the seeding particle and is also recorded by the LDA. Transit time weighting proofs to be especially effective in the near-wall region. Here, the data rates are lower, and the bias is thus more pronounced. The weighting approach has to be applied for mean quantities, for variances, covariances and higher statistical moments as will be shown later in Sec. 3.2. In general, the equations for the weighted statistical moments were used with the transit time as weights (Kokoska and Zwillinger, 2000).

For most of the measurements in this work, the probe and correspondingly the measurement volume were aligned as accurately as possible according to the wind-tunnel coordinate system. In some cases though, it was not possible to achieve near-wall data because of beam blocking by obstacles. A workaround is, to slightly tilt the probe by a

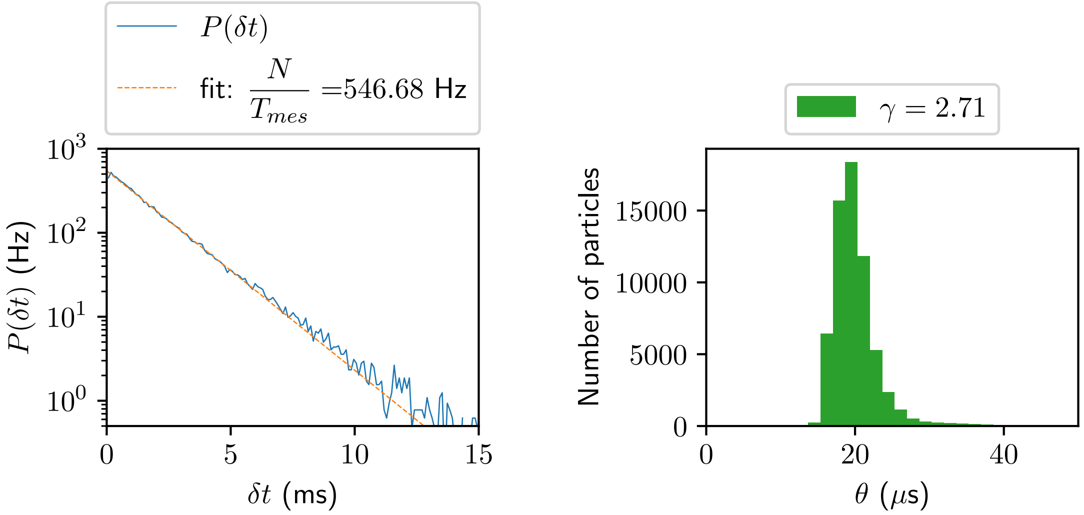

(a) **(b)**

Figure 3.5: (a) The particle arrival distribution with the fitted expected curve. The fitted mean data rate is at 546.68 Hz. The actual mean data rate was 525.56 Hz. (b) Histogram of the LDA transit times. A strong skew illustrates the apparent bias to higher velocities. Both figures were made using the same LDA time series taken 300mm above the ground in a fully developed boundary-layer flow in *WOTAN*.

known angle and reconstruct the occurring offset in the measured velocities. This offset increases with the tilting angle but remains negligibly small for the tilting angles used in this work (order of $\approx 10^{-4}$ m/s). It will be indicated throughout this thesis when a tilted probe setting was used.

Free-Stream and Reference Velocities

The comparability of wind-tunnel experiments with each other and with LES simulations requires that the flow variables in the wind tunnel can be scaled. To this end, reference velocities are necessary. By taking the mean velocity at the constant-flux layer height from the reference profile, the mean reference wind for a single point measurement are derived by scaling the measured free-stream velocity down by the scaling factor $s_u = \overline{u}(\delta_{cf})/\overline{u}_{fs}$. This factor stays constant over a whole measurement campaign. To calculate the reference velocity for any measurement in the test section, the simultaneously measured free-stream velocity is multiplied by the factor s_u such that $u_{ref} = s_u \overline{u}_{fs}$. The free-stream velocity u_{fs} was measured at the wind-tunnel inlet at a height of 1.9 m (see Fig. 3.3). At this position, the flow is still undisturbed and does not correspond to an actual physical counterpart in atmospheric boundary-layer flows. This is the reason why the above mentioned scaling factor s_u is used. The constant-flux layer height for both experiments was $\delta_{cf} = 300$ mm at wind-tunnel scale and $\overline{u}(\delta_{cf})$ was obtained at horizontal wind-tunnel coordinates of $x = -2300$ mm and $y = 0$ mm (reference profile position marked by the blue dot in Fig. 3.2).

In the course of this work, the free-stream velocity was measured with two different devices. For the first model configuration, the *Prandtl tube* was used. For the single building case, the velocity reference was obtained by a WSWD ultrasonic anemometer (Konstanz, Germany). The change in measurement devices was not necessary for the experiments done here but is due to a general upgrade of the measurement infrastructure in the laboratory, as the ultrasonic anemometer can also measure very low reference winds.

With Prandtl tubes, wind speeds are determined via pressure differences. The total pressure, which is composed of the dynamic and static pressure, is measured at the tip of the Prandtl tube. The static air pressure is measured at two slots at the side of the Prandtl tube perpendicular to the direction of flow. The dynamic pressure is then determined from the difference of the total pressure and the static pressure. Finally, the wind speed is determined from the dynamic pressure and the density of air as $u = (p_{dyn}/2\rho)^{1/2}$. Thus, the density of air has to be determined by documenting the current ambient conditions as the atmospheric pressure and the temperature in the wind tunnel.

Ultrasonic anemometers (USA) basically use the property of sound waves that their propagation speed depends on the medium they travel through. The sound waves between two pairs of transducers are accelerated or decelerated with the flow, and the wind speed is calculated from the run-times of the sound waves. The WSWD ultrasonic anemometer has a temporal resolution of 100 Hz.

Data Quality Assurance

Before measuring time series at single points with the LDA, the duration of the measurements T_{mes} is specified since the ergodicity of the captured flow must be guaranteed. Furthermore, the duration must be chosen such that the inherent uncertainty of the turbulent flow signal is captured. A good estimate can be achieved by performing a *convergence test*. For each experiment, this test has been done, by measuring for an extra long duration T. The time series are then split into n intervals of smaller time series of different lengths T/n. For each of these n intervals, flow statistics are calculated. This is done for different values of $n = 1$ up to $n = 100$. The spread of the calculated flow statistic is expected not to decrease significantly at a high enough value of T/n. This value was then chosen as the measurement duration T_{mes}. Convergence test results for both experiments are shown in Sec. 4.1 and Appendix A.

Scatter in wind-tunnel data does not only depend on the precision of LDA, Prandtl tube or USA measurements. An experiment is always a complex system with many influencing factors, which are surely not all known or understood to the full degree (ambient conditions, etc.). The only chance to face the statistical errors is by statistical means. A given value obtained from a measurement is never the exact value. Rather, the exact value lies somewhere in an interval defined by the uncertainties. The uncertainties of a flow statistic (e.g. $\overline{u}$, $\overline{u'u'}$ or $\overline{u'w'}$) are determined via repetitive measurements made on several days at representative locations. As a conservative approximation the difference between the largest and the smallest observed value, i.e. the statistical range, from all taken repetitive measurements is chosen as the data scatter. Tables summarising all uncertainties can be found in the sections on the respective experiments.

3.1.2 The PALM Model System

The LES model *PALM* has so far been mainly developed by the *PALM* group at the Institute of Meteorology and Climatology of Leibniz Universität Hannover in Germany with collaborators across Europe. Raasch and Schröter (2001) started the development, and by now *PALM* is one of the most used LES models in urban climate research. At the time of writing, it contains more than 18 modules, that can be used to study the propagation of reacting gas mixtures, cloud cover, thermal radiation on buildings and also the influence of plant canopies. Even though *PALM* is a highly specialised LES with lots of applications, it is still crucial to investigate the core features in critical cases as near-wall flows. In this work, the focus is therefore on the dynamic core of *PALM*.

The computations were carried out with Release *21.10-rc.2* of the *PALM* model system which is mainly described in Maronga et al. (2015, 2020a). Simulations were done on the CPU (standard memory) nodes of the *Levante* supercomputer at the *Deutsches Klimarechenzentrum* (DKRZ) located in Hamburg. Preparatory runs and testing was done on the *Mistral* supercomputer at DKRZ and on the *Thunder* cluster administered by the *Centrum für Erdsystemforschung und Nachhaltigkeit* (CEN).

LES Implementation

Applying the widely used implicit filtering approach by Schumann (1975), the model solves the governing equations Eq. 2.30 and 2.31 as introduced earlier. Spatial discretisation is done by a fifth-order scheme according to Wicker and Skamarock (2002). The prognostic equations are computed directly on an Arakawa staggered C-grid (Arakawa and Lamb, 1977; Harlow and Welch, 1965) in which the velocity components are defined at the centres of the grid-cell edges as can be seen in Fig. 3.6a. Scalar quantities as the SGS-TKE are calculated in the centre of the grid volume. Note that the single

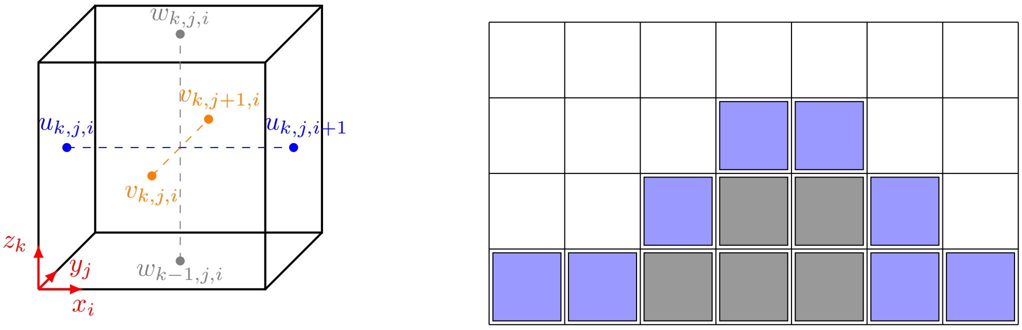

(a) **(b)**

Figure 3.6: (a) The Arakawa staggered C-grid with the positions defining the velocity components u (blue), v (orange) and w (gray). The subscripts i, j, k correspond to the dimensions x, y, z as also indicated by the small coordinate system (red) at the lower left. The dashed lines intersect in the cell center where scalar quantities can be defined. (b) At blue grid cells the topography implementation is applied, if the ground surface or adjacent obstacles (grey grid cells) are present. White grid cells indicate the grid cells where the standard equations without any boundary conditions are solved.

velocity components are not saved at the same location on the grid. The resulting offset of $\Delta x_i/2$ with i depending on the wind component considered has to be taken into account when covariances and other measures are computed since interpolation to the centre of the grid cell is necessary.

A third-order Runge-Kutta scheme was chosen as the time stepping method (Williamson, 1980). The value of the time step is computed automatically for every new time integration step and follows the Courant–Friedrichs–Levy (CFL) criterion. Thus, the step size Δt changes at every time step depending on the flow velocity and higher flow velocities lead to smaller step sizes. Temporal sampling (data output), if not chosen far bigger than the mean step size, is directly determined by the current global maximum velocity in the modeled domain.

To ensure non-divergence of the flow, a predictor-corrector method was applied. First, at every time step, the modified pressure term from Eq. 2.30 is excluded from the momentum equation and a preliminary velocity $u_{i,pre}^{t+\Delta t}$ is computed (predictor step). After integration and by forcing incompressibility onto the velocity field, a Poisson equation is derived:

$$\frac{\partial^2 \tilde{p}^m}{\partial x_i^2} = \frac{\rho}{\Delta t} \frac{\partial u_{i,pre}^{t+\Delta t}}{\partial x_i}. \tag{3.2}$$

With lateral cyclic boundary conditions applied, this equation can be solved by transforming it into the Fourier space. This procedure saves computational time and delivers exact solutions at the Fourier nodes. It was therefore preferred over the also implemented multi-grid scheme which allows for non-cyclic lateral boundary conditions.

PALM uses a 1.5-order turbulence closure after Deardorff (1980) modified by Moeng and Wyngaard (1988) and Saiki et al. (2000). The fundamental principles of this closure have already been explained in Sec. 2.1.2 and Sec. 2.3.2. The comparison between the modified D80 model and the G91 model by Germano et al. (1991) would have been especially interesting since the latter model addresses the heuristic mixing-length estimation with a dynamic approach. However, the existing implementation of the G91 model in *PALM* did not proof to be stable, if sharp edges and small obstacles are introduced to the flow. Thus, the comparison was only possible for empty boundary-layer flows. Furthermore, the transport equation for turbulence kinetic energy (Eq. 2.34) is solved at each grid center.

The momentum boundary conditions between surfaces and the first adjacent grid level are based on MOST (Monin and Obukhov, 1954; Garratt, 1992), and in our case they are simplified for the neutral case as in Eq. 2.22. The commonly used IL method was applied as introduced earlier. The boundary condition proposed by Maronga et al. (2020b) was not tested, since it was not included into the official PALM releases yet and is not expected to proof practical in densely build cities with e.g. narrow street canyons. Figure 3.6b shows the regions in the flow where wall-bounded code is applied and the surface boundary conditions are solved.

Technical Properties

The *PALM* model system is designed as a modularised *Fortran* code. Subroutines are organised according to their functionality in individual Fortran files (modules) and are called from a main routine. *PALM* also calls many external libraries including the Fastest Fourier Transform in the West *FFTW* (see e.g. pressure solver), the Network Common Data Form (*NetCDF*) as well as parallelisation libraries as the Message Passing Interface (*MPI*, Gropp et al. (1999)) and the shared-memory Open Multi-Processing interface (*OpenMP*).

Parallelisation in *PALM* is implemented in a hybrid form of *MPI* and *OpenMP* (Raasch and Schröter, 2001). The domain is decomposed into equally sized subdomains in x- and y-direction. Each subdomain is then distributed to the used processor elements (Processor Elements (PEs)). On each processor, parallelisation on loop-level is achieved via *OpenMP*.

The limit of the wall-clock time on *Levante* is 8 h. Many runs (and especially the longer runs at higher resolutions) exceed this time limit even before the spin-up time of the simulation is reached. *PALM* offers the possibility to schedule so called job-chains. After the initial job is finalised, restart data are written to binary files, which contain the state of all flow variables at the final time step of the previous run. Using the restart data, a new run can be started automatically after the wall-clock time limit has expired. This run is called *restart run* and the process can be repeated until the end of the simulation is reached.

Data Output

PALM offers multiple ways to output the generated data. Since a comparison of wind-tunnel and LES data is desired, time series of the three velocity components u,v and w (resolved) and the SGS-TKE were written to *NetCDF*-files for single points of interest, which could be chosen freely in the whole model domain. For a maximum temporal resolution, data was output at every time step. A lower sampling rate would have reduced the computing time considerably, as the communication between the nodes could have been reduced. However, the loss of information, especially for small-scale eddies near the wall, would have been too high in this case. As with the LDA measurements in the wind tunnel, the time series written by *PALM* are sampled with a non-uniform time step. A bias towards higher velocities is not expected since the CFL-criterion is applied globally and data output of time series was only started when the simulations reached a statistically stationary state. Nevertheless, resampling is necessary for the computation of spectra and integral length scales.

Global time series of 3D domain averages of other measures calculated during run time were written for testing and ensuring that the model worked as wished. These measures include the evolution of:

- the maximum velocity in the whole system u_{max} to determine the spin-up time of a model run (also visible in other measures as the TKE),
- the mean divergence of the flow before $(\frac{\partial u_i}{\partial x_i})_{old}$ and after $(\frac{\partial u_i}{\partial x_i})_{new}$ the predictor-corrector method is applied,
- the resolved TKE and the total TKE, to ensure that a proper grid size was chosen (at least 90% of TKE should be resolved (Heus et al., 2010)) and
- the time step Δt.

Additionally, snapshots of 3D volume data were taken to get a qualitative overview of the flow itself.

3.2 Data Processing

In this section, the computation of the analysed quantities is documented and explained. Focus shall be on particular wind-tunnel or LES specific processing steps. All processing steps described in this work have been implemented in *Python* and can be reviewed on the *Gitlab* page of the *EWTL* hosted by the *DKRZ*.[1] Testing of the implemented routines was done by analysing well-known signals like oscillations with distinct frequencies or *White Gaussian noise*.

3.2.1 Statistical Measures

Statistical moments of first, second, third and fourth order were computed to analyse the mean flow, the turbulence and also the replication of the near-wall flow by the LES model. While some of the statistical moments of the flow field were already introduced earlier and have a direct physical meaning (see Sec. 2.1.2), some might be less intuitive and will be explained in more detail.

The Mean Flow

For the computation of LDA data, *transit time weighting* has to be applied because of the inherent bias in the velocity signal illustrated in Fig. 3.5b. Thus, the mean velocity of a LDA time series is computed as

$$\overline{u_i} = \frac{\sum_{k=1}^{N} \theta_k u_{i,k}}{\sum_{k=1}^{N} \theta_k}, \tag{3.3}$$

with θ being the transit time, i being the subscript determining the spatial direction and k being the subscript counting every sample in the time series.

The mean velocity calculated from *PALM* data does not have to be corrected for a bias. Nevertheless, for a proper interpretation of the data, some restraints should be regarded. The time series of the velocity components in *PALM* are always the filtered, resolved velocities. For isotropic turbulence, this should not affect the mean values. However, if the small scales in the modeled system are anisotropic (e.g. close to surfaces), this can also affect the filtered mean values. The degree of this problem also depends on the chosen grid size Δ_i. Moreover, the temporal resolution of the time series always depends on the time step Δt of the simulation.

---

[1] `https://gitlab.dkrz.de/ewtl/windtunnel`

Variances and Turbulence Intensities

Besides mean wind speeds, the normalised variances and turbulence intensities are calculated. Since the aforementioned bias also affects the variances, transit time weighting is applied here as well as can be seen in the following equation for the variances:

$$\overline{u_i'u_i'} = \frac{\sum_{k=1}^{N}(u_{i,k} - \overline{u}_i)^2 \cdot \theta_k}{\sum_{k=1}^{N}\theta_k}, \tag{3.4}$$

with subscripts defined as above. Note, that the mean values used in this equation are already the transit time weighted means. For a proper comparison, the variances are normalised by the square of the reference velocity u_{ref}^2.

The turbulence intensity I_{u_i} is defined as the standard deviation divided by the local mean velocity amplitude $\overline{u_a}$ and is mainly computed for validation of the modeled boundary layers:

$$I_{u_i} = \sqrt{\frac{\sum_{k=1}^{N}(u_{i,k} - \overline{u}_i)^2 \cdot \theta_k}{\sum_{k=1}^{N}\theta_k}} \cdot \overline{u}_a^{-1}. \tag{3.5}$$

For wind-tunnel measurements, the local velocity amplitude is determined by using the two measured velocity components $\overline{u}_a = \overline{(u_i^2 + u_j^2)^{1/2}}$ (either UV-mode or UW-mode).

For the *PALM* time series, variances and turbulence intensities are computed directly. As mentioned above, the determined values are only based on the resolved velocities. There is no SGS-model for the variances and thus the total variances (resolved + sub-grid) cannot be determined. Thus, at regions where the SGS-contributions are relatively high, the resolved variances in *PALM* might be smaller than the wind-tunnel variances. One solution could be, to approximate the missing SGS-contributions by adding one third of the SGS-TKE to the calculated resolved variances. However, this approximation again only holds for isotropic turbulence and becomes inaccurate in the near-wall region. In this work, the SGS-TKE was not added to the resolved variances but additionally analysed for each measurement location to get an idea of the local loss of information due to filtering.

Covariances

The turbulent fluxes, i.e. the covariances based on LDA time series were also computed with the weighting approach:

$$\overline{u_i'u_j'} = \frac{\sum_{k=1}^{N}(u_{i,k} - \overline{u}_i) \cdot (u_{j,k} - \overline{u}_j) \cdot \theta_k}{\sum_{k=1}^{N} \theta_k}, \tag{3.6}$$

with i and j being the subscripts determining the spatial direction and k being the subscript counting every sample in the time series. The covariances are normalised by the square of the reference velocity u_{ref}^2.

In *PALM*, the resolved and sub-grid values of the horizontally averaged turbulent fluxes are computed during runtime and can be investigated as part of the output. These prognostic measures were especially helpful when the boundary-layer configurations in *PALM* were adjusted such that they match the wind-tunnel boundary layer. For local comparisons, e.g. for wall-normal profiles at vertical surfaces, the aforementioned time series output of u, v and w was used to compute the resolved turbulent fluxes. Again, the sub-grid scale contributions had to be approximated from the local SGS-TKE.

Higher Order Statistics

Next to first and second order statistics, higher order statistics were computed to get an idea of the shape of the velocity distribution. The third moment is the *skewness* γ, which is a measure for the asymmetry of the distribution. If the distribution is symmetric, the skewness equals zero. For a distribution skewed to the left (longer left tail and more outliers on the left) the skewness is $\gamma < 0$. A positive skewness $\gamma > 0$ indicates a distribution that is skewed to the right and that has more extreme values that are larger than the mean. The fourth moment is the *kurtosis* β, which is a measure for the flatness of the distribution. Normal distributions posses a kurtosis of $\beta = 3$. If $\beta < 3$, the distribution tends to be broader with steep tails and is called *platykurtic*. A kurtosis of $\beta > 3$ indicates a narrower distribution with flat tails and steep slopes. Such distributions are called *leptokurtic*.

As with the above statistical moments, here again the transit time weighting is applied for the obtained LDA signals as described in Kokoska and Zwillinger (2000). The *PALM* skewness and kurtosis were computed without any weights.

3.2.2 Quadrant Analysis

The quadrant analysis of the Reynolds shear stress is a simple but useful and widely used processing technique. Its success story is rooted in the fact that precise statements can be made about the structure of turbulence in a wide variety of flow situations (Wallace, 2016). The first to carry out a quadrant analysis were Wallace et al. (1972). They recognised the additional information that can be gained by looking at the individual signs of the fluctuations u', v' and w'. For example, if the components u and v were obtained, and the calculated turbulent flux $\overline{u'v'}$ is determined, then the containing fluctuations are divided into four quadrants: $Q1(+u,+v)$, $Q2(-u,+v)$, $Q3(-u,-v)$ and $Q4(+u,-v)$. At a vertical wall, parallel to x, the quadrants $Q1$ and $Q3$ are associated with motions away from the wall ($Q1$) and motions towards the wall ($Q3$) respectively. Quadrants $Q2$ and $Q4$ are associated with ejection and sweep motions respectively (Wallace, 2016).

The straight-forward approach to show the results of a quadrant analysis is via scatter plots of the measured components. While the spread and the shape of the distribution of velocity fluctuations can be obtained qualitatively, it is still hard to get an impression of the mean centre of gravity of the fluctuations. Therefore, *Joint Probability Density Functions* (Joint Probability Density Functions (JPDFs)) $P(u',v')$ are calculated with

$$\overline{u'v'} = \int_{-\infty}^{+\infty} u'v'P(u',v')du'dv'. \tag{3.7}$$

In this work, JPDFs are calculated by the non-parametric 2D Gaussian kernel density estimation.

Conditional sampling based on the four quadrants divides the time series of e.g. u and v into four time series. Using these distinct time series, the quadrant contributions $\overline{u'v'}_{q_i}/\overline{u'v'}$ of the turbulent flux are computed. Each are normalised by the total turbulent flux. In isotropic turbulence, the contributions would equal each other. Thus, the comparison of quadrant contributions is a reliable indicator for the understanding of flow anisotropy and can further the understanding of the structure of near-wall turbulence.

3.2.3 Spectral Analysis

In this work, the (co-)spectra of the turbulent velocity fields obtained from the wind-tunnel experiment and the LES were analysed with various goals. First, it is important to verify if the general shapes of the calculated spectra are in agreement with the theory. Second, differences between *PALM* and wind-tunnel spectra are to be expected due to the filtering approach in the LES. This effect is going to be reviewed in Sec. 5.1.2. Finally, the spectra are analysed in terms of their inertial-subrange scaling, because deviations from the classical K41-scalings might indicate strong flow anisotropy or energy production due to strong shear. Since in many LES models including *PALM* the spectra often fall off to lower energy contents already within the inertial subrange, this last step was just done for the wind-tunnel results.

Energy density spectra are computed in just a few steps which can be looked up in Stull (1988). Before the actual calculation of spectra, the time series has to be interpolated to an equidistant time series. This step is necessary to avoid systematic errors due to time intervals of higher data rate. The time steps are chosen linearly based on the mean data rate of the time series. Based on the new sampling intervals, the measured velocity signals are resampled using a *nearest neighbour* scheme. In a second step, the *Discrete Fourier Transform* frequencies f_k are calculated from the equidistant time series. Then the *Fourier Coefficients* $F_{u_iu_j}(f_k)$ are calculated for the resampled velocity signal by applying the *Fast Fourier Transform* after Cooley and Tukey (1965). If $i \neq j$, the co-spectrum is computed, otherwise the resulting spectra are auto-spectra. The energy density of the discrete signal is calculated as

$$S_{u_iu_j}(f_k) = \frac{1}{N f_s} |F_{u_iu_j}|^2, \tag{3.8}$$

with N being the total number of samples and f_s being the mean sampling frequency of the time series.

The comparability of energy spectra is ensured by normalising the energy contents and the Fourier frequencies. Using the Fourier frequencies f_k and the local variances of the respective velocity component σ_{u_i}, the energy density is normalised such that

$$S^*_{u_iu_j}(f_k) = \frac{f_k}{\sigma_{u_i}\sigma_{u_j}} S_{u_iu_j}. \tag{3.9}$$

Note that due to normalisation of the energy density with the frequency f_k, the Kolmogorov scaling exponent is reduced from $m = -5/3$ to $m = -2/3$.

In boundary-layer studies, Fourier frequencies f_k are usually scaled by the measurement height z and the mean of the local stream-wise velocity component $\overline{u}$, which yields the reduced frequency

$$f^*_k = \frac{f_k z}{\overline{u}}. \tag{3.10}$$

The scaling of the Fourier frequencies confronts us with the question if z is still the proper scaling length in the vicinity of vertical walls. Besides, the complex flow in the wake of buildings makes the choice of $\overline{u}$ as the scaling velocity questionable. After testing several combinations (horizontal mean $\overline{u}_h$, wall-normal mean $\overline{v}$), it was decided to stay with the local mean stream-wise velocity for all flow cases. For boundary-layer flows, the Fourier frequency was normalised using the height above ground z. For cases in the vicinity of building models, the distance to the building surface was chosen as the scaling length.

Calculating the inertial subrange scalings $m(S_{u_iu_j})$ automatically turns out to be difficult. The determination of the frequency limits of the inertial subrange are difficult to automate. Reasons for this are aliasing effects occurring at high frequencies or the general uncertainty in the calculation of $S_{u_iu_j}$. Because of that, the limits for fitting the scalings were performed manually for each calculated spectrum. This approach is error-prone, but proved to be the most reliable strategy due to the difficulties mentioned above.

4 Model Configurations

The two model configurations (wind tunnel and LES) utilised in this thesis were both designed to investigate distinct properties of the near-wall flow over surfaces of various roughnesses.

First of all, it is of interest, how the flow reacts to surface roughness changes in general. Especially the distinction made in Sec. 2.2.1, between the near-wall flow within the RSL and the flow usually not directly affected by the surface roughness is relevant for urban climate simulations. In addition, the near-wall anisotropy of the turbulent motions as a function of the surface roughness is of particular concern. To investigate these questions, a wind tunnel and a LES study of the flow over a horizontal plate of homogeneous roughness were designed. The two SGS models from Deardorff (1980) and Germano et al. (1991) are also compared using this model configuration. It will be introduced in Sec. 4.1.

After learning from that simple, generic case, the complexity of the model configuration is increased. The aim is to understand, how *PALM* represents a flow which is dominated by multiple length scales h_r and H_u. The model design to study the flow close to single buildings with different facade roughnesses is introduced in Sec. 4.2.

4.1 Horizontal Plate of Homogeneous Roughness

As a first step, the simple and well studied setup of a flow over a horizontal plate of homogeneous roughness was modeled in *WOTAN* and with *PALM*. The focus in this experiment is on the effect of small-scale roughness elements on the near-wall flow. These small-scale roughness elements are not directly resolved by the *PALM* model configuration and it is thus important to understand how much information is lost in the LES model results due to the sub-grid scale roughness elements of size h_r. The roughness changes in the wind-tunnel experiment are therefore not taken into account in the *PALM* model.

In the following, I will describe the setup of the model configuration in *WOTAN* and *PALM* including a description of the modeled boundary layer, Reynolds number independence testing for the wind-tunnel measurements and the determination of the measurement uncertainty.

4.1.1 The Wind-Tunnel Setup

The photograph in Fig. 4.1 shows the experimental setup from a downstream perspective. In the rear, the large vortex-generating spires are visible in red. The small metal elements, which are distributed all over the wind-tunnel floor, are used to generate small-scale turbulence features, replicating the aerodynamic effect of surface roughness and contribute to an artificial thickened turbulent boundary-layer flow. As mentioned earlier, the exact configuration of spires and floor roughness elements is given in Appendix A. The rectangular black area in the foreground of Fig. 4.1 is located in the test section of the wind tunnel and shows the area where the surface roughness changes were placed.

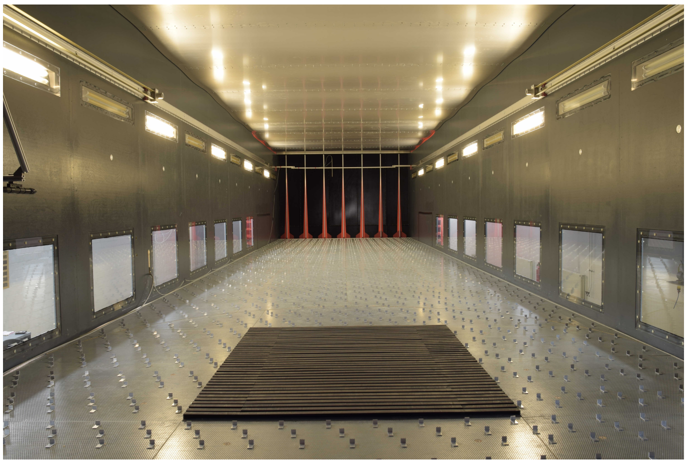

Figure 4.1: Upwind view of the experimental setup in the test section of *WOTAN*. Foreground: Rectangular black area with balcoiny-shaped roughness elements at $s_b = 5$ m. Background: Upstream area with the red spires and floor roughness used for generating an artificial thickened, turbulent, equilibrium boundary-layer flow.

With the described setup an isothermal turbulent boundary-layer flow is generated at a geometric scale of $1{:}100$. In the remainder of the text, length scales are always given in full scale if not explicitly stated otherwise. In contrast to regular boundary-layer wind-tunnel applications, the aim is not to model an urban boundary layer (UBL). Rather, the aerodynamic effect of the small-scale roughness elements within a turbulent boundary-layer flow is supposed to be replicated and investigated systematically. Thus, turbulence properties of the flow are particularly important for this experiment.

Data Quality and Scaling

The obtained velocities are normalised using the reference velocity $u_{ref} = s_u \overline{u}_{fs}$. The scaling factor in this model configuration is $s_u = 0.731$. During a series of measurements, the free stream velocities varied by a standard deviation of $\sigma_{u_{fs}} = 0.01$ m s^{-1}, which indicates a constant and temporally stable inflow into the wind tunnel.

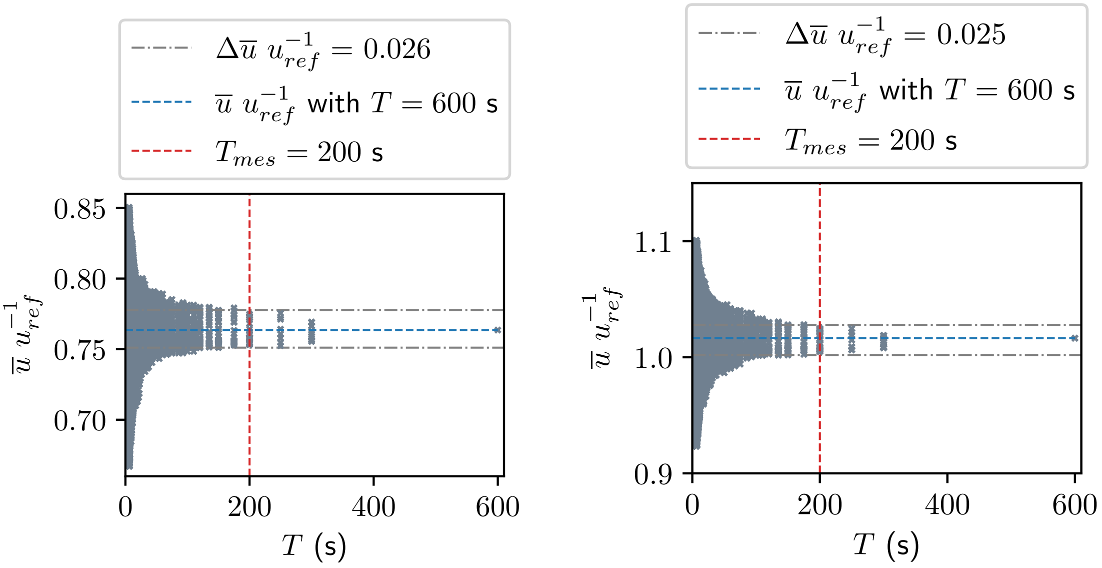

(a) **(b)**

Figure 4.2: The convergence tests for the mean stream-wise velocity $\overline{u}$ at the two heights (a) $z = 5$ m and (b) $z = \delta_{cf} = 30$ m. Note that the normalised mean in (b) is not exactly 1 what would be expected at $z = \delta_{cf}$ with the normalisation chosen. For the convergence test processing routine though, the velocity bias was not corrected by transit time weighting. The convergence test results thus have an added value as they show the effect of non-weighted data. The time in seconds is given in model scale.

Convergence tests were done for different flow measures at 5 m and 30 m above ground at the location of the reference profile (see Fig. 3.2). As will be shown later (Fig. 4.3), the two testing heights were chosen such that the time series represent the main features of the flow to be studied. The lower height of 5 m was located close to the ground and the flow is still affected by the roughness elements. The testing height of 30 m, corresponds to the constant-flux layer height δ_{cf}. The convergence tests show that with $T_{mes} = 200$ s, a sufficient length of the measurement duration was reached because the range of calculated means did not decrease sufficiently at larger time intervals (Fig. 4.2). Of course, this limit is a trade-off between accuracy and expenditure of time. Here, the scatter of the mean flow was 0.026 and 0.025 for the two measurement heights. The length of the recorded time series corresponds to 5 hours and 33 minutes of measurements at full scale. The full scale measurement time was calculated by dividing the measurement time by the scale, since the full scale velocity was kept the same as in model scale.

Nine repetitive measurements were done each for three heights (4.5 m, 6 m and 10 m) at three different locations in x-direction over the rectangular base plate. As described earlier, the data scatter was assumed via the maximum range of all values to get a conservative approximation of data quality. Table 4.1 documents the data scatter for all quantities analysed in the course of this experiment.

Table 4.1: Reproducibility of the calculated flow statistics for the flow over a horizontal plate of homogeneous roughness.

Mean velocity	Turbulence intensity	Turbulent fluxes	Integral length scale
$\overline{u}\ u_{ref}^{-1} \pm 0.0096$	$I_u \pm 0.0044$	$\overline{u'w'}u_{ref}^{-2} \pm 0.0005$	$L_u^x \pm 8.298$ m
$\overline{w}\ u_{ref}^{-1} \pm 0.0012$	$I_w \pm 0.0024$		

The Modeled Boundary Layer

To estimate the roughness length z_0 of the approach boundary layer, first, the bounds of the constant-flux layer need to be specified, since MOST is only valid in this region of the flow. Conventionally, the constant-flux layer is defined as the region where the turbulent fluxes vary within a 10% range (Snyder, 1981). For the measured flow profile, this is the case for 7 m $\leq z \leq 30$ m distance from the surface as can be seen in Fig. 4.3b. Fitting Eq. 2.22 to the described extract of the wind profile (red triangles in Fig. 4.3a) yields a roughness length of $z_0 = 0.021$ m. The log-law fits the measured data well up to a height above ground of 30 m which is also the upper boundary of the modeled constant-flux layer. Above this height, the power law (blue dashed line) matches well too. It was fitted with an exponent of $\alpha = 0.17$, and does not only replicate conditions within the constant-flux layer but still matches consistently further away from the wall. This is well in agreement with the concepts of boundary layers introduced in Sec. 2.2.1. An overview of the core boundary-layer properties is given in Tab. 4.2.

The mean velocity and turbulent flux profiles already contribute strongly to the understanding and characterisation of the turbulent boundary layer (see Fig. 4.4). With the vertical profiles of the integral length scales and the turbulence intensities, further analysis possibilities arise to assess the boundary layer's similarity to nature. The turbulence intensities show a typical shape of the curve for both components (see VDI 3783 Blatt 12 (2000)), whereby the values from a height of 40 m show a decrease to lower turbulence intensities and correspondingly less rough boundary layers. For the integral length scales too, the upper seven measurements show significantly lower values than the theory

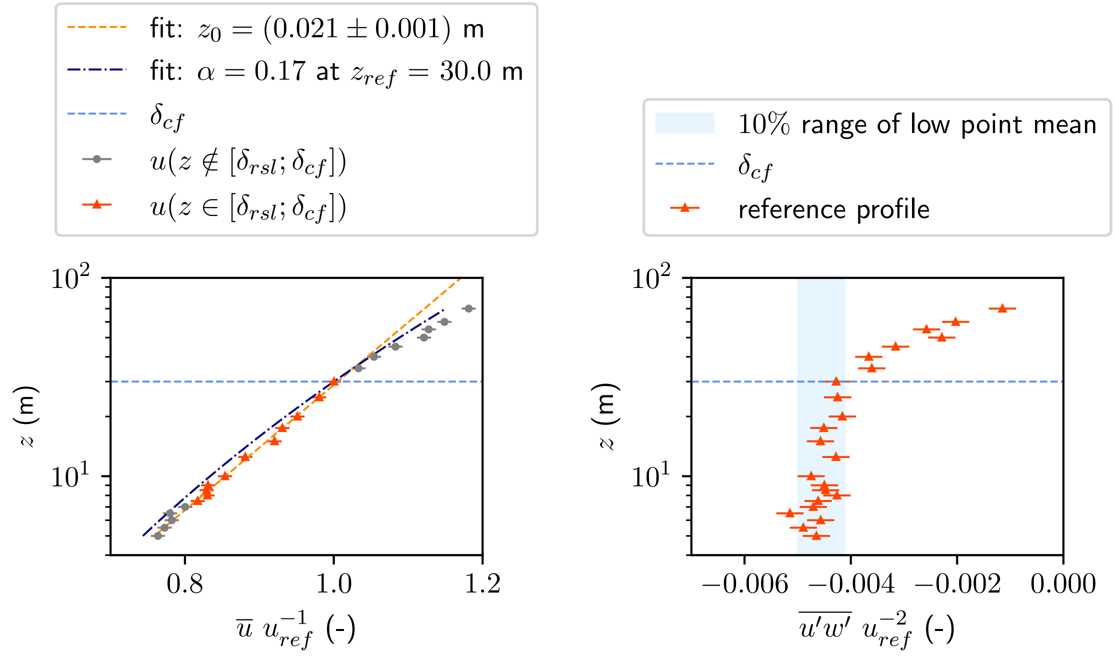

(a) **(b)**

Figure 4.3: (a) Mean velocity profile of the approach boundary layer. Red triangles mark the measurement positions within the constant-flux layer. Grey points are not included into fitting the log-law of the wall (orange dashed) to obtain z_0. The blue dash-dotted line shows the profile of the fitted power law. (b) The mean vertical turbulent fluxes are shown for the reference profile position. The ten-percent margin to define the constant-flux layer is shown in light blue. At the lower end of the flux profile, one outlier can be seen. Up to this height, the time series were not regarded for fitting the log-law.

predicts. The focus of the experiment is mainly on the area close to the wall that is why the mismatch with the expected values can be tolerated at these heights. In general, the integral length scales of the modeled boundary layer are half an order of magnitude too low for the obtained roughness length of $z_0 = 0.021$ m. One reason for this could be that, in contrast to an atmospheric boundary-layer flow, the wind-tunnel flow is limited by the wind-tunnel size (ceiling and lateral boundaries). The chosen model scale of $1{:}100$ is fairly large for *WOTAN* and the effect of too small integral length scales is particularly apparent here.

Table 4.2: Boundary-layer properties of the approach flow in the wind tunnel (see also Fig. 4.3a). Values are given in full scale

$\mathbf{s_u}$	$\boldsymbol{\delta_{cf}}$ **(m)**	**Re**	$\mathbf{Re_{u_*}}$	$\mathbf{u_*}$ **(m s^{-1})**	$\mathbf{z_0}$ **(m)**
0.731	30	83000	5400	0.27	0.021

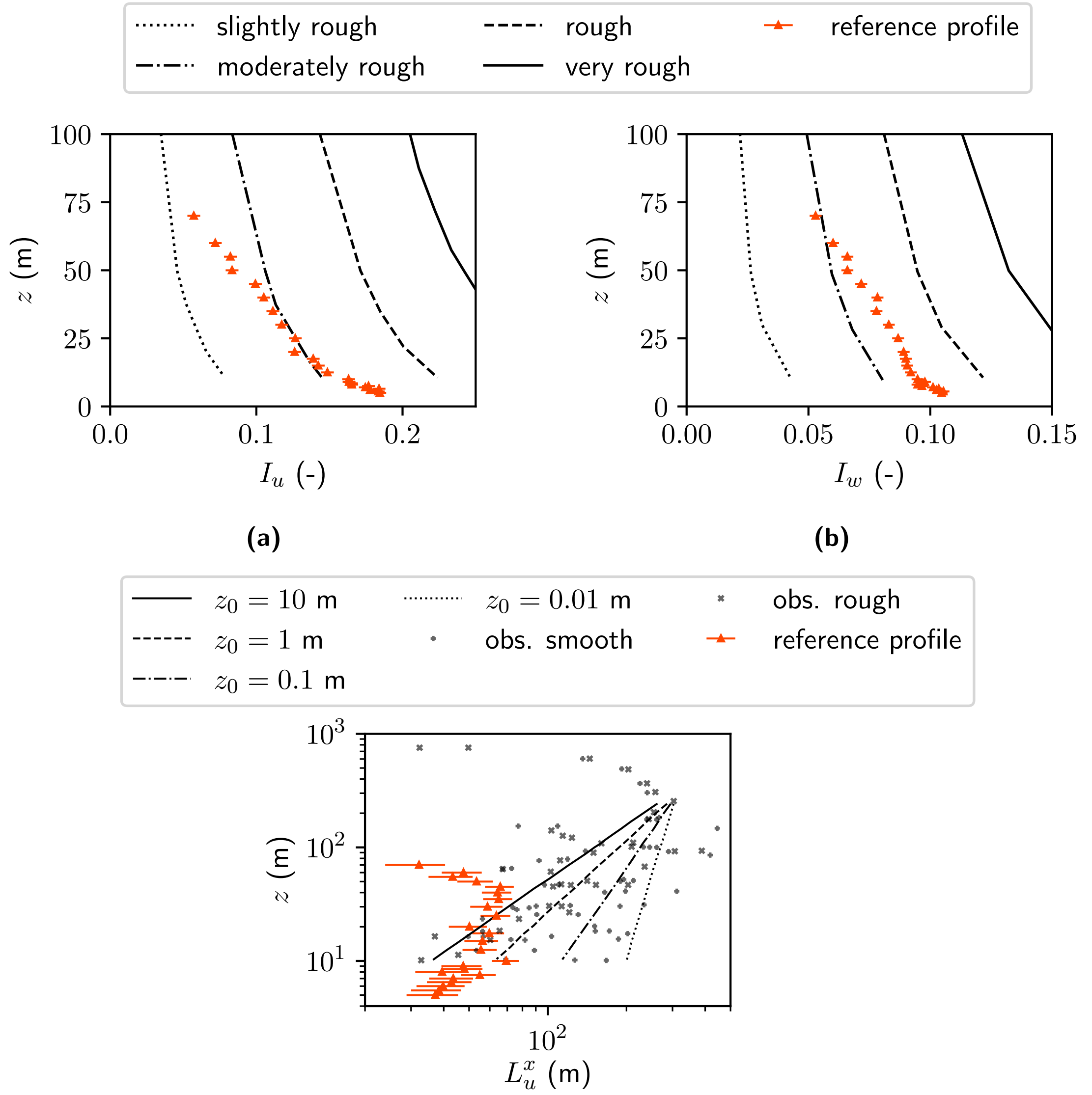

(a)

(b)

(c)

Figure 4.4: (a) Turbulence intensity of the stream-wise velocity component I_u. The black curves mark the lower bounds of the roughness regimes defined by VDI 3783 Blatt 12 (2000). (b) Turbulence intensity of the vertical velocity component I_w. Here again the roughness regimes give orientation. (c) The integral length scales are shown with theoretical values for different roughness lengths. The observed field data for a smooth and rough boundary-layer flow are also shown (Counihan, 1975).

Due to the chosen model scale of $1{:}100$ and in turn the lower Reynolds number of the model flow, the viscous sublayer is thicker than at full scale (Snyder, 1981). For the modeled boundary-layer flow described here, the Reynolds number is $Re \approx 83000$ and the friction Reynolds number is $Re_{u_*} \approx 5400$ with $u_* = 0.27$ m s^{-1}. The friction velocity was estimated by taking the square-root of the mean vertical turbulent flux values $u_* = \overline{u'w'}^{1/2}$ averaged over the constant-flux layer. Critical Reynolds numbers in wind-tunnel experiments are usually in the order of 10^4 (VDI 3783 Blatt 12, 2000). The flow can thus be understood as sufficiently turbulent. Nevertheless, a Reynolds number independence test was done to ensure that the results are not affected by downscaling.

The Aerodynamically Rough Plate

In the following paragraphs, the actual model placed into the wind tunnel will be introduced. The goal was to model the influence of different building facade roughnesses on the near-wall flow. For this purpose, a systematic variation of the modeled facade roughness was achieved by placing rows of L-shaped balcony-like roughness elements (Fig. 4.5) onto the test area in the flow. In Fig. 4.1 these elements can be seen in the front of the picture on the black rectangular base plate corresponding to a 200 m by 150 m facade area in full scale.

It should be noted, that the modeled facade in the experiment is oriented horizontally and thus obviously differs from actual facades in urban geometries. However, as long as gravity-driven flow phenomena are negligible, this model configuration does not effect the results of corresponding flow measurements and has the advantage of establishing a nearly perfect equilibrium boundary-layer flow developing along the test area. The experimental design is strongly idealised and is not meant to represent urban environments, where flow separation around buildings, spatially varying reattachment points, etc. are predominant. Rather, it is designed to allow targeted investigation of only the momentum properties. Even though a complex interplay of meteorological variables influences the urban climate, it is necessary that models correctly represent each of the individual physical processes. Thus, statements can be made about the near-wall interpretation of flow results from LES in urban climate studies.

As can be seen in Fig. 4.5, the balcony-shaped elements are 2.1 m high and 3.4 m long. Amongst others, the thickness of the balcony structures of about 0.3 m makes them

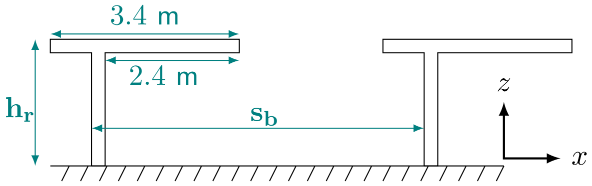

s_b (m)	label
5	medium rough
8	rough
/	flat

Figure 4.5: Schematic cross section through two rows of balcony-shaped roughness elements. The dimensions of the elements are the same for all configurations. The height is $h_r = 2.1$ m and all elements are 0.3 m thick. The spacing s_b between them has been changed from minimum 5 m (medium rough) up to 8 m (rough).

impossible to be explicitly resolved by grid resolutions commonly applied in LES for urban climate simulations. The setups differ in the spacing s_b between rows of balconies. They are chosen to result in different flow regimes (Britter and Hanna, 2003). At narrow spacings of $s_b = 5$ m, the flow is expected not to interact strongly with the placed balcony-shaped elements and a skimming-flow should emerge. If the distance between the roughness elements becomes larger ($s_b = 8$ m), the flow reacts to the rows of balconies as to isolated objects, i.e. recirculation zones similar to those found behind individual balcony-models are formed between the modeled balconies.

This setup is still valid for larger and smaller roughness elements and grid spacings if we assume that on all length scales there will always be objects in urban climate models that cannot be resolved by the numerical grid. Admittedly, with the modeled approach flow the results are limited to be applied to a building height range of up to 30 to 40 m. A lower bound for the facade roughness elements is set by the thickness of the viscous sublayer in the wind-tunnel model.

Reynolds Number Independence Testing

The flow was tested for sufficient Reynolds number independence to ensure scaleability of the measurement results. This was done above the centre of the base plate's surface at distances of $z = 3$ m and $z = 20$ m from the wall. The reference velocity is varied in seven steps from values of $u_{ref} = 0.85$ m s^{-1} up to 4.68 m s^{-1}. For both distances, the mean flow statistics do not change with varying reference velocity, and the flow can be considered sufficiently independent from the actual Reynolds number during measurements (see Fig. 4.6). The wind tunnel was operated such that the average reference velocities did not fall below 3 m s^{-1}.

Measurements were taken at various downwind distances along the base plate's centre to capture the boundary layer developing above the balcony structures and to assure that this newly formed and growing boundary layer is already fully developed. Data shown in this thesis have been obtained after 75% of the base plates length (see Fig. A.3 for justification). This also applies to the flat surface configuration with no balcony models on the test area.

For typical mean wind speeds measured in the model, the temporal resolution corresponds to a sub-meter spatial resolution at full scale. Assuming that about 5 data points have to be recorded to resolve a single vortex, a turbulent eddy size of approximately 1 m could be sufficiently resolved in the near-wall region.

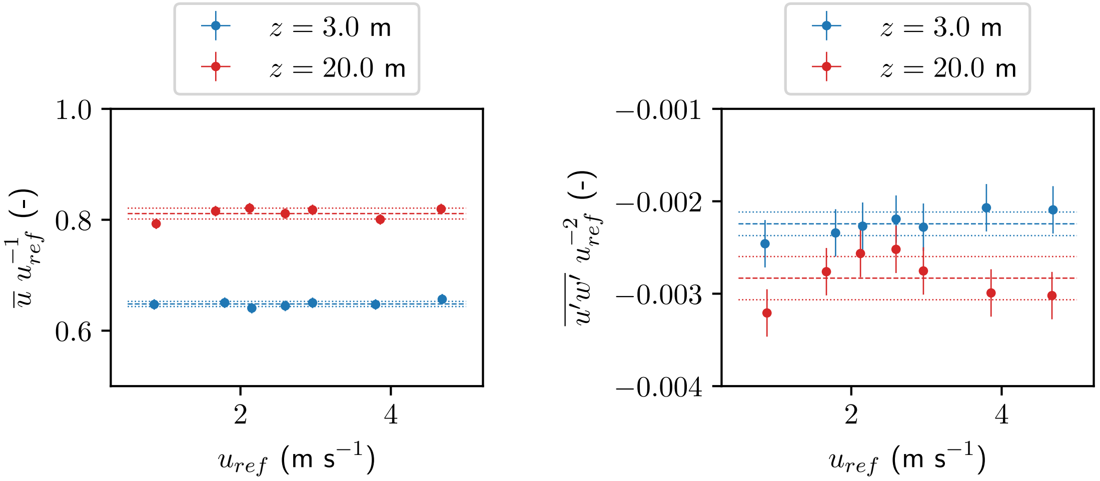

(a) **(b)**

Figure 4.6: Reynolds number independence test for the two measurement heights above ground for (a) the mean velocity and (b) the vertical turbulent fluxes. The dashed lines show the mean value for all 7 reference velocities. The dotted lines show the corridor within the standard deviations.

4.1.2 The PALM Setup

Empty neutral boundary-layer flows were modeled as comparative simulations to the flow over a horizontal plane of homogeneous roughness in *PALM* (Release *21.10-rc.2*). The model system itself is mainly described in Sec. 3.1.2. In this section, the focus is more on the actual configuration used.

Configuration of the PALM Runs

The aim is not to replicate the flow over the different rough surfaces but rather to investigate which roughness-induced deviations in the near-wall area are not directly replicated by the LES model. For this reason, the surface roughnesses described in Fig. 4.5 are not directly resolved in *PALM*. In addition, when choosing the grid width, explicit care should be taken that the specifications of Basu and Lacser (2017) and Maronga et al. (2020b) are complied with. With an estimated roughness length of $z_0 = 0.021$ m (see Fig. 4.3a), the minimum allowed grid size is $50z_0 = 1.05$. Because of these reasons, the grid size of the *PALM* simulations was set to $\Delta_i = 2$ m, with a domain height of 128 m and lateral extents of 1024 m each.[1]

A total of 9 h was simulated, but the first 5400 s were skipped until data output was started because of a spin-up time of about 5000 s (see Fig. 4.7). This makes 7.5 h of

---

[1] The number of grid cells in each spatial direction had to be factoriseable into primes 2, 3 or 5 for the FFT to work with parallelised runs.

representative flow to be used. The six segments of different colors stand for the six restart runs necessary to model the flow. In the first segment (blue), the needed spin up time can be identified as the time that the model needs to steady itself. The mean time step for all simulations in this model configuration was ≈ 0.31 s. It depends on the maximum velocity within the complete model domain u_{max} and the grid size $\Delta_i = 2$ m. Data output for the comparative *PALM* simulations was configured such that time series of a vertical profile in the middle of the domain were output at each numerical time step. The vertical dashed line in Fig. 4.7 marks the time step ($t = 5400$s) at which the output of time series was started.

The boundary conditions for solid surfaces have already been explained in detail in Sec. 3.1.2. However, the numerical model domain has 5 more borders for which boundary conditions have to be defined. Cyclic boundary conditions are specified for the lateral boundaries. The upper (roof) border of the model domain is prescribed with a Dirichlet condition, meaning that the velocities at the top margin of the domain are set to the value of the initial profile at maximum height.

Initial conditions are achieved by taking the full scale mean velocities from the reference profile $\overline{u}$ measured in *WOTAN* (Fig. 4.3a). As the wind-tunnel flow is laterally homogeneous, the lateral mean velocity $\overline{v}$ was set to zero. Choosing the *conserve volume flow* method as a forcing ensured that the mean flow profile stays the same as prescribed by the initial profile. Here, the target volume flow is calculated at the first time step and after each time step, the outflow at the right domain edge is corrected to guarantee that the fluid volume entering the domain at the inflow equals the fluid volume leaving the domain. Besides, tuning via predetermined pressure gradients is not necessary when using this method.

Validation of the PALM Runs

Several analytical variables were investigated to ensure that the simulation was performed correctly. Even though tests were performed for all *PALM* runs, results are only shown for the case with $z_0 = 0.021$ and the D80 model in order to avoid repetition (Fig. 4.7 and 4.8).

As mentioned before, it is important for a LES model that most of the kinetic energy is resolved directly. The proportion of parameterised energy should not exceed 10% of the total energy (Heus et al., 2010). Figure 4.8a shows that the SGS energy accounts for about 1% of the total energy and the flow is thus well-resolved.

The integration of the governing equations inherently produces divergence and thus incompressibility is not given anymore. The predictor-corrector method artificially reduces

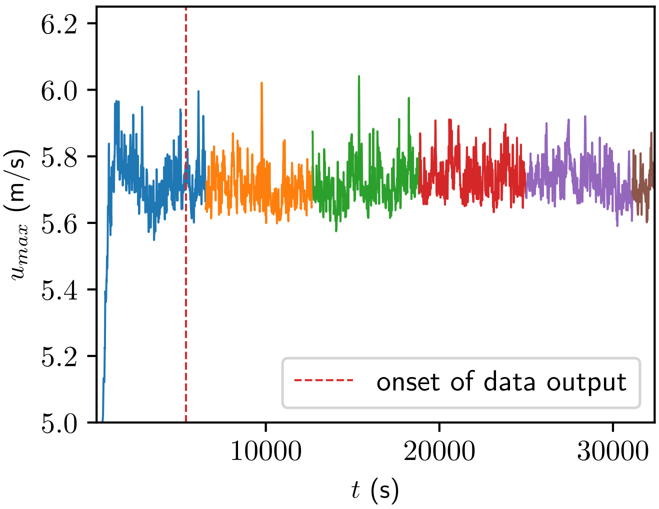

Figure 4.7: Time series of the maximum velocity u_{max} within the whole modeling domain for the *PALM*-run with $z_0 = 0.021$ m and the D80 SGS model.

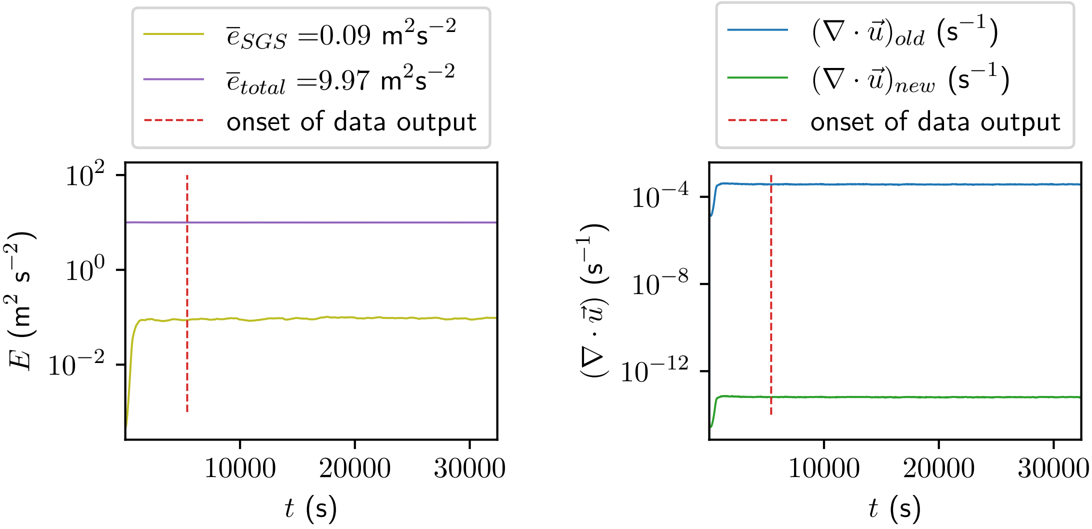

(a) **(b)**

Figure 4.8: Time series of the (a) SGS and total energy and (b) domain-averaged flow divergence before and after the predictor-corrector scheme was applied. The data is shown for the *PALM*-run with $z_0 = 0.021$ m and the D80 SGS model.

the divergence after each time step (see Sec. 3.1.2). It has been shown that a reduction of the divergence by several orders of magnitude is sufficient (Maronga et al., 2015). Figure 4.8b shows that the divergence could be reduced by ten orders of magnitude and the flow can be interpreted as divergence-free.

Convergence analyses were also carried out to estimate the uncertainty of the PALM simulations, since numerical and systematic errors could best be estimated cumulatively in this way. For the determination of the uncertainty, the entire bandwidth of the scatter of the corresponding quantity was chosen for the averaging time interval of 7.5 h used later. Table 4.3 shows the uncertainties estimated for the *PALM* simulations. The Figures for the convergence tests can be found in Appendix B.2.

Table 4.3: Reproducibility of the calculated flow statistics for the *PALM* simulations

	$\overline{\mathbf{u}}_{\mathrm{i}}\mathbf{u}_{\mathbf{ref}}^{-1}$	$\overline{\mathbf{u}_{\mathrm{i}}'^{2}}\mathbf{u}_{\mathbf{ref}}^{-2}$	$\overline{\mathbf{u}_{1}'\mathbf{u}_{\mathrm{j}}'}\mathbf{u}_{\mathbf{ref}}^{-2}$
u:	± 0.0109	± 0.0044	
v:	± 0.0035	± 0.0008	± 0.001
w:	± 0.0010	± 0.0060	± 0.001

Overview on PALM Runs Done

Altogether, four different simulations of the empty boundary layer were carried out (Tab. 4.4). These differ on the one hand in the choice of roughness lengths and on the other hand in the choice of SGS models (D80 by Deardorff (1980) or G91 by Germano et al. (1991)). All simulations were done at a 2 m grid spacing using the reference wind profile from Fig. 4.3a.

Table 4.4: Overview on comparative *PALM* runs done for the horizontal plate experiment.

Run name	SGS model	Δ_{i} (m)	z_0 (m)
BA_BL_z0_021	D80	2	0.021
BA_BL_z0_06	D80	2	0.06
Ger_BA_BL_z0_021	G91	2	0.021
Ger_BA_BL_z0_06	G91	2	0.06

4.1.3 Measurement and Output Positions

The *PALM* output positions for vertical profiles were always located in the middle of the empty domain. This choice is valid because the LES flow is laterally homogeneous and no roughness change was modeled since the aim was to monitor deviations of roughness sublayer flow statistics over surfaces of different roughness in real flows to a parameterised roughness effect not explicitly resolved in a LES.

Measurements in the wind tunnel were done at several locations, since the wind-tunnel setup differs from the *PALM* setup. Figure 4.9 shows the measurement positions in the wind-tunnel experiment for vertical profiles (circles) and lateral profiles (line) in the region of the test section. The two main measurement positions are marked in blue and red. The **reference profile** from Fig. 4.3a was measured at position **BA_BL** located

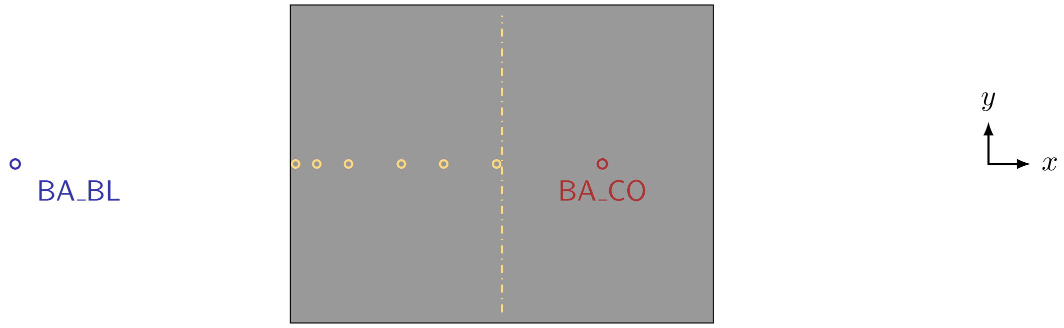

Figure 4.9: Overview on the measurement positions for the model configuration of a horizontal plate with homogeneous roughness. The reference profile was measured at location **BA_BL** (blue). The comparison position for the different roughnesses is **BA_CO** (red). The yellow circles and dashed lines mark the positions for validation of the model configuration. Lines mark lateral profiles. Circles mark vertical profile positions.

230 m upwind from the base plate's centre. The vertical profiles at position **BA_CO** were used for the flow comparison over surfaces of varying roughness. This position was chosen since the flow over the horizontal plate adjusted to the roughness change after a fetch length of 75% of the base plate. Figure A.3 in Appendix A.2 shows vertical profiles of the mean velocity and the longitudinal turbulence intensity I_u at increasing fetch lengths over the base plate, which prove that the chosen comparison position is valid.

4.2 Single Buildings with Different Roughnesses

To make statements about the influence of facade roughness in more complex flow cases, the preceding experiment is not sufficient. By studying single-building cases with different attached facade roughnesses, the influence of such roughnesses on the near-wall flow was investigated. In addition to the roughness length scale h_r, another length scale is now introduced: the building length scale H_u (see Fig. 2.7).

In the following, the setup and model configuration in *WOTAN* and *PALM* are introduced as before with the horizontal plate of homogeneous roughness.

4.2.1 The Wind-Tunnel Setup

For the single-building cases, the model building is placed in the middle of the turntable such that with a rotation of the model, the wind direction could be altered (Fig. 4.10). As with the previously introduced experiment, the configuration of spires and floor roughness elements is further described in Appendix A. What has been changed is the scale of the model configuration. In the previous experiment, the scale was $1{:}100$. Now it is $1{:}150$, because of many reasons connected to the length scales of interest. The size of the building model was mainly determined by small-scale roughnesses h_r. First of all, the ratio between small scales h_r and large length scales H_u should be about the same as for actual buildings. At the same time, the construction of such a model requires very accurate fabrication in the millimeter range by the model workshop. The small length scales could therefore not become too small on the model scale either. To ensure a long enough fetch along the building facade, H_u had to be sufficiently high.

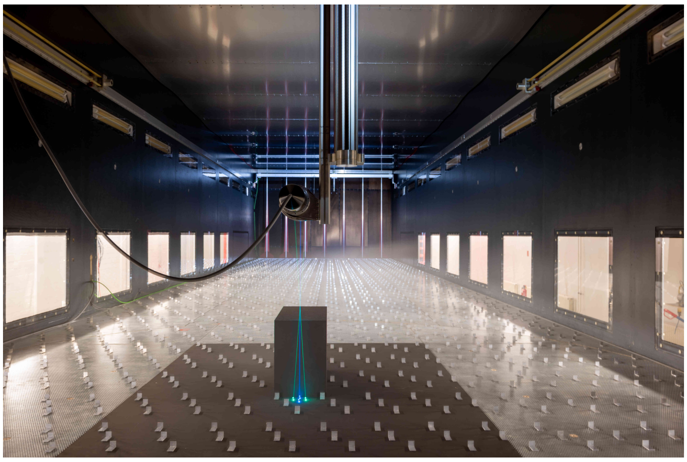

Figure 4.10: Upwind view of the experimental setup in the test section of *WOTAN*. Foreground: The test section with the single-building model placed in the middle of the turntable. The turned on large LDA probe is visible located in top of the model building. Background: Upstream area with red spires and floor roughness elements.

The large LDA probe (Tab. 3.1) with a focal length of 500 mm in model scale was used for this experiment since the higher focal length made non-intrusive measurements close to the building possible, as can be also seen in Fig. 4.10. With a smaller focal length, the probe would have collided with the model building.

Data Quality and Scaling

Except for the used model scale, the same boundary-layer setup was used as with the above experiments. However, a year passed between the two experiments. In addition, a different LDA probe was used, and the free stream velocity was no longer determined by means of the Prandtl tube, but by the USA. It was therefore helpful to revise and update the obtained values and boundary-layer characteristics at the new model scale.

The scaling factor in this model configuration is $s_u = 0.738$ and was computed by taking the quotient of the mean velocity from the reference profile at constant-flux layer height $\delta_{cf} = 45$ m and the free-stream velocity. As with the model configuration for the horizontal plate, the free stream velocity did not vary significantly.

Convergence tests were done at two different distances from the model building surface at mid-building height of $z = 25.5$ m (Fig. A.9 in Appendix A). Based on the obtained spread, the measurement time was set to $T_{mes} = 180$ s in model scale. This corresponds to a measurement time of 7 hours and 30 minutes in full scale and proved to be sufficient to capture the whole inertial subrange dynamics as well as the dynamics of the larger eddies.

Repetitive measurements were taken for all single-building model facades at five different wall-distances (3 m, 6.75 m, 10.6 m, 15 m and 35.2 m in full scale). These repetitions were taken on the side, leewards and in front of the model building for each of the measured components. At each position, the measurements were repeated ten times, and the data scatter was estimated by taking the maximum range of all values to again get a conservative approximation of the corresponding flow measure's reproducibility. Table 4.5 shows the uncertainties for each building-facade roughness (flat: FL, balcony rows: BR, windows with balconies: WB) and for each investigation location (side, upwind (luv) and leeward). For approach boundary-layer values, the same uncertainties as with the first experiment were used.

Table 4.5: Reproducibility of the calculated flow statistics for the near-wall flow at a single building for the studied surface roughnesses (FL, BR and WB). The uncertainty was obtained for the flow next to the building (side) as well as upwind and downwind of the building (luv and lee).

Position	**Model**	$\overline{\mathbf{u}}_\mathbf{i}\mathbf{u}_\mathbf{ref}^{-1}$	$\overline{\mathbf{u}_\mathbf{i}'^2}\mathbf{u}_\mathbf{ref}^{-2}$	$\overline{\mathbf{u}_\mathbf{1}'\mathbf{u}_\mathbf{j}'}\mathbf{u}_\mathbf{ref}^{-2}$	$\mathbf{L}_\mathbf{u}^\mathbf{x}$
Side	FL: u	± 0.0192	± 0.0085		± 3.6480 m
	v	± 0.0085	± 0.0030	± 0.0021	
	WB: u	± 0.0195	± 0.0052		± 3.5338 m
	v	± 0.0069	± 0.0029	± 0.0021	
	BR: u	± 0.0165	± 0.0051		± 4.4744 m
	v	± 0.0076	± 0.0034	± 0.0018	
Luv/ Lee	FL: u	± 0.0179	± 0.0021		± 1.1119 m
	w	± 0.0140	± 0.0014	± 0.0020	
	WB: u	± 0.0120	± 0.0022		± 0.8757 m
	w	± 0.0084	± 0.0038	± 0.0016	
	BR: u	± 0.0224	± 0.0029		± 0.9680 m
	w	± 0.0151	± 0.0019	± 0.0013	

The Modeled Boundary Layer

The mean velocity profile and the vertical turbulent fluxes of the approach boundary layer are now studied at a scale of $1{:}150$ (Fig. 4.11). The fitting ranges for the z_0-estimation were determined according to the vertical development of the measured vertical turbulent fluxes. The same criteria for constant-flux layer identification by Snyder (1981) are applied here. The constant-flux layer height was thus identified at $\delta_{cf} = 45$ m. For the measured flow profile, the range was 10.5 m $\leq z \leq 45$ m. With a determined roughness length of $z_0 = 0.084$ m, the sensitivity of this quantity is also demonstrated. Although the value in the previous experiment should be significantly lower when scaled up (it would be 0.315), it is now four times as high in this experiment. The power-law fit has a profile exponent of $\alpha = 0.18$ at an estimation height of $z_{ref} = \delta_{cf}$.

For the modeled boundary-layer flow described here, the Reynolds number is $Re \approx 55067$ and the friction Reynolds number is $Re_{u_*} \approx 3603$ with $u_* = 0.27$ m s^{-1}. An overview of the core boundary-layer properties is given in Tab. 4.6.

Table 4.6: Boundary-layer properties of the approach flow in the wind tunnel (see also Fig. 4.11a). Values are given in full scale.

$\mathbf{s_u}$	$\boldsymbol{\delta_{cf}}$ **(m)**	**Re**	$\mathbf{Re_{u_*}}$	$\mathbf{u_*}$ **(m s^{-1})**	$\mathbf{z_0}$ **(m)**
0.738	45	55067	3603	0.27	0.084

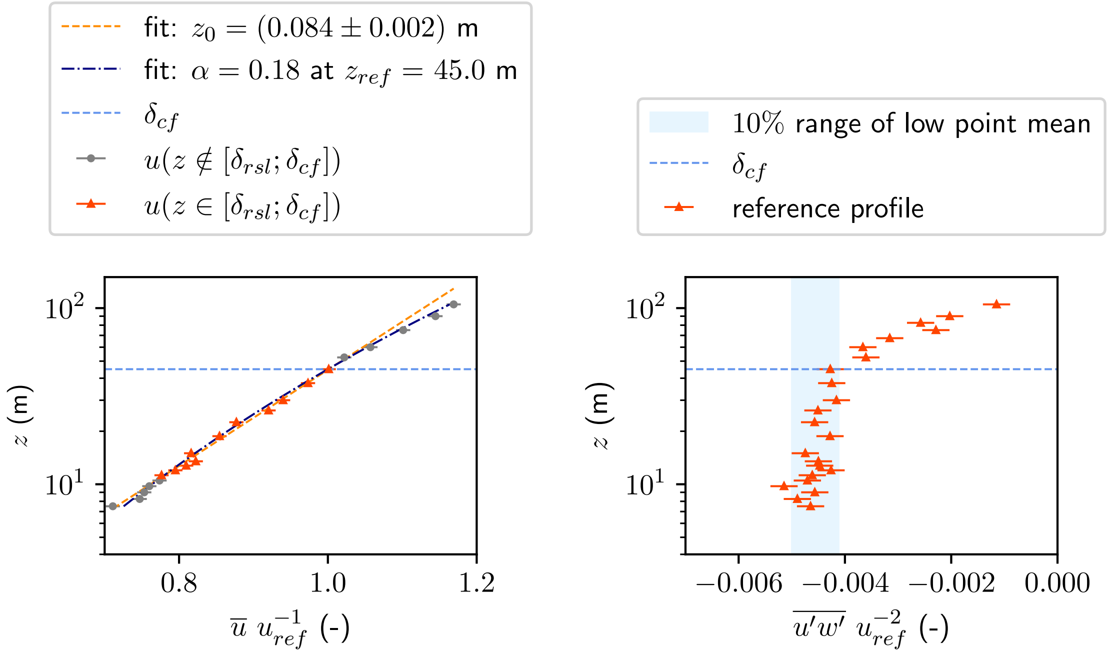

(a)

(b)

Figure 4.11: (a) Mean velocity profile of the approach boundary layer. Red triangles mark the measurement positions within the constant-flux layer. Grey points are not included into fitting the log-law of the wall (orange dashed) to obtain z_0. The blue dashed line shows the profile of the fitted power law. (b) The mean vertical turbulent fluxes are shown for the reference profile position. The ten-percent margin to define the constant-flux layer is shown in light blue.

With the changed model scale, vertical profiles of the turbulence intensities I_u and I_w and the integral length scale L_u^x (Fig. 4.12) agree better with the reference data by Counihan (1975) and the VDI 3783 Blatt 12 (2000). This is due to the fact that the boundary layer dimensions get artificially stretched along the z-axis by further downscaling. Turbulence intensities are well within the moderately rough regime within the constant-flux layer. The integral length scales are still too small though and correspond more to a rough boundary-layer flow. Both, the turbulence intensity I_u and the integral length scale cross roughness regimes at higher elevations.

Since the flow around a stand-alone building is to be investigated, it should usually be ensured that the model building itself is located in an area of the boundary layer in which the roughness class of the boundary layer is still maintained. However, the aim of this experiment is to investigate if a separation of flow regimes into near-wall and UCL flow is observable with roughness elements attached to the building surface and if *PALM* can replicate the flow around such a building. Accordingly, the best possible similarity to nature in the area of the model building height is not the most decisive point. The model building has a height of $H_u = 50.4$ m and the measurements presented in this work are done at a height of $z = 25.5$ m which is about mid-building height. The model building is just outside the constant-flux layer at the upper edge. Measurement profiles, however, lie well within the constant-flux layer. Thus, mean flow and turbulence quantities are consistent in the region of interest.

The Single-Building Model

The single-building models that will be investigated are placed onto the middle of the turntable. The single buildings are cuboids of height $H_u = 50.4$ m, length $L_u = 76.5$ m and depth $D_u = 34.5$ m. A total of three different building facades were examined. For each, the vertical facade surface aligned with the long edge L_u is equipped with small facade elements of length scales $h_r = 0.9$ m. The flow at this plane was then studied. The first facade is a completely flat facade without window openings and balconies. It is referred to as the **flat facade** and abbreviated with **FL** (Fig. A.4) and also acts as a reference case for the later done LES runs. The next building case attached with small window openings and individual balconies is referred to as the **medium rough facade** (**WB**). The third building studied has vertically alternating rows of window openings and balconies attached to the long edge plane. It is referred to as the **rough facade** (**BR**). A detailed description of the measures and arrangements of the facade roughnesses is given in Appendix A.3.

Placing the model into the wind-tunnel test section and perfectly aligning it with the wind-tunnel axes and also the approach flow is an important prerequisite for a proper

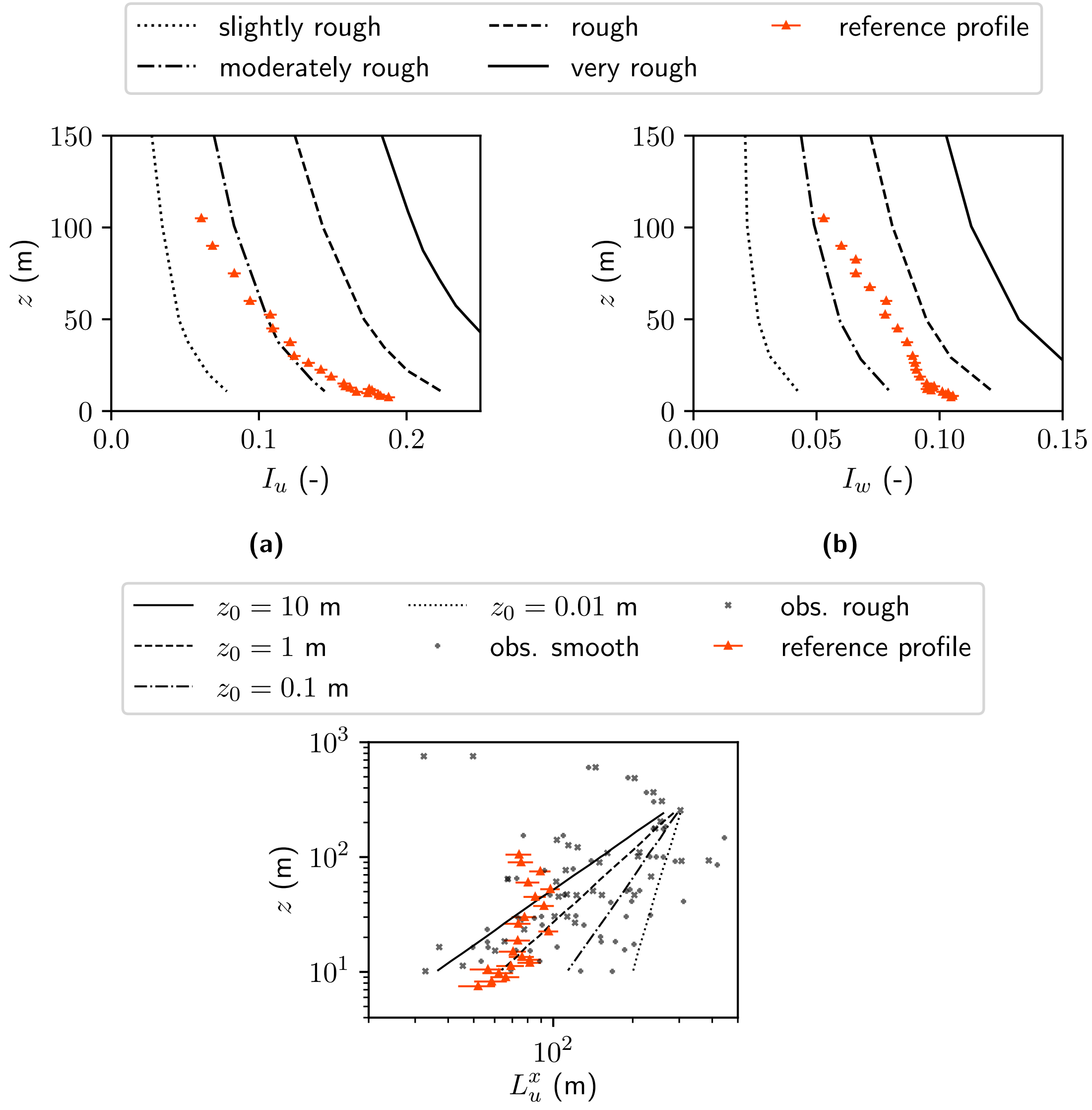

(a) **(b)**

(c)

Figure 4.12: (a) Turbulence intensity of the stream-wise velocity component I_u. The black curves mark the lower bounds of the roughness regimes defined by VDI 3783 Blatt 12 (2000). (b) Turbulence intensity of the vertical velocity component I_w. Here again the roughness regimes give orientation. (c) The integral length scales are shown with theoretical values for different roughness lengths. Observed field data for a smooth and rough boundary-layer flow are again shown (Counihan, 1975).

comparison with the LES model. The long building edge L_u was first aligned parallel to the x axis by eye. The LDA laser on the traverse was then used to determine whether the alignment was accurate by moving along the edge of the building and checking whether the laser beam moved away from the edge of the building over the distance travelled. In this way, it was possible to align the model building as parallel as possible to the wind-tunnel axis. However, it should also be ensured that the model building is also aligned appropriately with the main flow direction. To this end, lateral profiles 96.75 m in front of and 96.75 m behind the building were measured. Figure 4.13 shows the respective lateral profiles of the mean wind speed and the turbulence intensities. The symmetry in the wake of the model building suggests that an accurate placement of the model has been achieved.

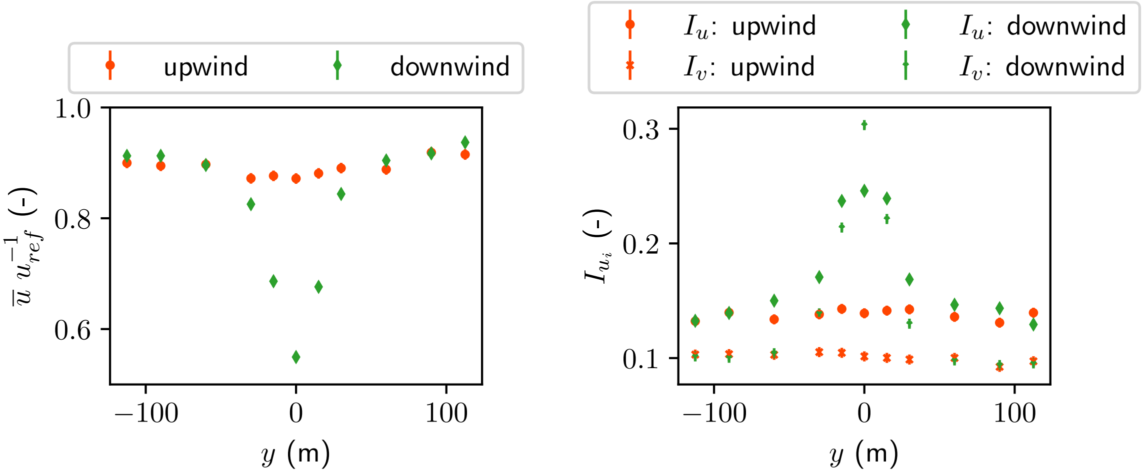

(a) **(b)**

Figure 4.13: Lateral profiles of (a) the mean stream-wise velocity $\overline{u}u_{ref}^{-1}$ and (b) the turbulence intensities I_u and I_v. For both values the lateral profiles were done 96.75 m upwind (red) and 96.75 m downwind (green) the building.

Turning of the LDA Probe

Due to its larger focal length of 500 mm (model scale), the large probe was used to carry out measurements close to the wall. Nevertheless, at a model building height of $H_u = 510$ mm in model scale, blocking of the laser beams prevents near-wall measurements closer to the wall than 2.11 m in full scale. To reach closer wall distances, the probe was turned by $4.8°$ such that the laser beam closest to the model building is aligned parallel to the vertical wall and not blocked anymore.

As a consequence, the measurement volume for the v-component is not perfectly aligned with the y-axis anymore. To correct for the occurring mismatch, the resulting velocities are multiplied with a rotational matrix. However, the resulting systematic error of about 10^{-5} m/s is significantly smaller than the statistical measurement uncertainty and can thus be neglected at such small rotation angles.

Reynolds Number Independence Testing

To ensure Reynolds number independence, the corresponding testing was done for the single-building model configuration as well. In this experiment, the regions close to the model building surface are particularly critical. This is due to very low velocities close to the facade and regions of high velocity shear and strong turbulence production e.g. in the wake of the building or at recirculation zones on edges. The tests were performed for near-wall flows upwind, leewards and sideways of the building. For this purpose, the reference velocity u_{ref} was reduced in seven steps from ≈ 6 m/s to about 1 m/s. Figure 4.14 shows the Reynolds number independence test results for the mean stream-wise velocity $\overline{u}$ and the wall-normal turbulent fluxes $\overline{u'v'}$. The shown tests were carried out for two different flow situations: within the recirculation zone (red) and further downstream (blue), where the flow along the vertical wall has reached a kind of equilibrium state. The wall distance for the two respective measurements is $\Delta y = 2.25$ m in full scale.

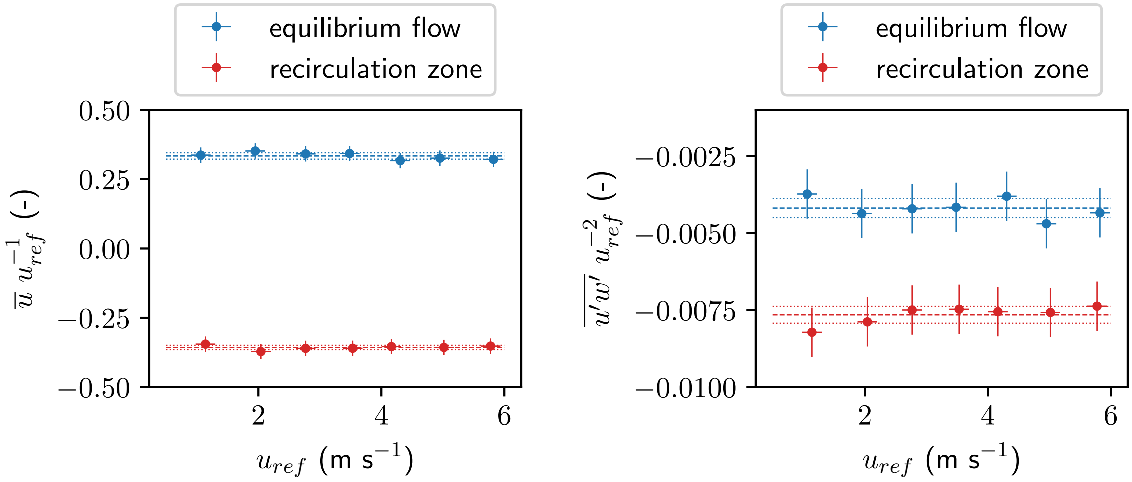

(a) **(b)**

Figure 4.14: Reynolds number independence test for the two measurement positions in the near-wall region for (a) the mean velocity and (b) the wall-normal turbulent fluxes. The dashed lines show the mean value for all 7 reference velocities. The dotted lines show the corridor within the standard deviations.

4.2.2 The Selected PALM Setup

The comparison of the near-wall flow of the single-building case with the wind-tunnel measurements requires that the wind-tunnel approach flow can be replicated as accurately as possible in the *PALM* model. For this purpose, the *PALM* configuration is tuned before the model building is inserted into the *PALM* model domain. First, the boundary layer flow without obstacles is modeled accordingly to the approaching wind-tunnel flow. Then it is ensured that the model building is correctly positioned in the flow and that the wake flow of the building does not influence the approach flow due to the cyclic boundary conditions.

Configuration of the PALM Runs

Before starting to model the approaching boundary layer, considerations about the necessary grid size have to be made. Following the train of thought from Sec. 2.3.5, the maximum allowed grid size possible for a sufficient resolution of the model building would be $max(\Delta_i) = 5$ m. With a floor roughness element size of 3 m in full scale, the minimum allowed grid size for the correct modeling of the approach boundary layer would thus be $min(\Delta_i) = 15$ m. This contradiction cannot be resolved in practice, which is why the floor roughness elements have to be resolved directly. Thus the maximum possible grid size reduces further to $\Delta_i = 3$ m. The approach flow was now modeled with grid sizes of 1 m to 3 m and the floor roughness elements were placed into the LES domain according to the actual arrangement used in *WOTAN* (see Fig. A.2). Only with a grid size of $\Delta_i = 1$ m, it was possible to not only model the mean flow properly, but also to achieve the best matching turbulence quantities and a valid ratio of SGS to resolved TKE (Fig. 4.17a).

Depending on the number of output positions for time series, the job-chains consisted of 46 to 50 single runs. Figure 4.15a shows the maximum velocity within the modeling domain for the final simulation setup chosen. The spin up time was similar to the previously mentioned setup in Sec. 4.1 and the start of time series output on each time step was again after 5400 s. With a full modeling time of 9 h, this again makes 7.5 h of time series to be evaluated. The mean time step for all runs was ≈ 0.12 s, which is reasonable because regions with higher velocities had to be numerically resolved due to acceleration effects at obstacles.

Boundary conditions for all surfaces and initial conditions as well as forcing via the conserve volume flow method have been applied for this model configuration as well. This time, the mean velocities documented in Fig. 4.11a were used in full scale. Figure 4.15b shows the good agreement of the mean velocity profile of the PALM and wind-tunnel flow. Both velocity profiles were scaled using the corresponding mean stream-wise flow velocity at $z = \delta_{cf}$. Note that the *PALM* velocity profile is shown for the domain with the model building already placed into the flow.

While the vertical and lateral turbulence intensities I_w and I_v agree well with the wind-tunnel reference profile up to the constant-flux layer height and even further, the lon-

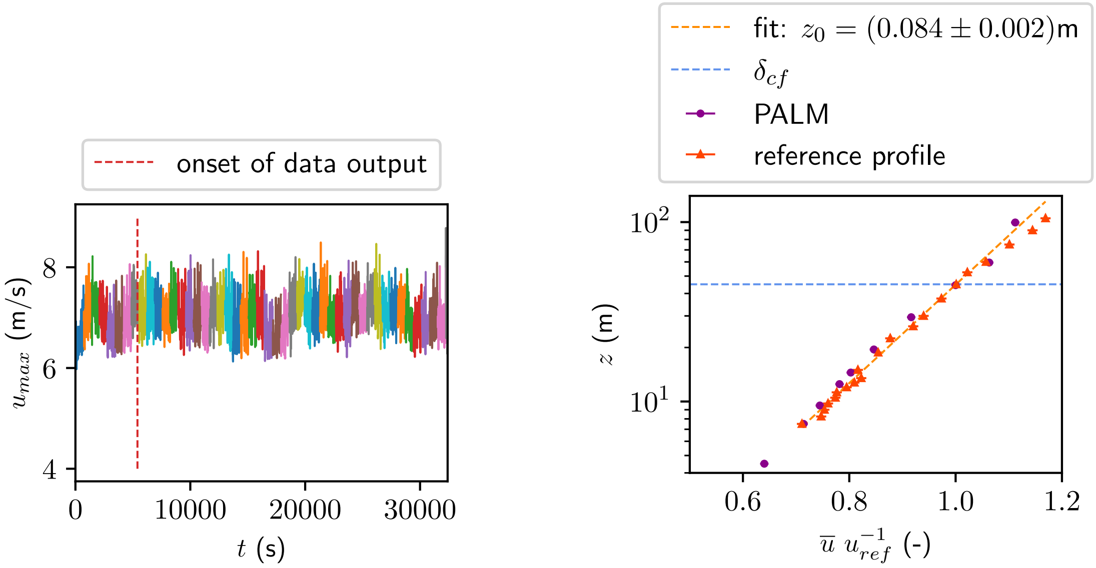

(a) **(b)**

Figure 4.15: (a) Time series of the maximum velocity u_{max} within the whole modeling domain for the *PALM*-run with $z_0 = 0.03$ m and the D80 SGS model. (b) The mean velocity profile from the wind tunnel (red triangles) and the final *PALM* setup (purple) with already mentioned roughness length and a grid size of $\Delta_i = 1$ m. The fit shows the best linear fit from the wind-tunnel data.

gitudinal turbulence intensity I_u is slightly underestimated throughout the whole model height as shown in Fig. 4.16. The LES boundary layer was first optimised such that the vertical profile of the mean wind speed corresponds to the profile measured in the wind tunnel. This was achieved mainly by adjusting the roughness length and setting the reference profile from the wind tunnel as the initial condition. Once the wind speed matched the reference, turbulence characteristics were considered. Since the results from PALM with an empty boundary layer showed too low turbulence intensities, the floor roughness elements were directly resolved as well; an approach, which already proved feasible in Gronemeier et al. (2021). This brought at least the turbulence intensities I_v and I_w into agreement with the reference data. To optimise the longitudinal turbulence intensity, an increase in the roughness length would have been necessary. However, this would have changed the wind profile again, so it was finally decided that this is the best possible boundary layer match and the experimental comparison can be carried out with this configuration.

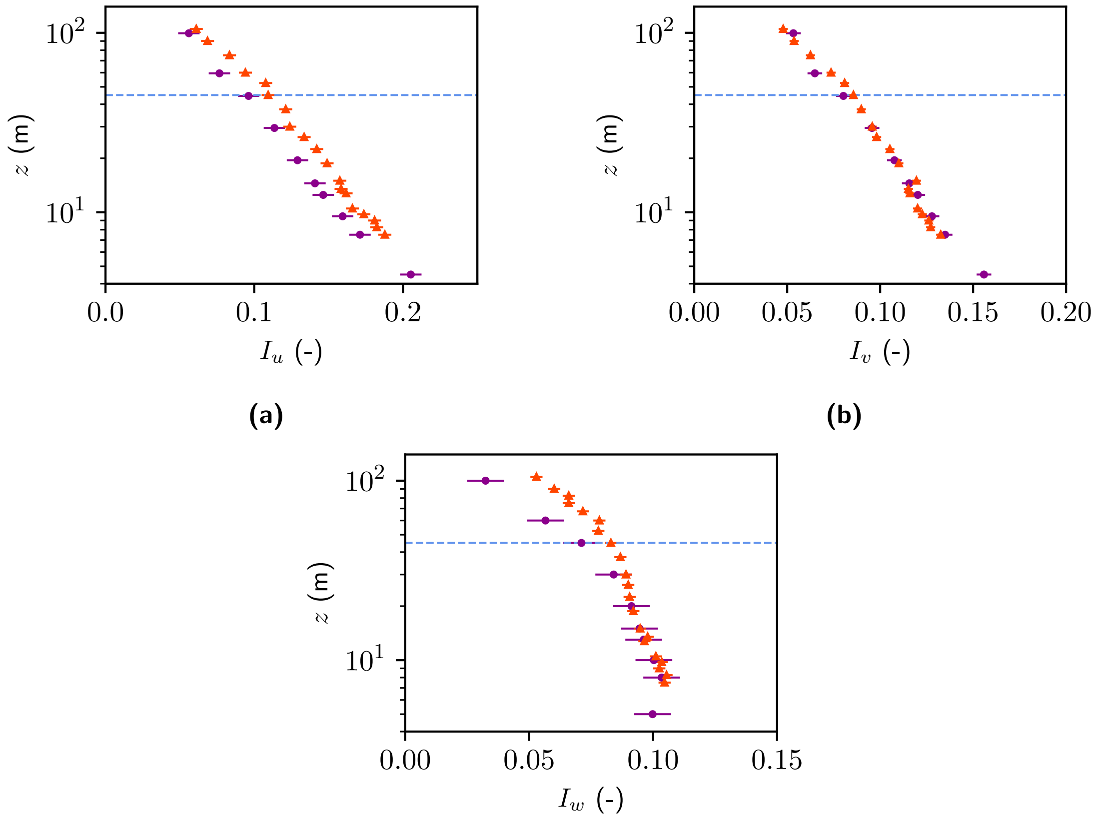

(a) **(b)**

(c)

Figure 4.16: Turbulence intensities for the three velocity components (a) I_u, (b) I_v and (c) I_w. The LES results agree well with wind-tunnel reference data for the second and third velocity component. The stream-wise turbulence intensity is lower in the LES than in the wind-tunnel boundary layer. The colour coding corresponds to the legend in Fig. 4.15b.

Validation of the PALM Runs

Before analysing the LES results in detail, we need to ensure that the ratio between SGS and total energy is sufficient and that the flow can be regarded as incompressible (Fig. 4.17). The SGS energies account for 2.1% of the total energy of the flow and the model setup is thus well resolved according to Heus et al. (2010). By applying the predictor-corrector method, the divergence was reduced by two orders of magnitude, which can just be considered as tolerable.

When implementing the model building into the model domain, it has to be assured that the wake of the building does not affect the flow in front of the same building since cyclic boundary conditions were used. The profile of the mean wind speeds in Fig. 4.15b shows that the model domain was chosen long enough such that mean wind speeds and turbulence quantities are not affected by the wake of the building. This also holds for the

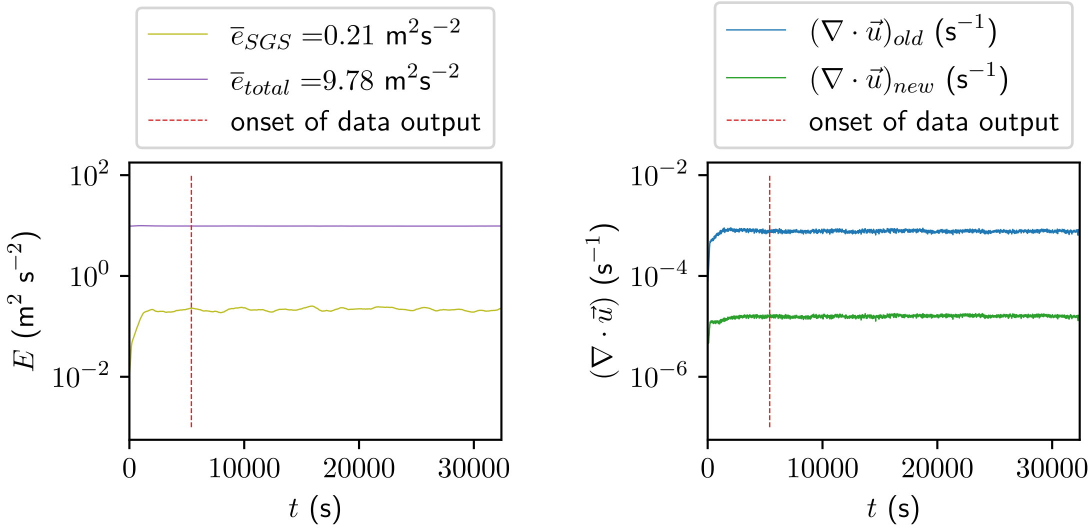

(a) **(b)**

Figure 4.17: Time series of the (a) SGS and total energy and (b) domain-averaged flow divergence before and after the predictor-corrector scheme was applied. The data is shown for the *PALM*-run with $z_0 = 0.03$ m.

turbulence intensities in Fig. 4.16. Additionally, correlation coefficients were computed for pairs of time series at several locations within the model domain. The time series for all three velocity components in front (BL) of the model building are not correlated with time series taken behind (B1 and B2) and next to (S1) the model building at a height of $z = 25$ m. The corresponding correlograms are shown in Appendix B.

The uncertainties for each quantity were again determined by applying a convergence test and choosing the whole range of data scatter (see Tab. 4.3).

Overview on PALM Runs Done

In total, three sets of *PALM* runs were carried out to model the single-building case (Tab. 4.7 and Tab. B.1). The first set #1 consists of preparatory model runs that aim to guarantee the correct configuration of the final model runs. These include runs at varying roughness lengths with and without resolved floor roughness elements, one long run for convergence testing and runs with time series output in front, behind and next the model building for computation of the above mentioned correlations.

The other two sets #2 and #3 include the final model runs which contribute to the findings that are presented in Sec. 5. The two sets differ in the inflow wind direction relative to the model building. Here, as in the wind tunnel, not the wind direction but the model building was rotated in the coordinate system by $90°$.

Table 4.7: Overview on *PALM* runs done in set #2 and #3. The total amount of runs including the runs from set #1 can be viewed in Tab. B.1.

Set	Run name	Wind direction	Δ_i (m)	z_0 (m)
#2	SB_BL	0°	1	0.03
#2	SB_SI	0°	1	0.03
#3	SB_LE	90°	1	0.03
#3	SB_LU	90°	1	0.03

4.2.3 Measurement and Output Positions

The measurement and output positions that are used in this work are depicted in Fig. 4.18. Figure 4.18a shows the profile positions for the wind direction of zero degrees, and Fig. 4.18b shows the up- and downwind profile position for the ninety degree wind direction. The red and green profiles depict the main comparison positions between the wind tunnel and LES results. The yellow profiles were also measured, but mainly served to select the comparison positions. The measurement positions for the correlation tests (see Fig. B.3) are marked in black at the zero degree approach wind direction.

The exact wall distances in the profiles depend on the respective facade roughness configuration in the wind tunnel and therefore vary slightly from each other (< 1 m). For example, significantly smaller wall distances could be achieved for the smooth facade. In *PALM*, the wall distances depend on the grid used and thus also vary from the wind-tunnel distances. Interpolating the *PALM* profile positions directly onto the wind-tunnel wall distances would have been a solution. However, the gain in comparability does not outweigh the loss of accuracy in the flow measures through interpolation, especially because the wall distances are already very close together.

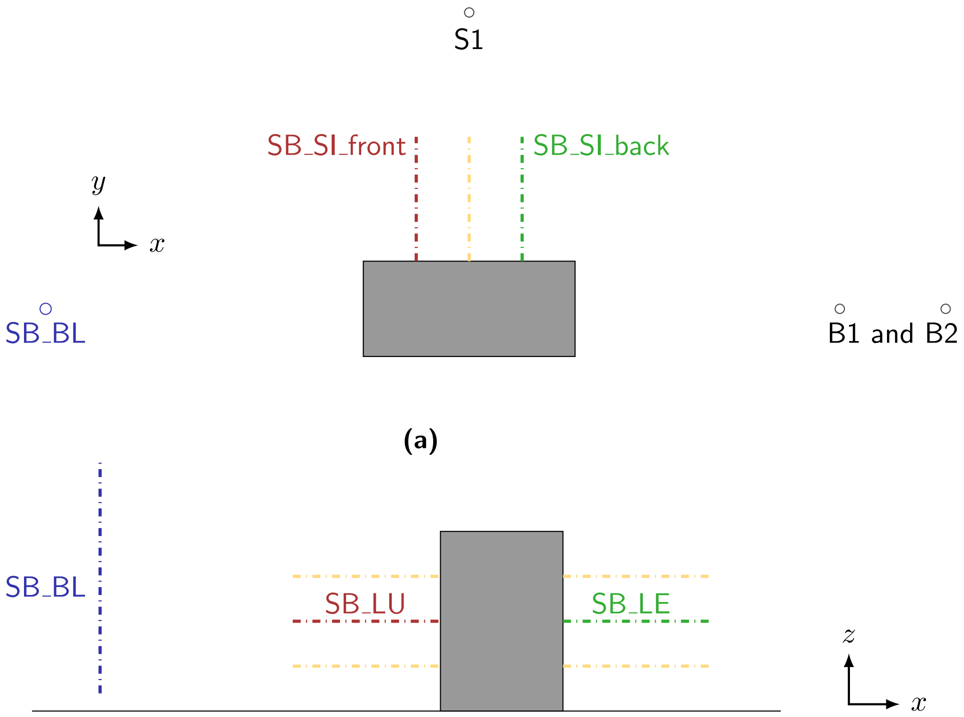

(a)

(b)

Figure 4.18: All wall-normal profiles were measured at mid-building height. The wall normal profile positions with a wind direction of $0°$ are shown in the upper sketch (a). The sketch below shows the near-wall profiles for an approach wind of $90°$. The blue profile **SI_BL** marks the position of the boundary-layer measurements 345 m upwind the building centre. For the blue boundary-layer profile the position in x-direction is shown closer in scale than in reality.

5 Results and Interpretation

So far, the theoretical background of turbulent flows in urban environments and at surfaces has been introduced (Sec. 2). In addition to physical modeling approaches, large-eddy simulations have been established as a widely used tool for studying such flows. In this context, three major issues in applying obstacle-resolving large-eddy simulations in urban climate studies were identified:

I 1 How can sub-grid scale surface roughnesses be considered properly in obstacle-resolving LES without violating the prerequisites formulated by Basu and Lacser (2017)?

I 2 SGS models used in contemporary LES are based on the local isotropy hypothesis. Furthermore, many SGS models are scale-invariant. Both properties are problematic close to solid surfaces.

I 3 What are practical implementations of the inherently present uncertainty of near-wall LES and how should be dealt with them?

Two experimental model configurations were designed to tackle these issues and gain further knowledge (Sec. 4). These issues then result in four different focal points of analysis in context of the research conducted here:

RQ 1 Can a roughness sublayer be identified in generic cases of flow above aerodynamically rough surfaces and for more complex model geometries?

RQ 2 How are local RSL dynamics at urban building surfaces as facades characterised?

RQ 3 What statements can be made about the local anisotropy of turbulence close to such surfaces?

RQ 4 Are local near-wall flows properly replicated in a contemporary LES model as *PALM*?

In Sec. 5.1, mainly issues **I 1** and **I 2** are regarded. First the flow statistics for both of the two experimental model configurations investigated in the wind tunnel are analyzed and compared to corresponding LES results. In a second step, the data obtained are considered under the aspects of local isotropy of turbulent motions. In Sec. 5.2, most of the results, presented before are discussed and placed in the context of real urban climate simulations (**I 3**).

5.1 Investigating the RSL

5.1.1 Flow Statistics

The investigation of the roughness sublayer first requires an identification of the same (RQ 1). A first approach is to consider wall-normal profiles of the statistical moments of the flow. This enables statements about the local dynamics within the RSL because flow statistics also have direct physical equivalents (RQ 2). For example, the momentum covariances correspond to the wall shear stress or turbulent fluxes. All flow statistics are also investigated with a focus on replicability by the LES model *PALM* (RQ 4). In the following, we will have a closer look at wall-normal profiles of flow statistics for the horizontal plate model configurations. Likewise, wall-normal profiles are investigated for the single-building cases with different facade roughness.

Horizontal Plate of Homogeneous Roughness — Results: The following figures contain the results of the wind-tunnel measurements described in Sec. 4.1. The corresponding *PALM* results of the runs listed in Tab. 4.4 are shown for the Deardorff (1980) (left) and for the Germano et al. (1991) (right) SGS model. The comparison of SGS models was possible for the simpler configuration without explicitly resolved roughness elements placed in the flow. If any morphologies (larger obstacles or small roughness elements) were resolved directly, the application of the G91 model lead to excessive production of SGS-TKE at sharp edges.[1] Hence, the comparison can unfortunately only be made for this simpler case.

Figure 5.1 shows the wall-normal profile of the dimensionless mean stream-wise velocity component $\overline{u}u_{ref}^{-1}$. Wind-tunnel results for all surface roughnesses show a high level of agreement at heights above ground larger than $z = 5h_r = 10.5$ m. In this region, the surface roughness elements mounted on the base plate do not influence the mean flow dynamics and the results match with the mean flow profile of the reference wind profile measurement taken upwind of the base plate. Note, that the measurement profile taken upwind of the base plate is called *reference profile* (red triangles), as it also served as the initial condition of the *PALM* runs. For the rough surface case, at the two highest measurement positions at 50 m and 70 m, the velocity values are higher than average.

---

[1] https://palm.muk.uni-hannover.de/trac/ticket/916 last visited on March 28, 2023.

At heights above ground lower than five times the small-scale roughness height h_r, wind-tunnel mean-velocity profiles diverge for the different roughness configurations.

As expected, for the more rough surface ($s_b = 8$ m) lower mean stream-wise velocity are observed while the flow over the flat surface with no roughness elements mounted on it experiences a strong speedup effect. The medium rough surface ($s_b = 5$ m) does not indicate a change in mean velocity and matches the reference profile measured upwind the test section. From measured mean wind profiles a roughness sublayer height of $\delta_{rsl} = 5h_r$ can be derived.

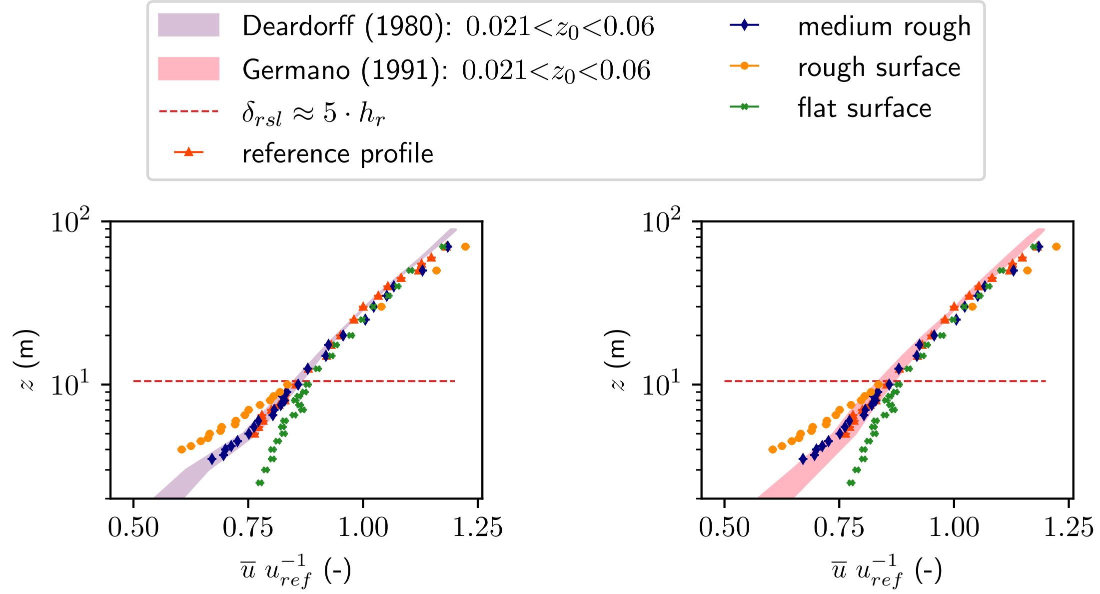

(a) **(b)**

Figure 5.1: Wall-normal profiles of the normalised mean stream-wise velocity $\overline{u}$ in comparison with *PALM* runs using (a) the D80 and (b) the G91 SGS model. The red dashed line marks the estimated roughness sublayer height of $\delta_{rsl} = 5h_r = 10.5$m.

The *PALM* results are shown for the two SGS models by Deardorff (1980) (D80) and Germano et al. (1991) (G91). In both cases the instantaneous logarithm method (IL) was used as the surface boundary condition. The LES mean stream-wise velocity agrees well with the reference profile close to the wall for measurement heights below $5h_r$ in both cases. The level of agreement is maintained also for measurement locations further away from the wall. At measurement positions farthest from the wall *PALM* results tend to underestimate wind speeds. The known log-layer mismatch which is typical for the IL boundary condition (Hultmark et al., 2013; Maronga et al., 2020b) can be seen in Fig. 5.1a, but is not visible in Fig. 5.1b. The overprediction in wind shear at the first few grid levels leads to a kink in the wind profile at about $z = 5$ m distance from the rough wall. The G91 model on the other side seems to be more sensitive to the choice of the roughness length. The spread of mean wind speeds is higher than for the D80 model. Nevertheless the log-layer mismatch is corrected at least in the setup using the G91 model.

As a next step, the second-order statistical moments, i.e. the variances and covariances are analysed (Fig. 5.2). Profiles for the wind-tunnel measurements show agreement for wall-distances larger than $5h_r$ and differ at lower heights. Deviations of the fluxes as a function of roughness configuration support the RSL height of $\delta_{rsl} = 5h_r$ estimated above. As expected, the fluxes for the flat surface have the smallest values, which is consistent with the measured velocity increase. The flux profiles for the medium rough surface also show lower values in the RSL while mean velocities match the ones of the reference profile. This suggests that the roughness spacing of $s_b = 5$ m leads to a skimming flow in this case. The mean wind profile of the approach flow is maintained while decreasing turbulent fluxes are observed. The turbulent fluxes of the rough surface do show values lower than for the reference profile.

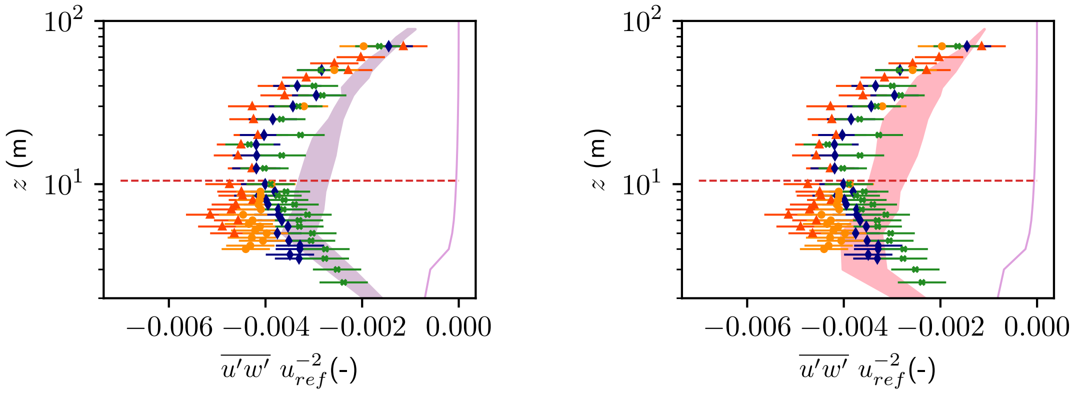

(a) **(b)**

Figure 5.2: Vertical turbulent flux profile for the wind-tunnel measurements in comparison with (a) runs with the D80 SGS model and (b) runs with the G91 model. The horizontally averaged SGS fluxes are shown as a light purple line and increase in the vicinity of the wall. The shaded areas show the resolved fluxes calculated from time series. Color coding is the same as in Fig. 5.1.

For both SGS models, the turbulent fluxes are substantially underestimated and are only about one third as strong as measured in the reference profile. In general, the range of scatter is higher for the G91 model. This again indicates a stronger sensitivity to the roughness length. The G91 model produces higher flux values than the D80 model. On the right hand side of each plot, the horizontally averaged sub-grid scale turbulent fluxes are shown as colored lines. The SGS contributions diminish for both SGS models at heights of about $z > 4$ m to 5 m from the ground. This finding is plausible, since small eddies are more frequent close to the surface. As SGS fluxes increase, the resolved fluxes should decrease. For the D80 model, the decrease in resolved fluxes happens already at wall-distance $z = 5$ m while for the G91 model, the resolved fluxes follow the expected curve better until $z = 3$ m from the wall.

It is also of interest to look at the turbulent contributions of each single measured velocity component. For this purpose, the turbulence intensities of the wind-tunnel measurements and the *PALM* results are compared in Fig. 5.3.

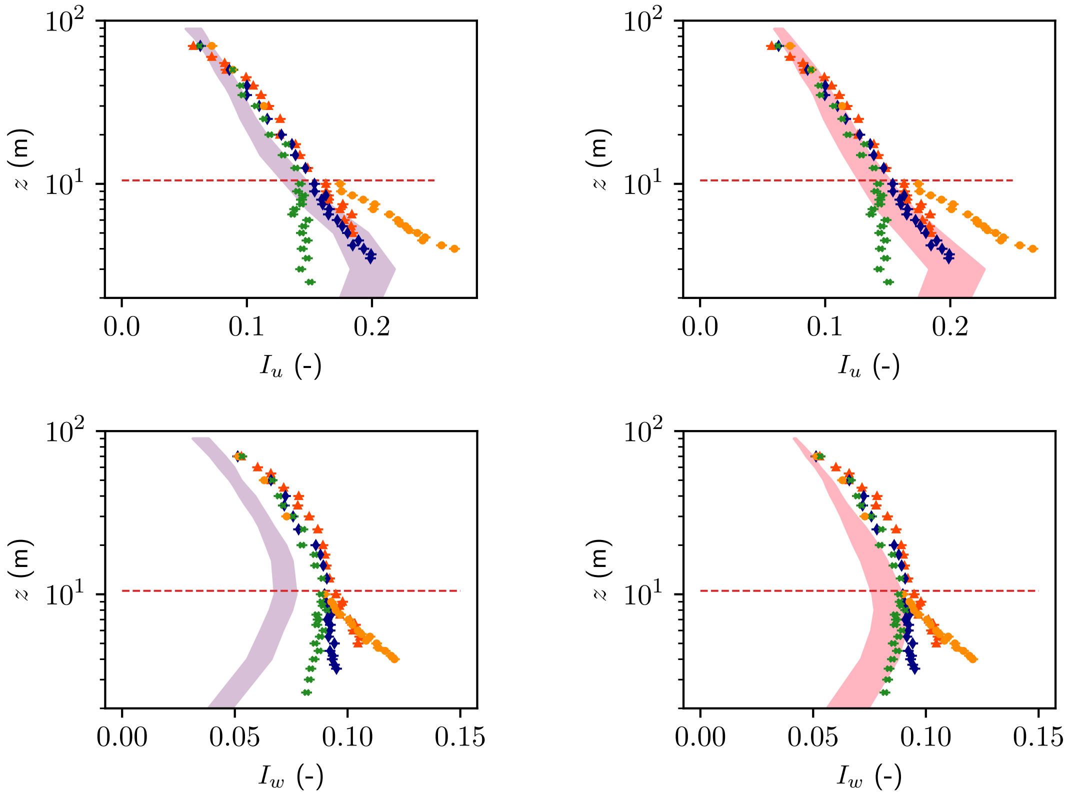

(a) **(b)**

Figure 5.3: Turbulence intensity profiles of the stream-wise I_u and wall-normal component I_w. The two profiles on the left show a comparison of the wind-tunnel data with the D80 model. Profiles on the right show the comparison with the G91 model. Color coding is the same as in Fig. 5.1.

The turbulence intensities derived from measurements over all surface roughnesses match the approach flow profile at higher wall-distances. Closer to the ground, diverging turbulence intensities are observed for different surface roughness within the RSL. Results support the RSL height $\delta_{rsl} = 5h_r$ estimated above. For the stream-wise turbulence intensities I_u, the rough surface shows the highest and the flat surface shows the lowest values. The medium rough surface shows similar stream-wise turbulence intensities within the RSL as measured at the reference position. This is consistent with the corresponding mean velocity profiles shown in Fig. 5.1. Within the RSL, turbulence intensity profiles for the vertical velocity component I_w depend on the roughness configuration. The rough surface shows the highest vertical turbulence intensities, which agree with the values from the approach flow reference profile. As expected, vertical turbulence intensities for the flat surface are the smallest, because no vortex separation at roughness elements can take place. Classifying the flow over the medium rough surface configuration as a skimming flow is also supported here, since there are smaller vertical fluctuations in the RSL.

While the values in *PALM* for the stream-wise component are only slightly smaller than the reference profile values, the vertical turbulence intensities are more clearly underestimated by the LES. The Germano model (Fig. 5.3b) provides stronger vertical turbulent fluctuations than the D80 model and thus is closer to the measured wind-tunnel flow. The more reliable performance of the G91 model in wall-bounded flows is expected, since the determination of the eddy diffusivity, in contrast to the D80 model, is based not only on heuristic assumptions but also on actual resolved fluctuations just larger than the grid size (see Sec. 2.3.2, Eq. 2.33 and the following paragraph).

So far, it was possible to clearly identify the roughness sublayer and estimate the height of that layer to $\delta_{rsl} = 5h_r$. Moreover, at least for the type of surface roughness used here, it has been shown that comparatively high velocities in the near-wall region tend to be associated with increases in stream-wise velocity fluctuations. Both, the stream-wise mean velocity and turbulent intensity are modeled properly by *PALM* with respect to the wind-tunnel reference profile. The underestimation of wall-normal turbulent fluxes $u'w'$ and wall-normal turbulence intensity I_w indicates that not resolving the sub-grid scale objects has a major impact here, independent from the SGS model. Such sub-grid scale surface roughnesses which are not directly resolved, but are also too big to account for in surface boundary conditions without violating basic principles (Basu and Lacser, 2017) are ubiquitous in urban environments.

The flow over a horizontal plate of homogeneous roughness was intentionally chosen as a generic case to study. The fundamental advantage of this setup is, that measured surface roughness effects can be traced back directly to changes in the surface roughness configuration. Nevertheless, an often used argument in the urban climate modeling community is that the complexity of urban flow cases often obliterates the small but measurable differences close to the wall. Whether this is really the case is examined in the following pages, among others.

Single-Building — Results: To study whether a roughness sublayer can also be identified in more complex flow cases, the flow around free-standing buildings with different surface roughness was investigated. In addition, *PALM* simulations were carried out for the case of a smooth facade as a reference case for comparison. The small-scale facade roughness elements were intentionally chosen smaller than the grid size used ($h_r < \Delta_i$) and refer to typical sizes of facade structures as e.g. balconies. The results are now presented in this section.

In the following, major flow statistics are presented for the measurement positions introduced in Fig. 4.18. Not all quantities are shown in the main document, ensuring clarity of the presentation. Additional results are collected in Appendix D. Before going into detail about the flow statistics for the different profile positions, an overview of the structure of the flow is given for both of the investigated wind directions (Fig. 5.4). Mean wind vector fields are shown for the flat facade case (FL) in the corresponding measurement planes (x-y- or x-z-plane). The red dashed line indicates the expected local RSL height of $5h_r$, as estimated from the above investigated experiment. The red and green values belong to comparison profiles shown in the following. Yellow vectors mark additional measurements which were done to identify positions suitable for comparison. For both single-building setups (Fig. 5.4a and 5.4b), the respective velocity vector at the upwind corner of the building (upper left corner in each figure) shows exceeding wind speeds.

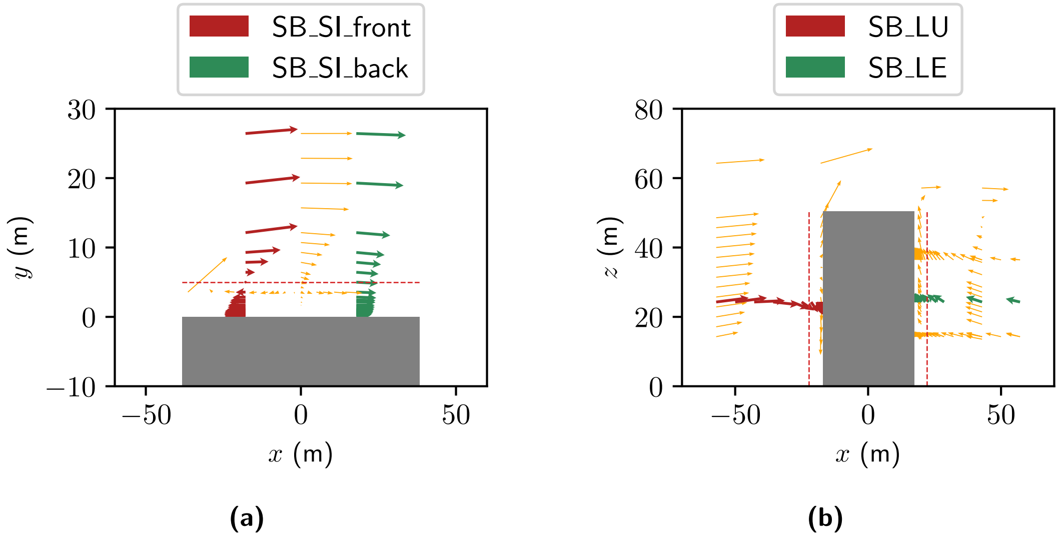

Figure 5.4: Vectorplots of the mean velocity for (a) the $0°$ case in x-y-plane and (b) the $90°$ case in x-z-plane. In both plots, the mean approach wind is from left to right. The data plotted are from wind-tunnel measurements of the single-building case with a flat facade. The grey block represents the studied buildings. The yellow arrows show additional measurements done for identifying suitable comparison positions. Color coding is the same as in Fig. 4.18.

Figure 5.4a shows a vector field of the mean wind in a horizontal x-y-plane. Measurements were taken at a mid-building height of $z = 25.5$ m above ground. The coordinate system was shifted in positive y-direction such that the origin lies directly at the wall. The profiles shown, were taken for the case of the mean wind direction of $0°$. Close to the model building wall at $x = 0$ m, in the middle between the red and green vectors, the point of reattachment can be identified. Here, the mean wind speed is zero. The stagnation point is not stationary and its position changes along the building facade. Even though the mean wind at this location is zero, the probability distribution of individually measured wind speeds at this location shows a clear bimodal behaviour (see Fig. D.4 in Appendix D). The red profile SB_SI_front was taken in the recirculation zone at the side of the building. Up to wall-distances of about 5 m the local mean wind blows from right to left (negative sign). At higher wall-distances the mean horizontal wind is parallel to the main wind direction in positive x-direction. The green profile SB_SI_back was taken behind the reattachment point and the mean horizontal wind is mainly directed parallel to the model building surface. The profiles chosen for comparison thus represent two different flow situations, both of which are of interest and frequently occur at facades exposed to the wind in urban environments.

Figure 5.4b shows the vector field reproduced from velocity measurements of the u and w component. In this configuration, the frontal facade is oriented perpendicular to the mean approach flow (rotated by $90°$). In front of the building, the comparison profile SB_LU was chosen at mid-building height $z = 25.5$ m. It is thus located in the vortex forming in front of the building. The near-wall vertical profile located there (yellow) indicates a stagnation point at a height of approximately $2/3H_u$. On the leeward side of the building, the comparison profile SB_LE is also located at a height of $z = 25.5$ m. It is located in the wake of the building and thus represents a flow case often occuring in cities.

The first order flow statistic of the measured time series is the mean velocity. In Fig. 5.5, wall-normal profiles of the mean velocity's respective wall-parallel component (u or w) are shown as a function of wall-distances Δy or Δx for all comparison positions defined above. All wall-normal profiles are shown as semi-logarithmic plots so that the values in the near-wall region are recognisable. Again, the roughness sublayer is marked in the plots by a dashed red line in the corresponding plots. For all RSL depths δ_{rsl} observable, an estimate of the roughness sublayer thickness is provided for each individual measurement location.

For the front position of the sideways flow (Fig. 5.5a) the mean wind shows now significant deviations in the near-wall region for the different building cases. The *PALM*

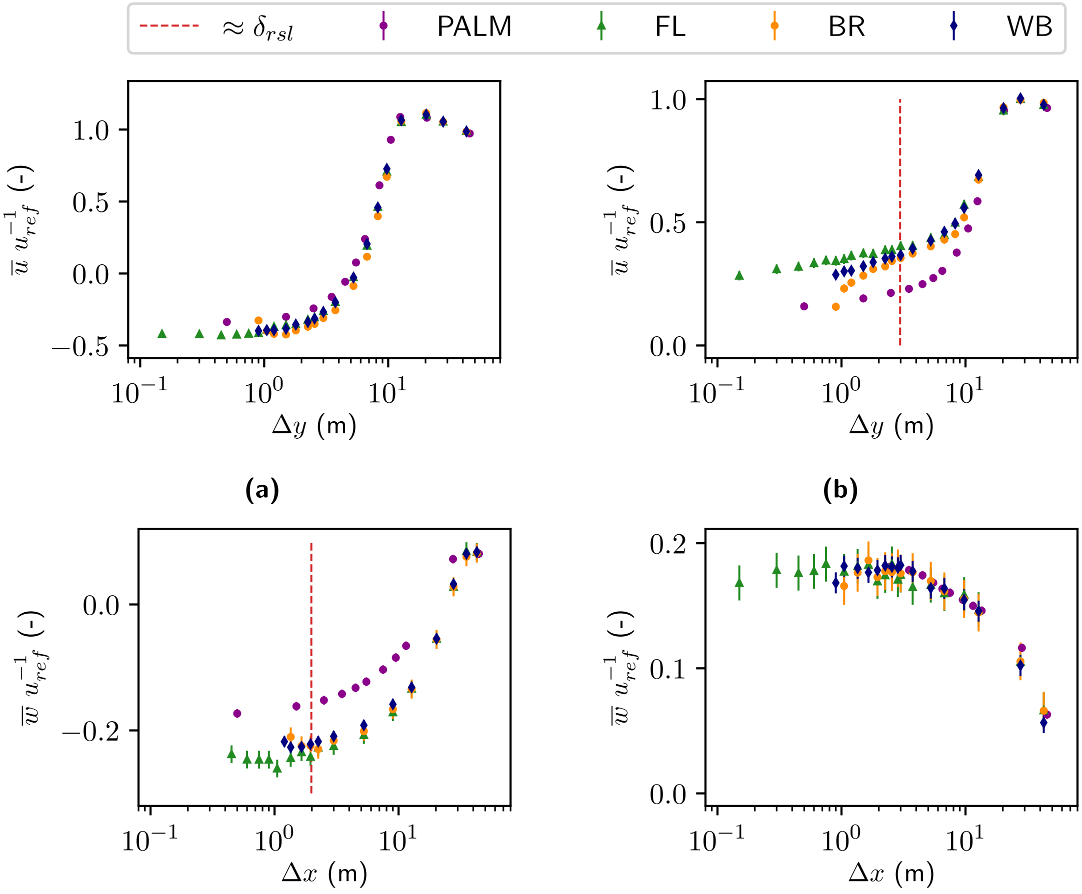

(a) **(b)**

(c) **(d)**

Figure 5.5: Mean wall-parallel velocity profiles for all measurement locations (a) SB_SI_front (b) SB_SI_back (c) SB_LU and (d) SB_LE. For two positions (b,c), a roughness sublayer could be identified (red dashed lines).

results match the wind-tunnel measurements for higher wall-distances and only underestimate the mean wind speed in the recirculation zone at wall-distances $\Delta y < 5$ m and overestimate the wind speed in the region of highest velocity gradients.

For the sideways mean flow comparison downwind of the reattachment point (SB_SI_back) in Fig. 5.5b the wind tunnel and *PALM* profiles agree well for wall-distances $\Delta y > 20$ m which are not affected by the large building length scales H_u. The mean velocity at the three building facade roughness configurations shows clear deviations in the near-wall region starting at $\Delta y < 3h_r \approx \delta_{rsl}$. The mean velocities of the BR configuration with continuous rows of small-scale facade-roughness elements (BR) are the slowest here and the values for the flat facade (FL) are the fastest. The *PALM* model does not represent the flow around the building at this comparison position at wall-distances smaller than

10 m from the wall. It underestimates the wind-tunnel mean flow by nearly 50%. This corresponds to the region of highest velocity gradients (wind shear) due to the nearby building wall; a flow phenomenon which is linked to the larger length scales H_u and L_u. As a result, the mean wall-parallel wind speed is strongly underestimated by the LES model. Another explanation is that the recirculation zone in *PALM* at the front corner of the building is stretched in x-direction in comparison to the wind-tunnel recirculation zone.

The mean wall-parallel wind speed at the upwind position SB_LU is shown in Fig. 5.5c. Again, wind-tunnel measurements and the *PALM* results agree further away from the wall for distances $\Delta x \leq 30$ m. In the region of highest wind shear, the wind-tunnel results for all facade configurations match and only at wall-distances of $\Delta x < 2h_r \approx 2$ m, the mean wind speeds deviate. The mean velocities calculated by *PALM* deviate from those measured in the wind tunnel beginning with the region of strongest wind shear between $\Delta x \approx 3$ m and 20 m. Here again the simulated wind speeds underestimate the measured wind-tunnel values.

The lower right velocity profile in Fig. 5.5d shows the wall-prallel mean velocity component for all building facade configurations and the *PALM* simulation at the leeward comparison position. Uncertainties in wind-tunnel measurements are higher here due to lower sampling rates, since the number of seeding particles needed for LDA data sampling is lower at this position than on the upwind side of the building model. No differences are observed with varying building surface roughness configurations. The mean velocities achieved from *PALM* agree well with the wind-tunnel results.

The turbulent fluxes (covariances) are second order statistics of the flow velocity. Figure 5.6 shows the turbulent fluxes for the sideways comparison positions. Profiles measured in the 90° approach wind case (SB_LU and SB_LE) do not show clear tendencies since all values are close to zero. Nevertheless, LES results lie well within the confidence range of the measured wind-tunnel turbulent fluxes (Appendix D, Fig. D.6). For the positions shown, roughness sublayer deviations could be observed for the different facade configurations. At the front location, differences start to occur for wall-distances smaller than $10h_r$. For the back location (Fig. 5.6b) facade dependent differences become significant for $\Delta y \leq 13h_r$.

The regions of maximum wind shear at around 10 m from the building surface do show maxima in the absolute values of the turbulent fluxes. This behaviour is expected, since regions of strong velocity gradients are associated with pronounced turbulent production. Because of that, the variances of the wall-parallel and wall-normal components also show maxima at these wall-distances (Figs. 5.7 and 5.8).

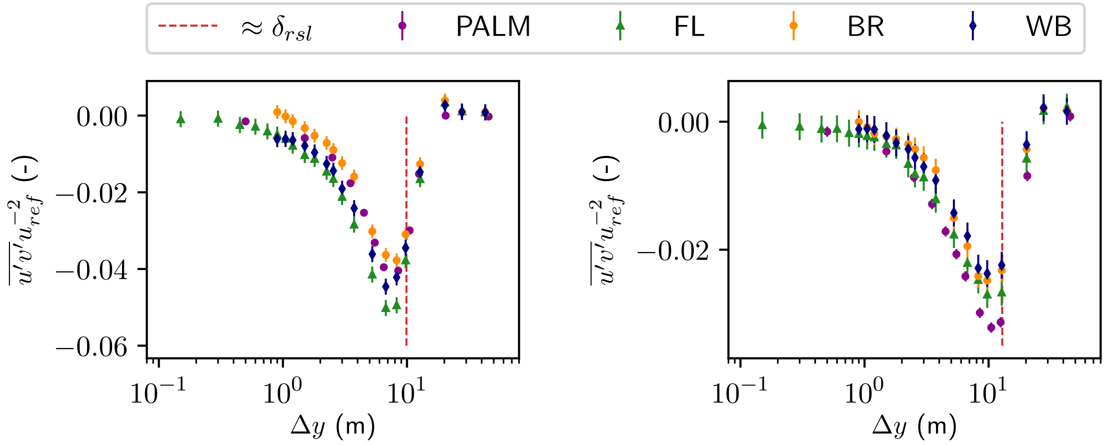

(a) **(b)**

Figure 5.6: The wall-normal turbulent flux profiles for measurement locations (a) SB_SI_front and (b) SB_SI_back.

Turbulent fluxes modeled by *PALM* follow the same pattern as the corresponding wind-tunnel flux profiles. Far away from the building facade, the LES model results coincide with corresponding wind-tunnel measurements. For the shear region at the comparison position SB_SI_front, the absolute turbulent fluxes simulated by *PALM* are lower than for the wind-tunnel configuration of the flat facade (FL) and match wind-tunnel results at the first two grid levels. This is in agreement with the weaker wind shear observed at this location. Downwind of the reattachment point, turbulent fluxes simulated by the *PALM* model show higher absolute values than the flat facade case at regions of highest velocity gradients, but also consistently agree with wind-tunnel results again closer to the wall (first four grid points). The higher turbulence production predicted by the *PALM* model is a direct consequence of the relatively high velocity gradient visible in Fig. 5.5b.

The resulting mismatch between *PALM* and wind-tunnel results in Figs. 5.5b and 5.5c can thus be attributed to difficulties in properly replicating the strong velocity gradients rather than to effects of not explicitly resolving surface roughness changes. Besides, Maronga et al. (2020b) state, that LES results up to the first seven grid cells may be affected if the ratio of Δ_i to z_0 is too low. Even though the ratio is lower than recommended ($\Delta_i/z_0 = 33.\overline{3} < 50$), the observed mismatch already starts further away from the building surface. The velocity difference can therefore not be attributed to the applied boundary conditions.

Figures 5.7 and 5.8 show the respective wall-parallel and wall-normal variances for selected measurement locations. Comparisons are presented only for profiles for which a roughness sublayer could be identified. For the remaining variance profiles, see Appendix D.2.

The variances for the profile comparison within the recirculation zone (SB_SI_front in Figs. 5.7a and 5.8a) show high level of agreement for all building facade configurations measured in the wind tunnel and the *PALM* results at wall-distances $z \geq 20$ m. A maximum of variance is reached at $\Delta y = 9$ m from the building surface for both velocity components $\overline{u'u'}$ (wall-parallel) and $\overline{v'v'}$ (wall-normal). At the same distance the turbulent fluxes reach a maximum and the wind shear intensifies. This local peak in all turbulent quantities can be attributed to the larger length scales H_u and L_u. A comparison of the variances calculated from wind-tunnel measurements at different facade roughnesses indicates, that also the smaller length scales h_r influence the flow in the shear region. Depending on the facade roughness, the variances of both velocity components start to deviate from each other at a wall-distances closer than $\Delta y = 9h_r$.

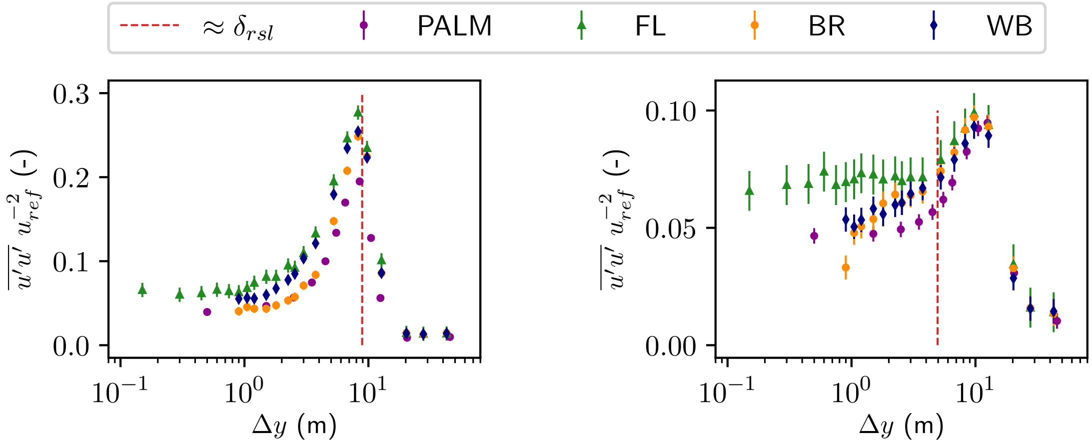

(a) **(b)**

Figure 5.7: The variance of the respective wall-parallel velocity component u for measurement locations (a) SB_SI_front and (b) SB_SI_back

At the comparison position downwind the reattachment point for the sideways flow (SB_SI_back in Figs. 5.7b and 5.8b), variances follow a similar pattern like within the recirculation zone. All wind tunnel and *PALM* variances match for wall-distances larger than $\Delta y > 15$ m. For the wall-parallel variance, this is even the case for wall-distances of 10 m from the building surface. For the two variance components measured, a roughness sublayer can be identified at two different wall-distances. The wall-parallel variance starts to diverge significantly at $\Delta y < 5h_r$, the wall-normal variance at $\Delta y < 9h_r$.

Variances of both velocity components modeled by *PALM* follow the wind-tunnel flow results with only a few exceptions. For the wall-parallel variances at SB_SI_front, the

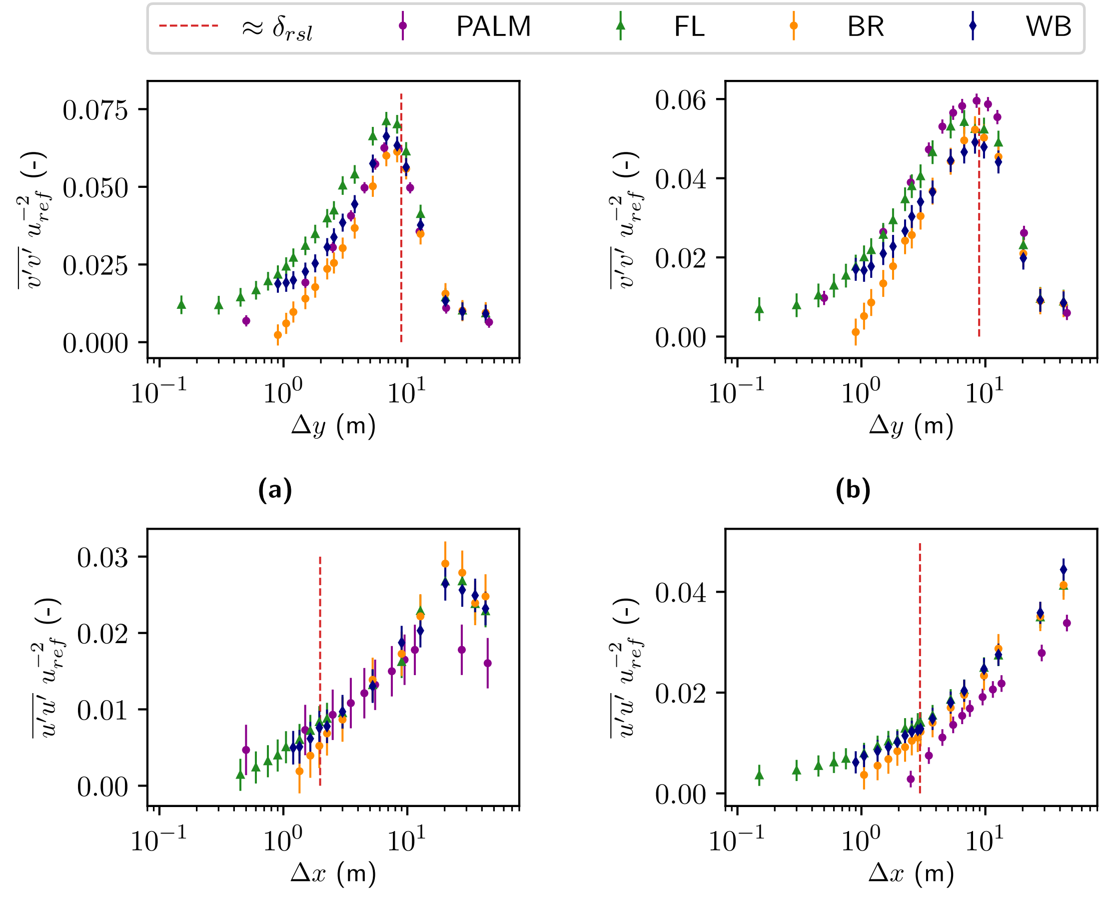

(a) **(b)** **(c)** **(d)**

Figure 5.8: The variance of the respective wall-normal velocity component v or u for all measurement locations (a) SB_SI_front (b) SB_SI_back (c) SB_LU and (d) SB_LE

maximum values modeled by *PALM* are about 20 % lower than measured in the wind tunnel. A slight underestimation of the variances can also be observed for the wall-normal component v when compared to the flat facade case. Downwind the reattachment point, the variances $\overline{u'u'}$ agree with wind-tunnel measurements further away from the wall and also the variance maximum is matched (Fig. 5.7b). In the near-wall region though, wall-parallel fluctuations are estimated far lower in the LES model. The wall-normal variance on the other side is properly replicated by *PALM*. Only the maximum values at $\Delta y = 9$ m are higher than observed in the wind tunnel.

For the wall-normal variance, the values of the flow cases with $90°$ approach wind direction (normal to the front wall of the building model) are shown as well (Figs. 5.8c and 5.8d). The case proofed to be interesting since for both cases RSL dynamics could be identified. For the flow upwind the building, a RSL height could be identified up to $2h_r$

away from the facade. Deviations are only visible for the BR-case (rough facade with attached rows of balconies). Leewards of the building a RSL height of $3h_r$ is estimated, but here again, only deviations for the rough facade (BR) can be identified. At the same time *PALM* results differ from the wind-tunnel variances in an unexpected manner. For the statistics already analysed, *PALM* results were mainly lacking accuracy in the near-wall region starting with the region of highest wind shear. In the upwind comparison position SB_LU, the near-wall variances agree well with the wind-tunnel measurements. The two profile points farthest away from the wall show significantly lower variances. The leewards variances show a strong systematic underestimation for the *PALM* results at all wall-distances. This might be due to the slight underestimation of the turbulence statistics in x-direction, which is already apparent in the approach flow (see also Fig. 4.16a).

The absolute values of all second order statistics are the highest in the recirculation zone of the $0°$-case directly behind the leading edge of the building. Here, also the strongest velocity gradients can be observed with $\overline{u}/u_{ref}$ ranging from -0.5 up to 1 within a distance of 8 m.

Figure 5.9 shows the higher order statistics (skewness: γ, kurtosis:β) for the two sideways comparison profiles SB_SI_front and SB_SI_back (further higher order statistics of the other comparison positions are provided in Appendix D). For both measures, the values of a normal distribution are marked by a dash-dotted line. The wind-tunnel velocities nearly follow a normal distribution further away from the wall for both comparison positions.

For the skewness and the kurtosis at the recirculation zone (Fig. 5.9a), a RSL can be identified. The flat facade (FL) and the medium rough facade (WB) distributions show the same shape along the profile. In the roughness sublayer, the flow at the rough facade (BR) shows kurtosis values which are indicating a more Gaussian velocity distribution (closer to three) than for the two other facade roughnesses. The skewness of flow at the rough facade (BR) is not constant within the roughness sublayer, strongly decays with decreasing distance from the wall and even shows a change in sign close to the wall. This indicates rare events of eddies with far lower velocities than the mean for this roughness configuration. For the SB_SI_front position, a RSL thickness of $3h_r$ can be estimated by analysing the kurtosis profiles. Similarly, a RSL thickness of $5h_r$ is estimated by evaluating the skewness profile.

The higher order statistics for the comparison position downwind the reattachment point mainly show values which are close to a normal distribution (Fig. 5.9b). For both measures, no deviations within the wind-tunnel configurations and thus no RSL could be located. The skewness calculated from *PALM* time series agrees with the wind-tunnel skewness at large wall-distances, but shows bigger values in the near-wall region. Distributions of the LES results are skewed stronger to the left and extreme values are more likely to be higher than the mean values than for the wind-tunnel velocity distributions. Kurtosis values of the *PALM* run mainly follow the profile of the wind-tunnel results.

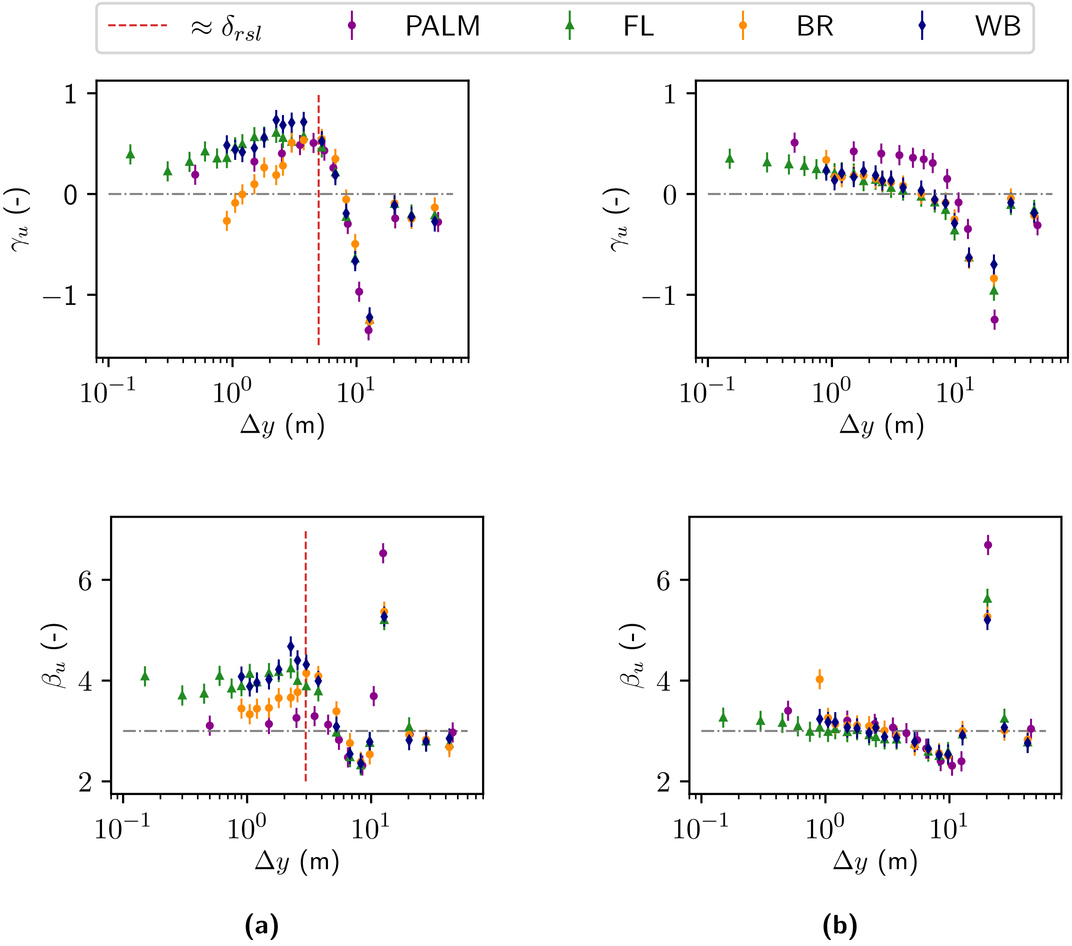

Figure 5.9: The skewness γ_u and the kurtosis β_u of the respective wall-parallel velocity component u for the measurement locations (a) SB_SI_front and (b) SB_SI_back.

In general, the higher order statistics indicate strongest deviations from Gaussian normal distributions at the beginning of the shear region at $\Delta y \approx 20$ m. Both skewness profiles indicate velocity distributions skewed strongly to the right here. This suggests rare but strong velocity signals which agrees with the large values of second order statistics at these wall-distances. *PALM* seems to model higher order statistics well. The maximum kurtosis for both *PALM* profiles (Figs. 5.9a and 5.9b) is higher than for the wind-tunnel measurements. Thus, *PALM* produces more extreme values and a stronger leptokurtic distribution at regions of high wind shear and intense turbulence values.

Preliminary Conclusions

The wind-tunnel data of the experiment over the horizontal plate of different roughnesses allows an identification of the RSL based on the flow statistics.

The wind profiles clearly differ at wall distances smaller than $5h_r$ for the different roughness configurations investigated (Figs. 5.1 - 5.3). For the case of the single building with small-scale roughness elements of size h_r attached to the facade, a clear identification of the RSL is more difficult, but possible for most of the measured profiles. Based on the flow statistics, question RQ 1 can be answered accordingly with a clear **"yes, but"**. **Yes**, a roughness sublayer can be identified, **but** its thickness depends on the local flow conditions and the surface roughness. The various RSL thicknesses δ_{rsl} determined above are further elaborated on in more detail in Sec. 5.2.

For the case of a horizontal plate of homogeneous roughness, flow variations within the roughness sublayer reveal a clear and consistent picture. A roughness sublayer depth of $5h_r$ can be identified for all roughness configurations and flow measures. The results are consistent in terms of the correlation of mean wind and turbulence measures. If a configuration triggers many vortices and correspondingly increased wall shear stresses, then the mean wind speeds are lower. As expected, the highest near-wall mean velocities are measured for the flat surface. Accordingly, the second-order statistics (turbulence intensities and fluxes) are lowest for this case.

For the flow around single buildings, it is much more difficult to get a clear consistent picture of the flow at different facade roughnesses. If near-wall flow velocities for one configuration are lower, that does not necessarily result in higher turbulence statistics at the same comparison profile (see e.g. SB_SI_back). This ambiguity makes a clear interpretation of the RSL results much more difficult. Nevertheless, the impact of strong wind shear on the turbulence production is evident and can be identified at all comparison positions.

The corresponding *PALM* results for both experiments (single building and horizontal plate) allow the following conclusions to be drawn. First, near-wall wall-normal fluctuations modeled by *PALM* are systematically underestimated for generic boundary-layer flows. Second, the SGS model by Germano et al. (1991) outperforms the model by Deardorff (1980) in terms of near-wall wall-normal fluctuations for simple boundary-layer flows. Third, at the more complex single-building case, if the *PALM* runs do not match wind-tunnel results, it is usually because regions with strong velocity gradients cannot be sufficiently replicated. This can be either due to insufficient grid resolution or due to the sudden change in eddy sizes, which cannot be modeled sufficiently by the scale-invariant D80 model.

5.1.2 Flow Anisotropy

Large-eddy simulation sub-grid scale models rely on the assumption of local isotropy established by Kolmogorov (1941, 1991) and on turbulent viscosity models (see also Sec. 2.3.2). As a measure of (an-)isotropy in turbulent flows, the quadrant contributions to the total flow on the one hand and the turbulence spectra scaling (K41 scaling) on the other hand are investigated. For isotropic flows, pairs of quadrant contributions $\overline{u'v'}_{q_i}/\overline{u'v'}$ should roughly balance each other out in strength. By looking at the inertial subrange scaling of turbulent spectra, indirect statements about anisotropy can be enabled. If the scaling $m(S_{u_iu_j})$ deviates significantly from the expected value of $-2/3$, this may be due to large wind shear and the anisotropy of turbulent fluctuations.[2]

Quadrant analysis results for the case of the horizontal plate as well as for chosen comparison positions at the single building are shown in this section. For both model configurations, first, example JPDFs are shown. After that, a comparison of quadrant contribution profiles is shown. In addition, results for turbulence co-spectra are discussed for the single-building configuration. Here, the focus is on the comparison of the wind tunnel and LES spectra as well as the inertial subrange scaling in the near-wall region as an indicator of anisotropy and enhanced turbulent production $\mathcal{P}$ and energy transfer $\mathcal{T}$.

Quadrant Analysis

Quadrant analysis results can deliver multiple information on the flow and offer many ways of interpretation. The standard motivation of applying a quadrant analysis is to identify flow events such as ejections from and sweeps towards the wall. In this work, there exists the additional motivation of identifying regions of flow anisotropy. First, the results of the quadrant analysis for the model configuration of the horizontal plate will be discussed. After that, the results for the model configuration of the single buildings with different surface roughness are considered. Since there are again many comparison positions for this model configuration, this section mainly considers the position downwind the reattachment point at a sideways approach flow. Additional results can be found in Appendix D.

Horizontal Plate of Homogeneous Roughness — Results: Joint propability density functions (JPDF) for normalised u' and w' distributions at $z = 5$ m above ground are shown in Fig. 5.10. As already learned by looking at the statistical measures computed from the wind-tunnel measurements, the measurement positions from which the JPDFs are computed lie well within the roughness sublayer. The JPDFs for all wind-tunnel

---

[2] The value changes from $-5/3$ to $-2/3$ by normalising the energy density with the Fourier frequency.

surfaces show similar ellipsoid shapes with a maximum in the second quadrant $Q2$ and a high proportion of fluxes being also located in the fourth quadrant $Q4$. Accordingly, it is also conclusive that the maximum of the distribution is closer to the coordinate origin in the flat surface case (Fig. 5.10b). At this surface, there are no roughness elements of size h_r which can cause ejection events or strong wall-normal fluctuations in general. The broadest distribution with the least distinct peak is that of the rough surface (5.10d). In particular, the maximum absolute values of the fluctuations for this surface are almost twice as high as for the flow over the flat surface.

In comparison with all wind-tunnel surfaces, the JPDF calculated from *PALM* time series has a similar spread for the u'-fluctuations, but is significantly narrower (less than 40%) along the w'-axis (see Fig. 5.10e). This is the case at all values of u'. The underestimation of wall-normal turbulence intensities in the *PALM* simulations was also identified in Fig. 5.3. The quadrant analysis delivers an added value, since it can now be said that this underestimation is not associated with any specific motion (sweeps, ejections), but happens at each state of the flow. *PALM* JPDFs for all roughness lengths and SGS models, which are four runs in total (Tab. 4.4), are displayed in Fig. D.1. A comparison between the JPDFs of the *PALM*-runs supports the observations made earlier for the turbulence intensities and the fluxes (Figs. 5.2 and 5.3). The use of the G91 model at higher roughness lengths than the one of the flow aimed for ($z_0 = 0.021$ m vs. $z_0 = 0.06$ m) delivers the results which agree best with the wind-tunnel cases.

In Fig. 5.11, the vertical profiles of quadrant contributions at the reference profile are shown in comparison with *PALM* results using the D80 (Fig. 5.11a) and the G91 model (Fig. 5.11b). Contributions from ejection and sweep events ($Q2$ and $Q4$) to the total flux dominate and have higher values than contributions from quadrants $Q1$ and $Q3$ at all heights above ground. The quadrant contribution profiles of *PALM* and the wind-tunnel reference show a high level of agreement of the quadrant contributions for both SGS models up to heights of $z \approx \delta_{cf} = 30$ m. Above, the quadrant contributions for the $Q2$ and $Q4$ quadrants diverge. Especially the $Q4$-quadrant associated with sweeps shows significantly larger values in the outer layer. At the same time, since contributions balance each other out, sweep events do contribute less to the total flux at these heights above ground. Here, the *PALM* model delivers lower contributions coming from sweeps than measured in the wind tunnel for both SGS models. Nevertheless, the divergence of quadrant contributions coming from quadrants $Q2$ and $Q4$ which is occuring at $z > 40$ m is generally underestimated in *PALM*. This is also the case for model runs with roughness lengths of $z_0 = 0.06$ m (Fig. D.3). However, it must be taken into account that differences that occur at these wall-distances ($z > \delta_{cf}$) are no longer necessarily similar to nature even in the wind tunnel (see Sec. 4.1).

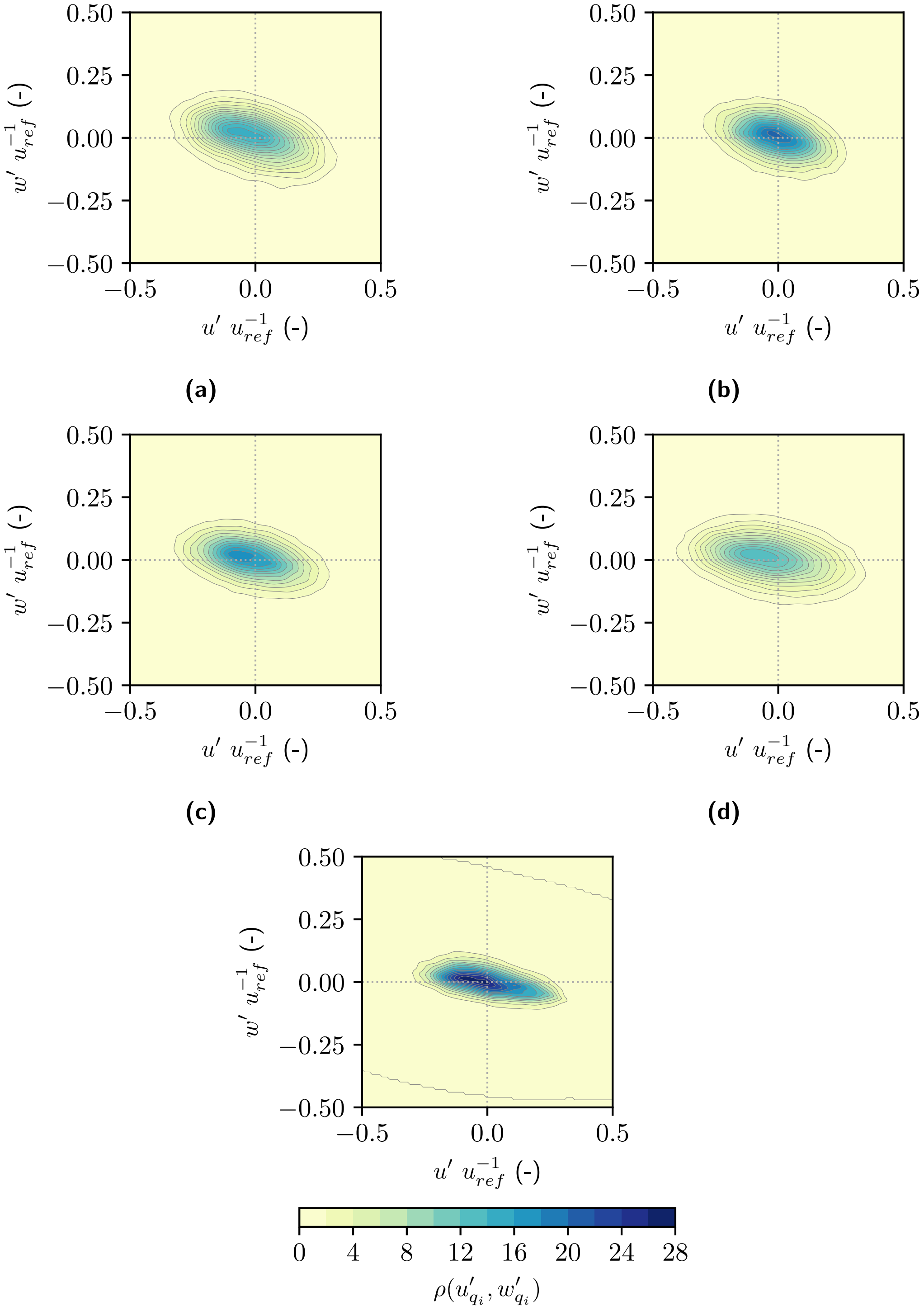

(a)

(b)

(c)

(d)

(e)

Figure 5.10: JPDFs for the (a) reference profile, the wind-tunnel measurement for the (b) flat, (c) medium rough and (d) rough surface and, finally, (e) the *PALM* simulation using the D80 model and a roughness length of $z_0 = 0.021$ m at a distance of $z = 5$ m from the surface.

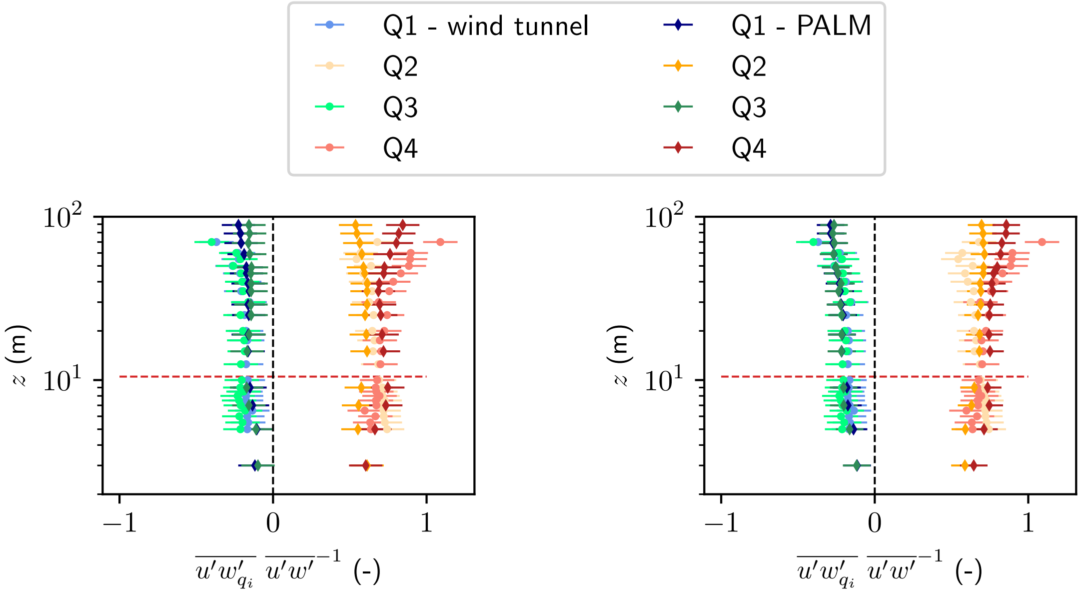

(a) Deardorff model, $z_0 = 0.021$ m

(b) Germano model, $z_0 = 0.021$ m

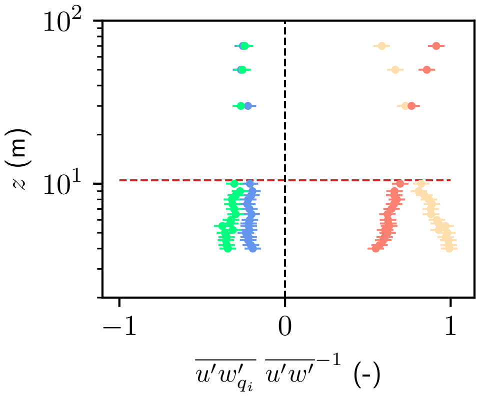

(c) rough surface

Figure 5.11: Quadrant contribution profiles of the wind-tunnel reference profile and the *PALM* runs (a and b). For both model runs, a roughness length of $z_0 = 0.021$ m was used. Quadrant contributions for the wind-tunnel measurements above the rough surface are also shown in (c).

In addition to the comparison of the wind-tunnel approach-flow profile at the reference position to the profiles from *PALM* runs, the quadrant contribution profiles for the different surface roughnesses are depicted in Fig. 5.11c and Fig. D.2. When comparing the near-wall quadrant contributions with the reference wind, a significant deviation of quadrant contributions within the roughness sublayer is visible. Ejection events play a bigger role above the rough surface compared to the reference case as the small-scale roughness elements mounted on the surface induce positive vertical fluctuations into the roughness sublayer, which dominate over sweeps from the outer regions. This is another indicator for a well established roughness sublayer, which cannot be replicated by the *PALM* simulations. Observations made for the rough surface are additionally supported by the quadrant contribution profiles calculated for the flat and rough surface (see Fig. D.2).

It can be concluded that for the flow over a horizontal plate the quadrant contributions modeled in *PALM* agree well with the wind-tunnel reference profile at wall-distances relevant in urban-climate studies. However, the rising contribution of ejection events within the RSL caused by sub-grid scale roughness elements cannot be resolved. The differences in quadrant contributions which are caused by sub-grid scale changes in surface roughness cannot be resolved explicitly by *PALM*.

Single-Building — Results: Figure 5.12 shows contour plots of the JPDFs for the single-building profile at position SB_SI_back at three distances Δy from the building facade. Note that for the single-building model configuration, the measured wind components at the sideways flow are u (wall-parallel) and v (wall-normal). Also, the wall-distances Δy in *PALM* and in the wind-tunnel experiment differ slightly from each other depending on the evaluated measurement point within the profile. The spatial difference is smaller than 0.25 m, which is a quarter of a grid cell size only.

At $\Delta y \approx 2.5$ m, distributions are circular with the wind-tunnel JPDF showing a slight dent on the right edge. Mean turbulent fluxes are close to zero at this wall-distance (Fig. 5.6) and most of u'-v'-pairs lie within quadrants $Q2$ and $Q3$. The *PALM* results also show a nearly circular JPDF, but the most frequent fluctuations are rooted in sweep events. Further away from the wall at $\Delta y \approx 6.5$ m the wind-tunnel JPDF has a more pronounced, drop-like shape with most of the fluctuations lying in quadrants $Q2$ and $Q4$. The general shape of the joint distribution is thus comparable to the near-wall distributions in the generic case of the horizontal plate (Fig. 5.10). The distribution of the *PALM* simulation at this wall-distance shows an elliptic shape aligned diagonally ($Q2$ and $Q4$) with its maximum lying in quadrant $Q4$. At larger wall-distances of $z \approx 12.5$ m, a major fraction of the JPDF maxima for the wind-tunnel measurements and the *PALM* run indicate fluctuations coming most likely from ejection events away from the wall and second from wallward sweeps. The spread of fluctuations along the w'-axis is wider for the *PALM* results in comparison with the wind-tunnel results. This finding is again in agreement with the variance profiles in Figs. 5.7 and 5.8.

While the maximum of the JPDFs lies in the second quadrant for all wind-tunnel measurements shown, the maximum of the *PALM*-JPDFs is located in the fourth quadrant for the two positions closer to the wall. It then also wanders to the second quadrant at

$\Delta y \approx 12.5$ m. This observation supports the earlier interpretation that the lower wind speed modeled in *PALM* in the near-wall region downwind the reattachment point might be due to a stretched recirculation zone. Reattachment and alignment of the streamlines with the building facade thus would happen slightly further downstream than in the wind tunnel. At larger wall-distances as for the example of $\Delta y = 12.5$ m, wallward motions do not dominate turbulence anymore, but sweeps are still more frequent than in the wind-tunnel measurements (Figs. 5.12a and 5.12b). This notion is also partly supported by the vector plot including all *PALM*-runs done for the 0° wind direction (Fig. D.5).

The contour lines of the JPDFs from *PALM* results are not as smooth as the ones of the wind-tunnel results. This is an observation already made by Hertwig et al. (2017b), who also compared wind tunnel to LES results for urban flows. The explanation given by them is related to the sharp truncation of directly resolvable eddies and thus a lower sampling range for turbulent fluctuations. In their comparison, the difference was pronounced stronger because the filter size used was 2.5 m and not 1 m as applied in this model configuration.

Wall-normal quadrant contributions for the comparison position SB_SI_back are shown in Fig. 5.13a - 5.13c for the three building facade configurations and in Fig. 5.13d the *PALM* run. For all profiles it can be said that values are largest close to the wall, then nearly vanish within the shear region and further away from the wall grow again at a smaller rate. Ejections and sweeps are the main drivers of turbulent motion and contribute stronger to the total turbulent flux. This finding is also in agreement with the results from the generic horizontal case. The beginning of the shear region can be identified in the wind-tunnel profiles as a local maximum in all quadrant contribution profiles at $\Delta y = 20$ m. This region is characterised by strong velocity gradients and strongly increasing turbulent fluxes (Figs. 5.5b and 5.6b). The local maximum is notably pronounced for the $Q4$-contributions that point in particular to sweep events. In particular, this can be interpreted as turbulent motion attracted to the wall by the strong velocity gradient.

At the first glance it is apparent that, for all facade roughnesses investigated in the wind tunnel, quadrant contributions start to diverge at wall-distances $\Delta y \leq 5$ m. Turbulent fluxes featuring the quadrants $Q2$ and $Q4$ diverge from each other further away from the wall at $\Delta y \approx 8$ m. Most turbulent motions in the near-wall region are due to ejections and inward motions (higher values of $\overline{u'u'}_{q2}$ and $\overline{u'u'}_{q3}$). Such near-wall divergences in turbulence contributions are found for all three facades in the wind tunnel, but there are differences in the characteristics of these deviations. While the contributions of quadrants $Q2$ and $Q3$ grow nearly up to the closest profile points measured for the flat

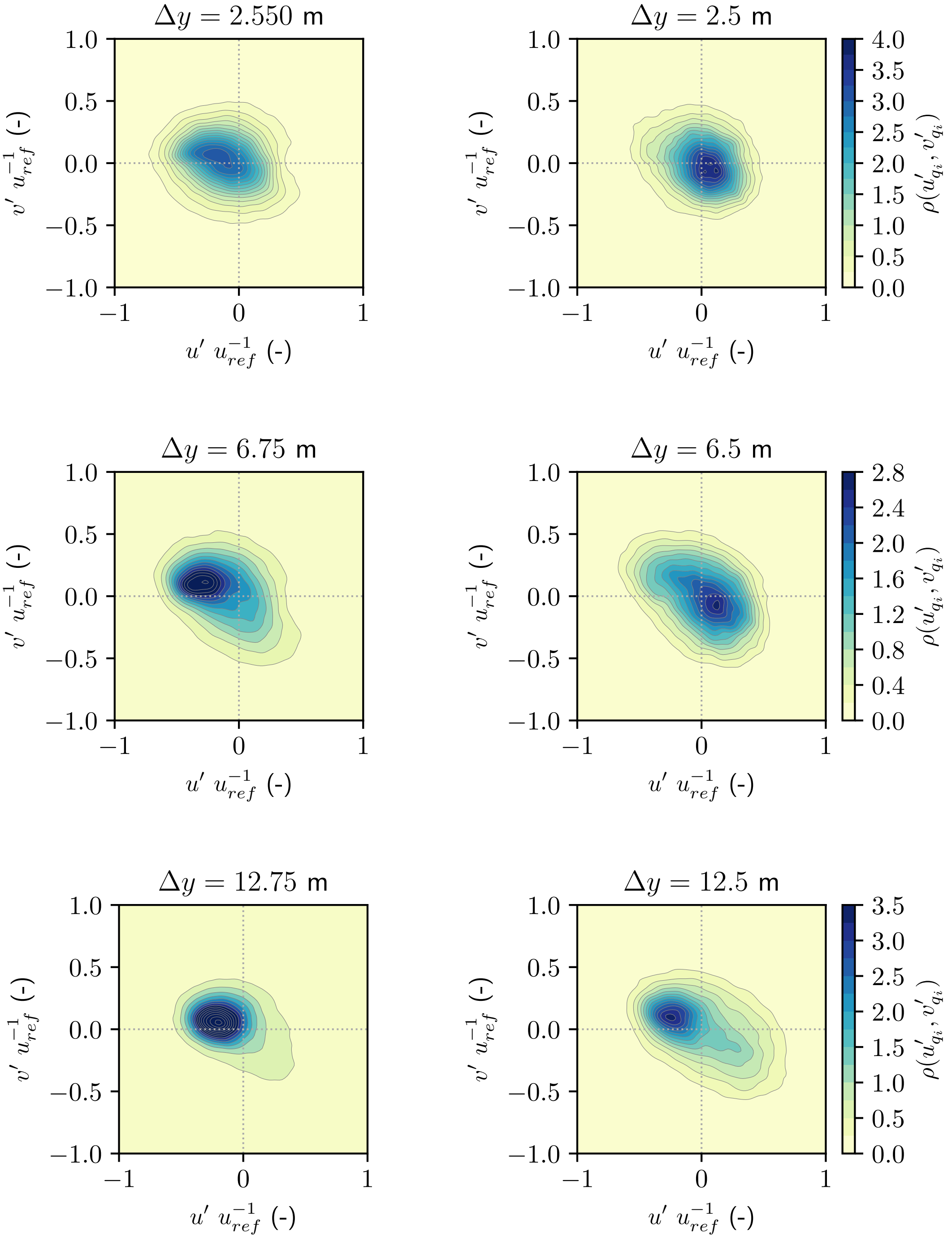

(a) **(b)**

Figure 5.12: JPDFs for the single-building case at different wall-distances for the SB_SI_back profile. The left column (a) shows the results for the wind-tunnel measurements with the flat facade building. The right column shows results for the corresponding *PALM* run.

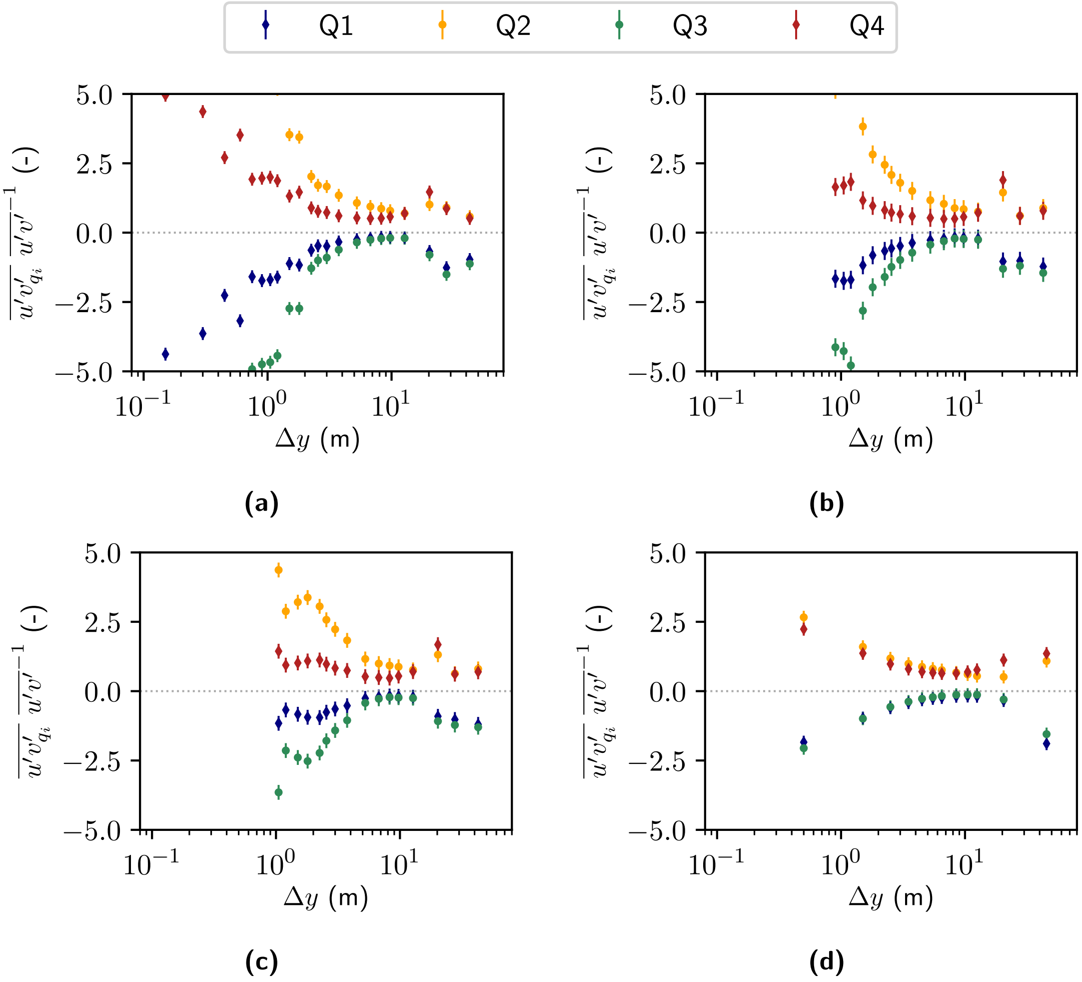

Figure 5.13: Quadrant contribution profiles for the single-building case at the profile position behind the reattachment point (SB_SI_back). Shown are results for all four single-building facades: (a) flat FL (b) medium rough WB and (c) rough (BR). The lower right panel (d) shows the results for the corresponding *PALM* simulation.

and medium rough facade, the quadrant contributions for the rough facade converge again from a wall-distance of $\Delta y = 2$ m on. So far, it is difficult to say whether the anisotropy, visible in the quadrant contributions, has its cause in the strong velocity gradients or in differences of facade roughnesses.

Looking at the quadrant contribution profiles for the other three comparison positions (Figs. D.12 - D.14) as well, site-specific and facade-specific differences are evident and each could be discussed in detail. However, the focus of the analysis is not aimed at these differences in detail, but is of a more general nature. The extent to which PALM can replicate the near-wall anisotropy of the flow shall be assessed. Quadrant contribution profiles of the *PALM* flow in Fig. 5.13d also show an increase of all contributions close to the wall and further away from the wall with lower values in between. The observed divergence of quadrant contributions in the wind-tunnel measurements is not visible in any of the *PALM* comparison positions (see Figs. D.12 - D.14). Thus, the absence of near-wall anisotropy is independent of the local flow conditions.

The missing anisotropy in near-wall turbulence modeled by *PALM* can have several reasons. First of all, the mixing length in the implementation of the D80 model is nearly constant and usually equals the grid size $\Delta_i = 1$ m. For a uniform grid, only at wall-distances where $1.8\Delta y \leq \Delta_i$, the mixing length is set to $1.8\Delta y$. This is only the case for wall-attached grid cells where the mixing length then reduces from 1m to 0.9 m. Under these circumstances, the SGS model is unlikely to respond adequately to restricted length scales due to adjacent surfaces. Second, contemporary SGS models like the D80 model are not only based on the turbulent-viscosity hypothesis, but also on the local isotropy hypothesis. Here, Kolmogorov (1941, 1991) states that small-scale turbulent motions are statistically isotropic if they are not close to the flow's boundary. But what does close to the boundary mean? The local isotropy hypothesis is based on the idea that the directional features of turbulent motions are lost as soon as the energy is transferred to smaller scales. Thus, at all scales smaller than the integral length scale, turbulence should become increasingly isotropic. This is not the case if sub-grid scale roughness elements are present which force eddies into directed motions as e.g. sweeps or ejections. Another cause for the lack of near-wall flow anisotropy could simply be the filtering LES approach itself. If the majority of fluctuations contributing to the anisotropy of turbulent fluxes is in the order of the grid size, turbulent motions cannot be resolved sufficiently.

After the detailed investigation of turbulent fluctuations, the energy density spectra are to be inspected. The aim is to understand if the energy cascade is affected by small-scale roughness elements of size h_r and to see how much of the small-scales' energy is actually resolved in *PALM*.

Spectral Analysis

After investigating the resolution of near-wall anisotropy by means of the quadrant analysis, facade roughness dependent deviations in the inertial subrange scaling are analysed. As stated above, if near-wall effects influence the energy scaling behaviour within the inertial subrange depending on the surface roughness, the flow would not be of universal character any more. Thus, the local isotropy hypothesis by Kolmogorov (1941, 1991) could no longer be assumed to be valid. Accordingly, the analysis of near-wall energy density spectra can support interpretations of near-wall anisotropy made above and, in particular, provides added value with respect to the missing near-wall anisotropy in *PALM*. In this section, only spectra for the single-building cases with varying facade roughness are presented.

Figure 5.14 shows co-spectra at four different wall-distances taken from the comparison profile downwind the reattachment point (SB_SI_back) at an approach-flow wind direction of $0°$. Each plot contains the co-spectra calculated from *PALM* time series and from wind-tunnel measurements for each facade roughness (flat FL, medium rough WB and rough BR). The K41 scaling of $-2/3$ is drawn as a black dashed line for orientation. The wall-distances shown are chosen such that two co-spectra represent the local RSL flow. Here, the influence of small-scale roughness elements is still visible ($\Delta y = 1.5$ m and 2.5 m). The other two co-spectra are calculated from measurements outside the local RSL. The position at $\Delta y = 6.5$ m lies at the border of the shear region caused by length-scales H_u and the region where small-scale roughness elements of size h_r cause near-wall deviations in turbulence statistics. The position at $\Delta y = 12.5$ m is located well within the shear zone at the wall-distance for which second-order statistics are at a maximum. Sampling rates for the used wind-tunnel measurements vary between 500 Hz at local mean wind speeds of $\overline{u} = 1.3$ m/s for the near-wall time series and 1800 Hz at local mean wind speeds of $\overline{u} = 2.9$ m/s for the comparison location furthest away from the wall. The sampling rates are thus kept on a reasonably high level. All co-spectra were computed over the whole range of the captured time series (7.5 h in full scale). Thus, at very low frequencies, the scatter of calculated energy densities is larger, since less events could be evaluated. Since the focus of this analysis is on near-wall deviations in the small-scales, this scatter is tolerable. The wind-tunnel co-spectra all show slight aliasing effects at highest frequencies. Frequencies affected by aliasing are plotted in brighter colors. Aliasing also happens for the *PALM* co-spectra, but only at energies lying outside the range of the shown values.

For all spectra shown, the *PALM* co-spectra agree well with the wind-tunnel results for the large energy-containing scales. These are the scales at lower frequencies left of the maximum of the co-spectra which corresponds to the integral length scale. The integral length scales in *PALM* are situated at slightly higher normalised frequencies, i.e. the maximum of the co-spectra is further to the right, than in the wind tunnel. This can be due to different normalising velocities $\overline{u}_h$. On the other hand, the large eddies in *PALM* and in the wind tunnel occur at the same frequencies. Accordingly, a certain relative overshoot in *PALM* is plausible. It is not only due to the normalisation of the frequencies. The largest eddies in *PALM* are not only occuring at higher frequencies than in the wind tunnel, but also show higher energy contents than the wind-tunnel equivalents. The effective resolution in the LES results becomes apparent shortly thereafter and the inertial subrange is only half replicated in terms of energy content. Then the energy density in

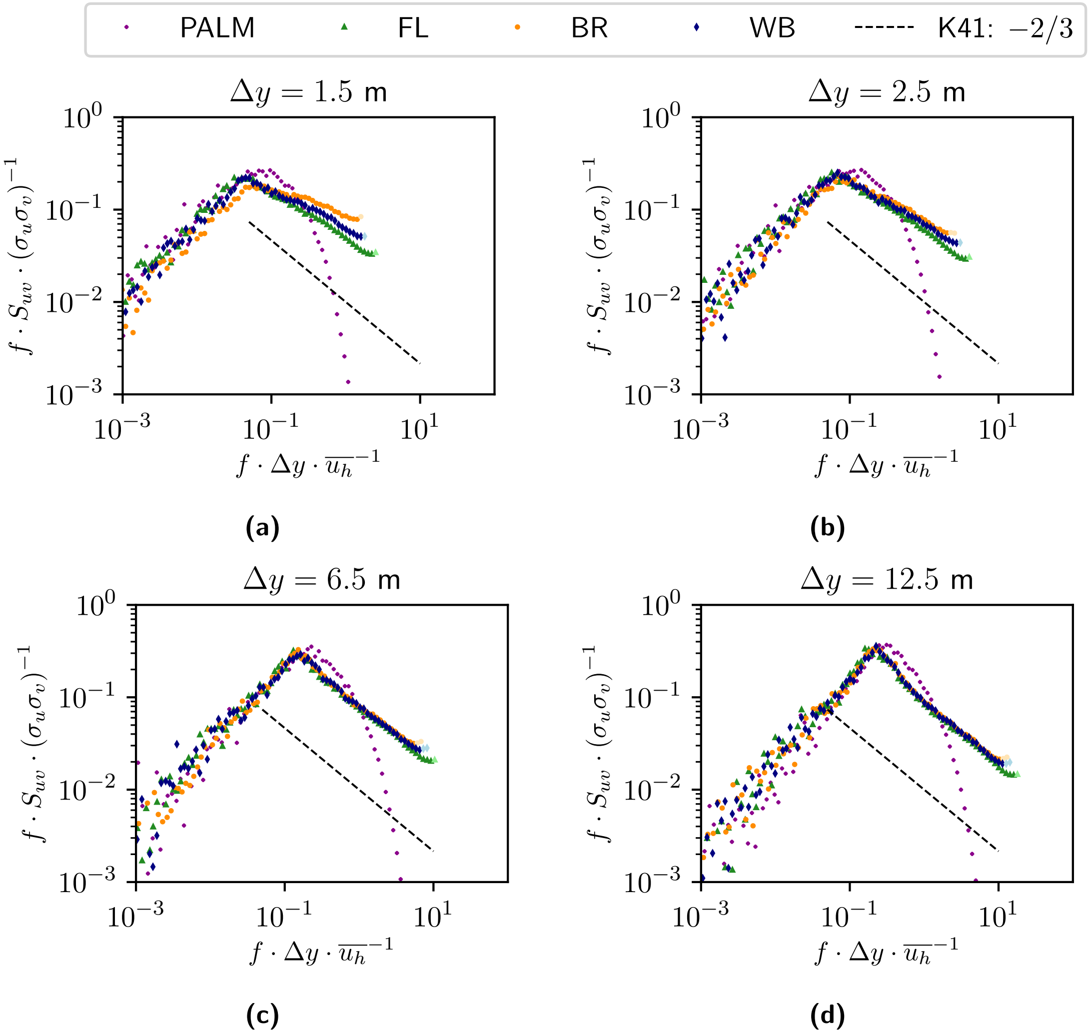

Figure 5.14: Energy density co-spectra taken at four wall-distances from the SB_SI_back comparison position. The black dashed line shows the expected K41 scaling.

the co-spectra drops sharply which is due to the explicit resolution of the LES model. The overshooting energy content in the scales slightly smaller than the integral length scale might be caused by the LES model compensating the missing resolved energy at even higher frequencies. The energy produced at larger scales is not sufficiently transferred to smaller scales, because of the implicit filtering by the grid. As the used D80-model underestimates turbulence (see e.g. Figs. 5.2a and 5.3a), there occurs an energy gap. Under this assumption, the energy transfer from the resolved scales to the sub-grid scales would not be effective enough.

Looking at the evolution of the energy content of the high-frequency vortices in the wind-tunnel measurements at different facades, the scaling differences in the inertial subrange are immediately noticeable. These differences occur at reduced frequencies between 10^-1 and 10^1 for the co-spectra at wall-distances of 1.5 m and 2.5 m (Figs. 5.14a and 5.14b). At scales which cannot be resolved directly in *PALM*, the small-scale energy content for the rough facade (BR) is sufficiently higher than for the flat facade (FL) with the medium rough facade (WB) lying in between. The diverging energy contents within the inertial subrange also lead to a roughness-dependent inertial subrange scaling which differs from the expected K41 scaling of $m(S_{u_i u_j}) = -2/3$. Most of the roughness dependent changes in spectral scaling happen at eddy sizes which were not explicitly resolved anymore by the used *PALM* setup.

At larger wall-distances (6.5 m and 12.5 m in Figs. 5.14c and 5.14d), the inertial subrange scaling is independent from the facade roughness. Here, co-spectra for all facade configurations agree well with each other throughout the whole range of scales. Also the inertial subrange scaling is mostly parallel to the K41 scaling. Both measurement locations lie within the region of highest wind shear. Nevertheless, the strong wind shear does not lead to an increased production of turbulent energy at these length scales. However, within the shear region, the integral length scales contain more energy than near the wall (maximum at ≈ 0.35).

This effect is also visible in the contour plots of the scaled energy density for all wall-distances which are shown in Fig. 5.15 for the two facade roughnesses FL and BR investiaged in the wind tunnel (yellow regions in contour plots). In this representation, the energy content can be compared for all wall spacings at each eddy size. Highest

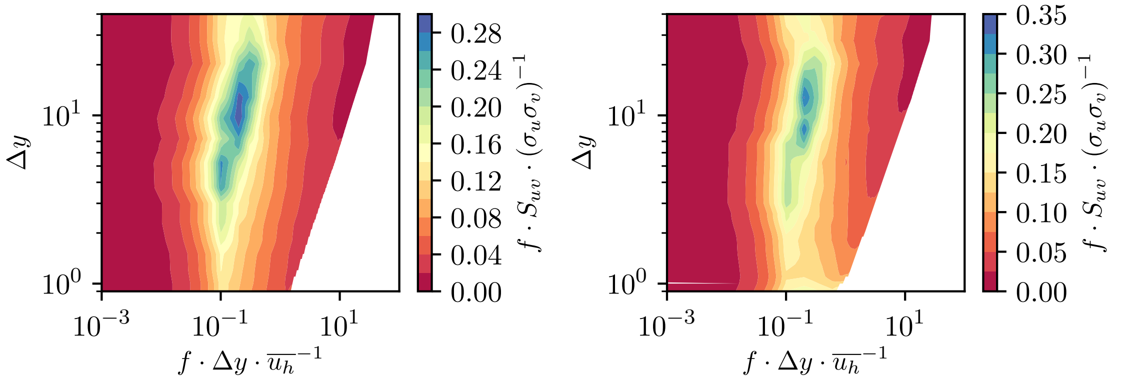

(a) **(b)**

Figure 5.15: Contour plots for the energy density co-spectra taken from the SB_SI_back profile position at all wall-distances (y-axis). Shown are the co-spectra for (a) the flat facade FL (b) the rough facade BR. The contour plot for the medium rough facade is shown in Fig. D.15. Contours are interpolated linearly with a spatial sampling density of (a) 22 and (b) 16 measurements along Δy (see also any of the wall-normal profiles above).

energy densities are detected within the shear region. The highest production rates of turbulence kinetic energy are thus associated with the region of highest velocity gradients and depend on the global mean approach wind and the building length scale H_u. When comparing the near-wall energy content for the flat and rough facades, the changed scaling due to the different facade roughness can be observed here too.

Figure 5.16 shows the linearly fitted inertial subrange scalings $m(S_{uv})$ as a function of wall-distance Δy. The values show the scalings for the comparison position SB_SI_back downwind the reattachment point and correspond to the co-spectra shown in Fig. 5.14 to 5.15 and Fig. D.15. For wall-distances larger than 10 m, the spectral scaling is in agreement with the K41 scaling (black dashed line). Closer to the building surface at 5 m $> \Delta y > 10$ m, the scaling $m(S_{uv})$ decreases for all facade configurations to a value of ≈ -0.6 which suggests an increased energy content in the inertial subrange. This change is most likely related to the wind shear as it occurs at the corresponding wall-distances and is independent of the facade roughness. Even closer to the building at $\Delta y < 5$ m, differences in facade roughness configurations are evident. While the scaling for the flat facade (FL) stays at values of ≈ -0.6, scalings for the medium rough (WB) and rough facade (BR) further decrease to values even smaller than -0.4.

So far, the interpretation of the data indicates several possible explanations for the deviations in near-wall inertial subrange scaling. Since there are no small-scale roughness elements of size h_r at the flat facade (FL), changes in inertial subrange scaling can be associated exclusively with the flow around the building and the velocity gradients generated here. This in turn means, that the energy input in the inertial subrange for

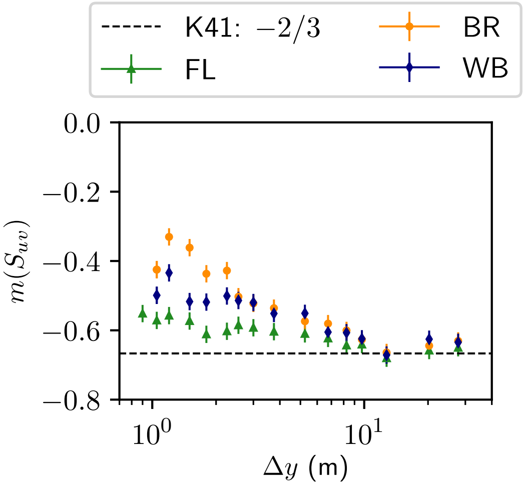

Figure 5.16: Profile of the inertial subrange scaling for all wind-tunnel measurements from the SB_SI_back profile position.

the rougher facades (WB and BR) must be due to the small-scale facade roughness elements. By interpreting the mean velocity profiles in Fig. 5.5b a second shear zone, i.e. an increased velocity gradient due to the differing facade roughnesses, is evident. The results of the quadrant analysis in Fig. 5.13 indicate higher contributions from outward ejections of turbulence kinetic energy and roughness-dependent differences in the anisotropy of turbulent motions. Whether it is the increased velocity gradient or the ejections of turbulence kinetic energy triggered by small-scale roughness elements which are interfering with the energy cascade in the near-wall region remains an open question. The presented findings support the notion that it is most likely both.

Preliminary Conclusions

The question to be answered in this section was whether statements can be made about the anisotropy of near-wall turbulence at horizontal rough surfaces and at single buildings with different facade roughness (RQ 3), and if so, which. The fact that the analysis focus was placed on the near-wall anisotropy of turbulent flows is mainly a consequence of the assumptions inherent in the turbulence parameterisation (D80 and G91 models). These SGS models tend to impose isotropic turbulence at the scales just larger than the grid size Δ_i. Another concern to pay attention to is the anisotropy on scales smaller than the effective grid size, which are not explicitly resolved in the LES model. In order to shed more light on these areas of the flow in particular, the wind-tunnel model configurations with different surface roughnesses were of great added value. Accordingly, it is of interest to understand how exactly near-wall anisotropy acts. Subsequently, it should be thought about how future SGS models might account for these effects.

The results of the quadrant analysis and the co-spectra allow the following conclusions about near-wall turbulence anisotropy to be made. Wind-tunnel quadrant-analysis results show spatially directed contributions in near-wall turbulent fluxes. This spatial alignment of the eddies is not resolved in the *PALM* results at any of the comparison positions. Further, the inertial subrange scalings of the wind-tunnel energy density spectra show near-wall surface roughness dependencies. Rough surfaces result in higher energy contents at the high frequency end than flat surfaces. These near-wall differences are no longer resolved in *PALM* due to the implicit filter width, i.e. the grid size.

5.2 Practical Implications for Near-Wall Analyses in Urban Climate Studies

The learnings from Sec. 5.1 can be converged into a few simple guidelines to follow when performing and interpreting large-eddy simulations in obstacle-resolved urban-climate

LES studies with a scope on near-wall flows. These guidelines are rather conservative and are based on considerations and data-based findings from this work. Furthermore, no claim to completeness should be made here, as urban climate simulations are a very complex matter. The model configurations studied in this thesis did not take into account thermal radiation, humidity, or even external forcing with data from weather models. Additionally more urban-like obstacle arrangements must be studied to see if the single-building case is sufficiently representative.

Grid Size Requirements

Even before the results from the two experiments were presented, it was possible to make initial conceptual considerations about grid sizes and the interpretation of LES results close to surfaces. In order to model near-wall flows within the UCL by means of LES, both the global flow phenomena (atmospheric conditions, wakes behind buildings, channelling effects in street canyons, etc.) and the local flow phenomena (wall-bounded flows at building facades or on the ground, turbulent transport of momentum, temperature or other scalars) must be sufficiently resolved. In Sec. 2.3.5, resolution requirements on these two scales (global and local) were considered.

According to Baggett et al. (1997), the grid size in LES must not exceed one tenth of the integral length scale in order to sufficiently resolve a flow. In the UCL, integral length scales are mainly determined by the building scale H_u and a requirement for the maximum grid size would thus be approximately $\Delta_i \leq 0.1 H_u$. A limit for the minimum applicable grid size was formulated by Basu and Lacser (2017). Based on estimations on roughness sublayer heights by Raupach et al. (1980) and the validity of the logarithmic law of the wall, it was concluded that the grid size must not exceed $\Delta_i > 50 z_0 \approx 5 h_r$ to allow the common surface boundary conditions to be applied. These two requirements are often mutually exclusive as illustrated in Fig. 2.7. The grid requirement for the maximum grid size is a *necessity* for urban climate LES studies to operate correctly. The limit for the minimum applicable grid size affects approximately the first 7 grid cells from the wall (Maronga et al., 2020b) and can thus be understood as a *sufficiency* if global UCL phenomena are studied and becomes a *necessity* as soon as near-wall flow phenomena are the scope of the study.

It is a common practice to artificially reduce the roughness length on urban surfaces such that the local grid requirements formulated by Basu and Lacser (2017) are met. This can lead to an overestimation of mean wind speeds and an underestimation of turbulence. Hence, modellers are adviced not to think of the roughness length as just another parameter that can be changed without consequence. It is a physical property of the flow along a surface. Another solution would be to further reduce the grid size and thus directly resolve urban morphologies such that more small-scale flow features can be resolved explicitly. This requires city models at even higher resolutions as input data. Whether such data sets are useful at all is questionable, since cities change on such length scales every day (parked cars, construction sites, weekly markets).

Grid refinement and nesting approaches are already in use at many contemporary LES studies. These approaches can significantly improve model results, but often only shift the near-wall problems to smaller scales. Grid refinement in the wall-normal direction is often considered and can improve near-wall turbulent transport of e.g. scalars sufficiently. Nevertheless, non-uniform grids can lead to unusual high anisotropy in the velocity gradients if the aspect ratio of a grid cell exceeds a certain value, which depends on the order of the discretisation. That is why this strategy should not be over-exploited.

In contemporary LES urban climate studies, the user has no choice but to deal with near-wall uncertainties and incorporate them into the interpretation. For this, the modeller's awareness of these uncertainties is a prerequisite. If it comes to pedestrian wind comfort or human exposure to air pollutants, usually LES results need to be interpreted in the first one to three grid cells. The wind-tunnel results for the flow on horizontal and vertical surfaces of varying roughness can provide a contribution here (see Sec. 5.1).

Roughness Sublayer Thickness

The limitation formulated by Basu and Lacser (2017) is based on estimates for the RSL thickness made on the basis of experiments over generic horizontal roughnesses (Raupach et al., 1991). But how thick is the RSL in UCL flows where complex topographies are present? This depends on the local flow situation and the surface roughness. Based on the wind-tunnel measurements presented in Sec. 5.1.1, an overview of the RSL thicknesses around the model building is given in Fig. 5.17. For this purpose, the mean RSL thicknesses determined for the respective comparison sites were estimated. In addition, the maximum values of the observed RSL thicknesses are also taken into account.

Even though the approach is not particularly scientific, a few general statements can be made this way. First, the maximum roughness sublayer thickness for each comparison position was observed in the second order statistics and the lowest values were obtained for the mean flow. Thus the variances and turbulent fluxes are disturbed more than the mean flow by the surface roughness. Second, the RSL thickness is significantly higher for the sideway flow at an approach wind direction of 0° (Fig. 5.17a) compared to the flow upwind or leewards the building (Fig. 5.17b). Also RSL dynamics could be observed for a majority of the evaluated statistics at the sideways comparison positions SB_SI_front

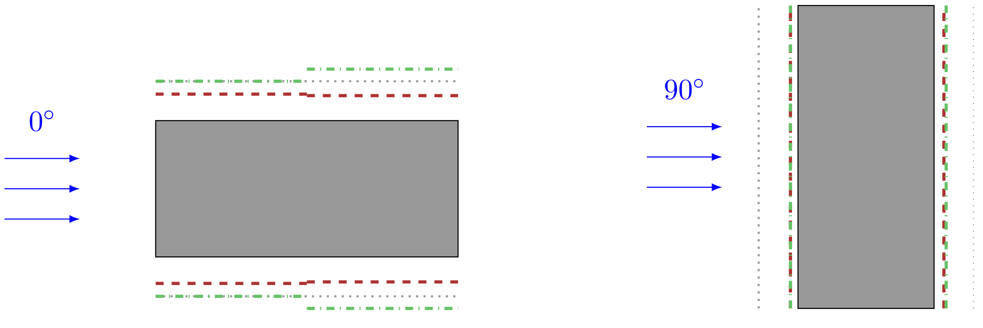

(a) **(b)**

Figure 5.17: Shown are a topviews onto the single buildings for the comparison positions at (a) 0° approach wind direction and (b) 90° approach wind direction. The colored lines show the observed mean (red) and maximum (green) roughness sublayer thicknesses. The dotted gray line marks a wall-distance of 10 m.

and SB_SI_back. Upwind and leewards the building, a roughness sublayer often cannot even be observed by evaluating most of the flow statistics. Since there are changing wind directions in cities and there are also inevitably always locations with lateral inflow and also locations leeward of buildings, it is not an option for modelers to configure the model accordingly (location-dependent grid adjustments). Windward and leeward of the building, the variability of the flow is not strongly dependent on the building surface. However, it can at least be pointed out that there is an increased flow variability at facades parallel to the main wind direction. This variability is usually not resolved in LES models and results at such locations should be interpreted with caveats.

Choice of the Sub-Grid Scale Model

Using the model configuration of the horizontal surface with homogeneous roughness, it was possible to compare the two SGS models implemented in *PALM* (D80 and G91), considering the corresponding wind-tunnel measurements. The advantages of dynamic turbulence closures as the G91 model were already discussed in Sec. 5.1 in terms of the replication of flow statistics and flow anisotropy. Especially the so far underestimated wall-normal turbulence intensity and the wall-normal turbulent fluxes $\overline{u'w'}$, crucial also for boundary conditions in LES, could be improved and agreed better with the wind-tunnel reference.

Dynamic turbulence models can furthermore also provide advantages in terms of computing time. To illustrate this, the wall-normal turbulence intensities at different grid sizes for the two used SGS models (D80 and G91) are compared (Fig. 5.18). Looking only at the results for the D80 model, the turbulence intensity levels simulated by *PALM* can be significantly increased by increasing the grid resolution. Using the G91 model instead of the D80 model nearly provides the same improvement in wall-normal turbulence as doubling the grid resolution. Thus, modelers should always consider using alternative SGS models instead of further increasing the resolution. That for, the *PALM* model still requires robust implementations of SGS models other than the standard D80 model by Deardorff (1980).

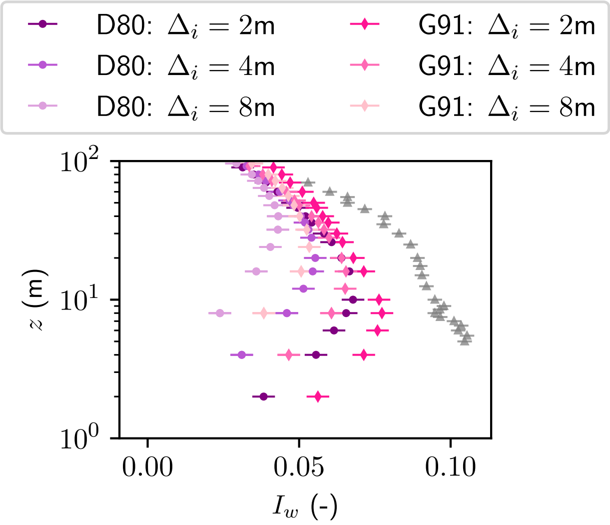

Figure 5.18: Grid convergence of the wall-normal turbulence intensity in the modeled approach boundary-layer flow at a scale of $1{:}100$. Shown are *PALM* results for the two SGS models at three different grid sizes. The gray triangles are measurements from the wind-tunnel reference profile.

6 Summary & Conclusions

6.1 Convergence

The motivation for undertaking this work was rooted in the recognition that as computing capabilities and model resolution improve, the outcomes of large-eddy simulations are being more frequently analyzed in proximity to the wall. Nowadays, there is a change in the scope of urban climate LES studies away from the neighborhood scale (several 100 m) towards the human scale (up to 2 m above ground), which is mainly due to reachable model resolutions of sometimes even less than one metre. It is generally a good sign that technological advances have the potential to accelerate scientific and societal progress. However, as the advantages of more efficient technologies come in handy, a demanding public interest and excessive belief in technology might lead model users to neglect reviewing the methods and concepts at play. This thesis was intended to make a contribution at precisely this point when it comes to large-eddy simulations in obstacle-resolving urban climate studies. Therefore, the near-wall flow at rough surfaces in two model configurations was studied by means of wind-tunnel modelling and then compared to results from the LES model *PALM*.

LESs were initially developed for meteorological applications and are based on assumptions that cannot hold up in complex urban environments especially in the vicinity of surfaces (facades and ground). Surface boundary conditions in most contemporary LES models are based on MOST, which itself is a highly idealised boundary layer theory. Sections 2.3.3 and 2.3.5 outlined why contemporary surface boundary conditions are often not suited for heterogeneous surfaces of constantly changing aerodynamic roughness such as building facades. Another integral part of LESs are the SGS parameterisations. The parameterisation of small-scale turbulence should replicate any anisotropies that occur close to surfaces or in complex flow situations as wakes behind buildings. The most widely used SGS model is the Smagorinsky model as implemented by Deardorff (1980) (D80). Here, it is assumed that SGS fluxes are isotropic, universal and scale-invariant; heuristic prerequisites often not fulfilled in the UCL. Germano et al. (1991) introduced a scale-dependent model (G91) which can show its advantages especially close to the wall, where the grid size approximately equals the local integral length scales. The G91 model is expected to perform better in the vicinity of walls than the D80 model. Thus, a comparison of the two SGS models was of particular interest.

The research questions were posed to gain a deeper understanding of near-wall flows and to evaluate the ability of the LES model *PALM* to function near rough surfaces:

RQ 1 Can a roughness sublayer be identified in generic cases of flow above aerodynamically rough surfaces and for more complex model geometries?
RQ 2 How are local roughness sublayer dynamics at urban building facades characterised?
RQ 3 What statements can be made about the local anisotropy of turbulence close to such surfaces?
RQ 4 Are local near-wall flows properly replicated in a contemporary LES model as *PALM*?

6.2 Contributions

To answer the research questions, two model configurations were designed. Both model configurations were studied using the wind tunnel *WOTAN* and the large-eddy simulation model *PALM*.

The first model configuration was designed to study the flow over a horizontal plate of homogeneous roughness for three different roughnesses. The roughness change was achieved by placing thin, L-shaped roughness elements of height h_r on the wind-tunnel floor with different spacings of the elements for each surface roughness. The shape and thickness of the elements was chosen such that it could not be resolved explicitly by the used *PALM* model set up. In this way, a comparison could be made between an actual rough surface in the wind tunnel and the parameterisation of the roughness in the LES model.

The second model configuration was designed to study the flow around single buildings with different surface roughness elements attached to the facades. The building model is composed of geometrical shapes at two length scales, namely the building scale H_u and the smaller roughness scale h_r. Again, the *PALM* model was configured such that the small roughness scale h_r was not resolved explicitly. LES and wind-tunnel results were compared at four wall-normal comparison profiles: an upwind profile, a leeward profile and two profiles at the side of the model building.

Data from both model configurations were processed to answer the research questions recapitulated above. First, a comparison of wall-normal profiles of statistical moments was performed for both experiments. On the basis of these, the roughness sublayer was identified, and its thickness was estimated. Furthermore, the local dynamics above ground were investigated, and an estimation of the dynamics that are not explicitly replicated by the *PALM* could be done. Second, a quadrant analysis and the investigation of turbulent spectra were carried out to understand the near-wall flow anisotropy and to test the extent to which PALM replicates it.

Based on the flow statistics, a roughness sublayer was identified at most of the profile positions. In general, flow variations in the roughness sublayer are visible in wall-normal profiles of all statistical moments (mean, (co)variance, skewness, kurtosis). For the horizontal plate of homogeneous roughness, a roughness sublayer thickness of five times the roughness element height was identified ($\delta_{rsl} \approx 5h_r$). This value supports previous estimations for flows over horizontal surfaces by Raupach et al. (1991) who estimated roughness sublayer heights of $2h_r$ up to $5h_r$. For the more complex flow case of the single buildings with facades of different roughness, roughness sublayer dynamics were observed at all comparison positions. However, it was not straight-forward to determine a distinct roughness sublayer thickness as it depends strongly on the comparison position. For the sideways profiles with the building facade aligned with the main wind direction, the observed RSL was at times thicker than in the generic horizontal case (up to $\delta_{rsl} \approx 12h_r$). This is rather surprising since the internal local boundary layer at the facade did not develop over such long fetches. Besides, the roughness sublayer for the upwind and leewards building facades is nearly not observable at all. If so, its thickness was only $\approx 2h_r$. It can be concluded that there is high ambiguity in roughness sublayer thickness and dynamics depending on the specific flow situation at the surface that is studied. The findings from more practical and geometrically more complex cases presented in this thesis extends conceptual work done by Raupach et al. (1991) and Basu and Lacser (2017). Furthermore, proposals for the adapted evaluation of boundary conditions, as e.g. by Hultmark et al. (2013) and Maronga et al. (2020b), may improve the calculation of near-wall velocities for academic cases but prove to be insufficient within the UCL.

Comparing the two SGS model implementations (D80 and G91) with the obtained wind-tunnel data, the scale-dependent G91 model by Germano et al. (1991) outperformed the widely used D80 model by Deardorff (1980). In particular, the wall-normal fluctuations agree better with the wind-tunnel results in the G91 model. The wall-parallel fluctuations show no significant difference for both SGS models. Using the G91 model improves the model results almost as much as doubling the grid resolution. It would have been interesting to compare the two models for more complex flow cases as well. Unfortunately, the implementation of the G91 model in *PALM* did not turn out to be numerically stable once obstacles were placed in the flow.

Furthermore, it was shown that the near-wall turbulence in *PALM* is clearly more isotropic than in the real flow. Turbulent fluxes from the wind-tunnel results always show a preferential spatial orientation in the results of the quadrant analysis as soon as the flow is close to the wall. The exact orientation of small-scale eddies depends on the local flow situation. Eddies that contribute to the anisotropy near the wall are of the same size as the grid sizes typically used in LES or even smaller. It is quite possible that the scale independency of the SGS models, i.e. the heuristic determination of the mixing length, imposes an artificial isotropy on the flow. Inertial subrange scalings of the wind-tunnel co-spectra show differences in the near-wall region depending on the surface roughness. An increasing roughness results in higher energy contents in the smaller eddies. Such increased production of turbulent kinetic energy is not accounted for in LES, if the roughness scales h_r are not explicitly resolved. Accordingly, future sub-grid scale models must not only be scale-dependent near the wall; it is also necessary that the roughness-dependent enhanced turbulent production is taken into account by such models.

The near-wall uncertainty in *PALM* can be divided into three categories. First, there is the inherent uncertainty within the roughness sublayer which cannot be resolved explicitly due to sub-grid scale obstacles. Second, wall-normal fluctuations (variances or turbulence intensities) are systematically underestimated in PALM, which is due to both the insufficient roughness parameterisation in boundary conditions and the scale-invariant SGS models. Third, the SGS models (D80 and G91) do not include a surface roughness-dependent parameterisation of turbulence production and dissipation.

6.3 Outlook

In order to make large-eddy simulations robust for their future application within the urban canopy layer, research should be directed towards two components of such urban climate models in particular. These two components are the surface boundary conditions and the sub-grid scale models.

So far, there is no boundary layer theory that can calculate the flow at heterogeneous surfaces such as in cities. It is also very unlikely or even impossible to find adequate analytical solutions. The plethora of proposed boundary conditions only address academic cases and will merely lead to cosmetic improvements for complex flows as in the urban canopy layer (Hultmark et al., 2013; Maronga et al., 2020b). Future research should therefore pursue alternative approaches to predict flows at non-horizontal, heterogeneous and rough surfaces (e.g. statistical methods from machine learning).

The experiments conducted here show that current scale-invariant sub-grid scale models cannot properly replicate the anisotropic near-wall flow. There exist many scale-dependent turbulence closure models (Gadde et al., 2021), which are expected to model the heterogeneous urban canopy layer flows more precisely than the standard Smagorinsky models (Smagorinsky, 1963; Lilly, 1966; Deardorff, 1980). Such models should be used more in the future, especially if near-wall results are of concern. The scientific community needs further knowledge on near-wall flow anisotropy and small-scale energy budgets dependent on surface roughness.

Until substantial technical advances are made, modelers must incorporate near-wall uncertainties into the interpretation of urban climate studies that make use of large-eddy simulations. For this, the modelers' knowledge and awareness of these uncertainties is a prerequisite. Accordingly, many more micro-meteorological field studies are needed to estimate near-wall uncertainties with long-term data.

A Wind-Tunnel Specifications

In this appendix additional information on the boundary layer configuration and the model configurations of the wind tunnel experiments of the horizontal plate with homogeneous roughness and the single building experiment are shown.

A.1 Boundary Layer Configuration

Figures A.1 and A.2 show the configurations for the medium rough boundary layer, which was modeled in *WOTAN*. The spire configuration consist of seven spires in total which were spaced unevenly to achieve lateral homogeneity for the approach flow.

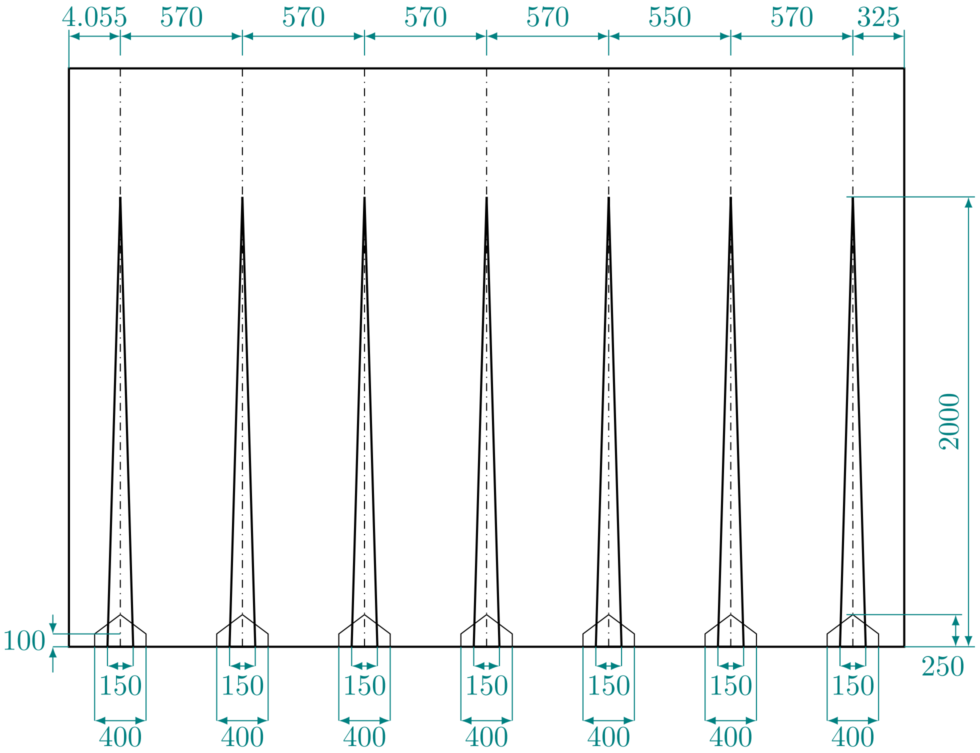

Figure A.1: Spire configuration used for a medium rough boundary layer in *WOTAN*. All lengths are given in milimeters.

The roughness element configuration shown in Fig. A.2 was also replicated in the *PALM* setup for the single building case which is described in Sec. 4.2.

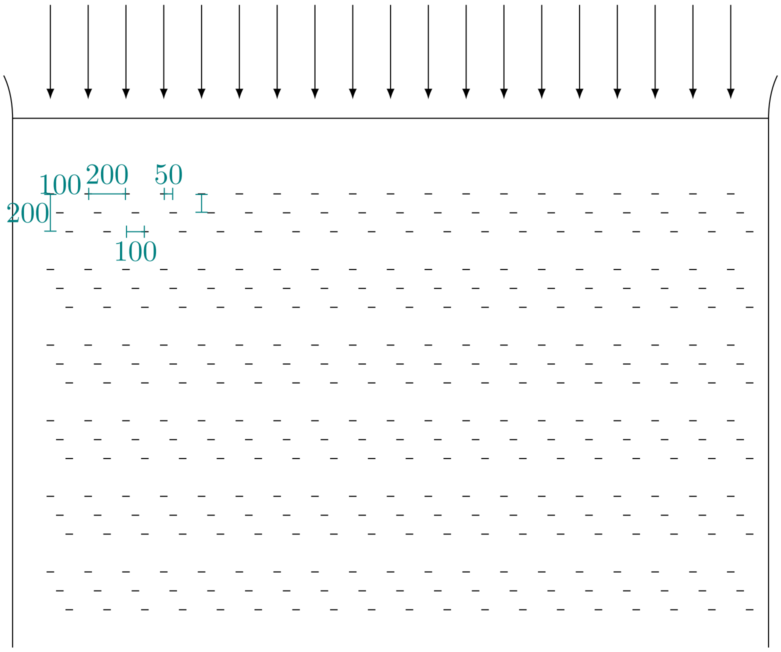

Figure A.2: Poisitioning of the roughness elements. The sketch shows only the first six rows of roughness-element clusters. The setup continues until the test section of the wind tunnel is reached. All length scales are given in milimeters.

A.2 Horizontal Plate Model Configuration

In this section, additional analyses are shown which ensure that the experiment is conducted properly. Figure A.3 shows the adjustment of flow quantities to the roughness change with increasing streak length (colorbar). The furthest measurement profile at a streak length of 147.5 m corresponds to the chosen comparison position. It can be seen that after a streak length of 72.5 m, the profile values do not change significantly any more. The flow dynamics in the near-wall region have thus adjusted themselves to the new surface roughness.

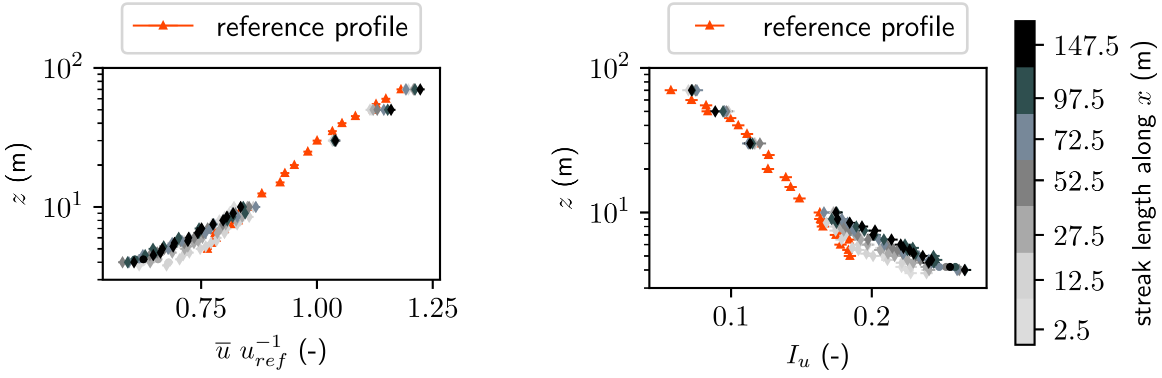

(a) **(b)**

Figure A.3: Vertical profiles of the mean velocity and the longitudinal turbulence intensity I_u at increasing streak lengths over the base plate. The example shows the flow of the rough facade.

A.3 Single Building Model Configurations

The model configurations of the single building model are described in detail in this section. The model configuration of the single building with a flat facade is shown in Fig. A.4. The building model with the medium rough facade (WB) is described in Fig. A.5 and in detail for the facade roughness in Fig. A.6. An overview of the single building model with the rough facade (BR) is given in Fig. A.7 with a closer view on the small scale facade roughness in Fig. A.8. The building length scales H_u, L_u and D_u are the same for all three model buildings.

Figure A.9 shows the results of the convergence tests at two distances from the building facade for the mean streamwise velocity. The convergence tests show no significant decrease of the data scatter for $T > 150$ s. The achieved scatter of minimum 0.022 for the near-wall measurement and 0.007 for the UCL flow was considered sufficiently accurate.

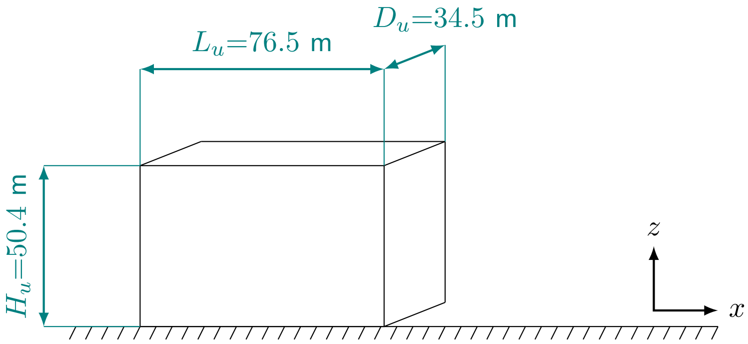

Figure A.4: Single building model with flat facade.

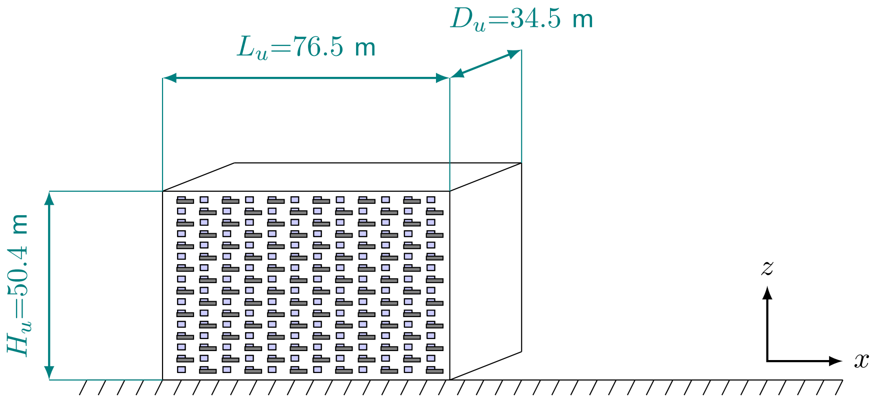

Figure A.5: Single building as a cuboid with facade including window savings and balconies. The balconies protrude from the facade by 0.9 m. The dimensions of the cuboid correspond to those in Figure A.4. Window frontages are present on the two long cuboid walls.

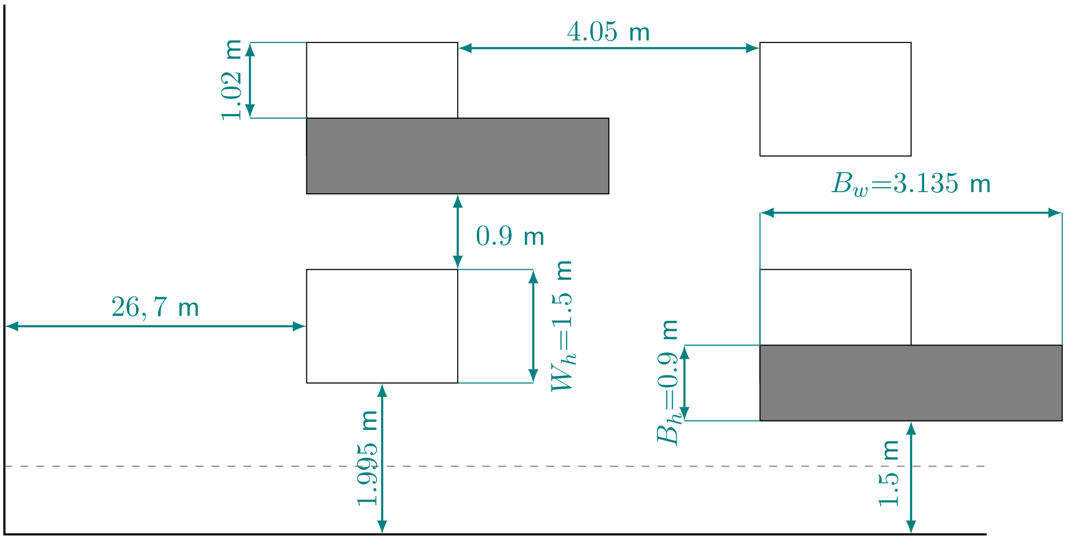

Figure A.6: Detail of the windows and two staggered cuboid balconies. This corresponds to the building from figure A.5. The window openings are 0.6 m deep. The balconies (dark grey) protrude from the facade by 0.9 m.

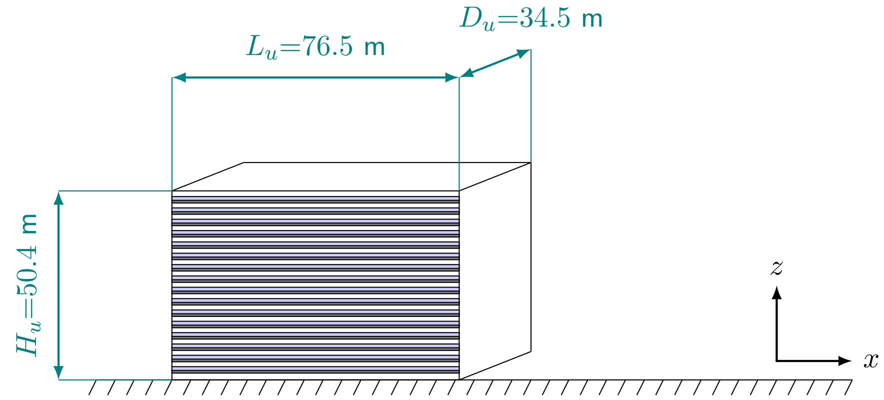

Figure A.7: Single building as a cuboid with facade including window openings and continuous balconies. The balconies protrude from the facade by 0.9 m. The dimensions of the cuboid correspond to those in Figure A.4. Window frontages and balconies are present on the two long edged walls.

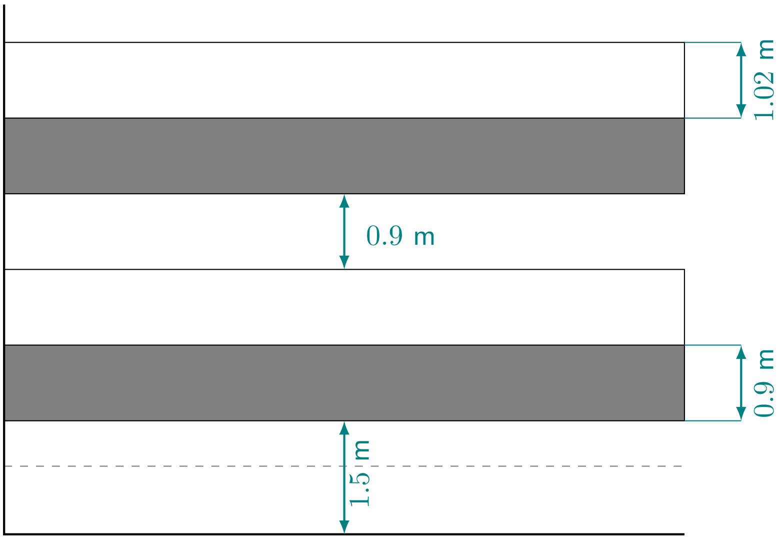

Figure A.8: Detail of the windows and two staggered cuboid balconies. This corresponds to the building from figure A.7. The window openings are 0.6 m deep. The balconies (dark grey) protrude from the facade by 0.9 m. All dimensions not given are the same as those in figure A.6.

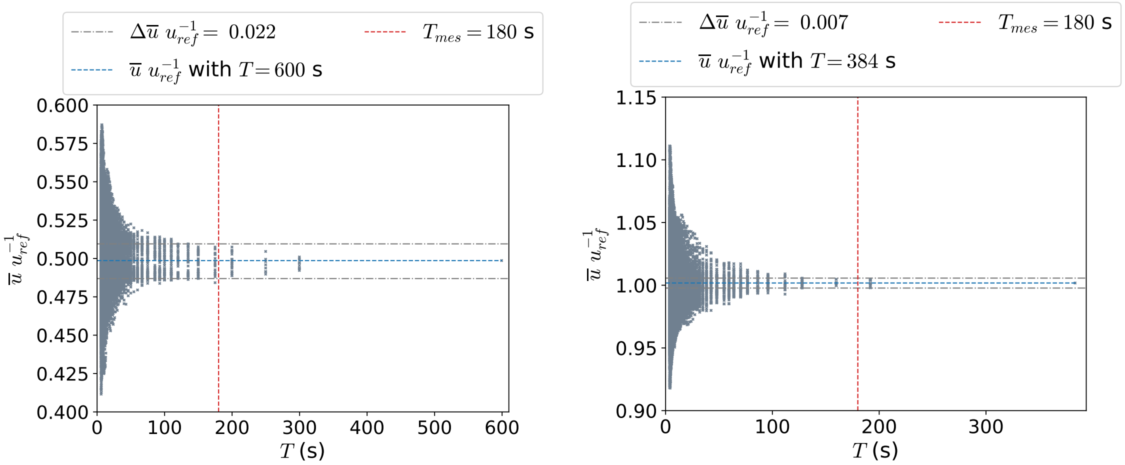

(a) **(b)**

Figure A.9: The convergence tests for the mean stream-wise velocity u at the two wall distances (a) $\Delta y = 3$ m and (b) $\Delta y = 35.25$ m. For the convergence test further away from the wall, the total measurement time was shorter than for the near-wall test.

B PALM and Levante Specifications

All model runs done in the course of this thesis were performed on the high performence computing system (HPC) *Levante* at the Deutsches Klimarechenzentrum (DKRZ) in Hamburg.[1] *Levante* is a *BullSequana XH2000* supercomputer by *Atos* which was installed at the DKRZ in early 2022. It consists of 2832 computing nodes. The CPUs used in this work, were 3rd generation *AMD EPYC* CPUs (Milan) with 256GB memory. Each CPU consists of 128 cores. Alltogether, *Levante*s CPU partition can reach a total performance of 14 PetaFLOPS.

B.1 Overview on PALM Runs

The following table shows an overview of all *PALM* runs carried out for the single building experiment. The runs from set # 1 mainly were performed for finding and validating the correct model setups. Sets # 2 and # 3 consist of the actual model runs which results were analised in Chapter 5.

Table B.1: Overview on *PALM* runs done in set # 1, # 2 and # 3.

Set	**Run name**	**Wind direction**	**Δ_i (m)**	**z_0 (m)**
# 1	SB_BL_1m	0°	1	0.084
# 1	SB_BL_2m	0°	2	0.084
# 1	SB_BL_4m	0°	4	0.084
# 1	SB_BL_1m_RE_z0x	0°	1	0.03, 0.04, 0.05, 0.06
# 1	SB_BL_1m_RE_z03_topo	0°	1	0.03
# 1	SB_BL_1m	0°	1	0.084
# 1	SB_SI_corr	0°	1	0.084
# 1	SB_SI_long	0°	1	0.084
# 2	SB_SI_BL	0°	1	0.03
# 2	SB_SI	0°	1	0.03
# 3	SB_LE	90°	1	0.03
# 3	SB_LU	90°	1	0.03

---

[1] https://docs.dkrz.de/doc/levante/

B.2 PALM Setup Validation

In this section, additional analyses are listed which mainly help validating the *PALM* run configurations used in this work.

The results of the convergence tests are shown in Figs. B.1 and B.2. For each flow quantity, the scatter for a signal duration of 7.5 h was calculated. This data scatter was then assumed as the uncertainty of the corresponding flow quantity.

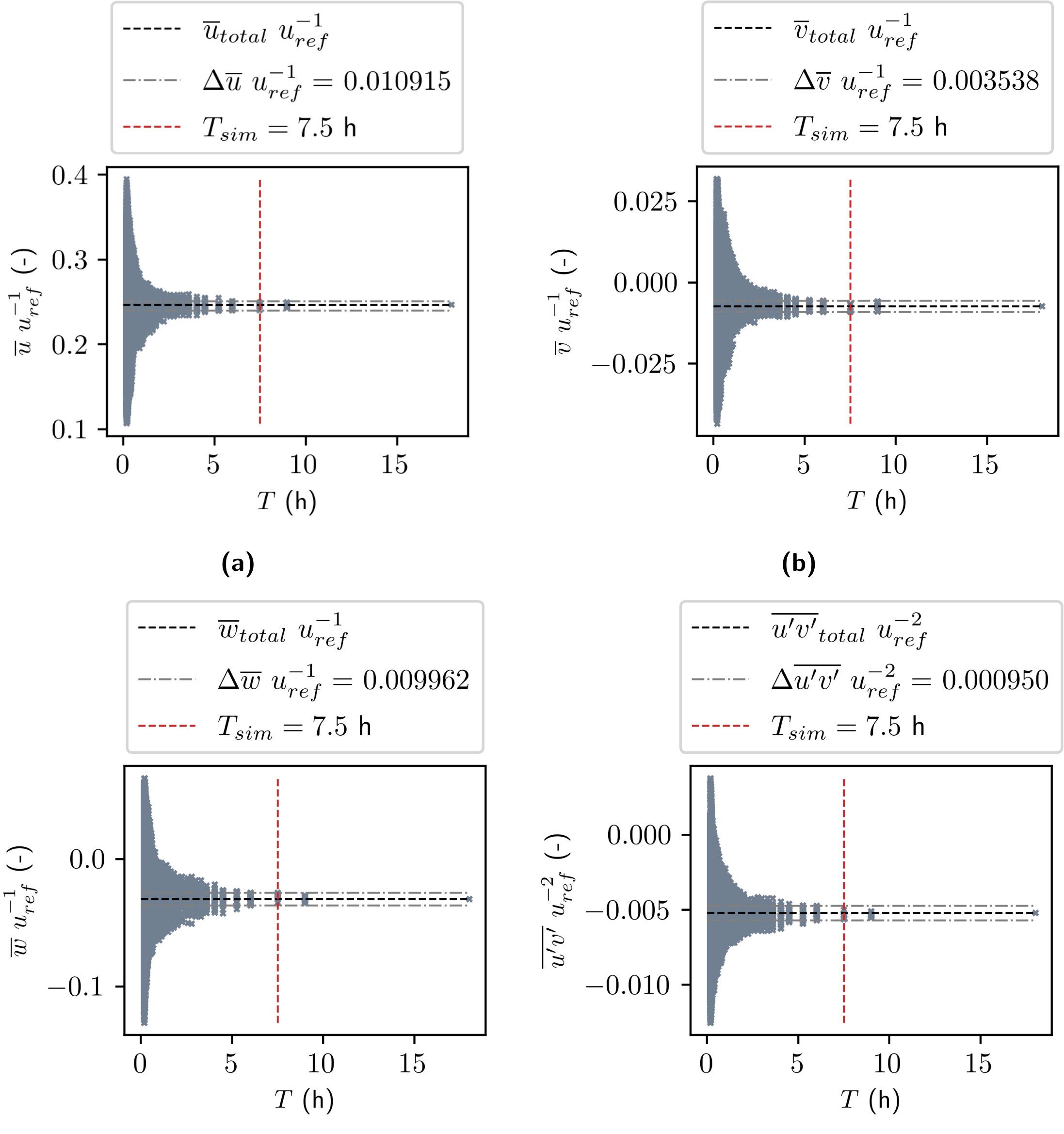

(a) (b)

(c) (d)

Figure B.1: Convergence test for the mean velocities and the co-variances of the *PALM*-simulations. Time series were output for a wall-distance of 4 m in full scale.

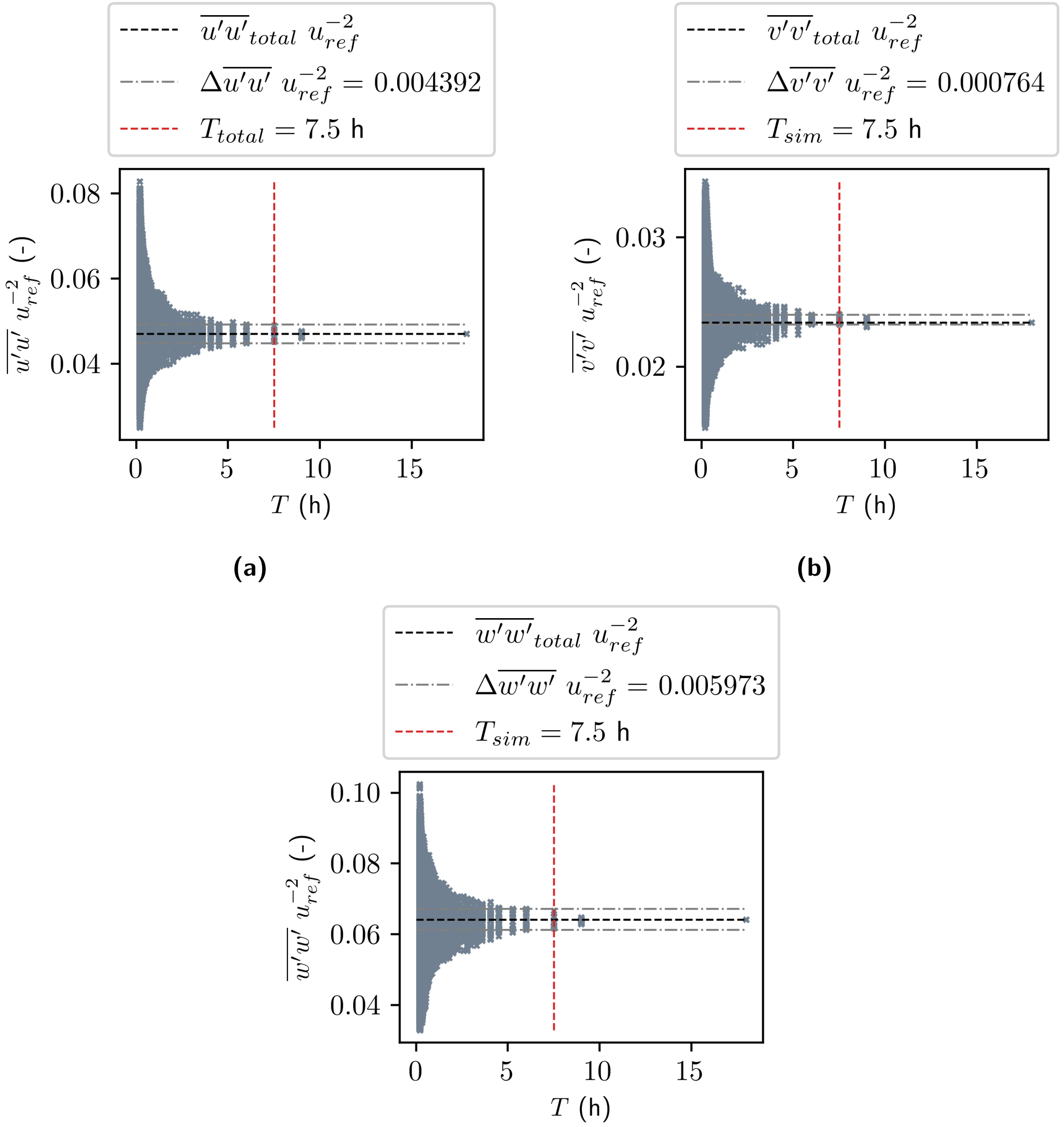

(a) **(b)**

(c)

Figure B.2: Convergence test for the variances of the *PALM*-simulations. Time series were output for a wall-distance of 4 m in full scale.

Correlograms for all three velocity components are shown in Fig. B.3. The correlation coefficients were calculated for time series between the approach boundary layer flow in front of the single building (BL), two positions behind (B1 and B2) and one position next the single building (S1). All positions are marked in Fig. 4.18a. There is no observable correlation between any of the time series. It can be concluded that the model domain is long enough for the turbulence, which was induced by the single building obstacle, to decay. The approach flow is not affected by the wake of the building.

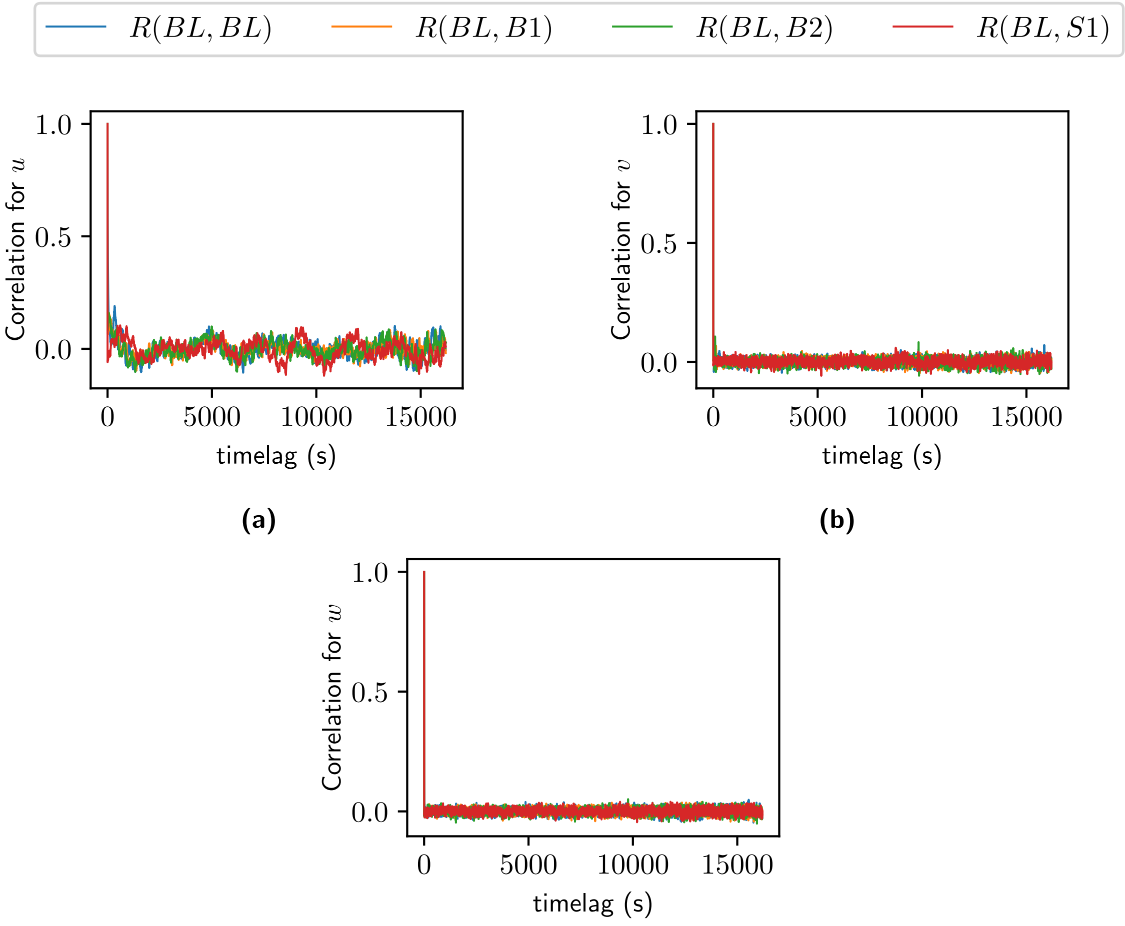

(a)

(b)

(c)

Figure B.3: Correlation coefficients of time series output in front (BL), behind (B1 and B2) and next (S1) to the model building at a height of $z = 25$m.

C Processing Software for Wind Tunnel and PALM Data

The processing routines used to compute the results presented in this thesis are publicly available in the Github repository `https://github.com/benediktseitzer/palm_python` and can be downloaded and applied to the collected data. The python scripts import the self-written *palm_py*-python package which is implemented to read and process NetCDF *PALM* output data of several types (masked output of time series, horizontally averaged profile data, 3D volume data). The *palm_py*-python package consists of four sub-packages:

- palm_py/
    1. env/
    2. read/
    3. calc/
    4. plot/

The first sub-package creates the local environment for saving plots and data and also automatically reads the needed *PALM* configuration-files from the *PALM*-run which is analysed. The second sub-package contains functions for reading the NetCDF-output data which is written in the *PALM* data format. The third sub-package contains functions calculating several flow statistics which are used in this work and more. The fourth sub-package contains simple plotting-functions in a chosen default style. It is advised to write own plotting routines, since use-cases differ.

Additionally, wind tunnel data was analised by using the *Wind tunnel python package* developed at the EWTL group over the course of the last decade. It can be downloaded under `https://gitlab.dkrz.de/ewtl/windtunnel` with a standard DKRZ-account. A proper documentation of the package is included.

D Additional Findings

In this appendix, additional results are shown, which were not directly included in Chapter 5 for the sake of brevity and readability. The results shown are sorted by model configuration and start with additional results for the quadrant analysis of the horizontal plate of homogeneous roughness.

D.1 Horizontal Plate of Homogeneous Roughness

The following Figures show quadrant analysis results that were not included in the main text. Figure D.1 shows the JPDFs for all *PALM* runs conducted (Tab. 4.4) for the model configuration of the horizontal plate of homogeneous roughness. They were computed using the time series taken at a height of $z = 5$ m. All JPDFs show the same elliptical shape aligned with the quadrants Q2 and Q4. This indicates the expected higher occurrence of ejection (Q2) and sweep (Q4) events. Wall-normal fluctuations (w') are more frequent at higher roughness lengths z_0 and also for the G91 model. The results of the G91 model thus agree better with the wind tunnel flow. This observation supports the general findings from Sec. 5.1.

The quadrant contribution profiles for wind tunnel measurements over the horizontal plate with a flat surface (Fig. D.2a) and a medium rough surface (Fig. D.2b) are shown. At both surfaces, ejection events contribute stronger to the total turbulent flux within the roughness sublayer. Figure D.3 shows the quadrant contribution of the *PALM* runs with roughness lengths of $z_0 = 0.06$ m for the D80 and the G91 model.

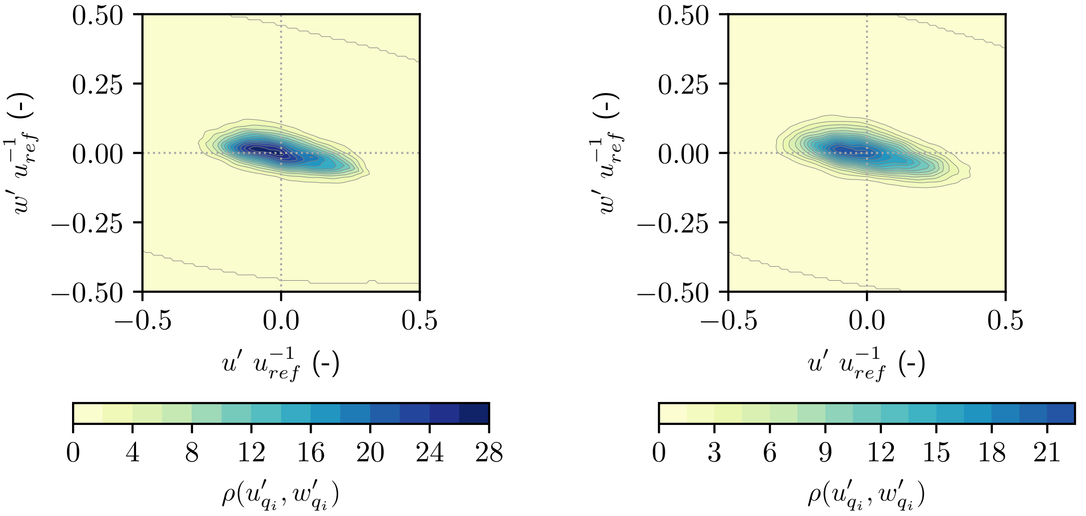

(a) Deardorff, $z_0 = 0.021$m **(b)** Deardorff, $z_0 = 0.06$m

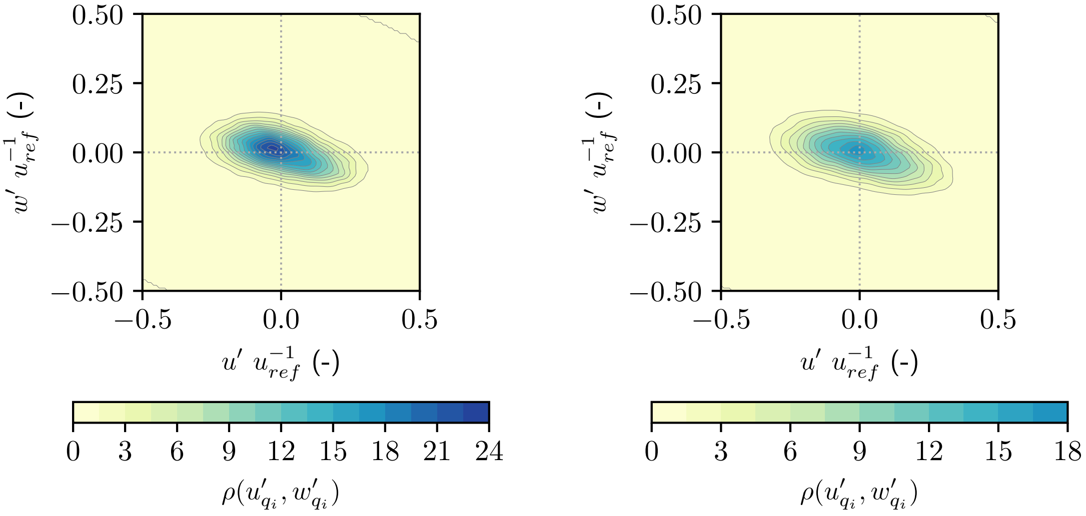

(c) Germano, $z_0 = 0.021$m **(d)** Germano, $z_0 = 0.06$m

Figure D.1: Shown are the JPDFs for all PALM runs listed in Tab. 4.4. These are (a) Deardorff model with $z_0 = 0.021$ m, (b) Deardorff model with $z_0 = 0.06$ m, (c) Germano model with $z_0 = 0.021$ m, (d) Germano model with $z_0 = 0.06$ m. The colorbar is normalised to the maximum value of the JPDF shown in (a).

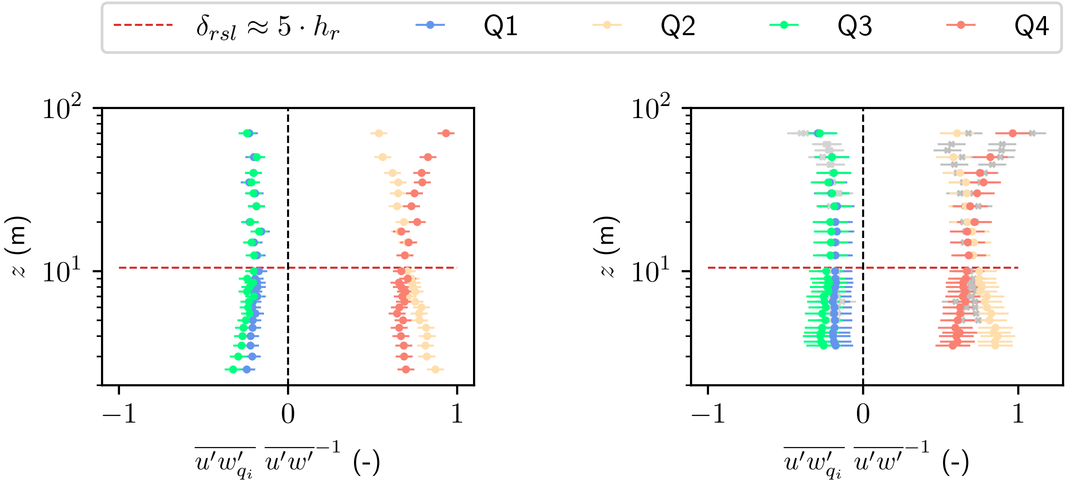

(a) flat surface **(b)** medium rough surface

Figure D.2: Vertical profiles of quadrant contributions for the two wind tunnel surfaces (a) flat and (b) medium rough.

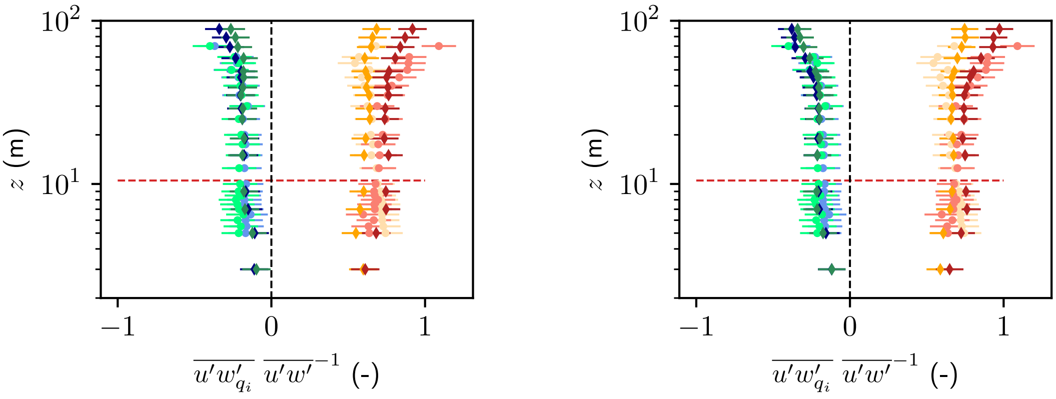

(a) Deardorff model **(b)** Germano model

Figure D.3: Quadrant contribution profiles of the wind tunnel reference profile and the *PALM* runs with (a) the Deardorff SGS model and (b) the Germano SGS model. For both model runs, a roughness length of $z_0 = 0.06$ m was used.

D.2 Single Buildings of different roughnesses

The following Figures show findings, which are associated with the model configuration of the single building with different facade roughness. Figure D.4 shows the velocity distribution of the streamwise velocity u measured close to the single building wall at the point of reattachment of the detaching vortex at the front corner of the building.

The vectorplot in Fig. D.5 shows the mean horizontal wind vectors at mid-building height calculated by *PALM*. The near-wall mean wind in the middle of the building points streams to the left. Thus, the reattachment point is not located at the middle of the building length but further downstream (to the right).

Figures D.6 to D.11 show the flow statistics for comparison positions, which were not included to the main text.

The quadrant contribution profiles for locations SB_SI_front, SB_LU and SB_LE are shown in Figs. D.12 to D.14. The observed effect of surpressed near-wall anisotropy in the *PALM* results is also visible at these comparison positions. Figure D.15 shows the contour plot of the (co-)spectral energy density for the medium rough facade (WB).

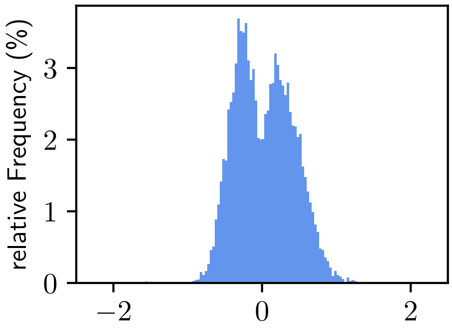

Figure D.4: The distribution of the streamwise velocity at the point of reattachment which is also visible in Fig. 5.4a.

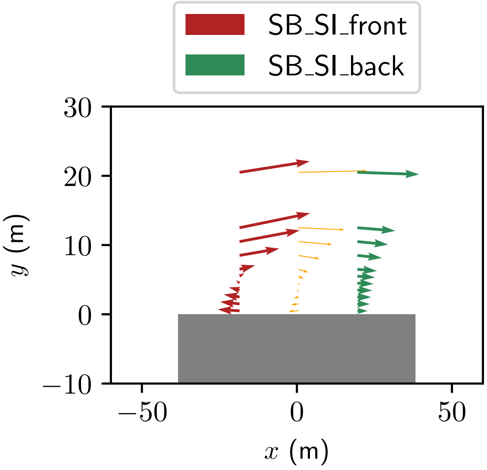

Figure D.5: The vectorplot of the horizontal flow components calculated by *PALM* for the single building case at 0° approach wind.

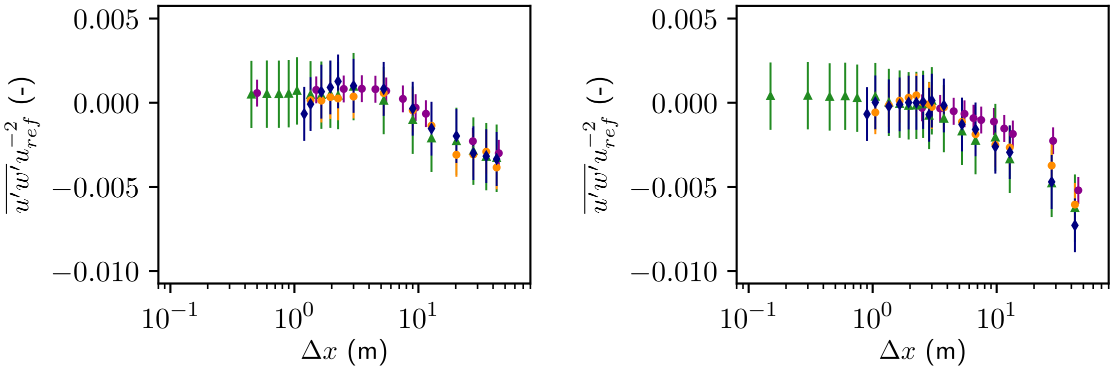

(a) **(b)**

Figure D.6: Shown are the wall-normal turbulent flux profiles for the measurement locations (a) SB_LU and (b) SB_LE

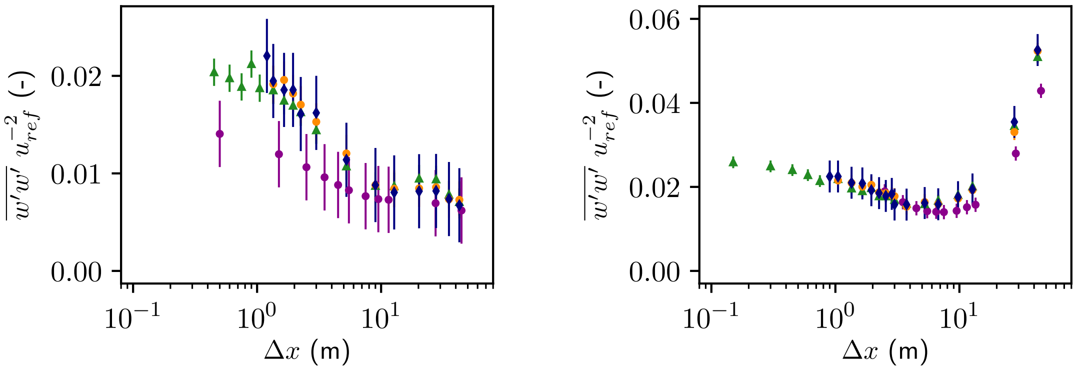

(a) **(b)**

Figure D.7: The variance of the respective wall-parallel velocity component w for the measurement locations (a) SB_LU and (b) SB_LE

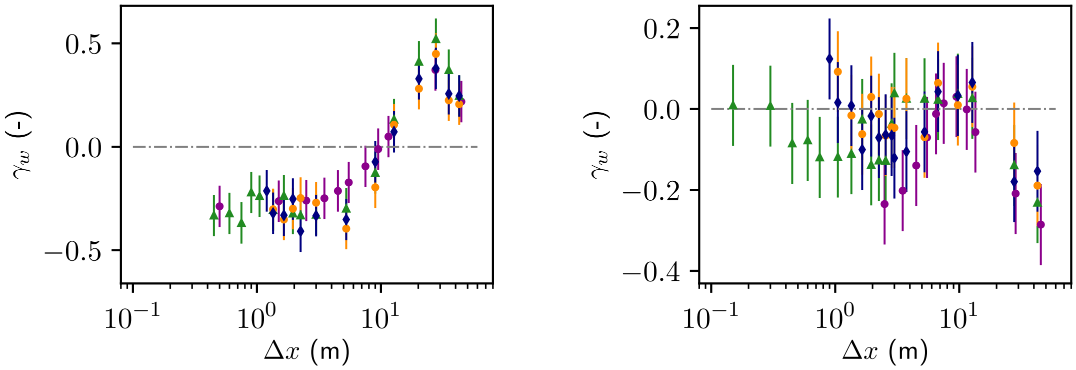

(a) **(b)**

Figure D.8: The skewness of the respective wall-parallel velocity component w for all measurement locations (a) SB_LU and (b) SB_LE

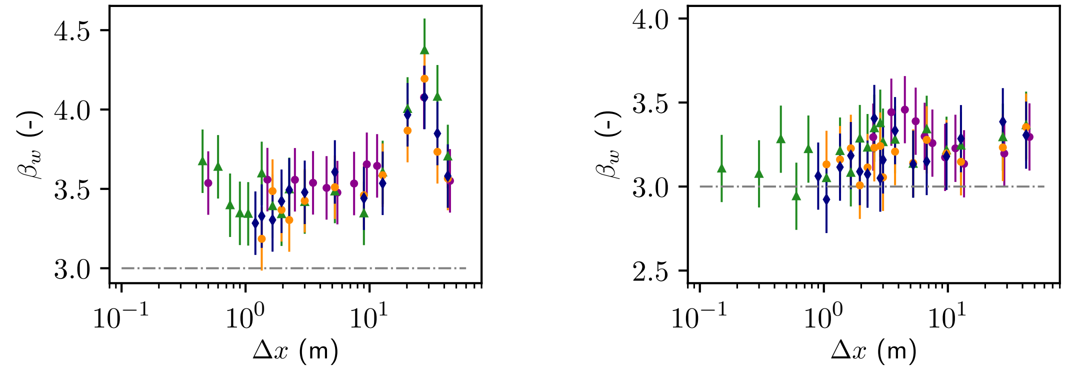

(a) **(b)**

Figure D.9: The kurtosis of the respective wall-parallel velocity component w for the measurement locations (a) SB_LU and (b) SB_LE

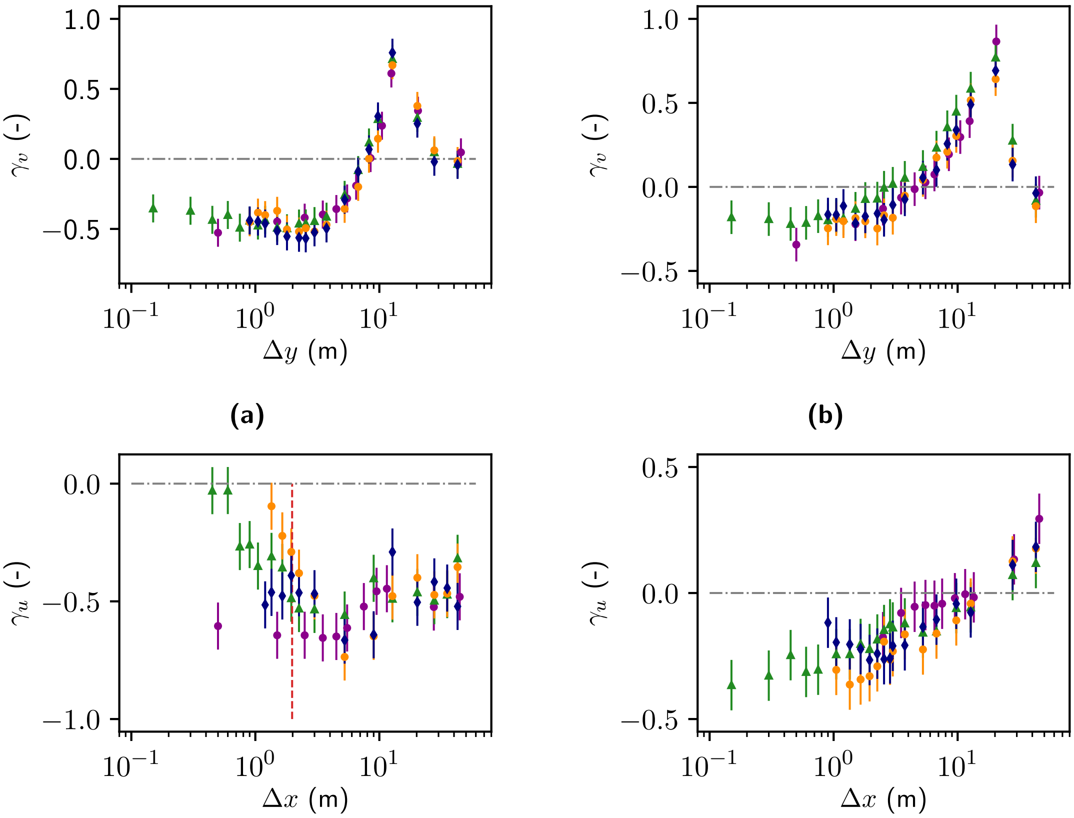

(a) **(b)**

(c) **(d)**

Figure D.10: The skewness of the respective wall-normal velocity component v or u for all measurement locations (a) SB_SI_front (b) SB_SI_back (c) SB_LU and (d) SB_LE.

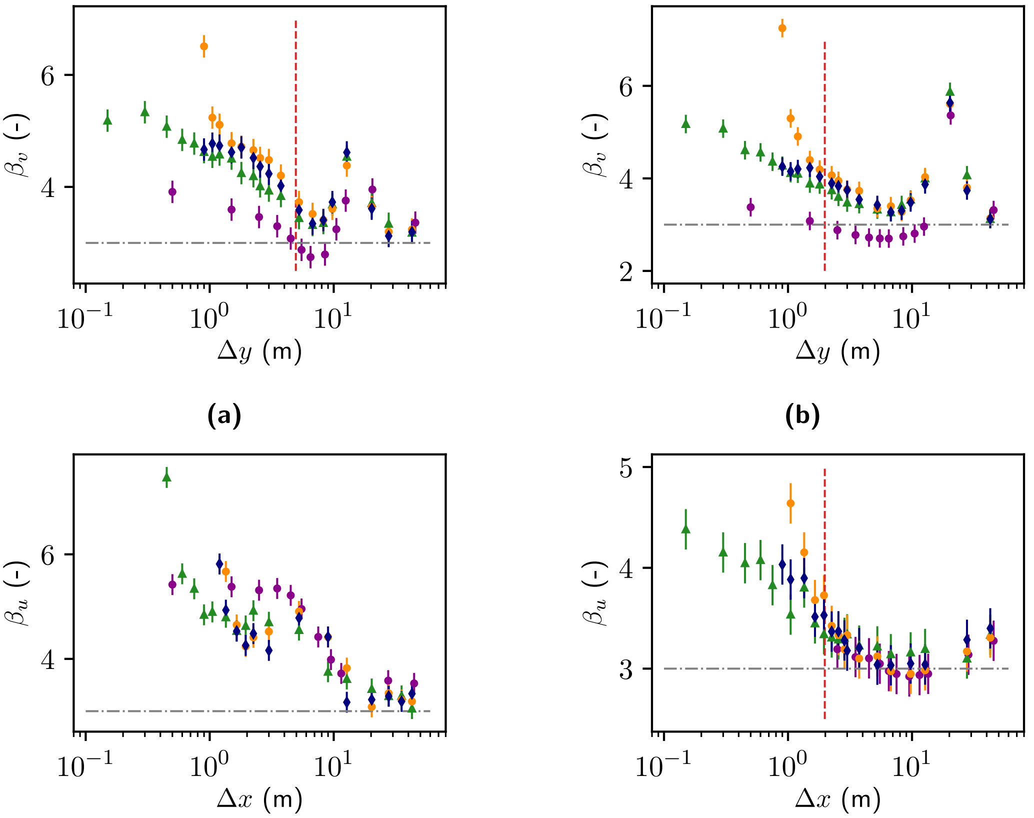

(a) **(b)**

(c) **(d)**

Figure D.11: The kurtosis of the respective wall-normal velocity component v or u for all measurement locations (a) SB_SI_front (b) SB_SI_back (c) SB_LU and (d) SB_LE.

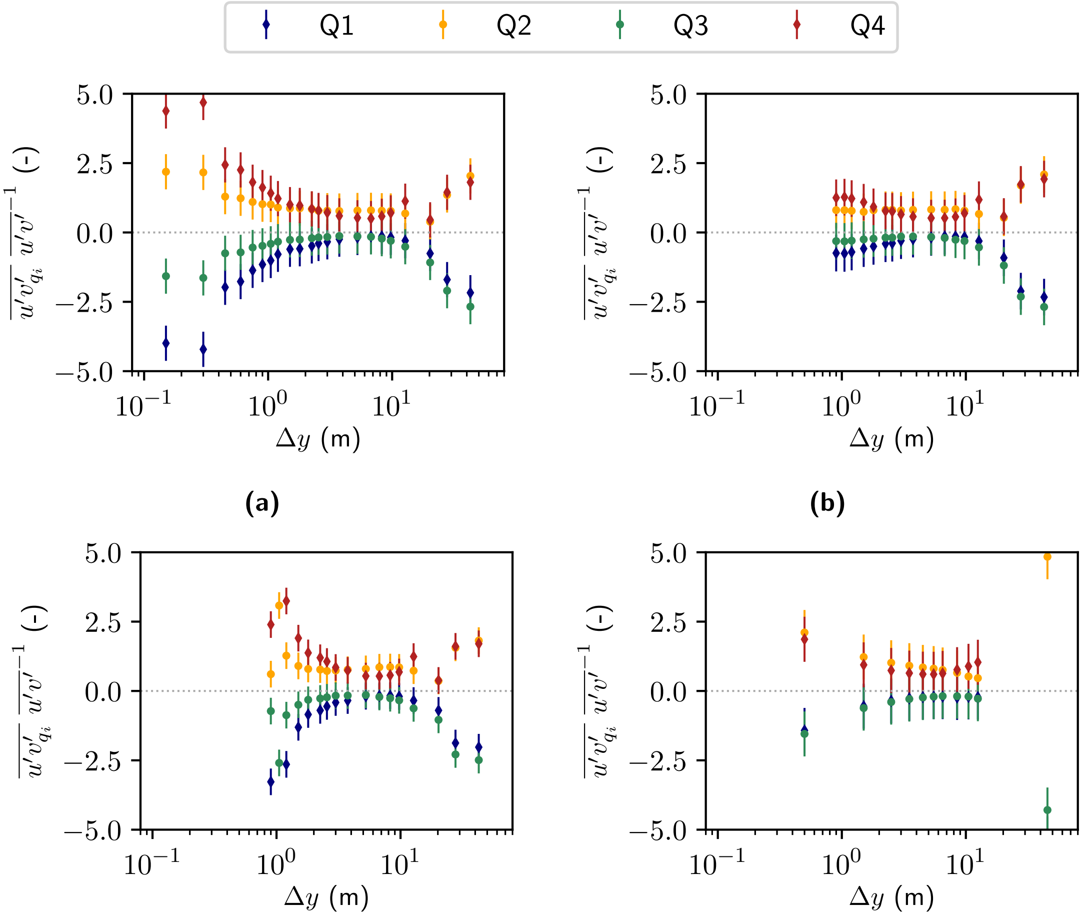

(a) (b) (c) (d)

Figure D.12: Quadrant contribution profiles for the single building case at the profile position in the recirculation zone (SB_SI_front). Shown are results for all four wind tunnel facades: (a) flat FL (b) medium rough WB and (c) rough (BR). The lower right panel (d) shows the results for the corresponding *PALM* simulation.

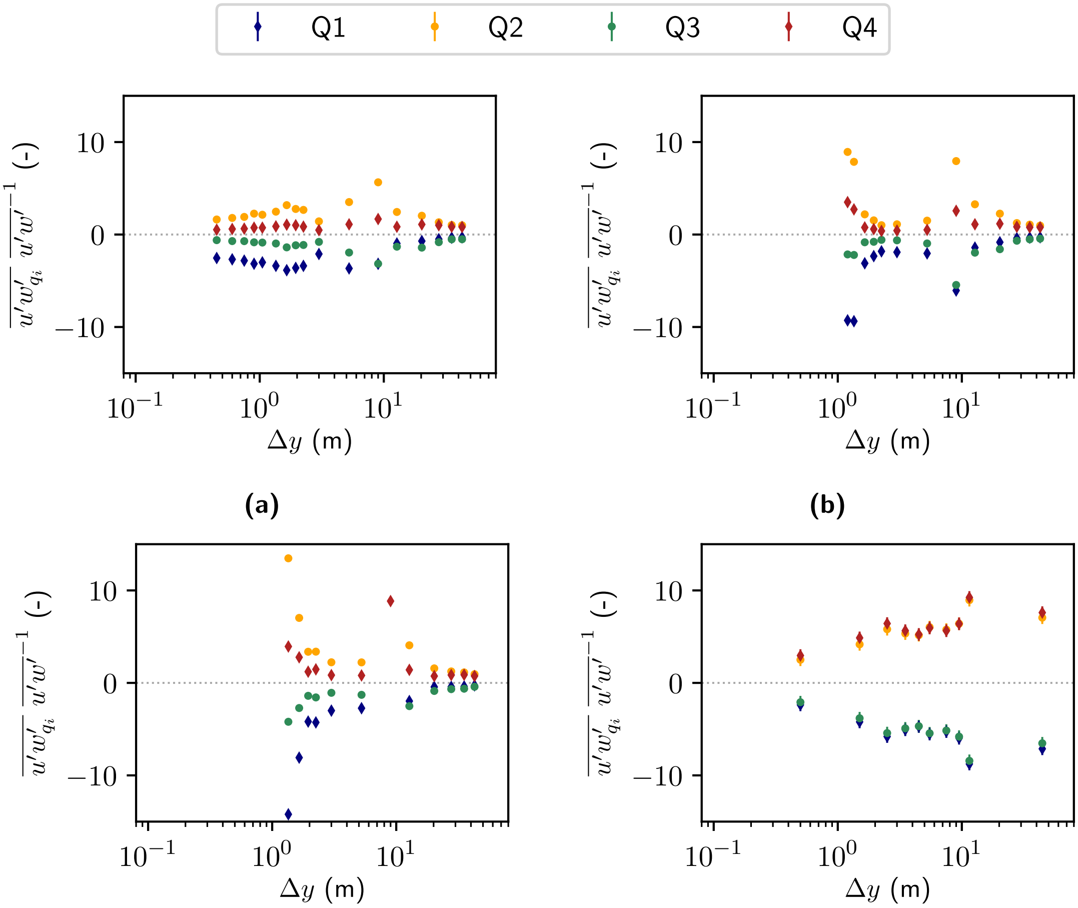

(a) **(b)**

(c) **(d)**

Figure D.13: Quadrant contribution profiles for the single building case and the approach wind of 90^0 measured in front of the building (SB_SI_LU). Shown are results for all four wind tunnel facades: (a) flat FL (b) medium rough WB and (c) rough (BR). The lower right panel (d) shows the results for the corresponding *PALM* simulation.

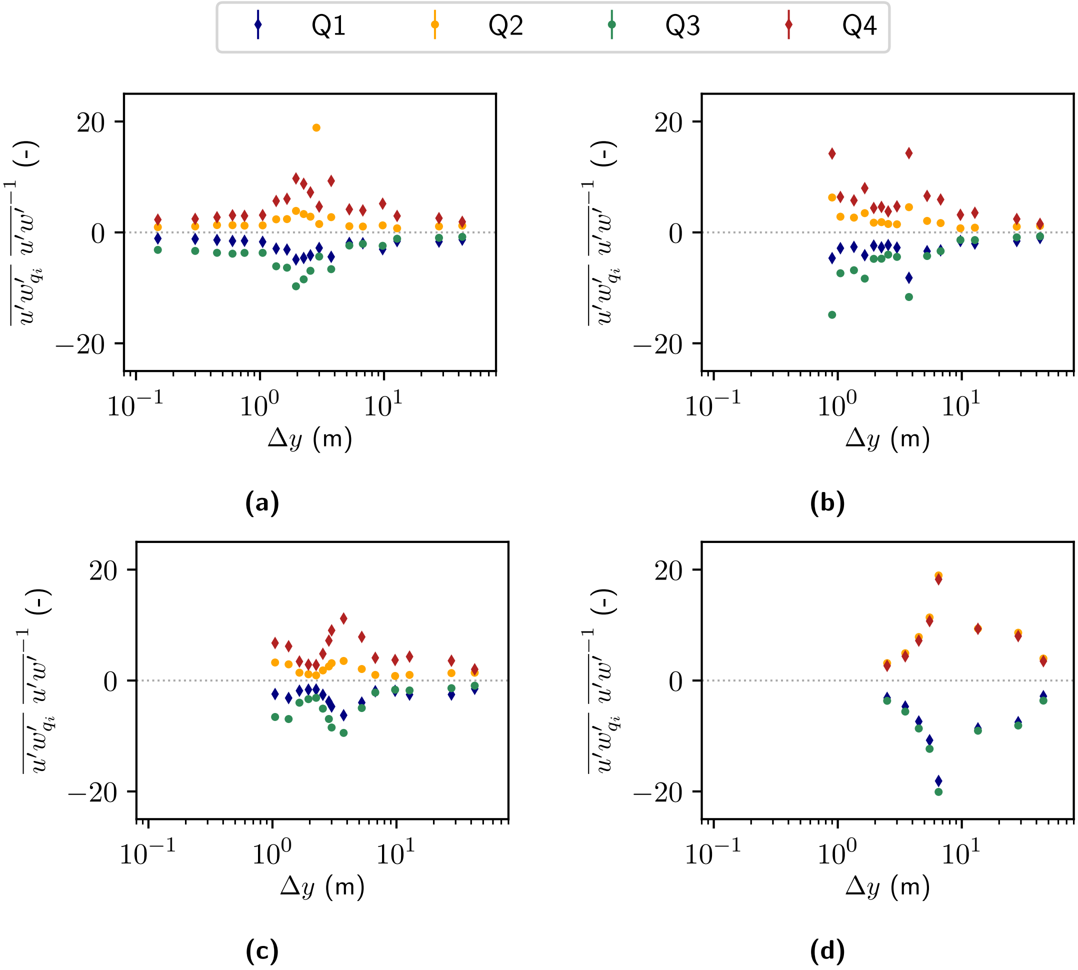

Figure D.14: Quadrant contribution profiles for the single building case and the approach wind of 90^0 measured behind the building (SB_SI_LE). Shown are results for all four wind tunnel facades: (a) flat FL (b) medium rough WB and (c) rough (BR). The lower right panel (d) shows the results for the corresponding *PALM* simulation.

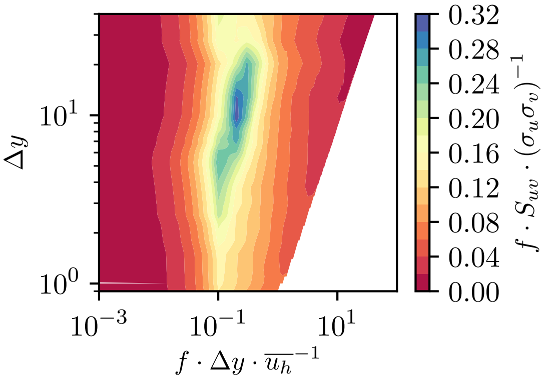

Figure D.15: Contour plots for the energy density co-spectra taken from the SB_SI_back profile position at all wall-distances (y-axis). Shown are the co-spectra for the medium rough facade WB.

Bibliography

Addepalli, B. and Pardyjak, E. R. (2013). Investigation of the Flow Structure in Step-Up Street Canyons-Mean Flow and Turbulence Statistics. *Boundary-Layer Meteorology*, 148(1):133–155.

Addepalli, B. and Pardyjak, E. R. (2015). A study of flow fields in step-down street canyons. *Environmental Fluid Mechanics*, 15(2):439–481.

Adrian, R. J. and Yao, C. S. (1986). Power spectra of fluid velocities measured by laser Doppler velocimetry. *Experiments in Fluids*, 5(1):17–28.

Akinlabi, E., Maronga, B., Giometto, M. G., and Li, D. (2022). Dispersive Fluxes Within and Over a Real Urban Canopy: A Large-Eddy Simulation Study. *Boundary-Layer Meteorology*, 185(1):93–128.

Albertson, J. D. and Parlange, M. B. (1999). Natural integration of scalar fluxes from complex terrain. *Advances in Water Resources*, 23(3):239–252.

Allegrini, J., Dorer, V., and Carmeliet, J. (2013a). Wind tunnel measurements of buoyant flows in street canyons. *Building and Environment*, 59:315–326.

Allegrini, J., Dorer, V., and Carmeliet, J. (2013b). Wind tunnel measurements of buoyant flows in street canyons. *Building and Environment*, 59:315–326.

Anderson, W. and Meneveau, C. (2011). Dynamic roughness model for large-eddy simulation of turbulent flow over multiscale, fractal-like rough surfaces. *Journal of Fluid Mechanics*, 679:288–314.

Anderson, W., Passalacqua, P., Porté-Agel, F., and Meneveau, C. (2012). Large-Eddy Simulation of Atmospheric Boundary-Layer Flow Over Fluvial-Like Landscapes Using a Dynamic Roughness Model. *Boundary-Layer Meteorology*, 144(2):263–286.

Anselmet, F., Gagne, Y., and Hopfinger, E. J. (1984). High-order velocity structure functions in turbulent shear flows. *Journal of Fluid Mechanics*, 140:63–89.

Arakawa, A. and Lamb, V. R. (1977). Computational design of the basic dynamical processes of the UCLA general circulation model. *General circulation models of the atmosphere*, 17(Supplement C):173–265.

Ashrafian, A., Andersson, H. I., and Manhart, M. (2004). DNS of turbulent flow in a rod-roughened channel. *International Journal of Heat and Fluid Flow*, 25(3):373–383.

Auvinen, M., Boi, S., Hellsten, A., Tanhuanpää, T., and Järvi, L. (2020). Study of realistic urban boundary layer turbulence with high-resolution large-eddy simulation. *Atmosphere*, 11(2):1–41.

Baetke, F. (1990). Numerical simulation of turbulent flow over surface-mounted obstacles with sharp edges and corners. *Journal of Wind Engineering and Industrial Aerodynamics*, 35:129–147.

Baggett, J., Jiménez, J., and Kravchenko, A. (1997). Resolution requirements in large-eddy simulations of shear flows. *Annual research briefs*, 343(December):51–66.

Barlow, J. F. and Coceal, O. (2009). A review of urban roughness sublayer turbulence. *Met Office Research and Development*, 1(527):1–68.

Bartzis, J. G. (1991). Adrea-hf: A three-dimensional finite volume code for vapour cloud dispersion in complex terrain. *EUR(Luxembourg)*.

Bastigkeit, I. (2011). *Erzeugung von Validierungsdaten für wirbelauflösende mikroskalige Strömungs- und Ausbreitungsmodelle*. PhD thesis, University of Hamburg.

Basu, S., Holtslag, A., and Bosveld, F. (2012). GABLS3-LES Intercomparison Study. In *Proceedings of the Workshop on Diurnal cycles and the stable boundary layer, 7-10 November 2011, Reading, UK*, pages 75–82.

Basu, S. and Lacser, A. (2017). A Cautionary Note on the Use of Monin–Obukhov Similarity Theory in Very High-Resolution Large-Eddy Simulations. *Boundary-Layer Meteorology*, 163(2):351–355.

Beare, R. J., Macvean, M. K., Holtslag, A. A., Cuxart, J., Esau, I., Golaz, J.-C., Jimenez, M. A., Khairoutdinov, M., Kosovic, B., Lewellen, D., Lund, T. S., Lundquist, J. K., McCabe, A., Moene, A. F., Noh, Y., Raasch, S., and Sullivan, P. (2006). An intercomparison of large-eddy simulations of the stable boundary layer. *Boundary-Layer Meteorology*, 118(2):247–272.

Bottema, M. (1997). Urban roughness modelling in relation to pollutant dispersion. *Atmospheric Environment*, 31(18):3059–3075.

Bou-Zeid, E., Overney, J., Rogers, B. D., and Parlange, M. B. (2009). The effects of building representation and clustering in large-eddy simulations of flows in urban canopies. *Boundary-Layer Meteorology*, 132(3):415–436.

Britter, R. E. and Hanna, S. R. (2003). Flow and dispersion in urban areas. *Annual Review of Fluid Mechanics*, 35:469–496.

Cabot, W. and Moin, P. (2000). Approximate wall boundary conditions in the large-eddy simulation of high Reynolds number flow. *Flow, Turbulence and Combustion*, 63(1):269–291.

Cantwell, B. J. (1981). Organized motion in turbulent flow. *Annual Review of Fluid Mechanics*, 13:457–515.

Castán Broto, V. and Bulkeley, H. (2013). A survey of urban climate change experiments in 100 cities. *Global Environmental Change*, 23(1):92–102.

Champagne, F. (1978). The fine-scale structure of the turbulent velocity field. *Journal of Fluid Mechanics*, 86(1):67–108.

Cheng, H. and Castro, I. P. (2002). Near-wall flow development after a step change in surface roughness. *Boundary-Layer Meteorology*, 105(3):411–432.

Coceal, O., Dobre, A., and Thomas, T. G. (2007a). Unsteady dynamics and organized structures from DNS over an idealized building canopy. *International Journal of Climatology*, 27(14):1943–1953.

Coceal, O., Dobre, A., Thomas, T. G., and Belcher, S. E. (2007b). Structure of turbulent flow over regular arrays of cubical roughness. *Journal of Fluid Mechanics*, 589:375–409.

Cooley, J. W. and Tukey, J. W. (1965). An Algorithm for the Machine Calculation of Complex Fourier Series. *Mathematics of Computation*, 19(90):297–301.

Counihan, J. (1975). Adiabatic atmospheric boundary layers: A review and analysis of data from the period 1880-1972. *Atmospheric Environment (1967)*, 9(10):871–905.

Cui, J., Patel, V. C., and Lin, C. L. (2003). Large-eddy simulation of turbulent flow in a channel with rib roughness. *International Journal of Heat and Fluid Flow*, 24(3):372–388.

Deardorff, J. W. (1980). Stratocumulus-capped mixed layers derived from a three-dimensional model. *Boundary-Layer Meteorology*, 18(4):495–527.

Dodman, D., Hayward, B., Pelling, M., Castan Broto, V., and Chow, W. T. (2022). Cities, settlements and key infrastructure.

Domaradzki, J. A. and Rogallo, R. S. (1990). Local energy transfer and nonlocal interactions in homogeneous, isotropic turbulence. *Physics of Fluids A*, 2(3):413–426.

Fischer, R., Bastigkeit, I., Leitl, B., and Schatzmann, M. (2010). Generation of spatio-temporally high resolved datasets for the validation of les-models simulating flow and dispersion phenomena within the lower atmospheric boundary layer. In *Proc. 5th International Symposium on Computational Wind Engineering (CWE2010), Chapel Hill, North Carolina, USA*.

Gadde, S. N., Stieren, A., and Stevens, R. J. (2021). Large-Eddy Simulations of Stratified Atmospheric Boundary Layers: Comparison of Different Subgrid Models. *Boundary-Layer Meteorology*, 178(3):363–382.

Garratt, J. R. (1978). Flux profile relations above tall vegetation. *Quarterly Journal of the Royal Meteorological Society*, 104(439):199–211.

Garratt, J. R. (1992). *The atmospheric boundary layer*. Cambridge University Press.

Germano, M., Piomelli, U., Moin, P., and Cabot, W. H. (1991). A dynamic subgrid-scale eddy viscosity model. *Physics of Fluids A*, 3(7):1760–1765.

Gousseau, P., Blocken, B., and Van Heijst, G. J. (2013). Quality assessment of Large-Eddy Simulation of wind flow around a high-rise building: Validation and solution verification. *Computers and Fluids*, 79(March):120–133.

Gronemeier, T. and Sühring, M. (2019). On the effects of lateral openings on courtyard ventilation and pollution-A large-eddy simulation study. *Atmosphere*, 10(2):63.

Gronemeier, T., Surm, K., Harms, F., Leitl, B., Maronga, B., and Raasch, S. (2021). Evaluation of the dynamic core of the PALM model system 6.0 in a neutrally stratified urban environment : comparison between LES and wind-tunnel experiments. *Geoscientific Model Development Discussions*, 14(6):3317–3333.

Gropp, W., Lusk, E., Skjellum, A., and Lusk, A. (1999). *Using MPI: portable parallel programming with the message-passing interface*, volume 1. MIT press.

Grötzbach, G. (1987). Direct numerical and large eddy simulation of turbulent channel flows. *Encyclopedia of fluid mechanics*, 6:1337–1391.

Harlow, F. H. and Welch, J. E. (1965). Numerical calculation of time-dependent viscous incompressible flow of fluid with free surface. *Physics of Fluids*, 8(12):2182–2189.

Hertwig, D., Gough, H. L., Grimmond, S., Barlow, J. F., Kent, C. W., Lin, W. E., Robins, A. G., and Hayden, P. (2019). Wake Characteristics of Tall Buildings in a Realistic Urban Canopy. *Boundary-Layer Meteorology*, 172(2):239–270.

Hertwig, D., Patnaik, G., and Leitl, B. (2017a). LES validation of urban flow, part I: flow statistics and frequency distributions. *Environmental Fluid Mechanics*, 17(3):521–550.

Hertwig, D., Patnaik, G., and Leitl, B. (2017b). LES validation of urban flow, part II: eddy statistics and flow structures. *Environmental Fluid Mechanics*, 17(3):551–578.

Heus, T., Van Heerwaarden, C. C., Jonker, H. J., Pier Siebesma, A., Axelsen, S., Van Den Dries, K., Geoffroy, O., Moene, A. F., Pino, D., De Roode, S. R., and De Arellano, J. V. G. (2010). Formulation of the Dutch Atmospheric Large-Eddy Simulation (DALES) and overview of its applications. *Geoscientific Model Development*, 3(2):415–444.

Högström, U. (1996). Review of some basic characteristics of the atmospheric surface layer. *Boundary-Layer Meteorology*, 78(3-4):215–246.

Huang, G., Simoëns, S., Vinkovic, I., Le Ribault, C., Dupont, S., and Bergametti, G. (2016). Law-of-the-wall in a boundary-layer over regularly distributed roughness elements. *Journal of Turbulence*, 17(5):518–541.

Hultmark, M., Calaf, M., and Parlange, M. B. (2013). A new wall shear stress model for atmospheric boundary layer simulations. *Journal of the Atmospheric Sciences*, 70(11):3460–3470.

Hussain, M. and Lee, B. (1980). A wind tunnel study of the mean pressure forces acting on large groups of low-rise buildings. *Journal of Wind Engineering and Industrial Aerodynamics*, 6(3-4):207–225.

Jackson, P. (1981). On the displacement height in the logarithmic velocity profile. *Journal of Fluid Mechanics*, 111:15–25.

Jones, W. and Launder, B. (1972). The prediction of laminarization with a two-equation model of turbulence. *International journal of heat and mass transfer*, 15(2):301–314.

Kaimal, J. C., Wyngaard, J. C., Izumi, Y., and Coté, O. R. (1972). Spectral characteristics of surface-layer turbulence. *Quarterly Journal of the Royal Meteorological Society*, 98(417):563–589.

Kawai, S. and Larsson, J. (2012). Wall-modeling in large eddy simulation: Length scales, grid resolution, and accuracy. *Physics of Fluids*, 24(1).

Kokoska, S. and Zwillinger, D. (2000). *CRC standard probability and statistics tables and formulae*. Crc Press.

Kolmogorov, A. (1942). The equations of turbulent motion in an incompressible flow. *Izvestia. Acad. Sci., USSR*, pages 56–58.

Kolmogorov, A. N. (1941). The local structure of turbulence in incompressible viscous fluid for very large reynolds numbers. *Cr Acad. Sci. URSS*, 30:301–305.

Kolmogorov, A. N. (1962). A refinement of previous hypotheses concerning the local structure of turbulence in a viscous incompressible fluid at high Reynolds number. *Journal of Fluid Mechanics*, 13(1):82–85.

Kolmogorov, A. N. (1991). The Local Structure of Turbulence in Incompressible Viscous Fluid for Very Large Reynolds Numbers. *Proceedings of the Royal Society A: Mathematical, Physical and Engineering Sciences*, 434(1890):9–13.

Kovasznay, L. S., Kibens, V., and Blackwelder, R. F. (1970). Large-scale motion in the intermittent region of a turbulent boundary layer. *Journal of Fluid Mechanics*, 41(2):283–325.

Krogstad, P. Å., Andersson, H. I., Bakken, O. M., and Ashrafian, A. (2005). An experimental and numerical study of channel flow with rough walls. *Journal of Fluid Mechanics*, 530:327–352.

Kundu, P. K., Cohen, I. M., and Dowling, D. R. (2015). *Fluid mechanics*. Academic press.

Leonard, A. (1975). Energy cascade in large-eddy simulations of turbulent fluid flows. *Advances in Geophysics*, 18(PA):237–248.

Letzel, M. O., Helmke, C., Ng, E., An, X., Lai, A., and Raasch, S. (2012). LES case study on pedestrian level ventilation in two neighbourhoods in Hong Kong. *Meteorologische Zeitschrift*, 21(6):575–589.

Letzel, M. O., Krane, M., and Raasch, S. (2008). High resolution urban large-eddy simulation studies from street canyon to neighbourhood scale. *Atmospheric Environment*, 42(38):8770–8784.

Lilly, D. K. (1966). On the Application of the Eddy Viscosity Concept in the Inertial Sub-range of Turbulence. *NCAR manuscript*, 123(1):1341–1349.

Lilly, D. K. (1992). A proposed modification of the Germano subgrid-scale closure method. *Physics of Fluids A*, 4(3):633–635.

Llaguno-Munitxa, M., Bou-Zeid, E., and Hultmark, M. (2017). The influence of building geometry on street canyon air flow: Validation of large eddy simulations against wind tunnel experiments. *Journal of Wind Engineering and Industrial Aerodynamics*, 165(March):115–130.

Macdonald, R. W. (2000). Modelling the mean velocity profile in the urban canopy layer. *Boundary-Layer Meteorology*, 97(1):25–45.

Maronga, B. (2014). Monin-obukhov similarity functions for the structure parameters of temperature and humidity in the unstable surface layer: Results from high-resolution large-eddy simulations. *Journal of the Atmospheric Sciences*, 71(2):716–733.

Maronga, B., Banzhaf, S., Burmeister, C., Esch, T., Forkel, R., Fröhlich, D., Fuka, V., Gehrke, K. F., Geletič, J., Giersch, S., Gronemeier, T., Groß, G., Heldens, W., Hellsten, A., Hoffmann, F., Inagaki, A., Kadasch, E., Kanani-Sühring, F., Ketelsen, K., Khan, B. A., Knigge, C., Knoop, H., Krč, P., Kurppa, M., Maamari, H., Matzarakis, A., Mauder, M., Pallasch, M., Pavlik, D., Pfafferott, J., Resler, J., Rissmann, S., Russo, E., Salim, M., Schrempf, M., Schwenkel, J., Seckmeyer, G., Schubert, S., Sühring, M., von Tils, R., Vollmer, L., Ward, S., Witha, B., Wurps, H., Zeidler, J., and Raasch, S. (2020a). Overview of the PALM model system 6.0. *Geoscientific Model Development Discussions*, 06(June):1–63.

Maronga, B., Gryschka, M., Heinze, R., Hoffmann, F., Kanani-Sühring, F., Keck, M., Ketelsen, K., Letzel, M. O., Sühring, M., and Raasch, S. (2015). The Parallelized Large-Eddy Simulation Model (PALM) version 4.0 for atmospheric and oceanic flows: Model formulation, recent developments, and future perspectives. *Geoscientific Model Development*, 8(8):2515–2551.

Maronga, B., Knigge, C., and Raasch, S. (2020b). An Improved Surface Boundary Condition for Large-Eddy Simulations Based on Monin–Obukhov Similarity Theory: Evaluation and Consequences for Grid Convergence in Neutral and Stable Conditions. *Boundary-Layer Meteorology*, 174(2):297–325.

Maronga, B., Winkler, M., and Li, D. (2022). Can Areawide Building Retrofitting Affect the Urban Microclimate? An LES Study for Berlin, Germany. *Journal of Applied Meteorology and Climatology*, 61(7):800–817.

Marusic, I., Kunkel, G. J., and Porté-Agel, F. (2001). Experimental study of wall boundary conditions for large-eddy simulation. *Journal of Fluid Mechanics*, 446:309–320.

Marusic, I. and Monty, J. P. (2019). Attached Eddy Model of Wall Turbulence. *Annual Review of Fluid Mechanics*, 51:49–74.

Mestayer, P. (1982). Local isotropy and anisotropy in a high-reynolds-number turbulent boundary layer. *Journal of Fluid Mechanics*, 125:475–503.

Moeng, C.-H. and Wyngaard, J. C. (1988). Spectral Analysis of Large-Eddy Simulations of the Convective Boundary Layer. *Journal of the Atmospheric Sciences*, 45(23):3573–3587.

Monin, A. S. and Obukhov, A. M. (1954). Basic laws of turbulent mixing in the surface layer of the atmosphere. *Contrib. Geophys. Inst. Acad. Sci. USSR*, 24(151):163–187.

Obukhov, A. M. (1962). Some specific features of atmospheric tubulence A. *Journal of Fluid Mechanics*, 13(1):77–81.

Oke, T. R. (1984). Methods in urban climatology. *Applied Climatology*, 14(18):19–29.

Oke, T. R. (1988). The urban energy balance. *Progress in Physical Geography*, 12(4):471–508.

Paas, B., Zimmermann, T., and Klemm, O. (2020). Analysis of a turbulent wind field in a street canyon: Good agreement between LES model results and data from a mobile platform. *Meteorologische Zeitschrift*.

Patnaik, G. and Boris, J. (2010). Fast3d-ct: an les model for urban aerodynamics. In *The Fifth International Symposium on Computational Wind Engineering (CWE2010), Chapel Hill, North Carolina, USA*.

Perry, A. and Chong, M. (1982). On the mechanism of wall turbulence. *Journal of Fluid Mechanics*, 119:173–217.

Piomelli, U. (1999). Large-eddy simulation: achievements and challenges. *Progress in Aerospace Sciences*, 35(4):335–362.

Piomelli, U., Ferziger, J., Moin, P., and Kim, J. (1989). New approximate boundary conditions for large eddy simulations of wall-bounded flows. *Physics of Fluids A*, 1(6):1061–1068.

Plate, E. J. (1999). Methods of investigating urban wind fields-physical models. *Atmospheric Environment*, 33(24-25):3981–3989.

Pope, S. B. (2000). *Turbulent Flows*. Cambridge University Press, 10th print edition.

Prandtl, L. (1925). 7. Bericht über Untersuchungen zur ausgebildeten Turbulenz. *ZAMM - Journal of Applied Mathematics and Mechanics / Zeitschrift für Angewandte Mathematik und Mechanik*, 5(2):136–139.

Prandtl, L. (1932). Zur turbulenten strömung in rohren und längs platten. *Ergeb. Aerodyn. Versuchsanst.*, 4:18–29.

Prandtl, L. (1945). Über ein neues formelsystem für die ausgebildete turbulenz. *Nachr. Akad. Wiss. Göttingen, Math-Phys. Kl*, pages 6–19.

Raasch, S. and Schröter, M. (2001). PALM - A large-eddy simulation model performing on massively parallel computers. *Meteorologische Zeitschrift*, 10(5):363–372.

Raupach, M. R., Antonia, R. A., and Rajagopalan, S. (1991). Rough-wall turbulent boundary layers. *Appl. Mech. Rev.*, 44(1):1–25.

Raupach, R., Thom, A. S., and Edwards, I. (1980). A wind-tunnel study of turbulent flow close to regularly arrayed rough surfaces. *Boundary-Layer Meteorology*, 18:373–397.

Raupach, MR and Legg, B. (1984). The uses and limitations of flux-gradient relationships in micrometeorology. *Developments in Agricultural and Managed Forest Ecology*, 13:119–131.

Reiter, S. (2010). Assessing wind comfort in urban planning. *Environment and Planning B: Planning and Design*, 37(5):857–874.

Reynolds, O. (1895). On the Dynamical Theory of Incompressible Viscous Fluids and the Determination of the Criterion. *Philosophical transactions of the royal society of london.(a.)*, 10(186):123–164.

Richardson, L. F. (1922). *Weather Prediction by Numerical Process*. Cambridge University Press.

Rotach, M. W. (1993). Turbulence close to a rough urban surface part I: reynolds stress. *Boundary-Layer Meteorology*, 65(2):1–28.

Saddoughi, S. G. and Veeravalli, S. V. (1994). Local Isotropy in Turbulent Boundary Layers at High Reynolds Number. *Journal of Fluid Mechanics*, 268:333–372.

Saiki, E. M., Moeng, C. H., and Sullivan, P. P. (2000). Large-eddy simulation of the stably stratified planetary boundary layer. *Boundary-Layer Meteorology*, 95(1):1–30.

Scherer, D., Ament, F., Emeis, S., Fehrenbach, U., Leitl, B., Scherber, K., Schneider, C., and Vogt, U. (2019). Three-dimensional observation of atmospheric processes in cities. *Meteorologische Zeitschrift*, 28(2):121–138.

Schumann, U. (1975). Subgrid scale model for finite difference simulations of turbulent flows in plane channels and annuli. *Journal of Computational Physics*, 18(4):376–404.

Smagorinsky, J. (1963). General circulation experiments with the primitive equations: I. The basic experiment. *Monthly weather review*, 91(3):99–164.

Snyder, W. H. (1981). *Guideline for Fluid Modeling of Atmospheric Diffusion*. Environmental Sciences Research Laboratory, Office of Research and Development, 81 edition.

Sreenivasan, K. R. (1989). The turbulent boundary layer. *Frontiers in experimental fluid mechanics*, pages 159–209.

Sreenivasan, K. R. (1995). On the universality of the Kolmogorov constant. *Physics of Fluids*, 7(11):2778–2784.

Stathopoulos, T. and Luchian, H. D. (1990). Wind pressures on buildings with stepped roofs. *Canadian Journal of Civil Engineering*, 17(4):569–577.

Stathopoulos, T. and Zhu, X. (1988). Wind pressures on building with appurtenances. *Journal of Wind Engineering and Industrial Aerodynamics*, 31(2-3):265–281.

Stathopoulos, T. and Zhu, X. (1990). Wind pressures on buildings with mullions. *Journal of Structural Engineering*, 116(8):2272–2291.

Stoll, R. and Porté-Agel, F. (2006). Effect of roughness on surface boundary conditions for large-eddy simulation. *Boundary-Layer Meteorology*, 118(1):169–187.

Stull, R. B. (1988). An introduction to boundary layer meteorology. *An introduction to boundary layer meteorology*.

Sullivan, P. P., Weil, J. C., Patton, E. G., Jonker, H. J., and Mironov, D. V. (2016). Turbulent winds and temperature fronts in large-eddy simulations of the stable atmospheric boundary layer. *Journal of the Atmospheric Sciences*, 73(4):1815–1840.

Taylor, G. I. (1935). Statistical theory of turbulence. *Proceedings of the Royal Society of London. Series A, Mathematical and Physical Sciences*, 151(873):421–444.

Taylor, G. I. (1938). The spectrum of turbulence. *Proceedings of the Royal Society of London. Series A, Mathematical and Physical Sciences*, 164(919):476–490.

Tennekes, H. and Lumley, J. L. (1972). *A first course in turbulence*. MIT press.

Thom, A., Stewart, J., Oliver, H., and Gash, J. (1975). Comparison of aerodynamic and energy budget estimates of fluxes over a pine forest. *Quarterly Journal of the Royal Meteorological Society*, 101(427):93–105.

Tolias, I. C., Koutsourakis, N., Hertwig, D., Efthimiou, G. C., Venetsanos, A. G., and Bartzis, J. G. (2018). Large Eddy Simulation study on the structure of turbulent flow in a complex city. *Journal of Wind Engineering and Industrial Aerodynamics*, 177(February):101–116.

Townsend, A. (1980). *The structure of turbulent shear flow*. Cambridge University Press.

Townsend, A. A. (1951). The structure of the turbulent boundary layer. *Mathematical Proceedings of the Cambridge Philosophical Society*, 47(2):375–395.

Townsend, A. A. (1961). Equilibrium layers and wall turbulence. *Journal of Fluid Mechanics*, 11(1):97–120.

Tropea, C., Yarin, A. L., and Foss, J. F. (2007). *Springer handbook of experimental fluid mechanics*. Springer, 1 edition.

Udina, M., Sun, J., Kosović, B., and Soler, M. R. (2016). Exploring Vertical Turbulence Structure in Neutrally and Stably Stratified Flows Using the Weather Research and Forecasting–Large-Eddy Simulation (WRF–LES) Model. *Boundary-Layer Meteorology*, 161(2):355–374.

VDI 3783 Blatt 12 (2000). *Physikalische Modellierung von Strömungs- und Ausbreitungsvorgängen in der atmosphärischen Grenzschicht - Windkanalanwendungend*. Beuth Verlag, Berlin.

Wallace, J. M. (2016). Quadrant Analysis in Turbulence Research: History and Evolution. *Annual Review of Fluid Mechanics*, 48:131–158.

Wallace, J. M., Eckelmann, H., and Brodkey, R. S. (1972). The wall region in turbulent shear flow. *Journal of Fluid Mechanics*, 54(1):39–48.

Wengle, H. and Werner, H. (1993). *Large-eddy simulation of turbulent flow over and around a cube in a plate channel*. Springer.

Wicker, L. J. and Skamarock, W. C. (2002). Time-splitting methods for elastic models using forward time schemes. *Monthly Weather Review*, 130(8):2088–2097.

Williamson, J. H. (1980). Low-storage Runge-Kutta schemes. *Journal of Computational Physics*, 35(1):48–56.

Willmarth, W. W. (1975). Structure of turbulence in boundary layers. *Advances in applied mechanics*, 15:159–254.

Wyngaard, J. C. and Tennekes, H. (1970). Measurements of the Small-Scale Structure of Turbulence at Moderate Reynolds Numbers. *The Physics of Fluids*, 13(8):1962–1969.

Eidesstattliche Versicherung — Declaration on Oath

—

Hiermit erkläre ich an Eides statt, dass ich die vorliegende Dissertationsschrift selbst verfasst und keine anderen als die angegebenen Quellen und Hilfsmittel benutzt habe.

—

I hereby declare upon oath that I have written the present dissertation independently and have not used further resources and aids than those stated.

Hamburg, 30.03.2023